TRANSPARENT CONDUCTING THIN FILMS FOR ELECTRO OPTICAL DEVICES

Thesis Submitted for the Award of the Degree of

DOCTOR OF PHILOSOPHY

in

Physics

By

Shruti Bakshi

Registration Number:12106369

Supervised By

Dr. Suman Rani (11795)

Department of Physics (Professor)

Lovely Professional University

LOVELY PROFESSIONAL UNIVERSITY, PUNJAB
2025

Dedicated to my loving parents,

Meena Kumari and Kapil Bakshi

DECLARATION

I, hereby declared that the presented work in the thesis entitled "**Transparent Conducting Thin films for Electro Optical Devices**" in fulfilment of degree of **Doctor of Philosophy (Ph. D.)** is outcome of research work carried out by me under the supervision of Dr. Suman Rani, working as professor in the Department of Physics of Lovely Professional University, Punjab, India. In keeping with general practice of reporting scientific observations, due acknowledgements have been made whenever work described here has been based on findings of other investigator. This work has not been submitted in part or full to any other University or Institute for the award of any degree.

(Signature of Scholar)

Name of the scholar: Shruti Bakshi

Registration No.: 1210639

Department/school: Physics/School of Chemical Engineering and Physical Sciences

Lovely Professional University,

Punjab, India

CERTIFICATE

This is to certify that the work reported in the Ph. D. thesis entitled "**Transparent Conducting Thin films for Electro Optical devices**" submitted in fulfillment of the requirement for the award of degree of **Doctor of Philosophy (Ph.D.)** in the Department of Physics, is a research work carried out by Shruti Bakshi,12106369, is bonafide record of his/her original work carried out under my supervision and that no part of thesis has been submitted for any other degree, diploma or equivalent course.

(Signature of Supervisor)

Name of supervisor: Dr. Suman Rani

Designation: Professor

Department/school: Department of Physics

University: Lovely Professional University

 Phagwara, Punjab.

Abstract

Innovations in display technologies and energy-harvesting devices are at the forefront of modern technological advancements, driven by the unique properties of a specialized class of materials. Among these, transparent conducting materials are indispensable components in the development of next-generation optoelectronic devices and renewable energy systems. Transparent conducting materials uniquely combine high transparency with excellent conductivity, which are two inherently contradictory characteristics, making them critical for applications including light-emitting diodes (LEDs), touchscreens, solar cells, smart windows, and display devices. Transparent conducting materials play an essential role in this transition by enabling the fabrication of devices that utilize less power while supporting sustainable energy production. Indium-doped tin oxide (ITO) and fluorine-doped tin oxide (FTO) have historically been the leading transparent conducting materials in commercial applications; a shift is occurring due to indium's restricted availability and high price. Consequently, there is an increasing interest in substitute materials, such as zinc oxide-based semiconductors and other cost-effective compounds. The objective of exploring these novel materials is to ensure the development of sustainable and economically feasible solutions for future optoelectronic and energy-related technologies.

The core aim of this research is to find alternative materials to Indium Tin Oxide (ITO) for optoelectronic devices, which depict excellent transparency of more than 80% and conductivity of approximately 10^2-10^4 Scm^{-1}. In this study, we explored three materials, two dopants, and their composites to analyse their transmission and conductivity.

1) ZnO, ZnS, SnO$_2$ thin films are synthesized by a cheap and cost-effective approach, sol-gel spin coating, and study their optical and electrical properties.

2) Further study the influence of dopants such as magnesium and copper at 0.1%, 0.5%, and 1.0% mol% concentration on the ZnO, ZnS, and SnO$_2$ thin films formed by the sol-gel spin coating approach and study their optical and electrical properties.

3) Also, study the optical and electrical properties of Composites such as Zn(O,S) (ZnO: SnO$_2$) and Zn(S, Sn) ZnS: SnO$_2$ thin films at different ratios, including

50%:50%, 40%:10%, 30%:20%, 20%:30% and 10%:40% prepared by sol gel spin coating approach.

The Synthesized materials were characterized by using a variety of techniques, including X-ray Diffraction (XRD) was employed for phase identification, while Field Emission Scanning Electron Microscopy (FESEM) provided surface morphological insights and thickness measurement of the thin films. Elemental composition was determined by Energy Dispersive X-ray Analysis (EDX). AFM has been carried out to determine the surface roughness of the thin films. UV-visible spectrometers were considered to analyze optical characteristics such as transmission (%), optical band gap, and refractive index. Electrical characteristics such as IV data and activation energy, conductivity, carrier type, carrier concentration, and mobility were determined by two-probe instruments (SES-CAM TPX setup) and by Hall measurement.

First studied the pure and magnesium/copper-doped ZnO thin films were studied by the sol-gel spin coating method, followed by a five-hour post-heating at 500°C. XRD analysis confirmed the hexagonal wurtzite structure for all films, with doping increasing crystallite size. UV-Visible spectroscopy revealed that Cu and Mg doping significantly influenced transmission. Transmission improved from 83% to 90% with magnesium doping. However, copper doping yielded a more significant increase, reaching an impressive 96.8% transparency in the visible range, especially at 1.0% concentration. This superior optical property makes the films highly promising for solar cell and display applications. Hall measurements showed that 1.0% Cu^{2+} doping yielded the highest conductivity ($1.21\times10^{4}Scm^{-1}$) among all samples, attributed to enhanced charge carrier transport. This same sample also exhibited the highest figure of merit ($2.2\times10^{-1}\Omega^{-1}$), underscoring its significant potential for transparent conducting oxide (TCO) applications in optoelectronic devices.

After that, synthesized undoped, magnesium (Mg)-doped, and copper (Cu)-doped SnO_2 thin films using a sol-gel spin coating approach, followed by one-hour annealing at 500 °C. Optical studies showed that both Mg and Cu doping enhanced the transmission of undoped SnO_2 films in the visible spectrum. Notably, 0.5% Mg doping achieved the highest transmission rate of 99.5%. 0.5% Mg^{2+} doping resulted in the highest conductivity of $8.42\times10^{3}Scm^{-1}$ and, surprisingly, demonstrated a transition from n-type

to p-type conduction. This 0.5% Mg-doped SnO_2 film also exhibited the highest figure of merit ($2.9 \times 10^{-2} \Omega^{-1}$), affirming its potential as a cost-effective TCO in optoelectronic devices such as flat panels, displays, photovoltaic devices, and solar cells.

Further studied the Cu^{2+}/Mg^{2}-doped ZnS thin films, synthesized via the sol-gel spin coating method and post-annealed at 500 °C for five hours. Doping at 0.1%, 0.5%, and 1.0% concentrations significantly improved their structural, morphological, optical, and electrical properties. X-ray Diffraction (XRD) confirmed that all films maintained a zinc blende structure with prominent (111), (220), and (311) planes, and no impurity phases were detected. Peak shifts and enhanced (111) intensity indicated successful substitution of Zn^{2+} by Cu^{2+} and Mg^{2+}, leading to improved crystallinity and growth orientation. UV-Visible spectroscopy demonstrated high transparency ($\sim$95–98%) in the visible range for all films, with 0.5% Cu^{2+} doping showing the best transmission. The highest conductivity (7.85×10^2 Scm^{-1}) was observed at 0.5% Cu^{2+} doping, driven by an optimal carrier concentration (1.5×10^{18} cm^{-3}), even with reduced mobility. Overall, ZnS thin films doped with 0.5% Cu^{2+} or Mg^{2+} exhibit superior electrical and optical characteristics, making them strong candidates for transparent conducting applications in solar cells, display panels, flat-panel displays, and other optoelectronic devices.

The study presents a comparative analysis of various host materials such as ZnO, SnO_2, and ZnS alongside their doped variations incorporating Mg and Cu. The materials were evaluated for their optical and electrical properties, including transmission percentage, conductivity, carrier concentration, and figure of merit. ZnS exhibited the highest transmission (95%), while ZnO showed the highest conductivity (1.0114×10^4 Scm^{-1}). The incorporation of Mg and Cu as dopants demonstrated notable improvements in carrier concentration and optical transmission, with Cu: SnO_2 achieving a transmission of up to 99.5%. Additionally, composite formulations combining ZnO, SnO_2, and ZnS revealed optimized properties with enhanced transmission and conductivity, highlighting their potential for applications in optoelectronic devices. Overall, ZnO and Zn(O, S) ZnO: SnO_2 composites emerge as the most promising candidates, balancing optical and electrical performance, thus holding significant potential for use in modern optoelectronic and photovoltaic devices.

Acknowledgments

Table of Contents

8.2. Conclusion

        8.2.1. Key Finding

8.3. Future Scope

References

List of Publications

List of Conferences attended

List of Workshops attended

List of Tables

List of Figures

Abbreviations and symbols

FTO = fluorine-doped oxide tin

ITO = Indium-doped tin oxide

ZnO = Zinc Oxide

ZnS = Zinc Sulfide

SnO_2 = Tin Oxide

TCO = Transparent Conducting Oxides

LED = Light Emitting Diode

Cu = Copper

Mg = Magnesium

CNT = Carbon nanotubes

CB = Conduction Band

VB = Valence Band

XRD = X-ray Diffraction

FE-SEM = Field Emission Scanning Electron Spectroscopy

FTIR = Fourier Transform Infrared Spectroscopy

UV-Vis = Ultraviolet-Visible Spectroscopy

TPX = Two Probe instruments

AFM = Atomic Force Microscope

HMS = Hall Effect Measurements

EDX = Energy Dispersive X-ray Spectroscopy

JCPDS = Joint Committee on Powder Diffraction Standards

Ra = Average roughness

RMS = Root Mean Square Roughness

FOM = Figure of Merit

Ea = Activation Energy

λ = Wavelength

α = Absorption Coefficients

k = Extinction Coefficient

n = Refractive index

S = Simon

eV = Electron Volt

nm = Nanometer

t = Thickness

T = Transmission

R = Reflection

A = Absorbance

D = Crystalline Size

δ = Dislocation Density

a = Lattice Constant

ε = Lattice Strain

Å = Angstrom

Θ = Bragg's Diffraction angle

Eg = Energy Band Gap

K = Kelvin

υ = Frequency

β = Full Width Half Maxima

d = Interplanar Spacing

V = Volume

ne = Carrier Concentration

σ = Conductivity

μ = Mobility

ρ = Resistivity

Chapter 1

Introduction

1. Introduction

In the modern age of technological advancement and industrialization, Transparent conducting oxides (TCOs) thin films have emerged as essential materials, revolutionizing various industries. It became the cornerstone of modern optoelectronic devices. As of 2025, the TCO market is valued at approximately $686.8 million and is projected to grow at a compound annual growth rate (CAGR) of 10.5%, reaching $2.27 billion by 2032. This outgrowth is driven by their extensive use in consumer electronics, architectural technologies, and renewable energy systems. In consumer electronics, TCOs are necessary for touchscreens and flat-panel displays, providing responsive interfaces and high-resolution display devices such as smartphones, tablets, and smart TVs[1]. In the field of renewable energy, Transparent Conducting Oxides are indispensable in solar panels, where they function as transparent electrodes to optimize light absorption and energy conversion[2]. This has significantly contributed to global efforts to transition to clean energy sources and reduce dependence on fossil fuels (coal and petroleum). Architectural applications also benefit from TCOs, particularly in innovative glass technologies that regulate heat and light transmission in buildings[3]. These coatings help conserve energy by reducing heating and cooling costs, aligning with global sustainability goals and urban development initiatives. TCOs directly support sustainability initiatives by enabling efficient energy solutions and reducing environmental footprints. Their applications in solar panels accelerate the adoption of renewable energy sources, while smart glass technologies promote energy conservation worldwide[4]. As industries continue to innovate and adopt advanced technologies, TCOs are poised to play an even greater role in shaping a sustainable future for human civilization while meeting the growing demands of modern technology-driven societies[5].

1.1. Transparent Conducting Materials

A class of materials known as transparent conducting materials is engineered to possess high electrical conductivity and strong transmission within the visible region of the electromagnetic spectrum[6]. Following the discovery of this material type, significant research and development efforts have focused on commercializing these thin-film coatings. Present-day commercial products utilize metal oxide thin films known as transparent conducting oxides (TCOs). Oxides possessing high visible light transmission and high electrical conductivity are termed transparent conductive oxides (TCOs)[7]. Transparent conducting materials typically have a wide band gap (> 3.1 eV), ensuring high transmittance in the visible range, along with an increased free carrier concentration (> 10^{20} cm^{-3}), resulting in metallic-like conductivity[8]. These two properties, such as transmission and conductivity, make this material particularly unique. In this kind of material, one property is closely interdependent on the other. The attainment of both properties within the same material poses a substantial challenge. Overcoming this challenge requires an examination of the surface, structure, electrical, and optical characteristics of the host material. These unique kinds of materials are highly beneficial in numerous optoelectronic devices, particularly for sunlight harvesting within the renewable energy industry[9], [10], and in storage devices[11], [12]. A variety of transparent conducting materials are utilized in less power-consuming devices including display units, smartphones, touch screens, sensors, LED/LCD, etc[13], [14], [15], [16]. Due to their lower production costs, compactness, dependability, and reduced power consumption, they are widely utilized in optoelectronic devices [17]. Figure 1.1 depicts the integration of Transparent conducting materials into energy-efficient devices, highlighting their specific requirements based on sheet resistance value.
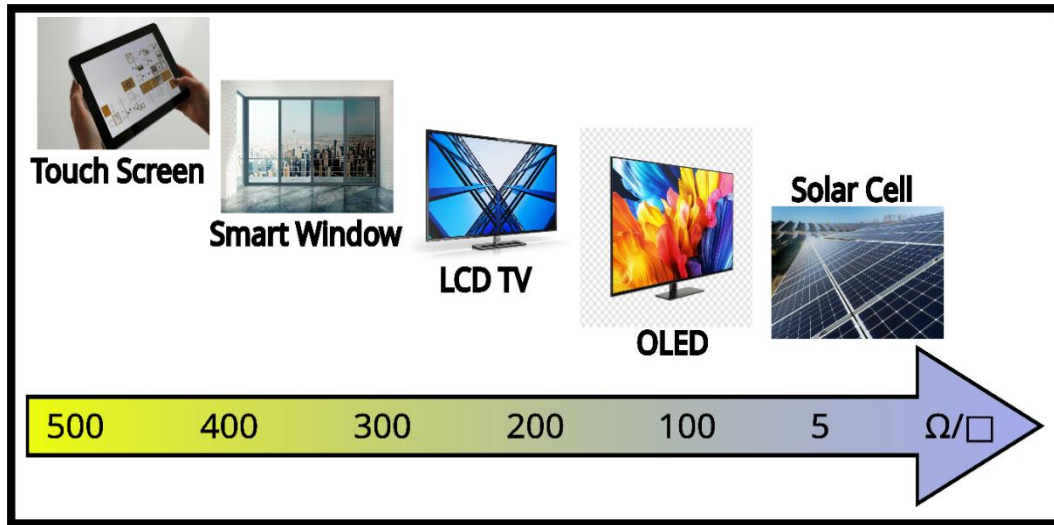
Fig.1.1. Sheet resistance values for various optoelectronic devices.

1.1.1. Tracing the History of Transparent Conductive Materials

The development of transparent conducting oxide (TCO) materials began in the early 1900s. In 1907, German physicist Karl Badekar explained cadmium oxide, the first transparent conducting material in solar cells. He indicated that n-type cadmium oxide (CdO) exhibits high conductivity by oxidizing 'Cd' metal with post-heated air[18]. Metallic-type conductivity in CdO is due to enhanced free carrier concentration caused by oxygen vacancies. While CdO toxicity restricts its commercial use though its high electron mobility makes it theoretically interesting. Badekar et al also described the production of other transparent conducting materials, such as Cu_2O and PbO, which were created through sputtering and subsequent oxidation in air[18]. A basic understanding of the physical and chemical behavior of Transparent conducting oxide materials, enabled by quantum mechanics, has contributed to their rapid development[19]. Harold McMaster, an American inventor, patented a Tin Oxide (SnO_2) thin film as a Transparent conducting oxide in 1947, which was formed by spray pyrolysis. During the time of World War II, SnO_2-based transparent heater film was utilized in aircraft windshields[20]. For the past three decades, tin-doped Indium oxide alloy (In_2O_3: Sn), which is commonly known as ITO, has been the most significant Transparent conducting oxide material (TCOs). The initial development of ITO as a Transparent conducting material occurred at Corning Laboratories during metal oxide insulator fabrication tests in the 1930s and later secured a patent in 1947[21].In a study

by Fraser and Cook, ITO thin films with a resistivity of 1.44 x $10^{-4}(\Omega cm)$ or conductivity $(0.69 \times 10^4 Scm^{-1})$ and 85% visible light transmission were identified as the best-performing transparent conductive material[22]. In 1954, Rupperecht was the first to commercialize Transparent conductive material. Currently, ITOs are an essential component in all flat panel display devices, driving significant profitability within the ITO manufacturing industry. Scholarly reviews on Transparent conducting materials have been published regularly. In 1953, Holland et al.[23] provided an initial overview of transparent conducting oxides (TCO) film research. Later in the mid-1970s, Hacke [24] contributed extensive research on Transparent conducting materials. Subsequently, Jarzebsk et al.[25] expanded upon this body with key review articles published up to 1982. Limitations exist with Indium tin oxide (ITO) thin film, notably the limited availability of indium and the elevated expenses associated with its manufacturing, necessitating the exploration of novel transparent conducting oxide materials.

1.1.2. Factors Leading to Indium Tin Oxide (ITO) Substitution

Global warming issues that became noticeable in the 1970s have created a greater need for renewable, conservative, and sustainable energy, driving the progress of Transparent conducting materials with desired characteristics. Indium-tin oxide (ITO), a commercially available transparent conducting material, is predominantly utilized in the optoelectronic sector because of its superior transmission (95%) and conductivity[26]. It is basically a ternary Composition of Indium, Tin, and varying compositions of oxygen. In ITO's 74% weightage of Indium, 18% weightage of Sn, and 8% weightage of Oxygen. A market analysis from 2011, detailing indium's availability and application, is presented in Figure 1.2 [27]. Therefore, because of ITO's widespread application, there is a substantial demand for indium, which was categorized as a 'critical raw element' in the 2015 Mineral Commodity Summaries [28].
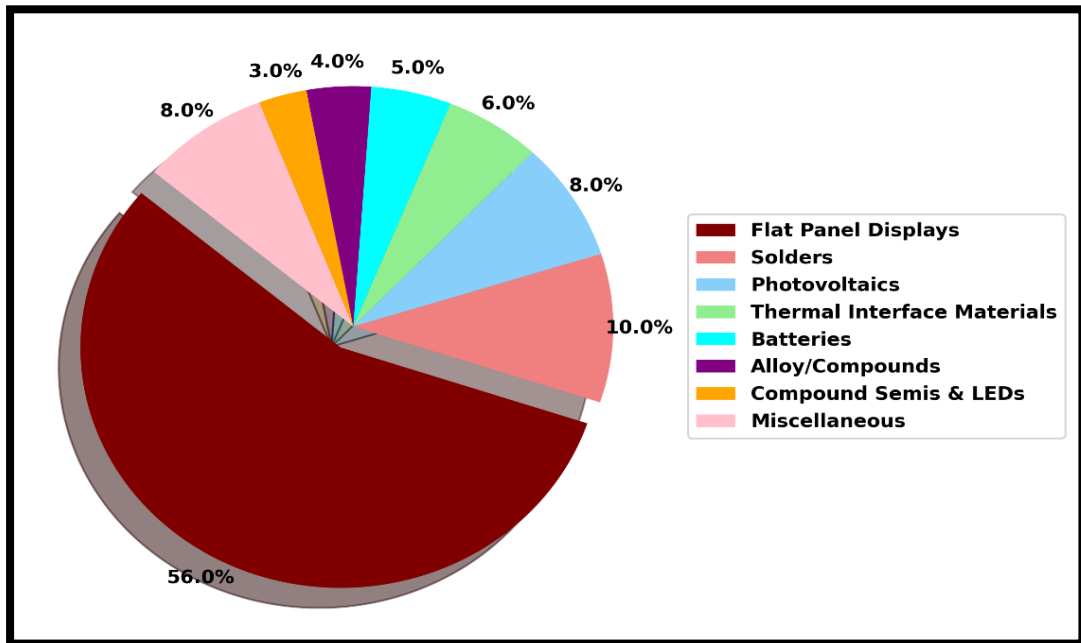
Fig.1.2. The widespread application of indium usage[29].

Moss et al. [30] informed the European Commission in 2011 that the annual global output of refined indium was 1,345 tons. A technical monitoring report [27] Figure 1.3 shows a significant anticipated deficit in indium supply by 2020. It is a rare and costly element due to its limited natural occurrence and extraction as a by-product of zinc and copper ores. Its concentration in the Earth's crust is approximately 0.05–0.1 parts per million, making it as scarce as silver. Additionally, producing indium tin oxide (ITO) is expensive and unsustainable for large-scale applications like photovoltaics and displays[31]. Market forecasts suggest the utilization of several TCO materials in mobile phones, tablets, laptops, monitors, televisions, OLED lighting, organic photovoltaics, solar cells, and electroluminescence devices. Innovative, transparent, and conductive materials can serve as alternatives to ITO for optoelectronic devices. Alternative materials in place of ITO for the optoelectronic devices such as ZnO, ZnS, aluminium-doped Zinc oxide (AZO), fluorine-doped tin oxide (FTO), ZnSe, ZnTe, SnO_2, TiO_2, CeO_2, Ga_2O_3, etc, Graphene, carbon nanotubes (CNT's), metal nanowires, and conducting polymers.
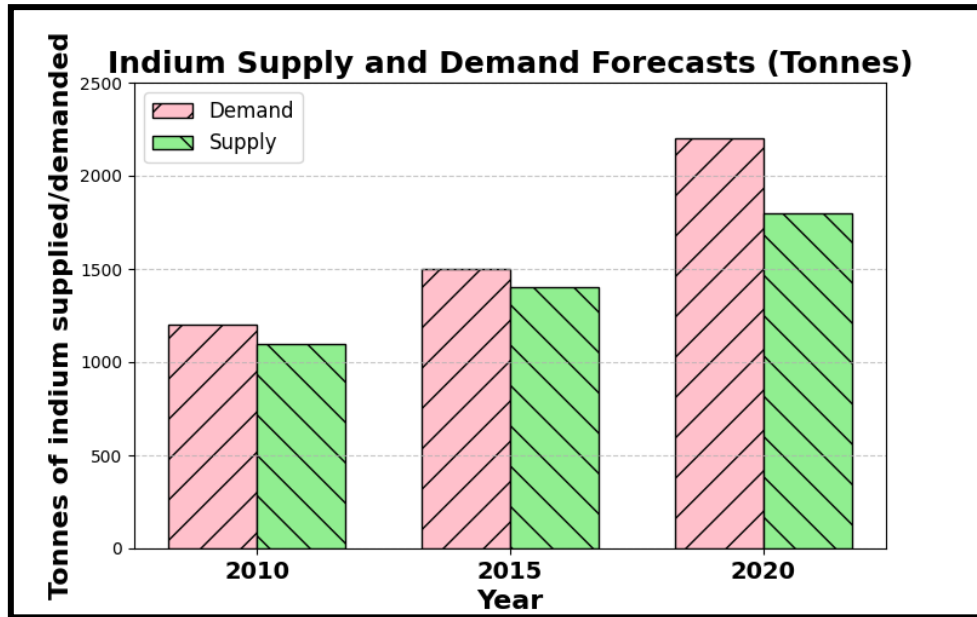
Fig.1.3. Indium supply-demand projections report[27].

1.2. Optical properties

When light interacts with Transparent Conducting oxide (TCO) materials undergoes processes such as transmission, reflection, refraction, and absorption. In cases where the material does not absorb light, it either transmits through it or reflects off its surface[32]. Surface roughness and structural defects within the material can also cause light scattering. These characteristics depend on the type of material. Transparency and conductivity are generally opposing characteristics because transparency demands a wide band gap, which, conversely, restricts the creation of charge carriers. Perfect 100% transmission in a TCO material would only be attainable if free electrons were unable to transition from the conduction band minimum to higher conduction band states[33]. TCOs need more than just transparency. Hence, a balanced approach is needed, where both transparency and charge carrier concentration are maximized. TCO transmittance is categorized into ultraviolet (UV) (10-400 nm), visible (400-700 nm), and near-infrared (above 700 nm) regions, indicated in the figure. Raising the charge carrier concentration leads to a corresponding rise in near-infrared absorption. A greater electron density in the conduction band intensifies absorption and reflection due to the free electron gas (plasma), which leads to a decline in transmittance for wavelengths above the plasma wavelength. This specific optical characteristic is commonly

observed in thin films composed of Fluorine tin oxide (FTO) and is essential for heat mirror applications[34]. The blue shifting of the plasma band onset, which relates to an increase in reflectance, is determined by the material's dielectric constant (a measure of capacitance, representing its ability to store electrical energy in an electric field) and the average time between electron collisions, or the mean free relaxation time (which is directly related to conductivity). This means that a higher electron density and a lower effective electron mass will decrease free relaxation time[35]. However, the conduction band's stability allows the thin films to stay optically transparent in the visible light range. The number and depth of interference fringes are determined by the thickness, which varies across the film. Interference fringes can also form due to multiple reflections at the interfaces between air and the thin film, the thin film and the substrate, and the barrier coating and the substrate's glass. Figure 1.4. depicts the influence of incident light on the thin film formed on the glass substrate.
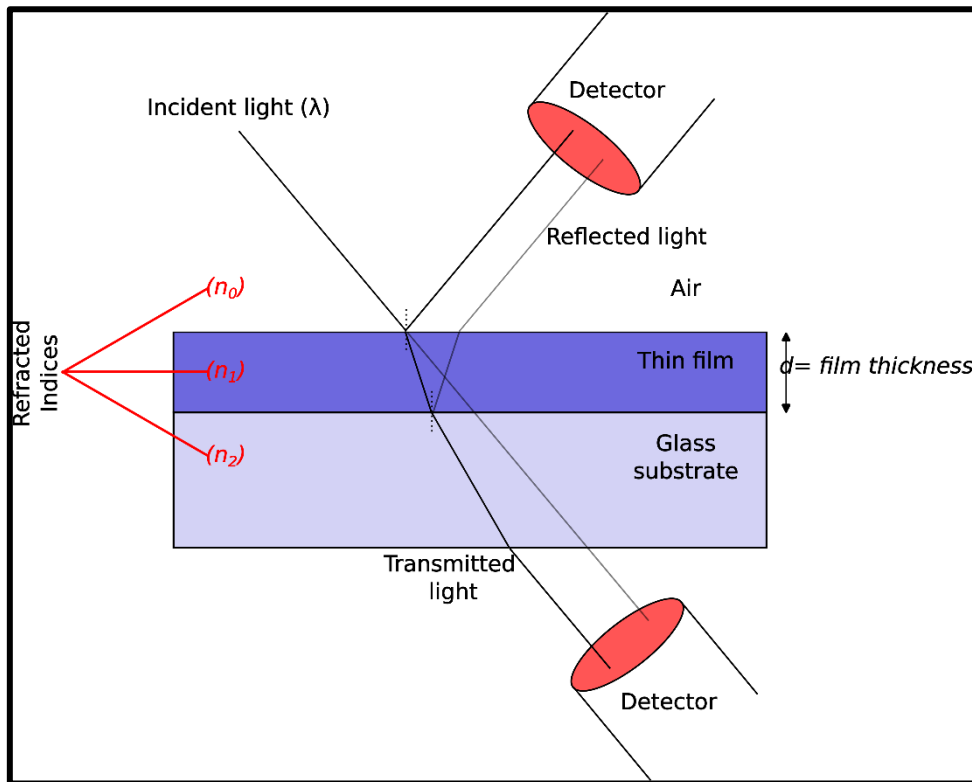
Fig.1.4 The interaction of light with a thin film.

1.2.1. Optical Bandgap

When atoms approach one another to form valence and conduction bands, the resulting splitting and overlapping of energy levels creates the band gap. Eg the band gap energy is the photon-provided energy required for electron movement from the valence band maximum (VBM) to the conduction band minimum (CBM). Energy band theory classifies materials into three distinct electronic states: metals, dielectrics/insulators, and semiconductors, as shown in Figure 1.5. In metals, the conduction band (CB) and valence band (VB) overlap, facilitating the unhindered movement of electrons. The conduction band (CB) and valence band (VB) in dielectrics and insulators are separated by a band gap of more than 4 eV. Due to this separation, electrons cannot exist at energy levels within the band gap, as seen in silicon dioxide (SiO_2) and germanium dioxide (GeO_2), which are insulating materials. A band gap exceeding 3 eV, but lower than that of insulators, is a defining characteristic of semiconductors. Electrons can be transferred from the valence band (VB) to the conduction band (CB) in semiconductors by absorbing photons. Due to their substantial band gap, they are frequently classified as wide-gap semiconductors. This property renders them unable to absorb photons with energy less than the band gap, resulting in their transparent nature. Tin oxide (SnO_2), Zinc sulfide (ZnS), and Zinc oxide (ZnO) a wide-bandgap semiconductors.
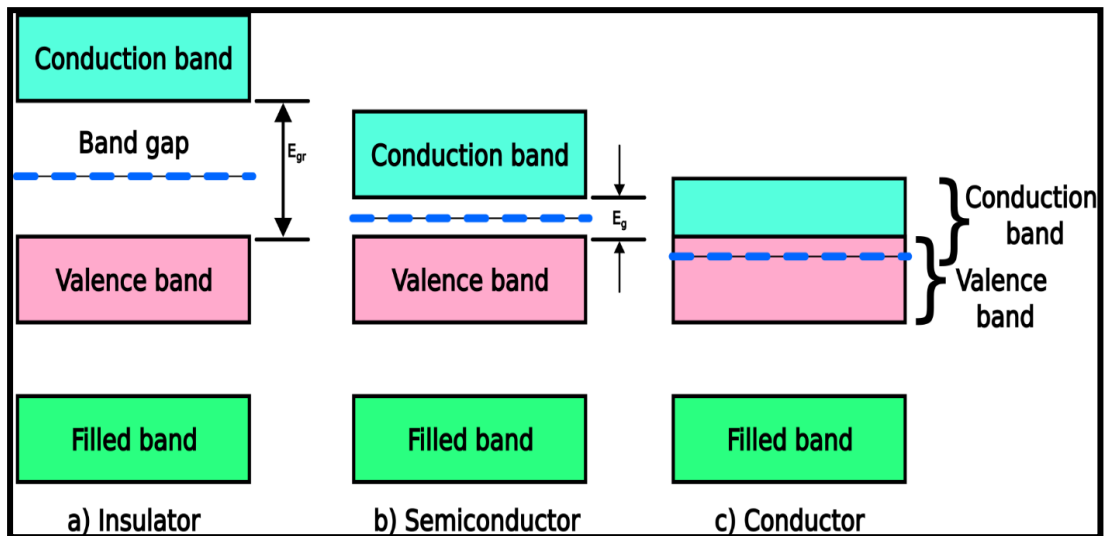
Fig.1.5. Energy band classification of (a) Insulator, (b) Semiconductors, (c) Conductors.

Numerous variables influenced the semiconductor's band gap[36]. Wideband gaps are associated with minimal interatomic distance and substantial electronegativity differences[37]. The band gap is also subject to measurable alterations due to orbital

8

hybridization and, predominantly, doping. Semiconductors can be categorized as either a direct band gap or an indirect band gap. In direct band gap semiconductors, the momenta of the valence band maximum (VBM) and the conduction band minimum (CBM) are the same (meaning the highest and lowest energy points of the respective bands are vertically aligned). Conversely, indirect band gap semiconductors, like silicon, do not exhibit this property. To ensure recombination between conduction band electrons and valence band holes, momentum must be conserved. Recombination can be either radiative or non-radiative, with radiative recombination being vital for optical properties. Indirect band gap semiconductors, however, rely on phonons, which are the vibrations of the crystal structure, for recombination[38]. However, the probability of electrons interacting with phonons is low in these materials, which leads to a reduced light emission rate and poor optical properties.
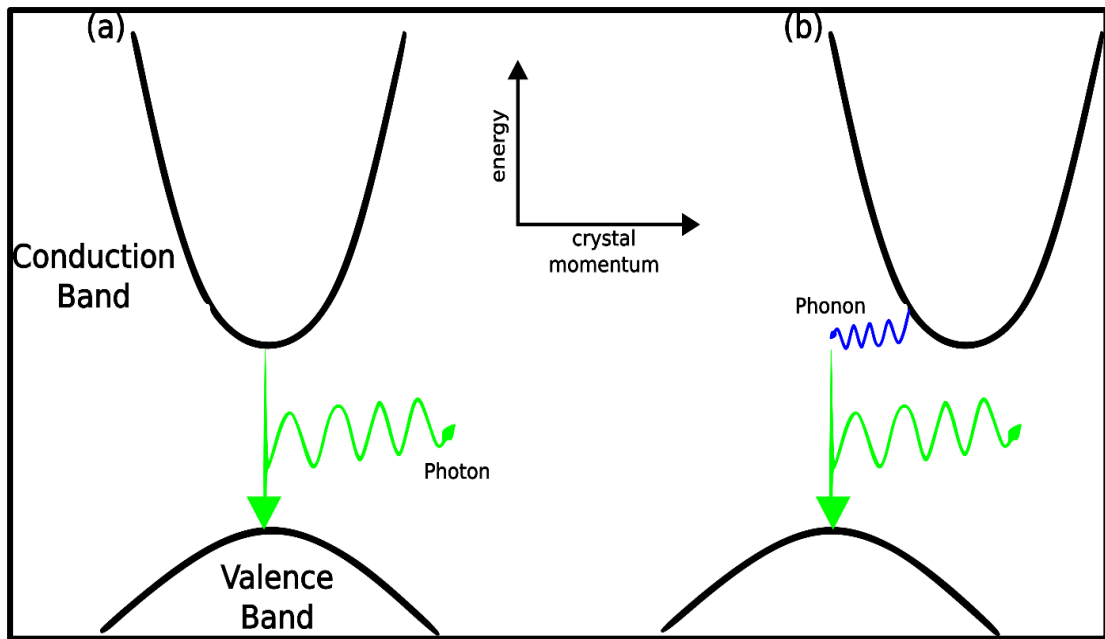
Fig.1.6. The phenomenon of (a) Direct Band gap, (b) Indirect Band gap.

1.2.1.1 Electronegativity

It is justifiable to consider the band gap of a semiconductor or insulator as dependent on the electronegativity difference between the anion and cation within a binary compound. Consequently, the relative electronegativities of the two elements are likely to influence the transition of electrons from the valence band (primarily anion orbitals)

to the conduction band (mainly cation orbitals. For example, a minimum electronegativity difference would create a smaller band gap. The Pauling electronegativity scale does not rely on individual atoms but, rather, on the dissociation energies (D), measured in electron volts, of chemical bonds between two atoms (A and B) in their gaseous form, as described by a mathematical equation(1.1)[39]

$$|x_A - x_B| = 0.102\{D(A - B) - 1/2[D(A - A) + (B - B)]\}^{1/2} \qquad (1.1)$$

Although the Pauling electronegativity differences have been employed to estimate the band gaps of various binary oxides, this approach fails to incorporate the covalency exhibited by some oxides. It follows that optical electronegativity, a relatively new idea that considers electron excitation in solid materials, is a more valid measure. It is evident that the polarizing capacity of the cation significantly affects the electronegative behaviour of oxygen. Consequently, one might inquire whether a relationship exists between optical electronegativity and band gap energy. However, a study that compared measured band gap values with calculated optical electronegativities found no such correlation in TCOs, which underscores the numerous variables that influence the band gap[40].

1.2.1.2 Hybridization

Chalcopyrite semiconductors (ternary compounds like $ZnSnP_2$, $CuAlS_2$, and $AgAlS_2$) exhibit smaller band gaps than binary semiconductors (e.g., ZnO). This is primarily attributed to p-d hybridization, though cation electronegativity and structural distortion also contribute. In I-III-VI2 chalcopyrites, hybridization dominates, while cation electronegativity is key in II-IV-V2 compounds. As shown in the study by Mishra and Ganguli, d-electrons are a key factor in lowering the band gap through p-d hybridization, which occurs when p-orbitals (from anions) and d-orbitals (from metals like Cu, Ag, or Zn) with the same symmetry interact and overlap. This generates a lower-energy bonding state, attributed to the d-states of the cation, and an antibonding state, at the highest point of the valence band, originating from the p-states of the anion. Perturbation theory establishes that states with equivalent symmetry experience mutual repulsion, with the repulsion strength inversely related to the energy difference between them[41]. Accordingly, the reduced band gap is attributed to the repulsive forces

between p-states and d-states of matching symmetry, causing the valence band maximum (VBM) to rise. While an increase in lattice parameters typically correlates with a reduction in the band gap, exceptions exist, as observed in $CuAlS_2$ and $AgAlS_2$ (where S can be substituted with Se). This deviation is explained by p-d hybridization, which produces a stronger repulsive force in Cu chalcopyrites due to the lower energy of the d-orbitals, and the larger atomic size of Ag compared to Cu, resulting in a greater separation between the anion and Ag than between the anion and the group III cation. This phenomenon leads to a decrease in the valence band maximum (VBM)[42].

1.2.1.3 Doping

Adding dopants to transparent conducting oxides (TCOs) materials improves electrical conductivity by creating mobile charge carriers, such as electrons in n-type materials like ZnO, ZnS, and SnO_2. However, this also causes changes in optical properties through three main pathways. First, free charge carrier absorption, which results from electron transitions within the conduction band, mainly in the near-infrared (NIR) region, increases proportionally with both charge carrier density and wavelength, as defined by the Drude model[43]. Second, doping alters the plasma frequency, affecting infrared reflectivity and transparency; for example, increasing charge carrier density reduces infrared transparency by decreasing the screened plasma wavelength[44]. Third, doping introduces defects in the crystal structure (Figure.1.7). Specifically, the absence of an ion from its ordered lattice position creates vacancies, sometimes referred to as Schottky defects. Atoms occupying locations where atoms are not typically found within the crystal structure are known as interstitials. The movement of an ion from its normal lattice position to a nearby interstitial space, resulting in a vacancy, forms a Frenkel pair; and substitutional defects, also called impurities, occur when a regular lattice ion or atom is replaced by a different ion or atom that may vary in size and valence.
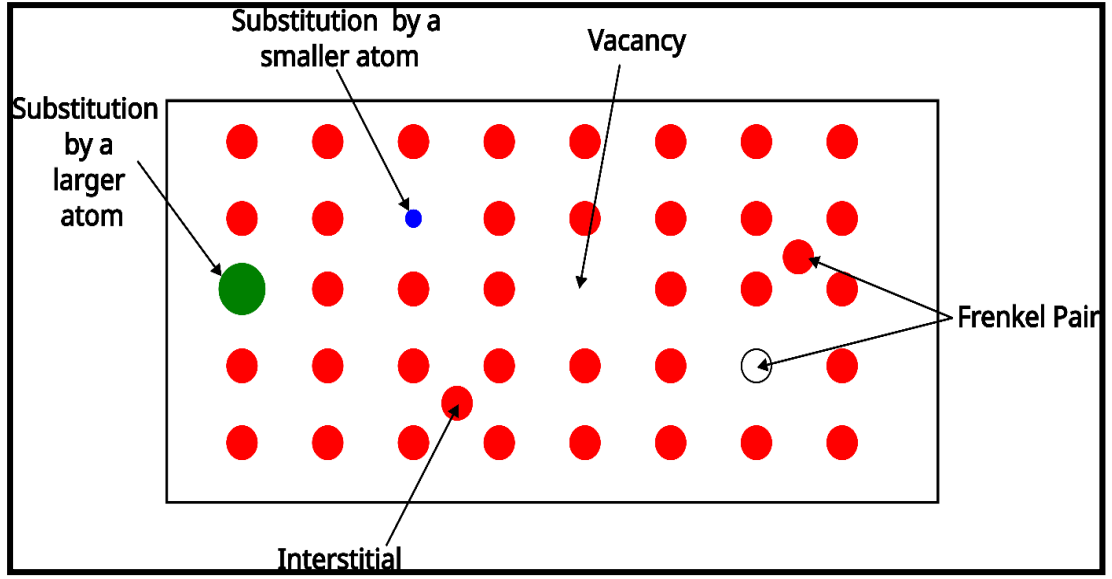
Fig.1.7. Defects type present in the crystal lattice.

1.3. Electrical Conductivity Properties

Electrical conductivity is another essential characteristic of transparent conducting materials in optoelectronic devices[45]. A variety of material properties, including electrical conductivity, are dependent on the thermal excitation of electrons transitioning from their ground state. The Boltzmann distribution determines the count of particles in an excited state at a specific temperature, as defined by equation (1.2).

$$N_i \propto e^{-\frac{E_i}{KT}} \tag{1.2}$$

Where N_i represents particle count in a specific state i, E depicts energy associated with the state, K indicates the Boltzmann constant, and T the temperature. However, the Boltzmann distribution is unsuitable for electrons within a solid because it fails to consider the indistinguishable nature of electrons and their adherence to Pauli's exclusion principle, which mandates opposite spins for two electrons in the same orbital. Therefore, the Fermi-Dirac distribution provides a more accurate representation, as shown in the following equation (1.3).

$$f(E) = \frac{1}{1+e^{\left[\frac{E-E_f}{KT}\right]}} \tag{1.3}$$

The fraction of permissible energy levels at energy E that are filled is represented by the function f(E). The Fermi level (Ef) distinguishes between the range of filled energy levels below it and the range of empty energy levels above it. It may also be described as the maximum energy an electron can have at absolute zero. The presence of the Fermi level within a band in metals accounts for their excellent conductive properties.

Semiconductor conductivity relies on electrons transferring from the valence band to the conduction band, meaning they require enough energy to surpass the band gap (Eg) shown in the figure. A pure semiconductor that exhibits this at room temperature is referred to as an intrinsic semiconductor(figure). The number of electrons that are excited into the conduction band in a pure semiconductor at any temperature is equal to the number of holes that are generated in the valence band. As a result, the Fermi level is located at the center of the band gap. However, doping can enhance the conductivity of semiconductors, creating extrinsic semiconductors, which are categorized as n-type or p-type based on whether the dopant atom's valence is higher or lower than the host atom's, respectively. The Fermi level in extrinsic semiconductors deviates from its ideal mid-band gap location, shifting towards the conduction band in n-type and towards the valence band in p-type.

1.4. Charge Transport Mechanism

The charge transport mechanism refers to the procedure by which charge carriers (electrons or holes) move through a semiconductor material under the influence of an external electric field. In transparent conducting oxides (TCOs) such as ZnO, SnO_2, and ZnS, the electrical conductivity primarily arises from electrons in the conduction band, making these materials typically n-type semiconductors. The nature of charge transport depends strongly on the material's crystallinity, defect structure, grain boundaries, and carrier concentration.

In general, TCOs exhibit n-type conductivity, which arises mainly due to the presence of intrinsic defects such as oxygen vacancies (V_o) and metal interstitials (Sn_i, Zn_i). These defects act as donor centers, releasing free electrons into the conduction band, thereby increasing carrier concentration. The relation can express the electrical conductivity (σ) of such materials:

$$\sigma = ne\mu \tag{1.4}$$

Where n, e, μ, σ presents carrier concentration, electron charge, carrier mobility, and conductivity.

The high conductivity of TCOs thus depends on both the number of available charge carriers and their availability to move freely through the crystal lattice. The mobility of carriers is primarily limited by various scattering processes, including lattice vibrations (phonon scattering), ionized impurity scattering, and grain boundary scattering. These scattering processes reduce the mean free path and relaxation time of carriers, thus lowering their mobility.

In highly crystalline TCOs, charge carriers are delocalized and move freely in the conduction band; this is referred to as band conduction. However, in polycrystalline or nanostructured thin films, the movement of electrons is often hindered by grain boundaries, which contain many trap states. These trapped charges create potential barriers that impede carrier transport. According to the Seto model (1975), the charge transport in polycrystalline semiconductors is governed by thermionic emission of electrons across these grain boundary barriers, and the conductivity can be expressed as

$$\sigma = \sigma_0 \exp\left(-\frac{q\emptyset_b}{k_B\,T}\right) \tag{1.5}$$

where $\emptyset_b$ represents the potential barrier height at grain boundaries, T indicates absolute temperature, k_B represents the Boltzmann constant, and q indicates the electronic charge. The barrier height decreases with increasing carrier concentration, thereby enhancing electrical conductivity. Larger grain size and reduced grain boundary defects also lead to higher mobility and improved transport charge.

In materials with high defect density or amorphous structure, conduction may occur through hopping mechanisms, in which electrons move between localized defect states or neighboring donor sites. Depending on the energy and spatial separation between localized sites, two major types of hopping conduction can occur:

1. **Nearest-neighbor hopping (NNH)** – electrons hop to the nearest available localized site.

2. **Variable-range hopping (VRH)** – electrons hop to more distant sites with lower energy barriers.

This process is thermally activated and follows an Arrhenius-type behavior, dominating in disordered or low-crystalline TCO films.

When the doping concentration or defect density becomes very high, the Fermi level shifts into the conduction band, and the material behaves as a degenerate semiconductor. In this regime, charge transport exhibits metal-like behavior, with high carrier concentration, weak temperature dependence of conductivity, and an apparent Burstein–Moss shift in the optical band gap due to the filling of lower conduction band states.

Hence, the charge transport mechanism proposed in TCOs involves a combined contribution from band conduction, grain boundary-limited transport, and hopping conduction, depending on the structural quality, defect concentration, and doping level. The overall conductivity and mobility are therefore determined by the interplay between intrinsic lattice order, extrinsic doping, and microstructural characteristics of the films.

1.5. n-type TCO's

When indium oxide is doped with tin, it results in an n-type semiconductor. This is because tin, a group IV element, is introduced into indium oxide, where indium is a group III element. In n-type semiconductors, electrons are the main charge carriers, as photons within the visible spectrum can elevate electrons from the donor energy level to the conduction band. A significant portion of the Transparent Conductive Oxides (TCOs) currently in use are n-type semiconductors [46]. It happens because of cation interstitials and oxygen vacancies in the oxide. While the majority are based on binary oxides of tin, indium, zinc, and cadmium, oxides consisting of two-binary systems (such as $ZnO-SnO_2$) and ternary, such as $ZnSnO_3,$ or quaternary oxides such as Cu_2ZnGeO_4 have also been produced. All these types have been further modified by doping with a wide range of elements or compounds[47]. Highly conductive and transparent thin films, exhibiting free electron concentrations of $10^{20}\,cm^{-3}$ or higher, can

be formed without doping, but these films lack stability at high temperatures. Several examples of binary transparent conductive materials are presented in the table1.1

Table 1.1. N-type binary transparent conducting materials.

S. No	Binary Material	Crystal structure	Band gap value	References
1.	In_2O_3	Bixbyite	2.9	[48]
2.	CdO	rock -salt	2.3	[49]
3.	ZnO	Hexagonal wurtzite	3.3	[50]
4.	SnO_2	rutile	3.6	[51]
5.	ZnS	zinc blende	3.6-3.8	[52]
6.	Ga_2O_3	Complex	4.5-4.9	[53]

It has been observed that electrical conductivity can be enhanced by doping with a metal. The prominent ITO formed by introducing tin in In_2O_3, enhanced conductivity from 10^3 to 10^5 Scm^{-1}. By incorporating metallic dopants into binary compounds, the number of free electrons is increased, given that these dopants provide electrons. While ITO is a prominent example, zinc oxide (ZnO), zinc sulfide (ZnS), and tin dioxide (SnO_2) are also utilized as binary material components, particularly in applications where indium scarcity is a concern.Mg^{2+} and Cu^{2+} are chosen as metallic cation dopants because their chemical and electronic properties allow them to effectively modify the conductivity and transmission characteristics of ZnO, ZnS, and SnO_2. By carefully controlling the doping process, researchers can tailor these materials for a wide range of optoelectronic applications.

1.6. p-type TCO's

The technological advances of Transparent Conductive Oxides (TCOs) have mainly focused on n-type materials. However, p-type TCOs are required for the creation of active TCO-based devices. P-type semiconductors are generated by doping a group IV element with a group III element, creating holes. The primary charge carriers in p-type Transparent Conductive Oxide (TCO) materials are holes. The initial p-type transparent conductive oxide reported as nickel oxide (NiO), which demonstrated a film

transmittance of 40%, a resistivity of 1.4×10^{-1} Ω cm, and stability restricted to temperatures less than 100°C[54]. P-type oxides play a critical role in the manufacture of complementary metal-oxide semiconductors (CMOS). It is also essential for the creation of junction devices, which are a key factor in the development of a new type of electronics called 'Transparent Electronics'. However, producing high-performance p-type TCOs is more complex because their valence band is predominantly formed by oxygen 2p orbitals, which are inherently localized. This localization makes it difficult to generate shallow acceptor levels, ultimately reducing hole mobility and electrical conductivity [55]. Therefore, p-type TCOs are less efficient and have limited use in commercial applications.

1.7. Figure of Merit (Φ_{TC})

On one side, a minimal band gap between the conduction and valence bands is usually desired to improve electrical conductivity in semiconductor materials. On the other side, when light interacts with the material, photons can be absorbed via the photoelectric effect. To reduce this absorption and enhance transmission, a wider band gap is required, which unfortunately leads to lower carrier concentration and consequently poorer conductivity. This creates an inherent difficulty in simultaneously optimizing conductivity and transmission. To overcome this challenge and provide a comprehensive evaluation of the electrical and optical properties of the transparent conducting thin films, the figure of merit (Φ_{TC}) is considered. The figure of Merit (Φ_{TC}) is a standardized benchmark for comparing the efficiency and applicability of transparent conducting materials in optoelectronic devices[56].The balance between two conflicting attributes, electrical conductivity, which is evaluated by sheet resistance (R_{sh}), and optical transparency, indicated as transmittance (T^{10}). A higher value of FOM (Φ_{TC}) indicates the superior performance of the material, signifying both a low sheet resistance (for effective charge movement) and a high transmittance (for a minimal amount of light absorption)[57] . The Figure of merit (Φ_{TC}) parameter is evaluated with the use of the Hacke equation (1.6)

$$\Phi_{TC} = \frac{T^{10}}{R_S} \tag{1.6}$$

The transmission and sheet resistance of the transparent conducting thin film are indicated by T^{10} and Rsh. A superior figure of merit signifies enhanced performance in transparent conducting materials (TCMs), making them highly desirable for optoelectronic devices like flat panels, display devices, and solar cells.

1.8. Host Materials

To overcome the scarcity of indium, the development of TCO thin films with ITO-equivalent conductivity and transmission is crucial. This necessitates exploring host materials such as ZnO, ZnS, and SnO_2.

1.8.1 Zinc Oxide (ZnO) thin films

ZnO material has emerged as a promising candidate in place of ITO due to its lower price, non-toxicity, and thermal and chemical stability. It has tremendous applications in the fields of optoelectronics, electronics, corrosion protection, pharmaceutical industries, and the chemical industry. ZnO thin film has versatile structural as well as optical, and electrical properties. Due to excellent transmission and conductive features, it is a useful candidate for touch screens, optoelectronics devices, and display devices[58]. ZnO thin films exhibit a major appearance in the II-VI semiconductor material. ZnO is an n-type semiconductor material with a direct wide band gap energy (3.37 eV) and large exciton binding energy (60 meV) at room temperature. ZnO has three different structures: hexagonal wurtzite, Zinc Blende, and Rock salt, shown in the figure1.8. Zinc oxide (ZnO) in its wurtzite form is the most stable and prevalent crystalline arrangement under standard environmental conditions. This structure is classified under the P6₃mc space group, which exhibits unit cell parameters of a = b = 3.249 Å and c = 5.207 Å, and angles α = β = 90° and γ = 120°. It can be imagined as a sequence of zinc (Zn) and oxygen (O) atoms arranged in alternating layers along the hexagonal c-axis. Both zinc and oxygen atoms exhibit tetrahedral coordination, with each zinc atom bonded to four oxygen atoms and vice versa. The strength of the ionic bonds, due to this tetrahedral coordination, is a factor in the material's stability. The absence of an inversion center in the wurtzite structure and its non-centrosymmetric nature generates piezoelectric and pyroelectric properties, which are utilized in sensors and transducers. The second structure of ZnO is zinc blende, which is less stable than

the hexagonal wurtzite phase and forms under synthesis conditions such as epitaxial growth on cubic substrates. It is assigned to the F43m space group. Like the wurtzite structure, zinc blende ZnO involves tetrahedral coordination between zinc and oxygen atoms. The atoms are arranged in a cubic pattern, resembling the diamond structure, with zinc and oxygen atoms in alternating locations. This structure is generally seen in thin films produced on cubic substrates and is not stable under typical environmental conditions. Zinc oxide (ZnO) transitions to the rock salt structure when subjected to significantly high pressure. This structure is defined by the Fm3m space group. It features octahedral coordination, where six oxygen atoms coordinate each zinc atom, and six zinc atoms coordinate each oxygen atom. As a result, this phase has a greater density than the wurtzite and zinc blende structures. Although this phase is not commonly observed in typical applications, it is valuable for understanding ZnO's response to extreme pressure.
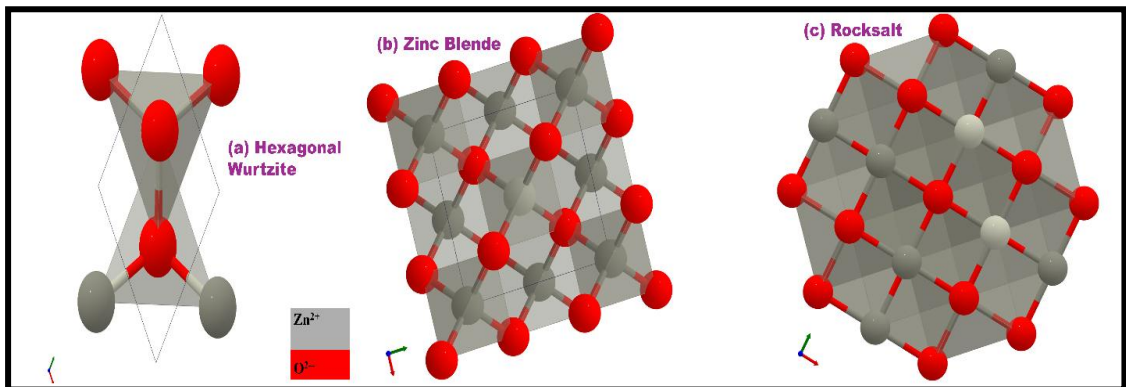
Fig.1.8. Crystal structure (a) Hexagonal wurtzite (b)Zinc Blende (c)Rocksalt of Zinc oxide (ZnO)

To determine the band structure of ZnO, numerous research teams have carried out computations using the local density approximation (LDA)[59]. The valence band is composed of six bands within the energy range of -5 to 0 eV and two core-like states at -20 eV, demonstrating the O 2p and O 2s bonding states. Within the conduction band, the first two states exhibit significant localization on zinc atoms, corresponding to empty Zn 3s energy levels, whereas the higher-energy conduction bands behave as free electrons.

Studies demonstrate that zinc oxide (ZnO) exhibits a trend of increasing conductivity, outperforming the stabilized conductivity values of other materials. Its wide band gap enables excellent visible light transmission, a key characteristic for both display and photovoltaic applications. Moreover, the transmission and conductivity of ZnO, in comparison to ITO, can be improved by the incorporation of divalent dopants, including magnesium (Mg^{2+}) and copper (Cu^{2+}), are provided within the results and discussion section.

1.8.2. Zinc Sulfide (ZnS) thin films

Zinc sulfide (ZnS) is a compound made of zinc (Zn) and sulfur(S) and belongs to the group of II-VI semiconductors. It commonly exists in two crystal structures: cubic (zinc blende) and hexagonal (wurtzite). Zinc blende, known as sphalerite, the more stable ZnS form under typical conditions, has a cubic structure with sulfide ions in a face-centered cubic (FCC) arrangement. Zinc ions fill half the tetrahedral voids, resulting in tetrahedral (4:4) coordination where each atom is surrounded by four of the other. It can be visualized as two interlocked FCC lattices of zinc and sulfur, offset along the cube's body diagonal. The wurtzite structure, on the other hand, is hexagonal and tends to form at higher temperatures. It features a hexagonal close-packed (HCP) arrangement of sulfide ions, with zinc ions also occupying half of the tetrahedral voids within this hexagonal lattice. Like zinc blende, the coordination between zinc and sulfur is tetrahedral (4:4). The distinction lies in the stacking sequence of the atomic layers, which differs from the cubic arrangement in zinc blende, leading to the overall hexagonal symmetry. The presence of tetrahedral coordination in the ZnS structure is a usual indication of sp^3 covalent bonding. In contrast, the Zn-O bond possesses a considerably high ionic nature, situating ZnS on the edge of being classified as either a covalent or an ionic compound based on the Phillips ionicity scale, where its ionicity is fi = 0.616.Fig.1.9. shows the crystal structure of ZnS.
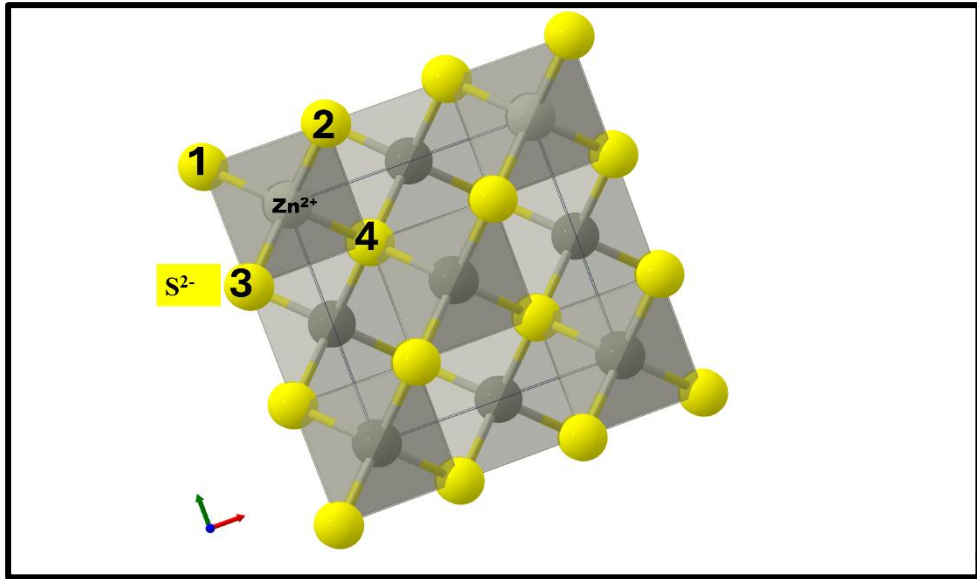
Fig.1.9. Zinc Sulfide (ZnS) crystal structure (Zn^{2+} and S^{2-}).

With a significant exciton binding energy of 39 meV, zinc sulfide (ZnS) is well-suited for optoelectronic applications operating at short wavelengths. The cubic form of ZnS features lattice parameters a = b = c = 5.41 Å and angles α = β = γ = 90°, while the hexagonal form exhibits lattice parameters a = b = 3.848 Å, c = 6.317 Å and angles α = β = 90°, γ = 120°.ZnS has a wide band gap of about 3.6 eV for the cubic phase and around 3.8 eV for the hexagonal phase, which makes it highly transparent in the visible and ultraviolet regions. It is known for its good optical properties, chemical stability, and strong photoluminescence. Due to these characteristics, ZnS is widely used in optoelectronic devices such as light-emitting diodes (LEDs) and lasers, as well as in gas sensors, photocatalysis, and as a buffer or window layer in thin-film solar cells. Indium Tin Oxide (ITO) stands as the well-known transparent conducting oxide (TCO)material, valued for its exceptional electrical conductivity and good optical transparency, making it essential in various optoelectronic devices like touchscreens and solar cells. In contrast, Zinc Sulfide (ZnS) is fundamentally a wide band gap semiconductor, praised for its luminescent and optical characteristics. While pure ZnS exhibits transparency comparable to ITO, its inherent electrical conductivity is significantly lower. Therefore, through specific doping with divalent elements such as Magnesium (Mg^{2+}) and copper (Cu^{2+}), the conductivity of ZnS can be enhanced. Although research explores doped ZnS as a potential alternative TCO, particularly

21

where cost and abundance are critical. Nevertheless, the unique properties of ZnS continue to make it a valuable material in diverse optoelectronic technologies, sometimes even integrated with ITO in hybrid structures to exploit their complementary strengths.

1.8.3 Tin Oxide (SnO₂)

Tin (IV)Oxide, often known as stannic oxide or SnO_2, is likely one of the simpler Transparent Conductive Oxides (TCOs) and is a compelling choice, primarily because tin is more abundant and less expensive than indium. Moreover, SnO_2 demonstrates both environmental stability and good mechanical resilience. Transparent Conductive Oxides (TCOs), composed of tin oxide, are frequently found in the architectural glass used for building windows. The electron arrangement of tin (Sn: $1s^2 2s^2 2p^6 3s^2 3p^6 3d^{10} 4s^2 4p^6 5s^2 5p^2$) exhibits similarities to that of indium (In: $1s^2 2s^2 2p^6 3s^2 3p^6 3d^{10} 4s^2 4p^6 5s^2 5p^1$). It is associated with elements from Group IV, which are known for their high mobility. This material is an n-type semiconductor with a wide band gap and a direct band gap value of 3.6 eV to 4.0eV. Cassiterite, the principal source of tin, presents SnO_2 in a tetragonal rutile structure, identified by the D_{4h}^{14}(P_{42}/mm) space group (figure). The crystal's unit cell of SnO_2 is composed of two tin atoms and four oxygen atoms with lattice parameters a = b = 4.737 Å and c = 3.185 Å, and all angles α, β, and γ equalling 90 degrees[60]. The structural feature of SnO_2 each atom of tin is enveloped by six octahedrally arranged oxygen atoms, and each oxygen atoms are enveloped by three tin atoms, which creates a nearly equilateral triangular arrangement. Sn^{4+} exhibits ionic radii of 0.69, and O^{2-} exhibits 1.24 ionic radii. Figure 1.10. shows the crystal structure of tin oxide.
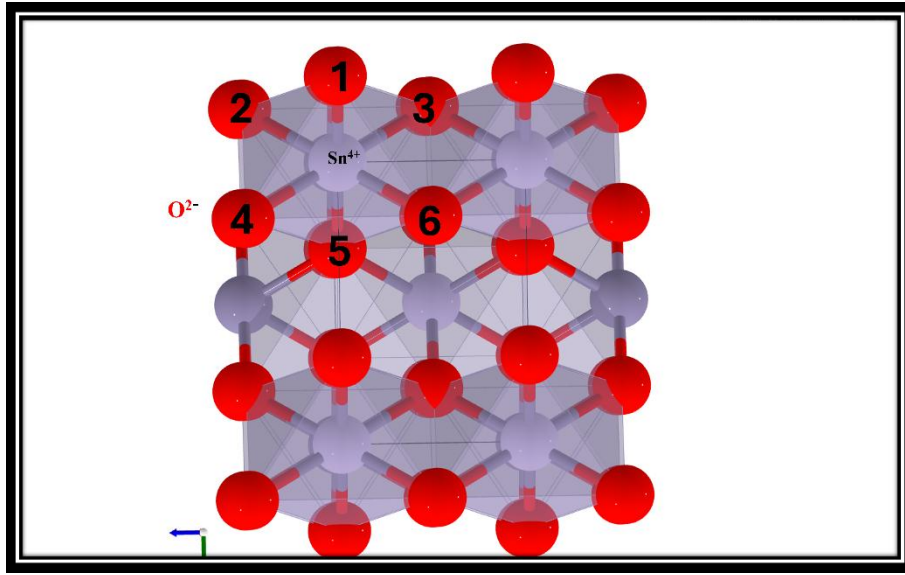
Fig1.10. Crystal structure of Tin oxide (SnO$_2$) which is Sn^{4+} and O^{2-}

In a fully stoichiometric state, SnO$_2$ would be an insulator. However, actual metal oxide systems are not perfectly stoichiometric. The presence of oxygen vacancies within the crystal structure due to this non-stoichiometry is the reason that electrical conductivity occurs. The electrical conductivity observed in undoped SnO$_2$ is attributable to oxygen vacancies (Vo) or interstitial tin atoms (Sni), which function as donors, as demonstrated in (A) and (B).

(A) $SnO_2 \leftrightarrow Sn_{Sn}^{4+} + O_o^{2-} + V_o^{2-} + \frac{1}{2}O_2$

(B) $SnO_2 \leftrightarrow Sn_i^{4+} + O_{2(g)}$
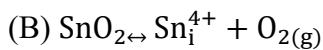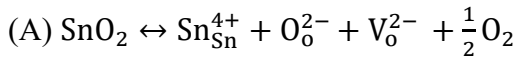
SnO$_2$'s ability to transmit light is high due to its band gap, which is above 3 eV, in the visible spectrum, and its electrical conduction is caused by free electrons formed from oxygen vacancies. Their features are equivalent to ITO properties. This results in SnO$_2$ having properties that make it useful in many optoelectronic devices. The improvement of conductivity and transmission in undoped SnO$_2$, through the inclusion of dopants like magnesium and copper, is discussed in the results and discussion section.

1.9. Applications for Transparent Conductive Materials

Transparent conductive materials are used in a variety of energy-efficient technologies, such as solar cells, liquid crystal displays, touchscreens, automotive window deicing and defogging systems, dye-sensitised solar cells, low-emissivity windows, organic and

photovoltaic solar cells, carbon nanotube-based devices, random metallic networks, perovskite-based devices, and LEDs. Predominantly found in n-type forms, Transparent conducting enhances material conductivity. Common translucent conducting substances contain ITO, aluminium, ZnO, doped zinc oxide, and p-type films. These materials are utilized in different industrial applications. Figure 1.11 illustrates some of the most prevalent applications of TCO thin films.
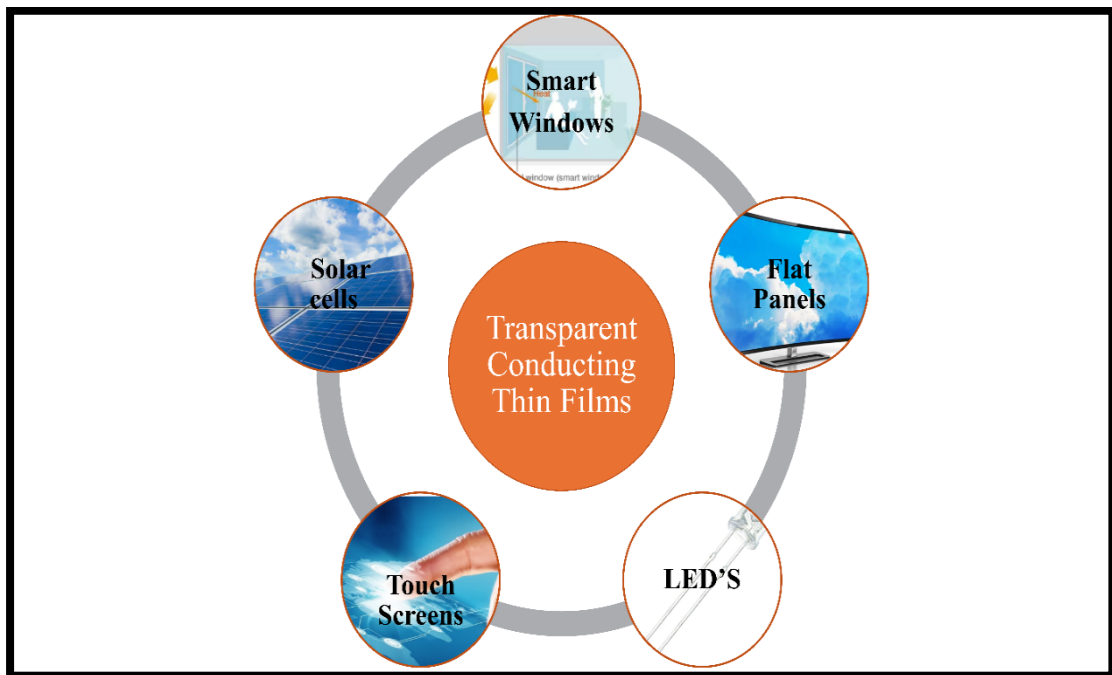
Fig1.11. Applications of Transparent Conducting thin films.

❖ **Solar Cells**: Photovoltaic devices, such as the widely utilized silicon solar cell, transform sunlight directly into electrical energy through the photovoltaic effect. When photons from sunlight impinge upon the cell's surface, they interact with the semiconductor material, typically silicon, which is engineered with a p-n junction. This junction is formed by the interface of p-type silicon, enriched with "holes" by doping with elements like boron, and n-type silicon, which has excess electrons due to doping with elements such as phosphorus. Photons possessing sufficient energy liberate electrons from their atomic bonds, generating electron-hole pairs. The inherent electric field within the p-n junction facilitates the separation of these charge carriers, directing electrons toward the n-type region and holes toward the p-type region. This charge

separation establishes a potential difference. To efficiently extract the generated current, a transparent conductive layer, often a metal oxide such as tin oxide (SnO_2) or zinc oxide (ZnO), is deposited on the cell's surface, allowing light penetration while serving as an electron collector. Metal contacts, positioned on both the front and back of the cell, enable the flow of this current to an external circuit. For example, in a solar-powered calculator, a small photovoltaic cell converts ambient light into the electrical energy required to power the device's display and processing functions. The efficiency of this process is influenced by factors such as the semiconductor's band gap, charge recombination rates, and operating temperature, driving continuous efforts to optimize solar cell design and performance.

❖ **LED:** A light-emitting diode (LED) is a semiconductor component that generates light while an electric current runs through it, operating on the electroluminescence principle. The core of an LED is a p-n junction, like that in a solar cell, but functioning in reverse. This junction is formed by joining p-type and n-type semiconductor materials, such as gallium arsenide or gallium nitride, each doped to create an abundance of holes (positive charge carriers) or electrons (negative charge carriers), respectively. When a voltage is applied across the junction, electrons from the n-type region and holes from the p-type region are forced to move toward the junction. As these charge carriers meet, they recombine. During this recombination, energy is released in the form of photons, or light. The energy band gap of the semiconductor material used determines the wavelength, and thus the color, of the emitted light. For example, a red LED might be made from gallium arsenide phosphide, while a blue LED is typically made from gallium nitride. The emitted light escapes the device through a transparent casing. This process is highly efficient, converting a significant portion of electrical energy directly into light, unlike incandescent bulbs that lose much energy as heat. A common example is the LED used in a traffic signal; electrical current is passed through the semiconductor, causing it to emit a bright, focused beam of light, signaling traffic flow. This direct

conversion of electricity to light, with minimized heat generation, makes LEDs a power-saving and long-lasting illumination source.

- ❖ **Touch screens:** Historians commonly credit E.A. Johnson, who worked at the Royal Radar Establishment in Malvern, UK, from 1965 to 1967, with creating the first touchscreen. In a 1968 article, he provided a full explanation of the touchscreen technology he invented for air traffic control. Essentially, a touchscreen is a computer display that simultaneously serves as an input device. When a finger or stylus contacts the display, the screen identifies the contact and transmits the data to a control for execution. These screens utilize a transparent conductor, often indium tin oxide (ITO), deposited on a glass substrate, creating a grid of capacitors. A touchscreen shows pictures or text that users can connect with through touch. A touchscreen functions on three major technologies: resistive, surface acoustic wave, and capacitive. **(a) Resistive:** This kind incorporates a thin metallic coating that is both conductive and resistive. When touched, it generates a change in the electric current, which is subsequently transferred to the controller and processed. It is much more affordable and not affected by dust and water.

  (b) Surface Acoustic Waves (SAW): In Surface Acoustic Waves, Ultrasonic waves pass through the screen. When the screen waves are absorbed, a touch point is recorded and delivered to the controller.

  (c) Capacitive: An electrically charged substance was added to the display. Once you tap the display, the amount of capacitance changes, and the position is detected and transmitted to the controller. In capacitive touchscreens, which are common in smartphones and tablets, the screen is coated with a transparent conductor.

For example, when a user taps an icon on a smartphone screen, their finger's presence modifies the capacitance at that specific location. The touchscreen's sensors register this change, and the processor interprets it as a selection command, launching the corresponding application. This mechanism allows for accurate and responsive user interaction, making touchscreens integral to modern devices.

❖ **Gas Sensing:** Gas sensing employs materials whose electrical properties change upon exposure to specific gases, enabling their detection and quantification. Metal oxides, such as tin oxide (SnO_2) or zinc oxide (ZnO), are frequently utilized due to their sensitivity and stability. The sensing mechanism typically involves surface adsorption and redox reactions. When a target gas meets the sensor's surface, it interacts with adsorbed oxygen species, altering the material's electrical conductivity. For example, when a reducing gas like carbon monoxide (CO) encounters an SnO_2 sensor, it reacts with adsorbed oxygen, releasing electrons back into the SnO_2 matrix, thereby increasing its conductivity. Conversely, oxidizing gases like nitrogen dioxide (NO_2) can trap electrons, decreasing conductivity. This change in conductivity is measured and correlated to the gas concentration. In a home smoke detector, an SnO_2 sensor might be used. When smoke particles, containing reducing gases from combustion, reach the sensor, the resulting conductivity change triggers an alarm, indicating the presence of fire. This principle allows for the development of sensitive and reliable gas sensors for various applications, including environmental monitoring, industrial safety, and medical diagnostics.

❖ **Smart Windows:** Many countries want to improve their energy use. A few of the researchers focused on less power consumption. So, the new advanced technologies are Smart Windows. Smart windows, also known as dynamic windows, regulate light and heat transmission, enhancing energy efficiency and user comfort. These windows employ materials whose optical properties can be altered in response to external stimuli, such as voltage, temperature, or light intensity. Electrochromic materials are commonly utilized, where a thin film of metal oxide, like tungsten oxide (WO_3), is sandwiched between transparent conductive layers. When a low voltage is applied, ions migrate into the metal oxide layer, causing a reversible change in its coloration and transparency. This modulation allows for control over the amount of sunlight and heat entering a building. For example, on a hot, sunny day, a smart window can be darkened electronically, reducing solar heat gain and minimizing the need for air conditioning. Conversely, during colder periods, the window can be made more

transparent to maximize solar heat input, reducing heating costs. Another method employs thermochromic materials, which change their optical properties in response to temperature variations, passively adjusting the window's tint. Photochromic materials, on the other hand, darken in response to sunlight, like transition lenses in eyeglasses. These technologies enable dynamic control over light and heat transmittance, leading to significant energy savings and improved indoor environmental conditions.

❖ **Low-emissive windows**: Low-emissive windows are widely used in the market and are often paired with window treatments. These windows are designed to reduce the transmission of infrared and ultraviolet light through the glass while still allowing plenty of visible light to pass through. This is achieved by applying a microscopically thin, transparent coating to one or more of the glass surfaces. It functions as a low transmission filter when one or more semi-transparent layers, such as aluminium or silver, are positioned between transparent conducting oxides, like zinc oxide, and transmissive dielectric layers such as tantalum pentoxide or titanium dioxide. It can even be positioned between two glass pans and on flexible plastic. Visible and infrared transmission are dependent on the solar coating and lower emissive window design. Heat reflection rises and transmission falls as the number of silver layers increases. For example, a double-paned low-e window in a residential home might have a coating applied to the inner surface of the outer pane. During a cold winter night, heat generated by the home's heating system attempts to escape through the window. The Low-E coating reflects this radiant heat into the room, reducing the need for the heating system to work as hard, resulting in energy savings. Simultaneously, the window allows visible light to pass through, maintaining natural illumination. This technology improves the thermal efficiency of windows, leading to substantial energy savings and enhanced comfort in buildings.

1.10. Research gap

Indium Tin Oxide, known as ITO, is the most widely utilized Transparent Conducting Oxide (TCO) material. Nonetheless, indium is considered rare and costly due to its limited natural abundance and its status as a by-product of zinc and copper ore processing. The Earth's crust contains only 0.05–0.1 parts per million of Indium, which is comparable to the rarity of silver. Also, ITO is unsustainable and very expensive for large-scale applications such as photovoltaics and display devices. Other materials in place of ITO, such as doped zinc oxide (AZO), fluorine-doped tin oxide (FTO), and carbon nanotubes (CNTs), offer comparable conductivity and transparency while being more cost-effective and environmentally friendly. So, we need a replacement material in place of ITO for the electro-optical devices.

1.11. Research Objectives

1) To synthesize the ZnO and Doped ZnO thin films, study its electrical and optical properties.

2) To synthesize the ZnS and Doped ZnS thin films, study its electrical and optical properties

3) To synthesize the SnO_2 thin films and study its electrical and optical properties

4) To synthesize Zn (O, S) and Zn (Sn, S) thin films and study the optical and electrical properties.

Chapter 2

2. Review of literature

2.1 Analysis of Existing Research

Mandal et al. (2025) studied the influence of low-energy nickel ion implantation on ZnO thin films, enhancing their structural, optical, and electrical properties. Deposited by RF sputtering on glass and ITO substrates, the thin films underwent ion implantation at fluences from 5×10^5 to 2×10^{16} ions/cm². XRD confirmed improved crystallinity at intermediate fluences, while higher doses caused structural damage. Optical analysis showed ~80% transmittance and a bandgap increase with fluence. Hall measurements revealed peak conductivity of 168 simon and carrier concentration of 6.3×10^{17} cm^{-3} at 1×10^{16} ions/cm² for ITO-based films, though excessive implantation reduced performance. The findings demonstrate ion implantation as an effective method to optimize ZnO films for transparent conductive oxide (TCO) applications [61]

Bayati et al. (2025) demonstrated the synthesis and characterization of ZnO/SnO₂ nanocomposite thin films utilizing spin coating and pulsed laser deposition. Structural analysis by XRD confirmed the presence of a hexagonal wurtzite ZnO phase and a tetragonal SnO₂ phase. FESEM images revealed an increase in particle size with higher ZnO concentrations, ranging from 11 nm to 18 nm for spin-coated films, while PLD-prepared films showed a minimum particle size of 6.5 nm at a ZnO: SnO₂ ratio of 70:30. Optical studies indicated that the bandgap of pure ZnO (3.2 eV) increased to 3.8 eV for 50ZnO/50SnO₂ spin-coated films and 3.7 eV for 70ZnO/30SnO₂ PLD films. The findings highlight the potential of ZnO/SnO₂ nanocomposites in optoelectronic applications[62]

Ceh-Cih et al. (2024) investigated Mg-doped SnO₂ (MTO), a highly adaptable material with tunable properties based on doping levels ranging from 0% to 23%. This flexibility makes it well-suited for applications in sensors and photovoltaic devices. The thin films were synthesized using the RF sputtering technique. Mg-doped SnO₂ depicts 90% transmittance and band gaps between 3.2 and 3.8 eV.

Fe-SEM analysis showed a compact, homogeneous surface with asymmetric grains that changed size as Mg was added. The resistivity of the thin films varied from 10^{-1} to 10^2 Ωcm depending on the concentration of Mg. It was utilized as a window layer in thin-film solar cells, attaining a maximum power conversion efficiency of 8.23% for all-sputtered CdTe cells[63].

Khouja et al. (2024) investigated undoped and magnesium (Mg)-doped zinc sulfide (ZnS) thin films. It was prepared utilizing the Mist CVD method on soda lime glass substrates at 450°C. Various analysis techniques were considered. The formation of polycrystalline thin films and the presence of Zn, S, and Mg were confirmed. The rise of Mg concentration led to rougher surfaces, larger crystalline sizes, and higher carrier concentrations (5.103×10^{18} cm^{-3}) and lower resistivity (5.021×10^{-3}(Scm^{-1}). Computational analysis considering DFT showed a reduction in the band gap with Mg doping. This study offers a foundation for future research on Mg-doped ZnS.[64]**.**

Mummadi et al. (2024) explored Cu-doped ZnS nanoparticles synthesized by a solid-state reaction method and analyzed their structural, optical, and electrical properties. XRD analysis confirmed the cubic zinc blende structure, with no secondary phases, indicating successful Cu incorporation. The crystallite size increased with Cu doping, enhancing material quality. Optical absorption spectra revealed a redshift in the band gap, attributed to the Moss-Burstein effect, where Cu doping reduced the band gap from 3.31 eV (pure ZnS) to 2.97 eV (ZnS: Cu 7%). The conductivity of ZnS material increases with Cu doping, reaching a maximum of 27.62 Scm^{-1}. These characteristics suggest that nanoparticles hold significant potential for optoelectronic applications[65].

Mathew et al. (2024) investigated Cu doping influence on SnO$_2$ electrodes, a promising metal oxide. Pure and Cu doped SnO$_2$(2%,7% and 15%) were formed by co- precipitation approach. Optimal performance was analyzed with the doping of 2%, yielding a 27.099 F/g specific capacitance. A higher value of capacitance reduced the value of capacitance, attributed to enhanced charge transfer resistance. The electrochemical analysis confirmed the pseudocapacitive behavior with excellent reversibility and a potential window, demonstrating the potential of Cu-doped SnO$_2$ for supercapacitor applications[66].

Akkera et al. (2023) synthesized thin films of pure SnO_2 and Sr-doped SnO_2 on a glass substrate by the sol-gel spin coating approach. XRD explained the polycrystalline tetragonal structure, while other characterizations, such as AFM, FTIR, and XPS analyses, characterized surface morphology, bonding, and oxidation states. The doping of Sr enhanced the average transmission of SnO_2 up to 76% and reduced the band gap value from 3.89 eV to 3.78 eV. Hence, 3% doped SnO_2 thin film shows a low sheet resistance value and high merit [67].

Mirza et.al. (2023) examined the structure, optical, and morphological properties of pure and Al-doped ZnO thin films by the sol-gel spin coating route. Structural study depicts that with the doping, the grain size and crystallinity decrease. SEM images showed that pure ZnO had clustered particles, while doping made the particles thinner. The optical transmission spectra reduce with the doping of aluminium from 75 to 50% in the visible spectra. The band gap value also reduces from 3.33 to 2.67 eV [68].

Alia et.al. (2023) demonstrated the Mg doping effect on the ZnS thin film prepared by chemical spray pyrolysis post-heated at 400℃. XRD study confirmed a cubic wurtzite structure with increased crystallite size from 10.99 nm (pure ZnS) to 12.27 nm (ZnS: Mg). The (220) plane exhibited the most prominent peak, with additional reflections along (111), (200), and (222) planes. AFM study showed a reduction in particle size and surface roughness with higher Mg doping, indicating improved film uniformity. Optical characterization revealed a decrease in the band gap from 3.52 eV (ZnS) to 3.42 eV (ZnS: Mg 3%), accompanied by reduced transmittance up to 65% and refractive index. The study highlights Mg doping as an effective method to modify ZnS thin films for optoelectronic applications by optimizing structural and optical properties.[69]

Kumar et al (2022) explored the annealing temperature effects (150- 300°C on ZnO thin films deposited on ITO glass substrate by pulsed laser deposition approach. Annealing slightly altered surface roughness and influenced the optical band gap (3.143 to 3.171 eV) while maintaining high visible transmission up to 70%.Results confirm ZnO formation and highlight the influence of annealing on the thin film properties[70].

Tounsi A et al. (2022) Thin films of undoped and Ce-doped ZnS thin films (2,4,6,8 and 10) on glass substrate formed by the sol-gel dip coating method. All the prepared films show an amorphous structure by utilizing XRD. The smoothness and uniformity of the samples were confirmed by AFM analysis. FTIR displays the ZnS band. The films were extremely transparent, with average visible transmittance values ranging from 60 to 85%, according to the UV-visible spectroscopy[71].

Kiruthiga et al. (2022) prepared tin-based conducting oxide material (SnO_2) utilizing tin (II) chloride with the help of the Nebulizer spray pyrolysis approach. The prepared films were deposited at 350 ±10°C and annealed for 3 hours at 300°C. After annealing, structural, optical, and electrical investigations revealed enhanced crystallinity, grain size, and stoichiometry. Low molar concentrations show high transmission up to 70%. It indicates that tin-based material exhibited a wide band gap, high transmission and high conductivity. It is necessary in the field of optoelectronics devices, superconductors, and perovskite solar cell fabrication[72].

Aghaei et al. (2022) described the effective utilization of the chemical bath route at the most suitable temperature to include Cu^{2+} into ZnS thin films. The crystallite size of cubic ZnS is less than 7 nm, verified by the XRD study. The shape of the thin film surface alters with the Cu doping, according to FE-SEM analysis.It displays transmission up to 60% after the addition of Cu. The influence of concentration quenching was also observed in the research, which was ascribed to non-radiative transitions between Cu^{2+} ions in the ZnS lattice. These results illustrate how well this approach performs on Cu doped ZnS on the glass surface[73].

Goudarzi et al. (2022) This work demonstrates a microwave-assisted chemical bath deposition approach for the formation of transparent and smooth ZnS and Mn ZnS nanostructured thin films. It indicates a well-crystallized cubic structure with an average crystallite size of 2.35nm. FE-SEM study shows dense and homogeneous thin films, although EDX showed a sulphur deficit. The band gap range rises from 3.60 to 3.85 eV. It shows more than 80% transmission in the

visible region. These optical properties signify the importance of the material in the field of optoelectronic devices[74].

Yusof et al. (2022) investigated the fabrication of ZnO/SnO_2 nanostructure-based humidity sensors using the electro spraying approach. Their study focused on the impact of varying ZnO, SnO_2, and SnO_2/ZnO compositions, as well as different Sol concentrations, on the sensor's sensitivity, response, and recovery time. XRD study confirmed the formation of hexagonal wurtzite ZnO and tetragonal SnO_2 phases, while FESEM images revealed that increasing sol concentration resulted in reduced crystallite size and nanostructure diameters. Electrical measurements indicated that higher sol concentrations led to a decrease in conductivity. The findings indicated that decreasing the Sol concentration led to increased crystallite size and enhanced sensing properties, with the 0.1:0.1 mol SnO_2/ZnO composite demonstrating superior sensitivity compared to other compositions tested[75].

Serrao et al. (2021) examined Sn doped ZnO thin films synthesized by sol gel spin coating approach, revealing a hexagonal structure with improved transparency such as 72% to 93% and reduced grain size (27 nm to 20nm). Sn doping widens the band gap's value from 3.23 eV to 3.29 eV and reduces the localized state while reducing the conductivity value from 41.32 to 9.44 Scm^{-1}. Sn: ZnO (3%) showed optimal performance indicating its best potential for optoelectronic applications[76].

Emegha et al. (2021) performed electrical characterization of Cu-ZnS deposited by metal organic chemical vapour deposition on soda lime glass annealed at temperatures between 370°C and 470°C using a four-point probe. The prepared thin films exhibited conductivities from 5.48 to 8.0 10^{-1} (Scm^{-1}) with activation energies 0.54 and 0.29 eV, their high resistivity indicated potential for utilization in optoelectronic semiconductor applications [77].

Abbas et al. (2021) indicated that the influence of Cu (0-3 wt%) doped on the SnO_2 thin films synthesized by chemical bath deposition approach. With the rise of Cu concentration, the crystallite size also rises from 17.6 to 35.42 nm. SEM analysis revealed the agglomerated spherical clusters. In the optical analysis, the visible transmission and the band gap reduced with the doping of Cu while the

refractive index, the extinction coefficient, and dielectric constant increased. Doping of Cu effectively tuned SnO_2 characteristics for diverse applications[78].

Wang Fu et al. (2021) This study achieves p-type conductivity in wide-bandgap SnO_2 using Mg doping and post-annealing. Mg-doped SnO_2 films, grown on c-Al_2O_3 by using pulsed laser deposition, were post-heated at 600°C for 0.5 hours, enhancing conductivity by removing interstitial Mg while preserving substitutional Mg. Hall measurements confirmed a hole concentration of $1.43 \times 10^{17} cm^{-3}$ and mobility of 4 cm²/V·s, with an activation energy of 85 meV. Optical analysis showed over 90% transparency in the visible range and a stable 4.13 eV bandgap. These results highlight Mg-doped SnO_2 as a promising material for p-n junctions and transparent conductive oxides in optoelectronics[79].

Bayan et al. (2021) investigated SnO_2–ZnO thin films, composed of nanoscale crystallites, fabricated on glass and silicon substrates using solid-phase low-temperature pyrolysis. The study revealed that all films exhibited optical transparency in the visible range (310–1000 nm), irrespective of their phase composition. Notably, the 50SnO_2–50ZnO thin film demonstrated the smallest nanocrystallite size, the highest conductivity activation energy, and the smallest calculated band gap for indirect transitions. The authors proposed that the reduction in the band gap could be attributed to the presence of surface electric fields exceeding 4×10^5 V/cm[80].

Petrov et al. (2021) synthesized ZnO-SnO_2 nanocomposite thin films with varying tin dioxide concentrations (0.5–5 mol.%) using solid-phase low-temperature pyrolysis. The prepared thin films exhibited a poly-nanocrystalline structure consisting of ZnO and SnO_2 crystals with grain sizes ranging from 10 to 15 nm. Optical study showed over 90% transparency (310–1000 nm) with bandgap variations from 3.32 to 3.90 eV. Electrical studies revealed reduced activation energy and inter-grain potential barrier, improving charge transport. Gas sensing tests demonstrated optimal NO_2 detection at a 1:99 Sn: Zn ratio, attributed to increased oxygen vacancies and enhanced charge transfer. These results highlight ZnO-SnO_2 nanocomposites as efficient materials for high-performance gas sensors[81].

Osanyilusi (2020) studied the formation of ZnS thin films using a Sol-gel spin coating approach with a spin variation. It analyzed structural, morphological, and optical characteristics. XRD analyses showed cubic structure and 8.8 nm crystallite size for single spin and (111) preferred orientation. The prepared thin films demonstrated high transmittance up to 81% and tunable band gap (3.70-3.87eV), exceeding bulk ZnS (3.65eV) with both influenced by spin time/thickness. FESEM verified uniform morphology. These properties indicate their potential usage in optoelectronic devices including photovoltaic windows[82].

Islam et al. (2020) In this research, transparent conductive Ba, Mg, and Ce doped SnO_2 thin films were developed by the nebulizer spray pyrolysis route. All the prepared films show tetragonal structure and uniform distribution. Among all Ba-doped SnO_2 thin films, displays 90% transmission in the visible range and high conductivity 21.27(Scm^{-1}) with high carrier concentration (8.38 $\times 10^{-18}$ cm^{-3}) and mobility 15.87 ($cm^2V^{-1}s^{-1}$). Due to these characteristics, Ba doped SnO_2 is a better option for utilization in transparent conducting electrodes for optoelectronic devices[83].

Radhi Devi et al. (2020) depicted Cu^{2+}-doped ZnO thin films synthesized by the SILAR approach and focusing on their structural, optical, and vapor-sensing properties. XRD confirmed a hexagonal wurtzite structure with reduced grain size, while SEM revealed a nanoflower-like morphology, enhancing surface area. Optical analysis showed increased transmittance up to 60% and a bandgap shift from 3.06 eV to 3.20 eV. Gas sensing tests demonstrated exceptional ammonia detection, achieving 12,300% sensitivity at 5 wt% Cu doping, with rapid response (37s) and recovery (8s) times. The improved performance is attributed to enhanced oxygen adsorption and defect-induced charge carrier modulation, making Cu-doped ZnO films highly suitable for room-temperature gas sensors[84].

 Heiba et al. (2020) explored the impact of Mg and Cu doping on zinc sulfide (ZnS) quantum dots formed by a simple chemical method at a low temperature of 300°C. Optical studies revealed that Mg doping increased the bandgap from 3.3 eV to 3.39 eV, while Cu doping reduced it to 3.26 eV, as supported by density

functional theory (DFT) calculations. Transmittance measurements showed a reduction with Cu doping, indicating enhanced absorption, while Mg doping slightly improved transparency. Electrical analysis demonstrated that doping influenced charge carrier concentration and conductivity, with Cu doping enhancing electrical conductivity due to defect-induced charge transport. These findings highlight Mg and Cu doping as effective strategies for tailoring ZnS quantum dots for optoelectronic and photocatalytic applications, optimizing their conductivity and optical properties[85].

Dong L et al. (2019) focused on the formation of tin-doped indium oxide (ITO) with preferred orientations (400) by the sol-gel spin coating route. ITO thin films with improved conductivity and high transmittance are prepared in this work by effectively combining thermal treatment at various temperatures with post-annealing treatment at 500°C. It was analysed that the preferred orientation depends upon the thermal treatment. The ITO thin film, which was thermally treated at 250 °C, had a strongly (400) preferred orientation and good conductivity (with a low resistivity of 4×10^{-3} Ω cm and a low sheet resistance of 230 Ω Sq^{-1}) with a highly average transmittance up to 85.12% and the highest figure of merit (8.68×10^{-4} Ω^{-1})[86].

Sayeed et al. (2019) explored the structural and optical characteristics of tin (Sn) doped ZnS thin film formed by the deposition of a chemical bath with Sn doping achieved by adding Tin Chloride ($SnCl_2$) solution as Sn source. XRD study confirms a hexagonal ZnS structure, with increased Sn doping enhancing crystallinity and introducing an additional (110) plane. Optical characterization reveals that higher Sn doping increases the bandgap from 3.60 eV (undoped ZnS) to 3.84 eV (20% Sn-doped ZnS), improves transmittance up to 83%, and reduces the refractive index. The results suggest that Sn doping can be an effective approach for tailoring the properties of ZnS thin films for specific applications in electronic and optoelectronic devices[87]

Hurma et al. (2019) demonstrated structural and optical characteristics of ZnS thin film synthesized using the ultrasonic spray pyrolysis approach at varying molar concentrations. X-ray diffraction (XRD) analysis revealed that the molarity of the solutions did not significantly affect the crystallization of the

films, with crystallite sizes ranging from 5.25 to 6.28 nm. Optical characterization showed that increasing molarity shifted the transmittance edge toward lower wavelengths, with a maximum transmittance of 85% at 350 nm. The optical bandgap values varied between 3.41 eV and 3.52 eV, influenced by structural defects and local bond distortions. Additionally, films with higher molarity exhibited increased optical conductivity. These findings suggest that while solution molarity has limited impact on the crystalline structure of USP-deposited ZnS films, it does influence their optical properties[88].

Wenwen Wu et al. (2018) explored the influence of thiourea concentration on the structural and optical properties of Zn (O, S) thin films formed with the help of sol–gel approach, as well as their impact on Cu (In, Ga)Se$_2$ (CIGS) solar cell performance. XRD and XPS analyses explained that the films were amorphous, consisting of ZnS, ZnO, and Zn (OH)$_2$. Optical measurements showed that the bandgap varied with sulfur content, reaching a minimum of 3.72 eV at an S/(S+O) ratio of 0.44. The highest solar cell efficiency of 7.28% was achieved with a 0.2M TU concentration, attributed to an optimized conduction band offset of +0.45 eV at the CIGS/Zn (O, S) interface. These findings highlight Zn(O, S) as a promising Cd-free buffer layer alternative for high-efficiency solar cells[89].

Hallani et al. (2017) A comparative study of ZnO thin films, focusing on the influence of aluminium and magnesium doping within a 5-30% range, was presented. These films were prepared using the sol-gel route. Both prepared films depict a hexagonal wurtzite structure, but MZO shows better crystallinity at high doping levels, unlike MZO forms smaller grains. AFM study depicts that MZO had a higher surface roughness than AZO.MZO shows a broader spectrum of transmission up to 95% and a high band gap of up to 3.67eV. AZO indicates the best conductivity 0.0032 Scm^{-1} and high mobility, which is more suitable for Transparent Conducting Oxides and photovoltaic applications[90].

2.2 A Systematic Literature Survey

Table 2.1 provides a detailed summary of previous studies on the synthesis, transmission (%), and conductivity (Scm^{-1}) characteristics of transparent conducting thin films. Each entry provides information including the authors'

names, the year of publication, the dopant used, the synthesis approach, transmission (%), conductivity (Scm^{-1}), and specific applications.

Table 2.1. Detailed summary of previous studies on the synthesis, transmission (%), and conductivity (Scm^{-1}) characteristics of transparent conducting thin films.

S. No	Author/year	Materials	Preparation method	Transmission (%)	Conductivity (Scm^{-1})	Applications	Reference
1)	Salman et.al. (2025)	Mg-ZnO	Sol-gel spin coating	96	0.00090	Transparent conducting oxides	[91]
2)	Hameed et al. (2025)	ZnO/SnO$_2$	Hydrothermal	80	36.22	Optoelectronics, UV detection, and environment monitoring	[92]
3)	Jayed et al. (2025)	Sn-ZnS	Spray pyrolysis	-------	0.59	Optoelectronics and gas sensing	[93]
4)	Namoune D et al. (2024)	Mg-SnO$_2$	Dip coating	87 to 62% decreases	11.76 to 0.002*10^{-3}	Photocatalytic	[94]
ssss 5)	Ahmad et al. (2024)	Sr-SnO$_2$	Sol gel	86% to 50 % decreases	0.22 to 4.95	Photoconductive, Photodetectors	[95]
6)	Filali et al. (2024)	ZnO: In:Al	Spray pyrolysis	80-90%	4.545*10^3	Transparent conducting oxides	[96]
7)	Gençyılmaz et al. (2024)	ZnS-ZnO	Thermal evaporation	70%	0.026	Solar cells	[97]
8)	Wang et al. (2024)	Al-SnO$_2$	High target utilization system	83%	4.629	Transparent conducting oxides	[98]

9)	Latif et al. (2023)	La-ZnO	Spray pyrolysis	70%	1.4	Solar cells	[99]
10)	Saoula1 et al. (2023)	Al, Cu, Zn and Sr-SnO_2	Spray pyrolysis	86.77	$6.92*10^2$	Transparent conducting oxides	[100]
11)	Chander Joshi et al. (2022)	Cu-ZnO	Sol gel	80%	0.0121	Optoelectronic devices	[101]
12)	Senthilkumar et al. (2022)	W-SnO_2	Spray pyrolysis	90%	260.41	Optoelectronic devices	[102]
13)	Salim et al. (2022)	ZnO	Spray pyrolysis	82%	0.013	Photovoltaic devices	[103]
14)	Derrar et al. (2022)	Sb-SnO_2	Spray pyrolysis	86%	0.011	Solar cells, transparent windows	[104]
15)	Nulhakim et al. (2020)	Ga-ZnO	DC magnetron sputtering	86.04%	$7.246*10^3$	Transparent conducting oxides	[105]
16)	Krishna et al. (2020)	Cu-ZnS	Spray pyrolysis	64%	1.37	Transparent LED	[106]
17)	Barman et al. (2019)	Cu-ZnS	Thermal evaporation	73%	$1.9*10^3$	Optoelectronic devices	[107]
18)	Palanichamy et al. (2019)	Gd-SnO_2	Spray pyrolysis	91%	$1.4*10^3$	Transparent conducting oxides	[108]
19)	C. Sabitha et al. (2018)	ZnS	Nebulized spray pyrolysis	82%	1.030	Solar cell	[109]

Chapter 3

Research Methodology, Materials, and Characterization

3.1. Introduction

This chapter outlines the detailed experimental methodology adopted for synthesizing transparent conducting oxide (TCO) thin films using the sol-gel spin coating technique. The primary objective is to fabricate uniform thin films with tunable optical and electrical properties. The core purpose of the synthesis was the formation of various transparent conducting thin film materials. This encompassed pure forms of ZnO, ZnS, and SnO_2, along with their dopant materials such as magnesium (Mg) and copper (Cu), and composite structures such as Zn (O, S) and Zn (S, Sn) ZnO: SnO_2 and ZnS: SnO_2. In the fabrication of transparent conducting oxide (TCO) thin films, the material is developed through a two-step process. First, a precursor solution is prepared using the sol-gel method. This solution is then deposited onto a glass substrate using a spin coating technique. Many conventional thin film deposition techniques, such as Chemical Vapor Deposition (CVD), Solution-based Chemistry, and Physical Vapor Deposition (PVD), have notable limitations despite their widespread industrial use. One major drawback is the requirement for high-cost, sophisticated equipment, including vacuum chambers, gas delivery systems, and plasma sources. These setups make the process economically unfeasible for low-budget or large-scale projects, especially in developing research environments. Among all the thin film deposition methods, the Sol-Gel method is a widely used chemical technique for depositing thin films, especially of metal oxides like ZnO, SnO_2, and others.

In the sol-gel process, a "sol" is first prepared by dissolving a metal precursor (such as a metal alkoxide or metal salt) in a solvent, typically an alcohol. Through controlled hydrolysis and condensation reactions, the sol forms a network-like structure that eventually transforms into a gel. In the thin film formation, 'Sol' is considered for the deposition of the thin film. The sol-gel method is a low-cost, low-temperature, and versatile chemical route for thin film deposition. Figure3.1. shows the procedure of sol sol-gel method. It does not require vacuum systems or expensive apparatus, making it

more accessible for laboratory-scale research and low-cost production. One of the greatest advantages of the sol-gel method is its excellent control over the chemical composition of the film at the molecular level, which is crucial for doping and tailoring material properties. Furthermore, it allows the formation of uniform, smooth, and porous films through simple deposition techniques, which include spin coating. Since the process can be carried out at low or moderate temperatures, it is suitable for a wide variety of substrates. Sol-gel-derived thin films are used in solar cells, gas sensors, transparent conductors, and optical coatings due to their high purity, uniformity, and functional properties.
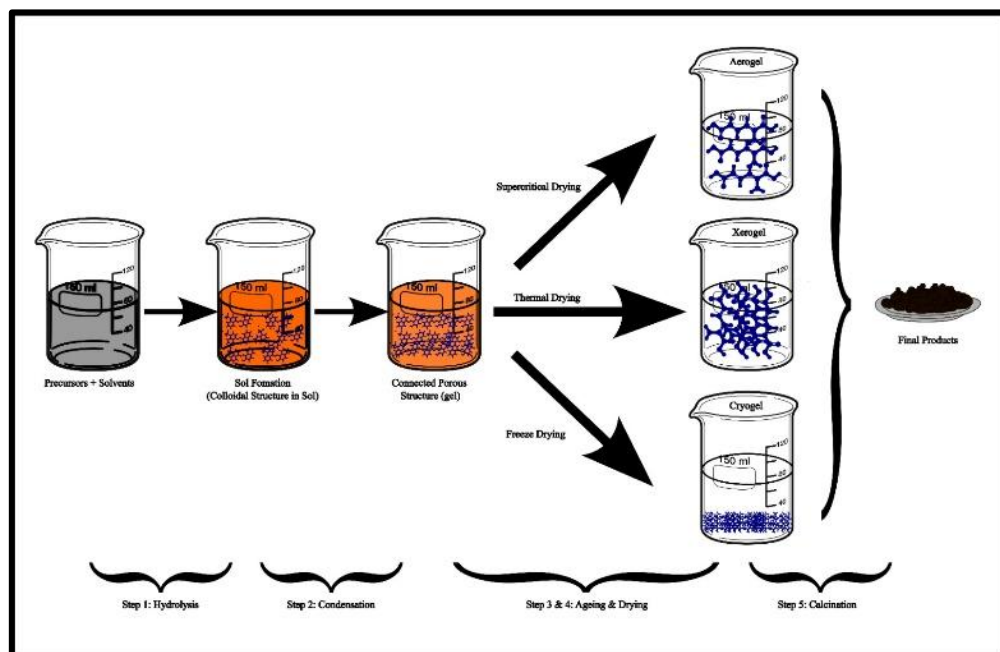
Fig.3.1. Procedure of Sol-gel.

3.2. Material Used

The chemical reagents utilized in synthesizing transparent conducting thin films are detailed in Table 3.1, which includes their chemical formulas, molar weights, purity levels, and suppliers.

Table 3.1. lists the chemicals employed in the formation of the host and dopant for Transparent conducting materials.

S.No.	Chemical Name	Chemical Formula	Molecular weight	Purity	Manufacture company
1.	Zinc acetate dihydrate (Precursor)	$Zn(CH_3COO)_2 \cdot 2H_2O$	219.50	99%	Loba Chemie Pvt. Ltd.
2.	Thiourea (Precursor)	$NH_2.CS.NH_2$	76.12	99%	Loba Chemie Pvt. Ltd.
3.	Stannous Chloride (Precursor)	$SnCl_2.2H_2O$	225.63	99%	CDH Pvt. Ltd.
4.	2-methoxy ethanol (Solvent)	$C_3H_8O_2$	76.10	99.5%	Loba Chemie Pvt. Ltd.
5.	Mono-ethanol amine (Stabilizer)	C_2H_7NO	61.08	99%	Loba Chemie Pvt. Ltd.
6.	Magnesium nitrate hexahydrate (dopant)	$Mg (NO_3)_2 \cdot 6H_2O$	256.41	98%	Loba Chemie Pvt. Ltd.
7.	Cupric nitrate Trihydrate (dopant)	$Cu (NO_3)_2 \cdot 3H_2O$	241.60	99%	Loba Chemie Pvt. Ltd.

3.3. Synthesis materials

3.3.1. Synthesis of Pure ZnO and Mg/Cu doped ZnO thin film

Pure ZnO, Cu-doped, and Mg-doped ZnO thin films were fabricated using the sol-gel spin coating route. Initially, solutions were prepared through the sol-gel method, and then the thin films were created using a spin coater. First, introduce 0.5M of Zinc acetate dihydrate as a starting material in 50 mL of 2-methoxy ethanol (solvent). After stirring the mixture for thirty minutes, introduce 0.6 mL of MEA (stabilizer). Once thoroughly mixed, copper nitrate (Cu $(NO_3)_2 \cdot 3H_2O$) and magnesium nitrate Mg $(NO_3)_2$ were introduced as a dopant in different containers at varying concentrations of 0.1%, 0.5%, and 1.0%. After the solution was heated at 50-60°C and stirred for two hours till it turned clear and translucent. The prepared solutions were kept at room temperature for aging (24 hours).

In the next step, thin films are formed using a spin coater. The 2×2 cm^2 glass substrate was first cleaned with acetone, ethanol, and distilled water to eliminate any impurities on the substrate. Three even drops of prepared solution were placed into the middle of the glass substrate and monitored by spinning at 2500 rpm for 10 seconds with the help of a spin coater. After each layer was applied, preheat the prepared substrate to 100 °C for 10 min and then dry for another 10 min. Coating and preheating have been repeated up to six times to get a better film on the substrate. In the end, prepared ZnO thin film and Cu-doped thin films (0.1%,0.5%, and 1.0%) and Mg-doped thin films were annealed at 500°C for 5 hours. The proper flow chart is illustrated in the figure3.2.
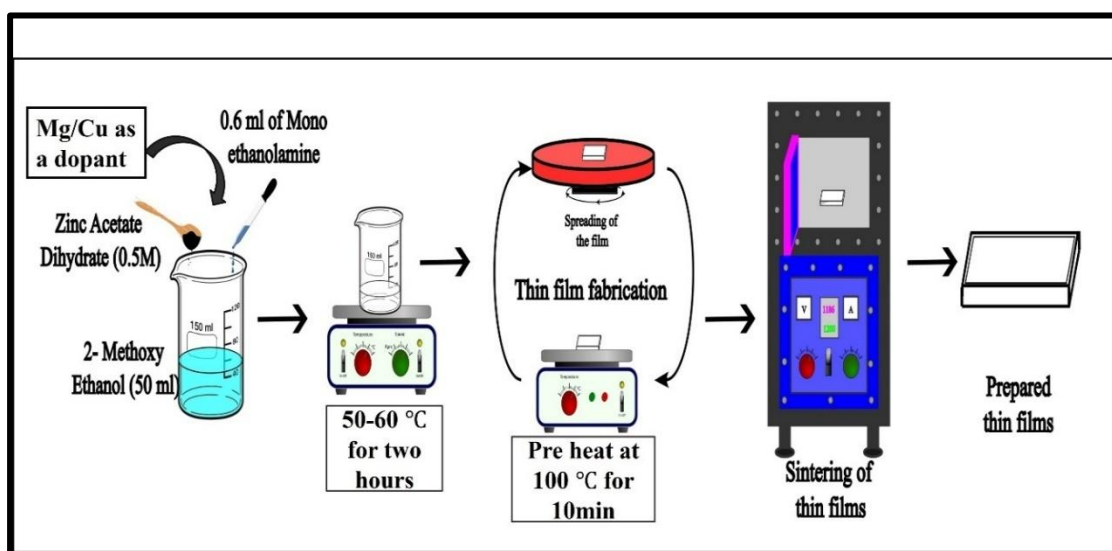
Fig.3.2. Process of synthesis of ZnO and Mg/Cu doped ZnO thin films with doping concentrations of 0.1, 0.5, and 1.0 mol%.

3.3.2. Synthesis of tin oxide and Mg/Cu doped tin oxide.

The Sol-gel spin coating approach was adopted for the synthesis of tin oxide (SnO$_2$), Mg/Cu-doped SnO$_2$ thin films on a glass substrate. For the synthesis of Mg and Cu-doped SnO$_2$ thin films, 0.5M of tin chloride (SnCl$_2$, 2H$_2$O) was added to 20 ml of 2-methoxy ethanol(solvent). After stirring the mixture for 30 minutes, incorporate 0.6ml of monoethanolamine (stabilizer). Subsequently, magnesium nitrate (Mg (NO$_3$)$_2$) and copper nitrate (Cu (NO$_3$)$_2$·3H$_2$O) were added as dopants, having concentrations of 0.1%, 0.5%, and 1.0%. After that, the solution was heated at 50-60°C and stirred for two hours, until it became clear and transparent. Next procedure, substrate cleaning

played a crucial role in eliminating impurities. This involved cleaning the substrate with acetone, ethanol, and distilled water. A thin film formation was done by utilizing a spin coater, dispensing three uniform drops of the prepared solution onto the cleaned glass substrate, and monitoring by spinning at 2500 rpm for 10 seconds. Then, the samples were preheated at 100°C for 10 minutes. To ensure the formation of a well-defined layer on the substrate, this entire procedure was repeated six times. Finally, undoped SnO_2, all concentrations of Mg, and Cu-doped SnO_2 thin films were post-heated at 500°C for one hour. Figure 3.3. shows the complete procedure for the preparation of thin films.
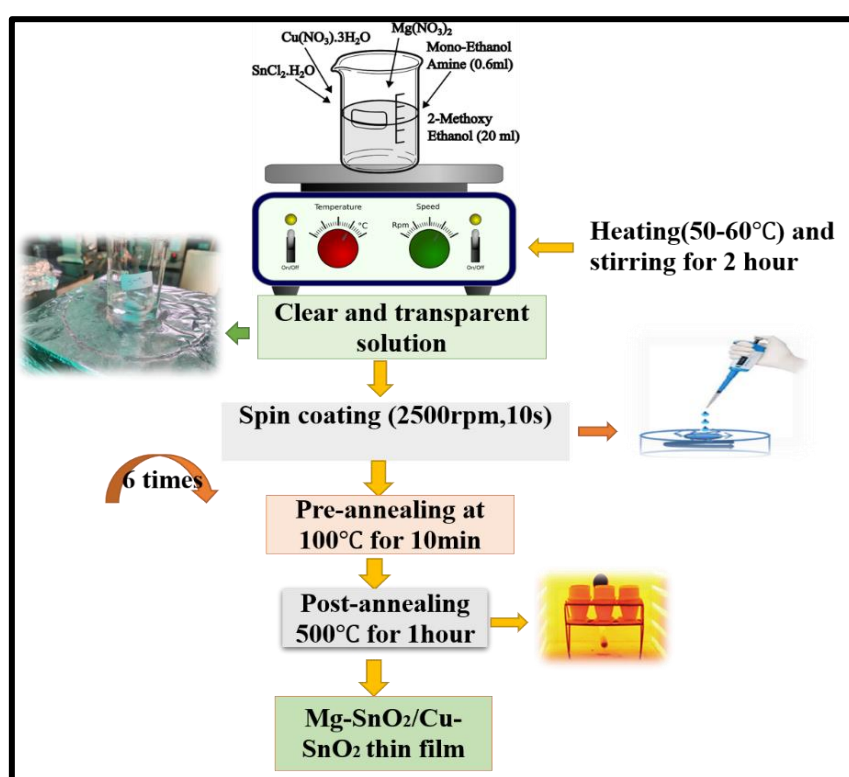
Fig.3.3. Flow of synthesis of SnO_2 and Mg/Cu doped SnO_2 thin films with doping concentrations of 0.1, 0.5, and 1.0 mol%.

3.3.3. Synthesis of Zinc Sulfide (ZnS) and Mg/Cu doped with ZnS thin films

The synthesis of ZnS, Mg/Cu-doped ZnS thin films begins by preparing three separate solutions. First, a 0.2 M solution of zinc acetate dihydrate is dissolved in isopropyl alcohol and stirred continuously at room temperature for 30 minutes. In parallel, a 0.3 M thiourea solution is prepared in isopropyl alcohol and stirred under the same

45

conditions. Additionally, Mg / Cu dopants (at different concentrations, 0.1%,0.5%, and 1.0%) are dissolved in isopropyl solvent and stirred for 30 minutes at room temperature. All three solutions are then combined and stirred together at a temperature range of 50–60°C for two hours, resulting in a clear and transparent mixture. After the solution is prepared, the spin coating method is applied to develop the thin films. Glass substrates (2 cm × 2 cm) were cleaned by acetone soaking (24 h), detergent washing, water rinsing, and air drying for uniform film adhesion. Thin ZnS films were deposited by spin coating at 2500 rpm, repeated 6 times with 3 drops per layer. After deposition, the films were subjected to a post-deposition sintering process at 500°C for five hours in a muffle furnace. The procedure is depicted in Figure 3.4.
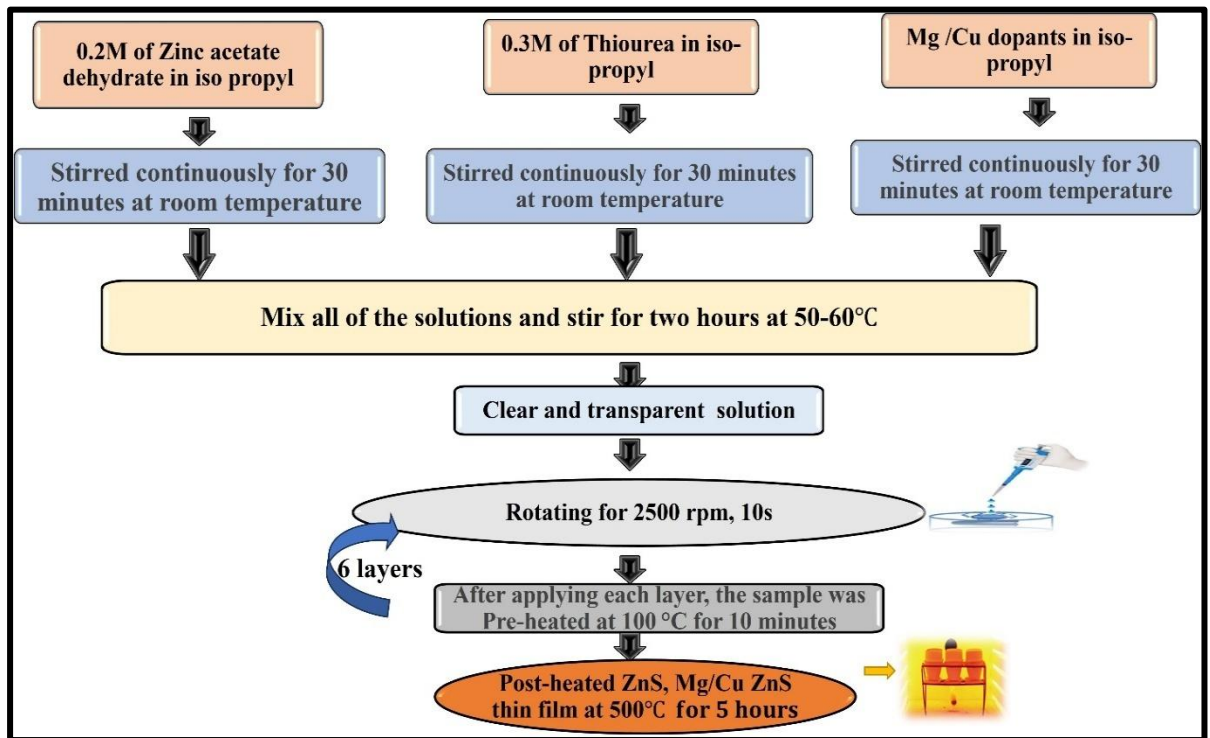
Fig.3.4. Flow of synthesis of ZnS and Mg/Cu doped ZnS thin films with doping concentrations of 0.1, 0.5, and 1.0 mol%.

3.3.4. Synthesis of Zn (O, S) composite thin films with different weight ratios of ZnO and SnO₂.

Synthesis of Zn (O, S) composite thin films (different weight ratios of ZnO and SnO$_2$) using the sol-gel spin coating technique. It involves a systematic, two-step process: (1) solution formulation and (2) film deposition. Initially, two separate precursor solutions

are prepared. For the first solution, a 0.5 M solution of zinc acetate dihydrate is dissolved in 2-methoxyethanol to form the zinc oxide (ZnO), and for the second solution, a 0.5 M solution of tin chloride is prepared in the same solvent to form the tin oxide (SnO_2). These solutions are then mixed in varying weight ratios such as 50%:50%, 40%:10%, 30%:20%, 20%:30%, and 10%:40% to explore the influence of composition on the final film properties. The combined solution is subjected to continuous stirring and gentle heating at 50–60°C for approximately two hours. This step facilitates uniform mixing at the molecular level, leading to the formation of a clear and homogeneous Zn (O, S) composite sol. Once the solution is ready, it is deposited onto pre-cleaned glass substrates using a spin coating process. The spin coater is operated at 2500 revolutions per minute (rpm) for 10 seconds, ensuring a thin, uniform six-layer of sol is spread across the substrate surface. After deposition, the coated substrates undergo annealing in a furnace at 500°C for five hours. This thermal treatment step is crucial for removing organic residues, promoting crystallization, and enhancing the adhesion and stability of .7the composite film. Figure 3.5. shows the procedure for the synthesis of Composite thin films.
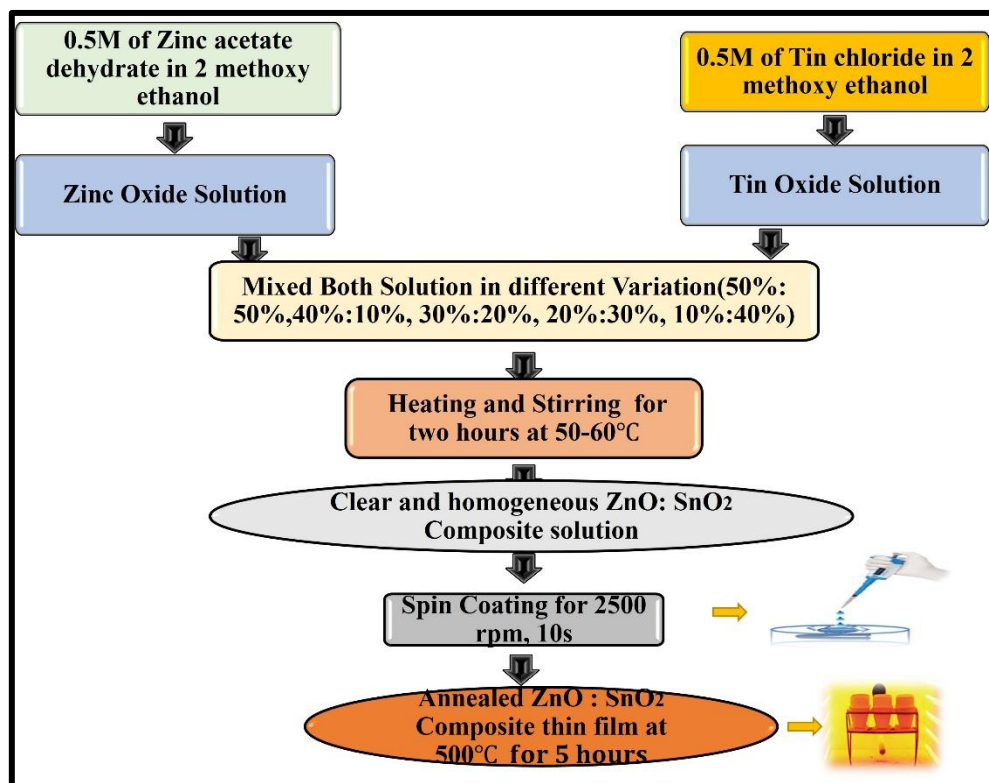
Fig.3.5. Flow chart for Zn (O, S) composite thin films (different weight ratios of ZnO and SnO$_2$).

3.3.5. Synthesis of Zn (S, Sn) ZnS: SnO$_2$ composite thin films with different weight ratios of ZnS and SnO$_2$.

Synthesis of Zn (S, Sn) composite thin films (different weight ratios of ZnS and SnO$_2$) with the use of a sol-gel spin coating approach. The first solution is to prepare sol-gel, and thin films are formed by a spin coater. First, prepare ZnS solution and SnO$_2$ in different containers simultaneously. After that, mix both solutions with a different ratio such as 50%:50%, 40%:10%, 30%:20%, 20%:30%, and 10%:40%. The mixture of different ratios of Composite solutions was continuously stirred and heated to 50–60°C for approximately two hours. This step facilitates uniform mixing at the molecular level, leading to the formation of a clear and homogeneous ZnS: SnO$_2$ composite sol. Once the solution is ready, it is deposited onto pre-cleaned glass substrates using a spin coating process. The spin coater is operated at 2500 revolutions per minute (rpm) for 10 seconds, ensuring a thin, uniform six-layer sol is spread across the substrate surface. The thin film was pre-heated at 100°C for an hour after the deposition of every layer. Once deposited, the films undergo a five-hour annealing process at 500°C in a furnace. This vital thermal treatment serves to eliminate organic components, encourage proper crystallization, and bolster the adhesion and stability of the composite layer. The comprehensive flowchart for preparing the composite thin films is provided in Figure 3.6.
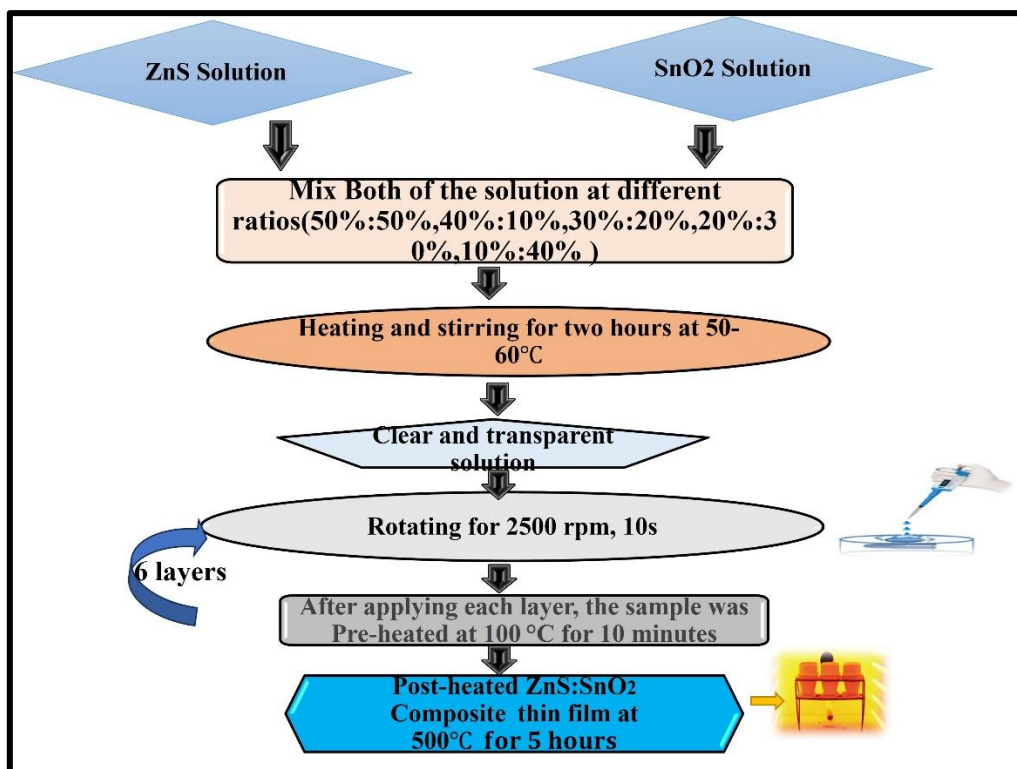
Fig.3.6. Flow chart for Zn (S, Sn) composite thin films (different weight ratios of ZnS and SnO$_2$).

3.4. Materials characterization techniques

Numerous characterization techniques have been utilized to analyze the optical and electrical properties of all the prepared thin film samples. The characterization apparatus used was XRD, UV-Vis Spectroscopy, FTIR, FE-SEM, AFM, 2-Probe, and Hall effect measurements. They were utilizing XRD (Bruker D8 Advance) with Cu-Kα radiation at 1.54056 A° and scanning in 0.02° steps from 20° to 80°, and the thin film structure was investigated. Optical features such as transmission, absorbance, refractive index, optical band gap, etc., were captured with the help of the Shimadzu UV-Vis spectrophotometer (UV-1900i). Fourier Transform Infrared Spectroscopy (FTIR) Perkin Elmer instrument with a scanning range of 400-4000 cm^{-1} was considered to study the material's functional group and chemical bonding. The surface roughness of the prepared thin films was observed by a Multimode Scanning Probe Microscope (Bruker) AFM. The surface morphology, thickness, and details of elements were identified by Field Emission Scanning Electron Microscope (FE-SEM: JEOLJSM-7610

F Plus). HMS-5000 series / HMS-7000 series Hall Effect Measurement System (Vander Pau configuration) and two-probe instruments (SES-CAM TPX setup) were considered to identify the electrical parameters for the thin films. Figure3.7. shows the characterization techniques along with their names.
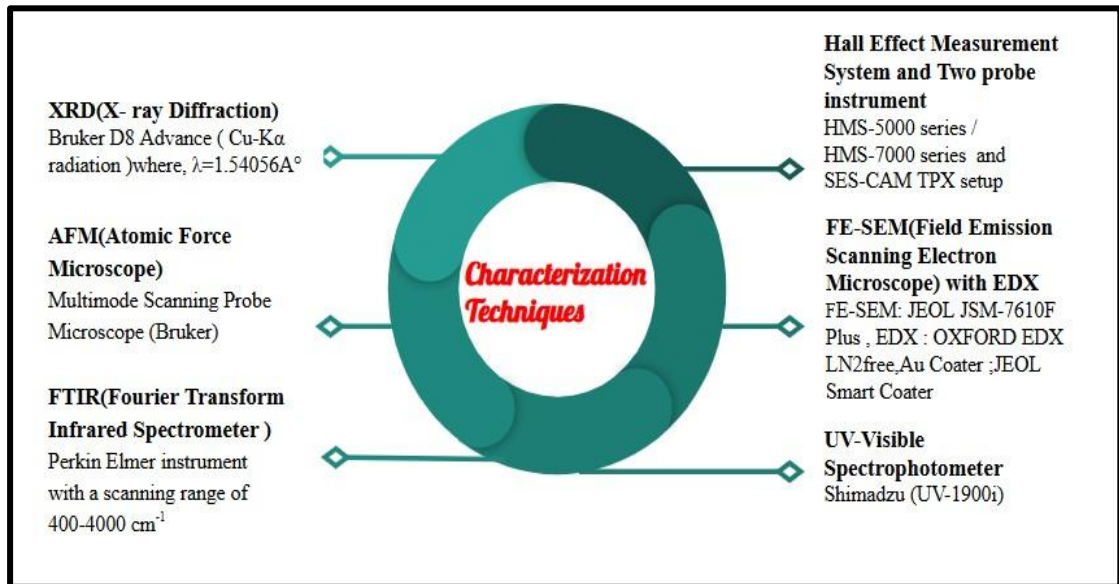
Fig.3.7. Several characterization techniques alongside their respective model names.

3.4.1. X-ray diffraction (XRD)

XRD is an abbreviation for X-ray Diffraction. XRD is predominantly employed for the unique identification of crystalline compounds, much like a fingerprint, and for the analysis of their internal atomic structures[110]. In contrast to spectroscopic techniques that operate by the absorption of radiation at specific wavelengths, the process of diffraction utilizes radiation of a singular wavelength, referred to as monochromatic radiation. It is a non-destructive and non-contact technique that provides insights into a material's structure, including lattice parameters, grain size, structural imperfections, and phase composition. X-ray Diffraction operates on the principle of constructive interference of single-wavelength radiation scattering at specific angles from the lattice planes of a sample, with variations in atomic arrangement influencing the intensity of the resulting peaks. X-rays with wavelengths ranging from 0.001 to 0.1 nanometres are generated in an X-ray tube by bombarding a metallic target with high-speed electrons[111].

3.4.1.1. Mechanism of XRD

X-ray Diffraction (XRD) works based on the interaction between X-rays and the atomic planes of a crystalline material. When a beam of X-rays strikes a crystal, the atoms within the structure cause the X-rays to scatter in specific directions. If these scattered waves interfere constructively, a diffraction pattern is formed. This entire process is governed by Bragg's Law, which describes the condition required for constructive interference explained in equation (3.1).

$$n\lambda = 2d \sin \theta \qquad (3.1)$$

Where n is an integer (order of diffraction), λ depicts the wavelength of the X-rays, d indicates the distance between atomic planes in the crystal (interplanar spacing), and θ represents the angle of incidence of the X-ray beam.

S. No	Component	Uses
1.	X-ray Generation	The instrument produces X-rays using a source, typically copper (Cu), which emits X-rays when high-energy electrons strike it.
2.	Irradiation of the Sample	The generated X-ray beam is directed toward the sample, which is usually in powdered or solid form. The sample contains many small crystals oriented in random directions.
3.	Diffraction by Atomic Planes	As the X-rays interact with the material, they are scattered by the electrons surrounding the atoms. In certain directions, the scattered waves from different atomic planes reinforce each other (constructive interference), producing a detectable diffracted beam.
4.	Detection of Diffracted Rays	A detector moves around the sample in a circular path, recording the intensity of the diffracted X-rays at various angles (2θ). Peaks are observed where Bragg's condition is satisfied.
5.	Formation of Diffraction Pattern	The output is a plot of intensity versus angle (2θ), known as the XRD pattern. Each peak in the pattern corresponds to a specific set of crystal planes.
6.	Analysis	The positions and intensities of the peaks are analyzed to determine structural information such as phase identification, crystal orientation, lattice spacing, crystallite size, and strain.

To determine the structural phases of the materials, the obtained XRD diffraction data were cross-referenced with the standard reference patterns provided by the Joint Committee on Powder Diffraction Standards (JCPDS) or the American Society for Testing and Materials (ASTM)[112]. Afterward, utilizing this XRD data, we can determine the structural parameters, including crystallite size, dislocation density, lattice strain, lattice parameters, d-spacing, and unit cell volume, by employing relevant equations[113], [114].

$$L = {K\lambda}/{\beta \cos \theta} \tag{3.2}$$

$$\delta = {1}/{L^2} \tag{3.3}$$

$$\epsilon = \frac{\beta \cot \theta}{4} \tag{3.4}$$

$$d = {n\lambda}/{2 \sin \theta} \tag{3.5}$$

$$a = d.(h^2 + k^2 + l^2)^{1/2} \tag{3.6}$$

$$V_{cell} = a^3 \tag{3.7}$$

Where L depicts crystallite size, λ presents wavelength, d indicate d-spacing, a represents the lattice constant, V represents cell volume, β displays full-width half maxima. Figure 3.8. signifies the setup of XRD.

3.5.1.2 Advantages of XRD

❖ It is used for the recognition of an unknown material.
❖ This instrument is easily available.
❖ Used for the identification of the Lattice constant and size of the particles.
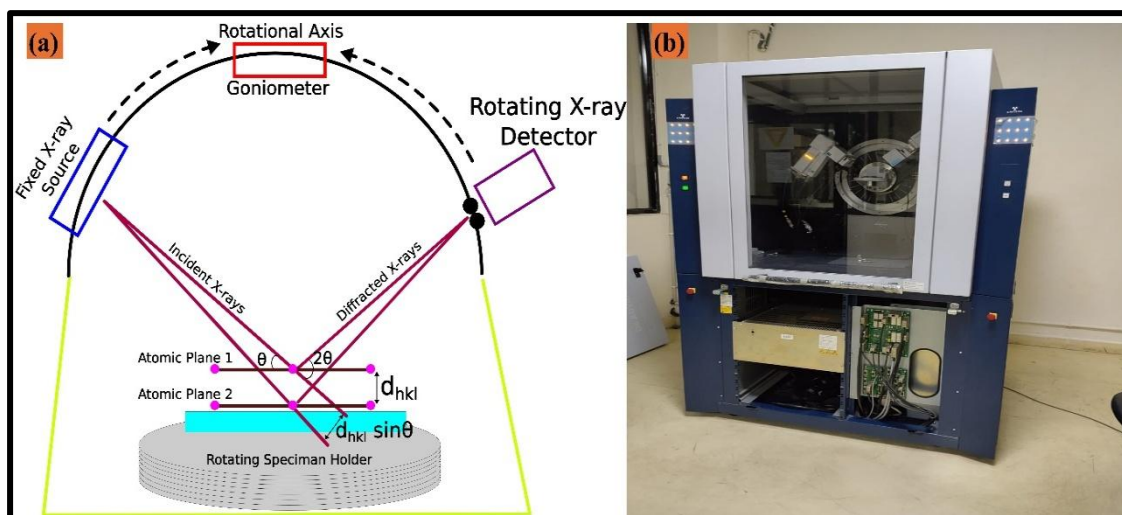
Fig.3.8. (a) Working mechanism of XRD (b) Original setup of XRD**.**

3.4.2. Fourier Transform Infrared Spectrometer (FTIR)

Fourier Transform Infrared Spectroscopy (FTIR) is a widely utilized analytical technique that helps identify the chemical composition and molecular structure of a material by measuring how it absorbs infrared (IR) radiation[115]. The infrared spectrum, spanning wavelengths from (0.7-1) to (200-350) μm, is commonly divided into three regions based on wavenumber: the Near-IR region (13000 - 4000 cm^{-1}), the Mid-IR region (4000 - 400 cm^{-1}), and the Far-IR region (400 - 10 cm^{-1}). It provides both qualitative and quantitative information about a sample by analysing the vibrational transitions of its molecules. FTIR operates on the principle that molecules absorb specific frequencies of infrared light, causing the bonds within them to vibrate[116]. These vibrations can be stretching, bending, or twisting motions. When IR radiation passes through a sample, specific frequencies are absorbed depending on the types of chemical bonds present. The resulting spectrum reflects these absorptions and acts like a unique fingerprint for each compound. The major components of FTIR spectroscopy are Infrared spectroscopy, an Interferometer, a Sample holder, a detector, a Computer, and Fourier software[117].Figure 3.9. illustrates the FTIR instrument.

3.4.2.1. Mechanism of FTIR

S. No	Component	Uses

1.	Broadband IR Source	An FTIR spectrometer emits a beam of infrared light containing a wide spectrum of frequencies
2.	Interferometer Modulation	The IR beam passes through an interferometer, often a Michelson interferometer. This device uses mirrors to create a unique interference pattern called an interferogram. The interferogram encodes all the IR frequencies as a function of the position of a moving mirror within the interferometer.
3.	Sample Interaction	The interferogram then travels through the sample. Molecules in the sample absorb specific IR frequencies that match the vibrational energies of their chemical bonds (stretching, bending, etc.). This absorption reduces the intensity of the transmitted light at those frequencies.
4.	Detection of Transmitted Light	A detector measures the intensity of the IR light that has passed through the sample as a function of the mirror position, generating a sample interferogram.
5.	Fourier Transform Processing	The core of FTIR lies in the Fourier Transform, a mathematical algorithm performed by a computer. This transform converts both a background interferogram (without the sample) and the sample interferogram from the time domain (mirror position) to the frequency domain. The result is an infrared spectrum, which is a plot of absorbance or transmittance versus frequency (or wavenumber).
6.	Spectral Interpretation	The resulting IR spectrum displays absorption peaks at specific frequencies. These frequencies are characteristic of the types of chemical bonds present in the sample (functional groups), and the intensity of the peaks is proportional to the concentration of those bonds. The material can be identified by comparing the sample's spectrum to spectral libraries of known compounds. FTIR can also be used for quantitative analysis to determine the number of specific components in a sample.

3.4.2.2. Advantages of FTIR

❖ Cost Efficiency (Long term)

❖ Ease of use

❖ Comprehensive molecular information

❖ Superior spectral resolution
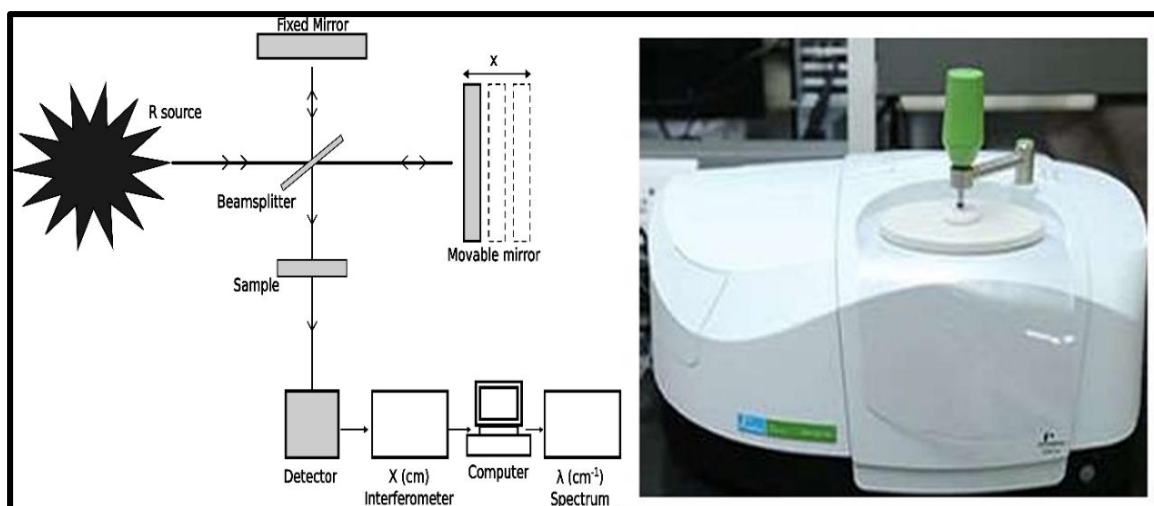
Fig.3.9. Working mechanism of FTIR and the Original setup of FTIR.

3.4.3 Field Emission Scanning Electron Microscope (FE-SEM)

Field Emission Scanning Electron Microscopy (FE-SEM) stands as a sophisticated advancement in electron microscopy, enabling high-resolution (such as 10,000 to 30,000 times) imaging and analysis of material surfaces at the nanometer scale and beyond[118]. It gives information about the surface morphology and thickness of the sample. While sharing the fundamental principles of conventional Scanning Electron Microscopy (SEM), FE-SEM distinguishes itself through its superior electron source: the field emission gun (FEG). This innovation underpins its enhanced capabilities and broader applicability. Figure .3.10. depicts the real setup of FE-SEM (FE SEM: JEOL JSM-7610 F Plus).

3.4.3.1. Core Principles and Operational Mechanism of FE-SEM

The fundamental operating principle of FE-SEM mirrors that of traditional SEM: a focused beam of high-energy electrons is meticulously scanned across the specimen's surface. The interaction of this electron beam with the sample's constituent atoms generates a variety of signals, most notably secondary electrons (SE) and backscattered electrons (BSE), which are subsequently detected to construct an image[119].

The critical divergence from conventional SEM lies within the electron generation process:

❖ **The Field Emission Gun (FEG): A High-Performance Electron Source:** Unlike the heated filaments used in conventional SEMs, the FEG employs a sharply pointed emitter tip, typically crafted from tungsten. By applying an intense electric field gradient to this tip, electrons are extracted via quantum mechanical tunneling (cold field emission) or a combination of field and thermal energy (Schottky emission), even at relatively low operating temperatures.

❖ **Generation of a Superior Electron Beam:** This field emission process yields an electron beam with several key advantages over thermionic emission:

  o **Minimized Source Size:** The virtual origin of the electron beam in an FEG is significantly smaller, leading to a more tightly focused probe.

  o **Enhanced Brightness:** The FEG produces a far greater number of electrons per unit area and solid angle, resulting in a brighter beam.

  o **Improved Monochromaticity:** The emitted electrons exhibit a narrower range of kinetic energies, contributing to reduced chromatic aberration in the electron optics.

❖ **Electron Beam Manipulation and Scanning:** Following generation, the electron beam is precisely shaped and focused by a series of electromagnetic lenses (condenser and objective lenses) and apertures. Scanning coils strategically deflect the finely focused beam across the sample surface in a controlled raster pattern.

❖ **Signal Acquisition and Image Formation:** Detectors strategically positioned around the sample collect the emitted secondary and backscattered electrons. The intensity of the detected signal at each scanned point on the sample is then translated into the brightness level of a corresponding pixel on a digital display, thereby constructing a high-resolution image that meticulously maps the surface topography and compositional variations of the specimen[120].

It is widely utilized in forensic sciences, the identification of semiconductors and nanowires, for the analysis of rocks and samples, biological sciences, etc.

3.4.3.2. Advantages of FE-SEM

❖ Ability to operate effectively at low voltages
❖ Superior image quality
❖ High magnification potential
❖ Unparalleled resolution.
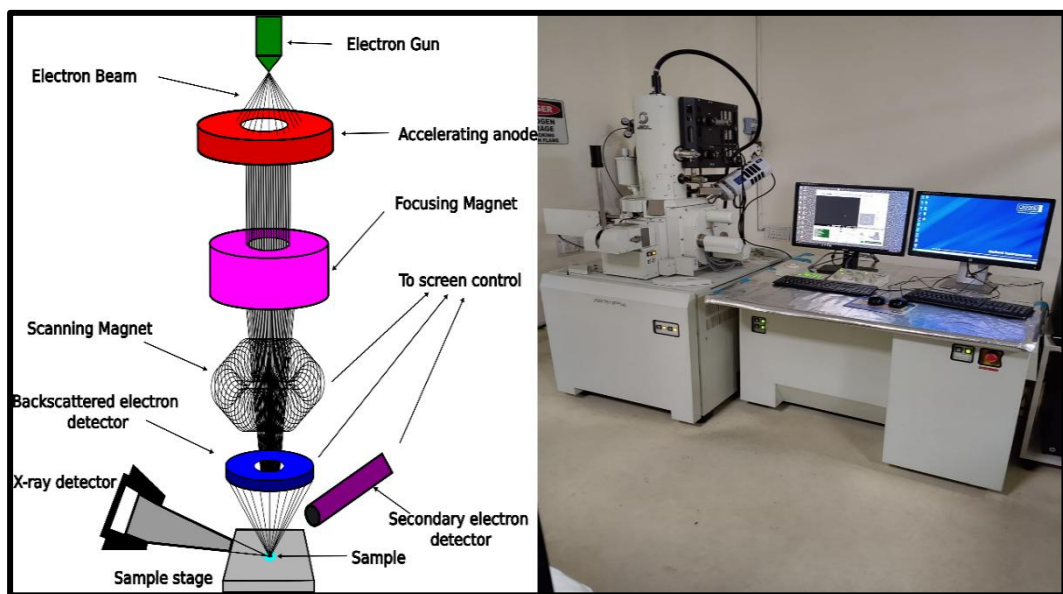
Fig.3.10. Working mechanism of FE-SEM and the Original setup of FE-SEM.

3.4.4. Energy Dispersive X-ray spectroscopy (EDAX)

Heinrich's work in 1968 established a methodology for quantifying the intensity of emitted X-rays. Energy-dispersive X-ray spectroscopy (EDX) is a technique employed to ascertain the elemental composition and the relative proportions of elements within a specimen[121]. The fundamental principle of EDX rests on the fact that each element possesses a unique atomic structure, which, upon excitation, results in a distinctive set of peaks in its X-ray emission spectrum. Figure 3.11. provides a schematic representation of the K, L, and M electron shells surrounding an atom's nucleus. In the EDX process, a sample is bombarded with a beam of electrons, inducing the emission of X-rays. This occurs when an incident electron ejects an electron from the inner

electron shell of an atom within the sample. Subsequently, an electron from an outer shell transition to fill this vacancy, releasing energy in the form of a characteristic X-ray [176]. The energy of this emitted X-ray corresponds precisely to the energy difference between the two electron shells involved in the transition. This characteristic energy signature allows for the unambiguous identification of the elements present in the analyzed specimen. The sensitivity of EDX, indicated by its low detection limit, typically ranges from approximately 0.1 to several atomic percentages. This limit is influenced by the specific element being analyzed and the overall composition (matrix) of the sample. In this context, the chemical composition was determined using EDX spectroscopy (specifically, an OXFORD EDX LN2 free system). An X-ray spectrometer within the EDX setup analyzes the emitted radiation and identifies the constituent elements of the test sample based on their characteristic X-ray wavelengths[122].
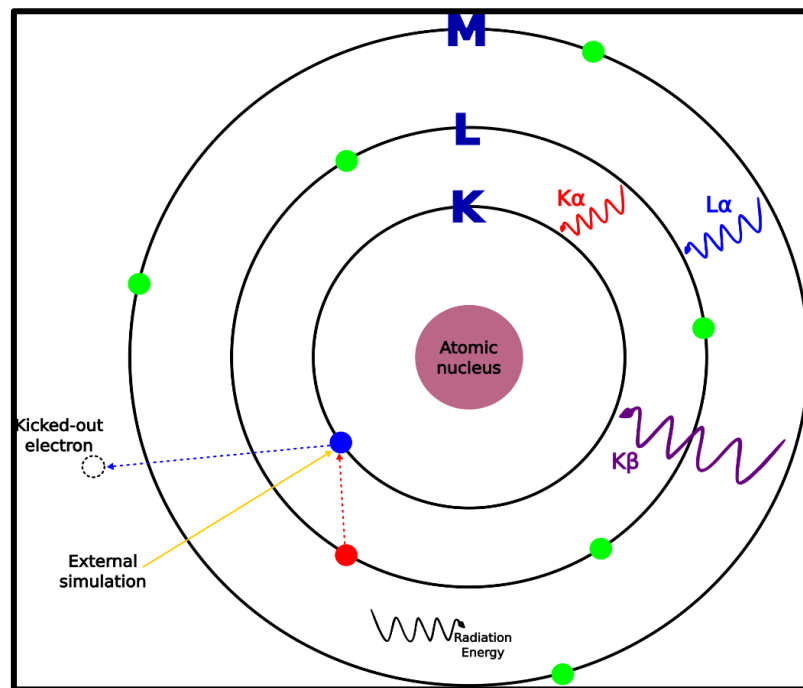
Fig.3.11. The fundamental principle of EDX spectroscopy.

3.4.5. Atomic Force Microscopy (AFM)

Atomic Force Microscopy (AFM) is a high-resolution scanning probe microscopy technique that generates two-dimensional (2D) and three-dimensional(3D) images of surfaces at the nanoscale by meticulously mapping the forces between an extremely

sharp tip and the sample[123]. It extends beyond simple topographical imaging, enabling the measurement of various local surface properties. AFM measurements were conducted to analyze the surface roughness of the thin films, a key factor influencing both the optical and electrical characteristics of the thin films.

3.4.5.1. Principle and Mechanism

The fundamental principle of AFM lies in detecting and quantifying the minute forces that arise when a nanoscale-sharp tip, affixed to a flexible beam known as a cantilever, is brought into proximity with a sample surface. The AFM operates by systematically scanning this tip across the surface and precisely measuring the resulting interactions[124].Figure 3.14 shows the working principle of the AFM setup.

- ❖ **The Nanoscale Probe:** The heart of the AFM is an acutely pointed tip, typically fabricated from silicon or silicon nitride, with an apex radius often just a few nanometers. This tip is situated at the free end of a cantilever, a microfabricated beam with a well-defined spring constant, a crucial parameter for force quantification.

- ❖ **Surface Scanning:** A sophisticated piezoelectric scanner orchestrates the precise movement of the sample (or, in some designs, the tip itself) in a raster pattern across the tip. This controlled scanning ensures that the entire area of interest is systematically probed.

- ❖ **Interatomic Force Sensing:** As the tip approaches the sample's surface, it experiences a range of interatomic forces. At larger separations, attractive forces, such as Van der Waals forces and capillary forces in ambient conditions, dominate. Upon closer approach, repulsive forces, arising from the overlap of electron clouds, become significant.

- ❖ **Cantilever Response:** These interaction forces induce a mechanical response in the cantilever, causing it to bend or deflect. The direction and magnitude of this deflection are directly proportional to the strength and nature (attractive or repulsive) of the forces acting between the tip and the sample, governed by the cantilever's spring constant (Hooke's Law: $F = -kx$).

- ❖ **Deflection Detection:** The minute deflections of the cantilever are typically amplified and precisely measured using an optical lever system. A laser beam is directed onto the reflective back surface of the cantilever, and the reflected

beam's position is monitored by a highly sensitive position-sensitive photodetector (PSPD). Even angstrom-level deflections of the cantilever result in readily detectable shifts in the laser spot's position on the detector.

❖ **Feedback Control and Image Construction:** To maintain a consistent interaction between the tip and the sample (either constant force or constant oscillation amplitude, depending on the chosen operating mode), a feedback loop is implemented. This system dynamically adjusts the vertical (z-axis) position of the scanner.

❖ In **contact mode**, the feedback loop strives to maintain a constant cantilever deflection, thus ensuring a relatively constant force between the tip and the surface. The vertical displacement of the scanner required to achieve this constant deflection at each (x, y) coordinate is recorded and subsequently used to construct the three-dimensional topographical image.

❖ **In dynamic modes** (such as tapping mode and non-contact mode), the cantilever is oscillated at or near its resonant frequency. Changes in the oscillation amplitude or phase, induced by the tip-sample interactions, serve as the feedback signal. The feedback loop adjusts the tip-sample distance to maintain a pre-set oscillation amplitude or frequency. The recorded z-movements of the scanner during this process are then used to generate the surface topography.

❖ **Image Generation:** The collected data, representing the vertical position of the scanner as a function of the lateral (x, y) coordinates, is processed by computer software to generate a high-resolution, three-dimensional topographical map of the sample surface.

Subsequently, the value of average roughness and root mean square roughness (RMS) was determined using Gwydion software. Figure 3.12 shows the working mechanism of AFM.

3.4.5.2. Advantages of AFM

❖ Exceptional Resolution

❖ Intrinsic Three-Dimensional Imaging

❖ Versatile Sample Compatibility
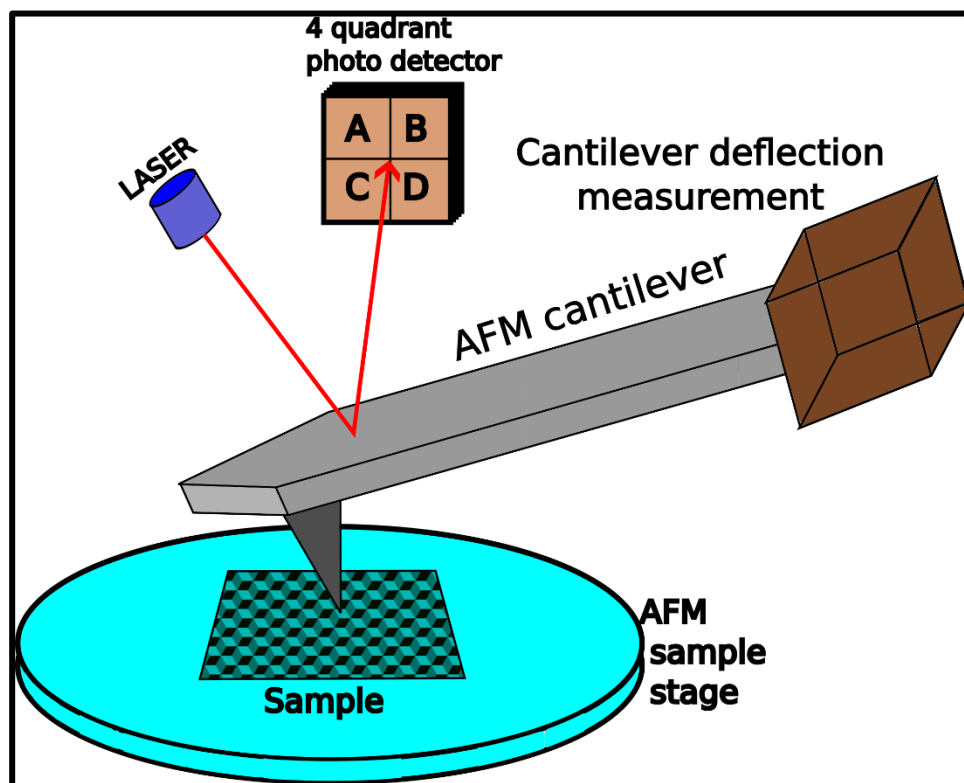
Fig.3.12. Working mechanism of AFM

3.4.6. UV-Visible spectroscopy

UV-visible spectroscopy is used to investigate how these thin films interact with light, thereby identifying their optical properties[125]. It is an analytical technique that measures how much light a thin film absorbs/transmits/reflects across the ultraviolet (UV)(200-400nm) and visible portions(400-800nm) of the electromagnetic spectrum. This interaction reveals information about the electronic structure of molecules. A material exhibiting greater light transmission within the visible spectrum inherently demonstrates reduced light absorption and reflection. They are inversely related to each other. When a sample does not absorb incident light across a specific wavelength range, the intensity of the incident light (I) equals the intensity of the transmitted light (Io), such as $I=I_0$. However, perfect transmittance is not observed in any material; the transmitted light intensity (Io) is invariably less than the incident light intensity (I), such as $I_0<I$. The relationship between absorption (A) and transmittance (T) is defined by

Beer-Lambert's law, and the material's absorption is expressed by the equation (3.8)[126].

$$\left(A = -\log(T) - log\,{}^{I_0}\!/_I\right) \hspace{4cm} (3.8.)$$

The optical band gap is determined by analysing the sample's transmittance and thickness. In semiconductors, incident light absorption can excite electrons from the valence band to the conduction band via two types of optical transitions: direct and indirect. Both transition types result from the interaction between electromagnetic radiation and the crystal lattice. The distinction between direct and indirect transitions arises from the momentum conservation requirements during photon absorption, specifically concerning the momentum vector of the photon relative to the crystal's momentum space. The Tauc relation[127] is used to estimate the direct and indirect band gaps of the samples.

3.4.6.1. Mechanism of UV-visible spectroscopy

❖ **Light Source:** A UV-Vis spectrophotometer uses a light source that emits a stable beam of light across the UV and visible regions (typically 190-800 nm). Common sources include deuterium lamps for the UV region and tungsten-halogen lamps for the visible region.

❖ **Wavelength Selection (Monochromator):** The polychromatic light beam is passed through a monochromator (such as a prism or diffraction grating) that separates the light into its wavelengths. A slit then selects a narrow band of wavelengths to pass through the sample.

❖ **Sample Compartment:** The selected monochromatic light beam passes through the sample, which is typically contained in a transparent cell called a cuvette (made of quartz for UV and glass or plastic for visible light).

❖ **Detector:** After passing through the sample, the intensity of the transmitted light is measured by a detector (such as a photomultiplier tube or a photodiode).

❖ **Reference Beam:** In a double-beam spectrophotometer (a common design), the light beam is split into two paths: one passes through the sample, and the other passes through a reference solution (usually the solvent). This allows for

automatic correction of any absorbance by the solvent and fluctuations in the light source.

❖ **Signal Processing:** The detector converts the light intensity into an electrical signal. The instrument then compares the intensity of the light that passed through the sample (I)to the intensity of the incident light (I_0) to determine the absorbance or transmittance

❖ **Spectrum Generation:** The spectrophotometer scans through the selected range of wavelengths and plots the absorbance (or transmittance) as a function of wavelength, generating a UV-Vis spectrum. This spectrum shows peaks at wavelengths where the sample absorbs the light the least.

❖ **Analysis:** The wavelengths of maximum absorbance (λ_{max}) and the magnitude of the absorbance values are characteristic of the analyte and can be used for identification and quantification based on the Beer-Lambert Law.

From the UV-visible data, we can determine the necessary optical parameters such as transmission(T), absorbance(A), reflectance(R), absorption coefficient(α), extinction coefficient(k), refractive index(n), band gap, etc. Figure3.13. shows the working mechanism of UV-Visible spectroscopy.

3.4.6.2. Advantages of UV-Visible spectroscopy

❖ The main advantage is that anyone can quickly handle it.

❖ It can be utilized in the form of qualitative and quantitative analysis.

❖ It's a very cost-effective instrument.

❖ It covers the complete study of the ultraviolet and visible regions.
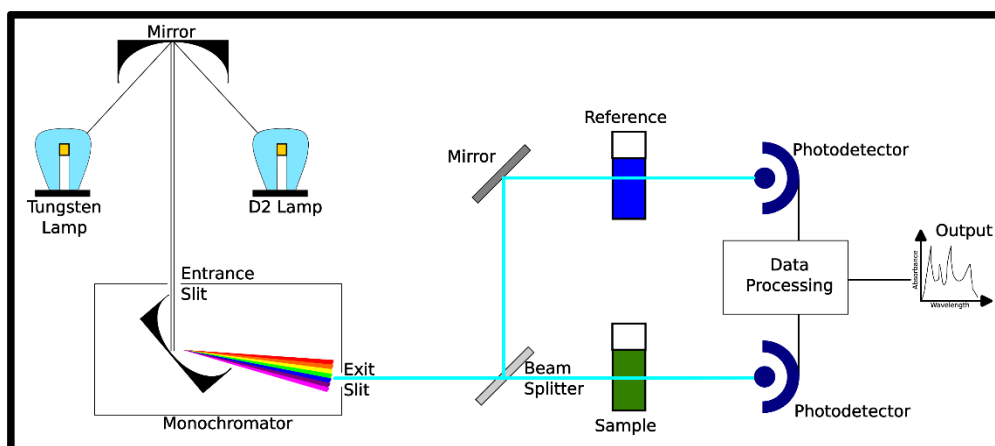
Fig.3.13. Working mechanism of UV-Visible spectroscopy.

3.4.7. Two-Probe Instrument (TPX)

A two-probe instrument is a fundamental setup for electrical characterization, primarily employed to determine the electrical resistance or analyze the current-voltage (I-V) relationship of a material or a component. It is a necessary instrument for measuring the electrical properties of the thin films. Its core mechanism involves establishing electrical contact with the sample at precisely two distinct locations using conductive probes[128].

3.4.7.1. Mechanism of two-probe instruments

The operational principle of a two-probe instrument hinges on Ohm's Law (V = IR), which posits a direct proportionality between the voltage (V) applied across a conductor and the resulting current (I) flowing through it, with the resistance (R) serving as the proportionality constant. The instrument functions by applying a controlled electrical stimulus (either a specific voltage or current) across the two probes in contact with the sample and subsequently measuring the corresponding electrical response (current or voltage)[129].

❖ **Establishing Electrical Contact:** Two conductive probes, typically fabricated from a conductive material like metal and often featuring a sharp tip or a flat contact pad, are brought into direct physical contact with the sample at two designated points. These probes serve as the conduits through which electrical current enters and exits the portion of the sample being investigated.

❖ **Applying an Electrical Bias:** An external electrical circuit, incorporating a power source and control elements, is used to apply a defined electrical bias across the two probes. This bias can take the form of a specific voltage applied between the probes or a controlled current forced to flow through the sample between the probe contacts.

❖ **Measuring the Electrical Response:** Depending on the type of bias applied, the instrument measures the resulting electrical parameter:

• If a voltage bias is applied across the two probes, a current-measuring device (ammeter) integrated into the circuit quantifies the magnitude of the electrical

current flowing through the sample segment situated between the points of probe contact.

- Conversely, if a current bias is forced to flow between the two probes, a voltage-measuring device (voltmeter) measures the potential difference (voltage drop) that develops across the sample segment between the probe contacts.

  - ❖ **Determining Electrical Properties:** Based on the measured voltage and current values, the electrical resistance (R) of the material or component segment between the two probes is calculated using Ohm's Law (R = V/I). By systematically varying the applied voltage or current and recording the corresponding current or voltage, the instrument can trace out the I-V characteristics of the sample. This I-V curve can reveal whether the sample exhibits ohmic (linear relationship) or non-ohmic (non-linear relationship) electrical behavior.

3.4.7.2. Components

1) Probe arrangement
2) Oven
3) PID – TZ Controller Unit

1) Probe arrangement

In the Probe arrangement, two Spring load probes are present. It is mounted on a better kind of alumina and holds a sample plate. To get better values of the temperature of the sample, a thermojunction couple is present between the sample plate under the sample. The stand works as a temperature controller. For better connection of EHT, DPM, and the temperature Controller, proper leads are available.

2)Oven

The oven has a high level of control overheat. The heating element that is used is called high-grade Kanthal-D. It is mounted on a high-grade, custom-made grooved. To avoid overheating, sintered alumina is used. The heat shield is also available to decrease the overload of the outer cover and improve its efficiency. The top portion is also covered

in terms of safety measures. The oven is especially present for fast cooling and heating, which increases the effectiveness of the controller.

3)PID -TZ Controller unit

The PID Controller unit is a high-quality controller unit. In this unit, temperature is measured and controlled easily. For the easily available, P, I, and D parameters are used. For small ovens (temperature up to 200) and large ovens (temperature up to 600), a Common type of controller can be used. These two parameters work as a switch selector. Thermocouples are used as temperature sensors.

3.4.8. Hall measurements

Accurately determining the electrical transport properties of transparent conducting thin films is crucial for their applications. These properties are influenced by the film's thickness, structure, and surface. The electrical transport properties were estimated by the Hall-Effect method using standard Van der Pauw geometry[130].When a current-carrying specimen is placed in a transverse magnetic field, a voltage is developed across the specimen in a direction perpendicular to both the current and magnetic field. This phenomenon is called the Hall Effect. It was discovered by Edwin Hall[131]. It is used to determine carrier concentration, electrical conductivity, carrier type (n-type or p-type), and mobility of carriers. It is low-cost and has a fast turnaround time, and hence it is of immense value for the semiconductor industry and research laboratories.

3.4.8.1. Principle

The Hall Effect is fundamentally based on the Lorentz force, which acts on charge carriers moving perpendicularly to a magnetic field. In a bar-shaped n-type semiconductor, when electrons carrying a current (I) along the x-axis are subjected to an external magnetic field in the z-direction, they experience a Lorentz force perpendicular to both their motion and the magnetic field, influencing their trajectory in conjunction with the internal electric field. This phenomenon is illustrated in Figure 3.16. The Lorentz force on these electrons is given by

$$F = -e\left[\frac{1}{c}V \times H_z\right] \tag{3.9}$$

where e represents the elementary charge, F denotes the Lorentz force, c is the speed of light in a vacuum, v is the velocity of the electrons, and Hz signifies the magnetic field component along the z-direction.
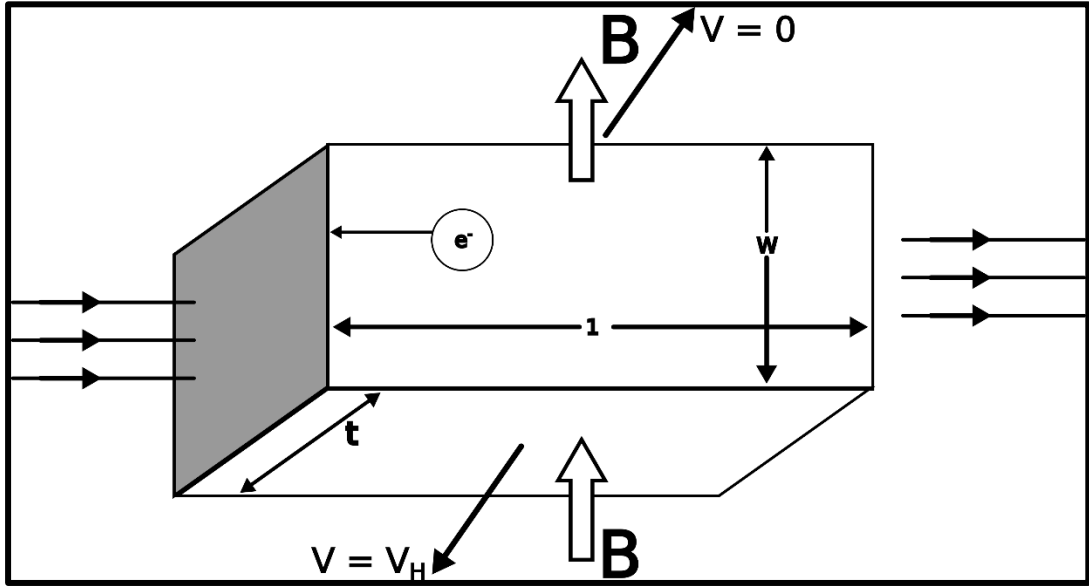
Fig.3.14. An n-type, bar-shaped semiconductor experiences a continuous current I am flowing from left to right along the x-axis when a z-directed magnetic field is present because of the voltage being applied.

The Lorentz force causes the moving electrons to deviate, accumulating on one side of the sample. This charge buildup creates a potential difference across the sample's width, known as the Hall voltage (V_H), the magnitude of which is given by

$$V_{H} = \frac{IB}{qnt} \tag{3.10}$$

where I = current, B = magnetic field, t = sample thickness, n = carrier density, and q (1.602×10^{-19} C) is the elementary charge. In some cases, it is convenient to use layer or sheet density ($n_s = nt$) instead of bulk density. One then obtains the equation

$$n_{s} = \frac{IB}{q|V_{H}|} \tag{3.11}$$

Therefore, by knowing the current(I), magnetic field(B), and elementary charge(q), the sheet density(n_s)of charge carriers in semiconductor materials can be determined through the measurement of the Hall voltage (V_H).

3.4.8.2. Vander Paw method

The convenient Van der Pauw method is widely employed for resistivity measurements of uniform samples[132].It utilizes a thin, arbitrarily shaped sample with four small, ohmic contacts at its periphery, ideally near the corners. These contacts must be on the sample's edge, sufficiently small, and the sample should have a uniform thickness, a continuous surface, and no isolated holes. A rectangular contact arrangement for this technique is depicted in Fig.3.17
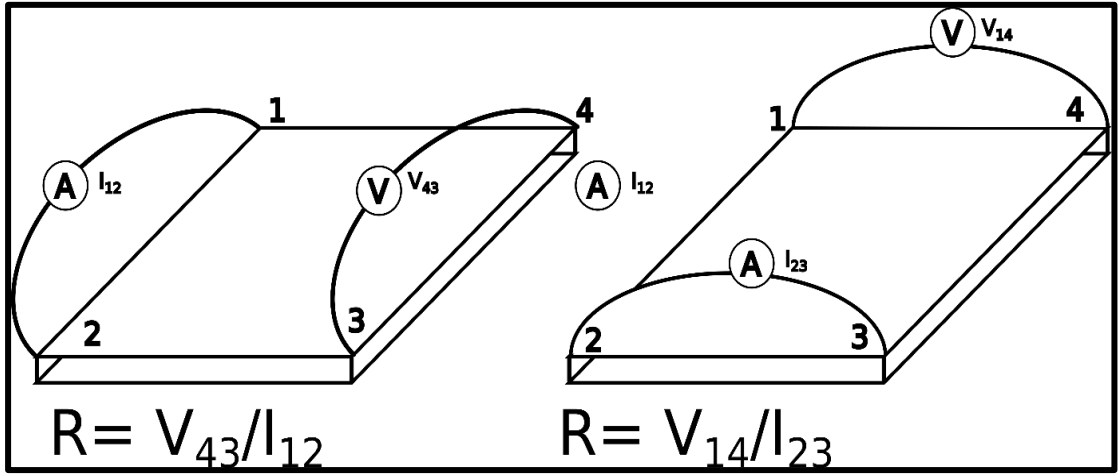
Fig.3.15. It demonstrates the Vander Pau techniques.

To obtain the two characteristic resistances, RA and RB, a DC voltage is applied across contacts 4 and 3, and the current, I12, is measured from contacts 1 and 2, as shown in Fig. 2.8(a). Next, apply the voltage across contacts 1 and 4 and measure current I_{23} from contacts 2 and 3 (Fig. 2.8 (b)). R_A and R_B are calculated employing the following expressions:

$$R_A = \frac{V_{43}}{I_{23}} \text{ and } R_B = \frac{V_{14}}{I_{23}}$$
(3.12)

To determine the sheet resistance Rs, van der Pauw demonstrated that there are two characteristic resistances R_A and R_B, associated with the corresponding terminals shown in Fig. 2.8. R_A and R_B are related to the sheet resistance Rs through the van der Pauw equation

68

$$\exp\frac{-\pi R_A}{R_s} + \exp\frac{-\pi R_B}{R_s} = 1 \qquad (3.13)$$

The bulk electrical resistivity ρ can be calculated using the value of Rs and thickness t of the samples.

$$\rho = R_s t \qquad (3.14)$$

In the Van der Pauw technique, Hall measurements aim to determine the sheet carrier density (n_s), by quantifying the Hall voltage (V_H). This involves a sequence of voltage measurements conducted under a constant current(I)and a constant magnetic field (B) oriented perpendicularly to the sample's surface. Notably, the same sample configuration as depicted in Fig.3.18.can be efficiently utilized for these Hall measurements.
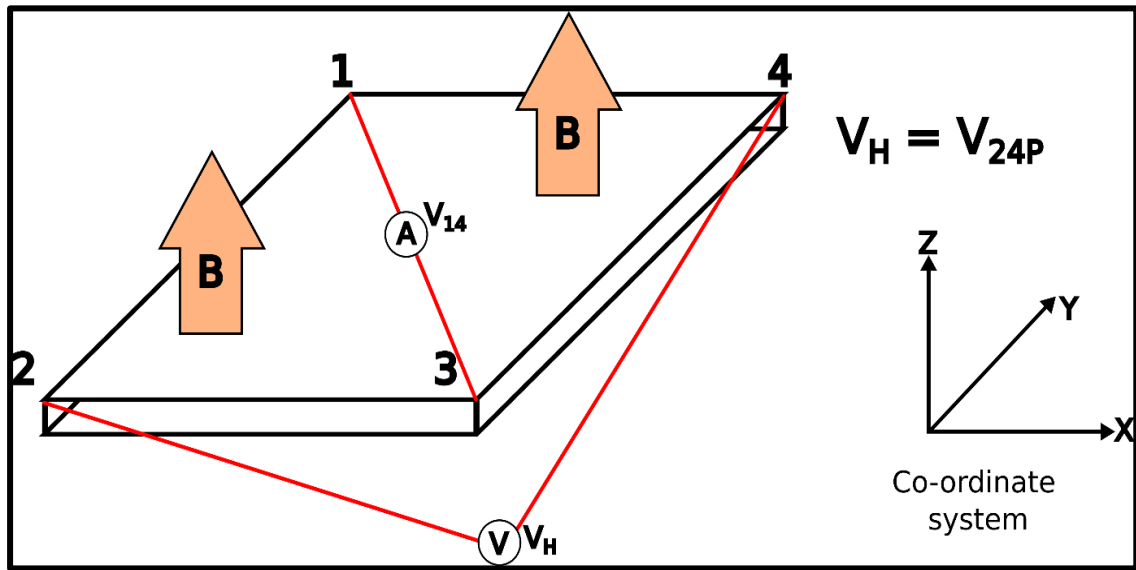
Fig.3.16. Set up for carrier density determination.

To measure the Hall voltage V_H, a current 'I' is passed through the opposing pair of contacts 1 and 3, and the Hall voltage V_H (= V_{24}) is measured across the remaining pair of contacts 2 and 4. Once the Hall voltage V_H is measured, the sheet carrier density ns can be calculated from the known values of I, B, and q using the following equation 3.15.

$$n_s = \frac{8\times10^{-8}\,IB}{q\,\Sigma|V_H|} \qquad (3.15)$$

In intrinsic semiconductors, charge carriers are thermally generated electron-hole pairs. The intrinsic carrier concentration varies with temperature and band gap. The carrier concentration is calculated by using the following relation.

$$n = \frac{n_s}{t} \tag{3.16}$$

The hall mobility (μ) of the charge carrier is an index to know how rapidly the charge carrier will move on the application of the electric field, or it is the average drift velocity per unit electric field. It is the characteristic of the material and the magnitude that can be altered by variations in temperature and purity of the material and can be calculated using the relation 3.16.

$$\mu = \frac{1}{q.R_{s.}\, n_s} \tag{3.17}$$

3.4.8.3. Advantages

❖ Identification of carrier type
❖ Fundamental Material Property
❖ Non-destructive technique

Chapter 4

Transparent conductive Zinc oxide in its pure form and Cu²⁺ and Mg²⁺doped ZnO thin films.

4.1. Introduction

In this regard, ZnO material has emerged as a promising candidate in place of ITO due to its lower price, non-toxicity, and thermal and chemical stability. ZnO thin film has versatile structural as well as optical, and electrical properties[133]. Due to excellent transmission and conductive features, it is a useful candidate for optoelectronic devices such as solar cells, display devices, light-emitting diodes, gas sensing, etc [68], [134], [135], [136]. Zinc oxide thin films are a prominent material within the II-VI semiconductor group. At room temperature, ZnO is an n-type semiconductor characterized by a direct wide band gap of 3.37 eV and a substantial exciton binding energy of 60 meV [137]. This chapter synthesizes Zinc Oxide (ZnO) thin film material using the sol-gel spin coating method, a cost-efficient and readily accessible technique. The pure ZnO host material was subjected to a post-heating process at 500°C for five hours, a condition informed by existing literature[138].

To further improve the transmission and conductive properties of pure ZnO for transparent conducting oxide (TCO) applications, dopants were introduced. These dopants generate charge carriers, modify the electronic band structure, and influence oxygen vacancies. In comparison to other doping elements, Copper (Cu²⁺) and Magnesium (Mg²⁺) can be easily incorporated into the ZnO lattice. This is attributed to their ionic radii, which are (0.72Å) and (0.73Å), and electronic configurations being like those of Zinc (Zn). Copper (Cu²⁺) and magnesium (Mg²⁺) exhibit excellent electrical conductivity, are cost-effective, and are abundantly found in the Earth's crust, making them valuable elements for doping[139]. Magnesium (Mg²⁺), related to a divalent alkaline earth metal, and copper (Cu²⁺) are related to transition metals[140].

Transition metal ions are the simplest and well-suited for doping since partially filled d shells characterize them. The transition metal Cu is an attractive dopant for ZnO because it is isomorphic to Zn and has different acceptor properties in the ZnO matrix.

This chapter is focused on the preparation of transparent conductive zinc oxide (ZnO) thin films in their pure form and copper (Cu^{2+}) and Magnesium (Mg^{2+}) doped ZnO thin films. Thin films were synthesized using the sol-gel spin coating approach with post-heated treatment for five hours at 500°C. Doping concentrations were 0.1%,0.5%, and 1.0%. The prepared thin films were characterized by utilizing XRD, FE-SEM, UV-Visible spectroscopy, AFM, FE-SEM, Hall measurements, and a two-probe instrument. The material is tested for transparent conducting oxide (TCO) thin films by measuring the figure of merit of the material. A higher FOM indicates superior performance of the material in terms of transmission and conductivity.

4.2. Results and Discussion

4.2.1 Structural study

The phase and structural analysis of the prepared thin films was carried out using an X-ray diffractometer. The XRD patterns of pure ZnO, Cu-doped ZnO, and Mg-doped ZnO (0.1%, 0.5%, and 1.0% doping concentration) were post-heated for five hours at 500 °C, as shown in Figure 4.1 (a,b). The most prominent diffraction peaks were observed at 2θ values of 31.66°, 34.37°, 36.18°, 47.45°, 55.91°, 56.61°, 62.80°, 66.37°, 67.99°, and 69.09°, corresponding to the (100), (002), (101), (002) (110), (103), (200), (112), and (201) crystallographic planes of the ZnO structure, consistent with the data provided in JCPDS Card No. 36-1451. These findings prove that all the thin films exhibit a polycrystalline hexagonal wurtzite structure[141]. The absence of additional diffraction peaks in all copper-doped samples suggests the effective integration of copper within the pure ZnO structure. An observation was made that as the copper doping concentration increased, the intensity of the (100), (002), and (101) diffraction peaks also increased. Notably, the (101) peak exhibited the highest intensity and the most significant increase among all peaks, indicating an improvement in the crystallinity.

Figure 4.1(b) illustrates the effects of Mg doping in ZnO thin films at concentrations of 0.1%, 0.5%, and 1.0%. After the introduction of Mg^{2+}, the XRD pattern exhibits no new diffraction peaks, and the existing peaks remain unchanged, suggesting the successful incorporation of Mg^{2+} within the ZnO lattice. The most intense diffraction peaks, specifically (100), (002), and (101), exhibited changes with Mg^{2+} doping. At a 0.1% Mg concentration, these peaks showed increased intensity, indicating improved crystallinity. However, with further doping at 0.5% and 1.0%, the intensity of these prominent peaks decreased. Also, the (110) peak shows a minor shift towards the higher angle. It happens because of compressive strain, which occurs after the introduction of Mg^{2+} into the host lattice[135]. The ionic radius of Mg^{2+} is less than that of Zn^{2+}. Other potential reasons for this peak shift include tensile strain, alterations in the lattice parameters, and the occupancy of interstitial sites within the host lattice by the dopant atoms, or conversely, the dopant atoms substituting host lattice ions of a different size.
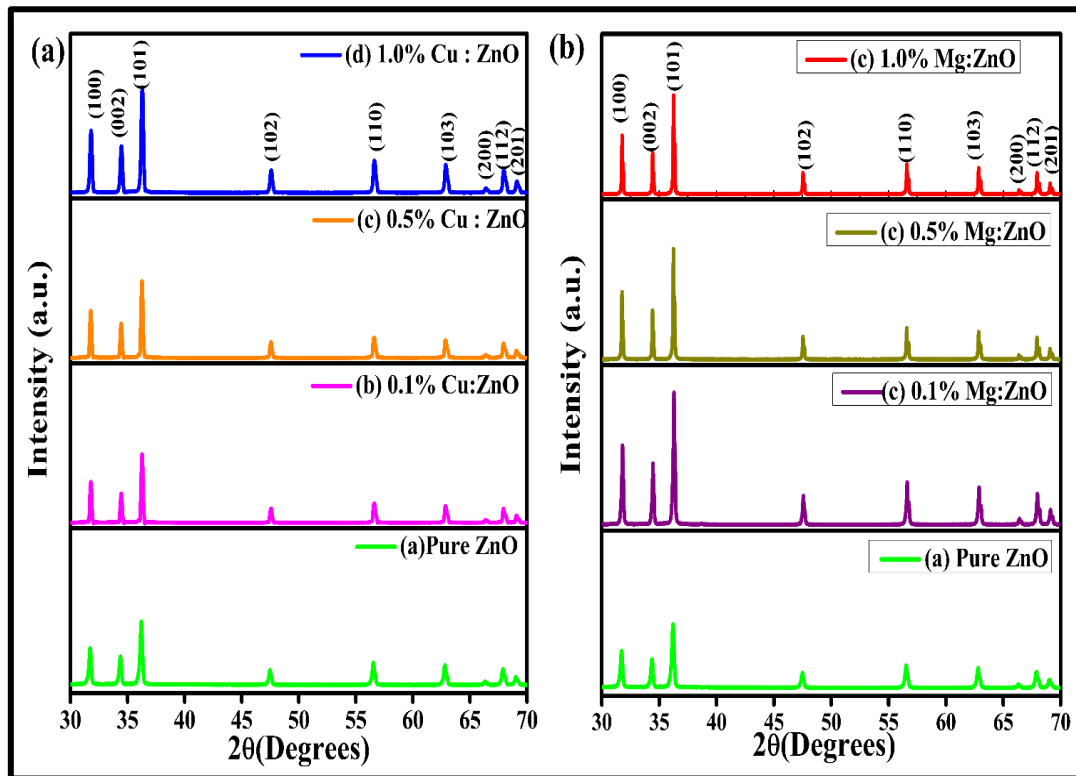
Fig.4.1(a,b) XRD spectra for pure ZnO, Cu: ZnO, and Mg: ZnO thin films at various concentrations.

The value of crystallite size (D) from the Scherrer formula, and the dislocation density(δ) and lattice strain ($\in$) of pure ZnO, Cu doped ZnO, and Mg-doped ZnO thin films were measured by using the equations in Chapter 3 (3.2), (3.3), (3.4)[142], [143].

Table4.1. The measured values of structural parameters of pure ZnO, $Cu^{2+,}$ and Mg^{2+} doped ZnO thin films.

Mg and Cu Content	(hkl) plane		Crystallite Size(nm)		Dislocation density(δ)(10^{-3}) (nm^{-2})		Strain ($\in$)$\times 10^{-3}$	
	Cu: ZnO	Mg:ZnO	Cu:ZnO	Mg: ZnO	Cu: ZnO	Mg:ZnO	Cu: ZnO	Mg:ZnO
Pure ZnO	(101)	(101)	32.14	32.14	0.96	0.96	3.47	3.47
0.1%	(101)	(101)	46.44	56.84	0.46	0.30	2.39	1.96
0.5%	(101)	(101)	49.17	52.24	0.41	0.36	2.26	2.13
1.0%	(101)	(101)	59.17	47.60	0.28	0.42	1.86	2.29

Table 4.1. summarizes the measured values of crystallite size, dislocation density of pure ZnO, Cu-doped ZnO, and Mg-doped ZnO at various concentrations. The findings revealed that as the concentration of Cu^{2+} dopant within the ZnO lattice increased, the crystallite size also expanded, progressing from 32.14 nm to 59.17 nm. Furthermore, the dislocation density and strain exhibited an inverse relationship with the crystallite. It reduces with the enhancement of doping. This enhanced crystallinity is often linked to improved electrical and optical characteristics because a more ordered structure minimizes the scattering of charge carriers and photons by defects and grain boundaries. Reduced scattering results in higher carrier mobility and thus increased electrical conductivity. A similar trend occurs in previous research[144], [145].

Table 4.1 further describes the crystallite size, dislocation density, and strain of Mg-doped ZnO thin films at different concentrations. Pure ZnO exhibits a 32.14nm crystallite size. Introducing 0.1% Mg^{2+} into pure ZnO leads to an increase in crystallite size to 56.84 nm. However, with further doping of 0.5% and 1.0% Mg^{2+}, the crystallite

size decreases to 52.24 nm and 47.60nm, respectively. Overall, the crystallite size of Mg^{2+} doping rises compared to pure ZnO. This growth in crystallite size is attributed to the substitution of Zn^{2+} ions by Mg^{2+} ions within the lattice[141]. The observed increase in crystallite size could be a result of improvements in crystal quality, reduced crystal distortion, and a decrease in crystal defects[146]. Furthermore, an inverse correlation was observed between crystallite size and both dislocation density and strain within the material.

4.2.2 FTIR Study

Fig.4.2 (a,b) indicates the FTIR spectra of pure ZnO, Cu doped ZnO, and Mg-doped ZnO thin films at 0.1%,0.5%, and 1.0% concentration. The spectra over a wavelength range of 400 to 4000cm^{-1}, were recorded during the process of light passing through the materials. It displays the same absorption band for all the films, but intensities vary. The absorption band observed across a broad range of approximately 400–550 cm^{-1} can be attributed to the Zn-O stretching mode. This proves the formation of Zinc oxide material[147],[148], [149]. The absorption band observed at 435 cm^{-1}, indicative of the Zn-O bond stretching vibration in the thin film[150]. With the addition of Cu doping on ZnO host,418 cm^{-1} shows the symmetric Cu-O stretching vibrations, and 518 cm^{-1} shows the Asymmetric Cu-O stretching vibrations. [151].409cm^{-1} signifies the Mg-O vibrations in Mg-doped ZnO thin films. These peaks overlap with the Zn–O vibrations, resulting in a merged and broadened absorption band in this region. A sharp absorption peak is analyzed at 886 cm^{-1} wavenumber, which depicts the variation in the vibrational mode of the C=O group[152]. The absorption bands observed in the range of 2944 cm^{-1} are characteristic of the C-H stretching vibration found in organic compounds. The analysis also revealed the absence of any additional peaks in the FTIR spectra of pure ZnO, as well as Mg and Cu doped ZnO samples. However, shifts in lattice vibrations and broadening of existing peaks towards higher wave numbers were observed with increasing dopant concentrations of Mg^{2+} and Cu^{2+}. This confirms the successful incorporation of the dopants into the ZnO lattice without altering its fundamental structure. A consistent pattern was noted in the previous study[153].
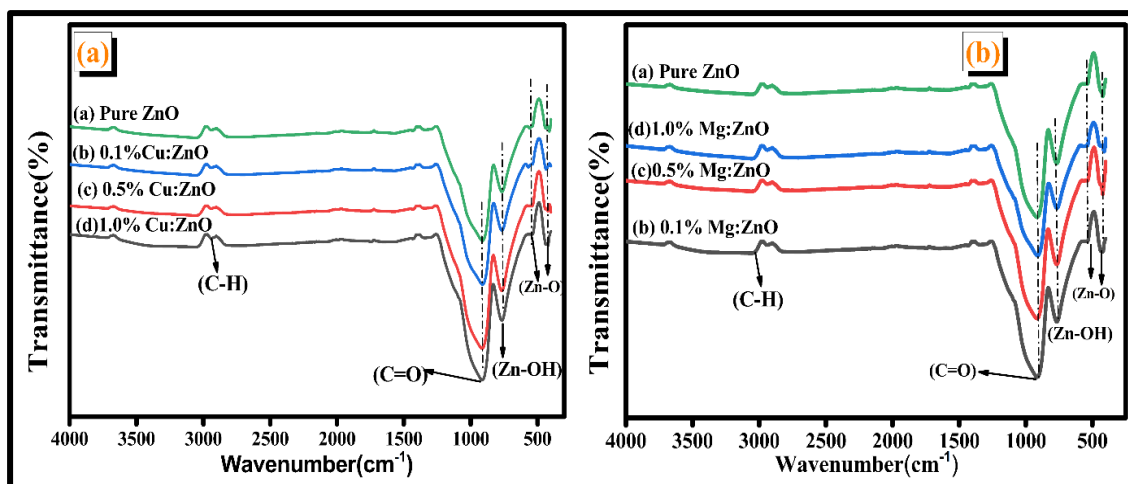
Fig.4.2. (a, b) FTIR spectra for pure ZnO, Cu: ZnO, and Mg: ZnO thin films at various concentrations.

4.2.3 FESM analysis

The surface morphology, thickness, and particle size of the thin films were investigated by FE-SEM micrographs. Figure 4.3. (a, b, c) present the micrograph of pure ZnO, Cu doped ZnO, and Mg-doped ZnO at 45000 magnification and a particle range of 100nm. All the thin film shows good adhesion, and particles are uniformly distributed over the glass substrate. It further confirms that the SEM micrographs show crackles and homogeneous grain distribution [154]. In pure ZnO, grains are tightly packed with minimal gaps, indicating dense and compact film formation. The morphology suggests controlled nucleation and good crystallinity in the pure ZnO. The Cu-doped ZnO shows slightly larger and more rounded grains compared to Pure ZnO, implying that Cu incorporation may encourage grain growth or influence surface energy. Also, the Mg-doped ZnO sample presents even bigger grains with a more irregular shape, indicating that Mg doping significantly impacts the growth process, possibly leading to increased grain coalescence. Overall, the introduction of Cu and Mg alters the surface morphology of ZnO, which could in turn affect characteristics such as surface area, porosity, and electronic properties[155].
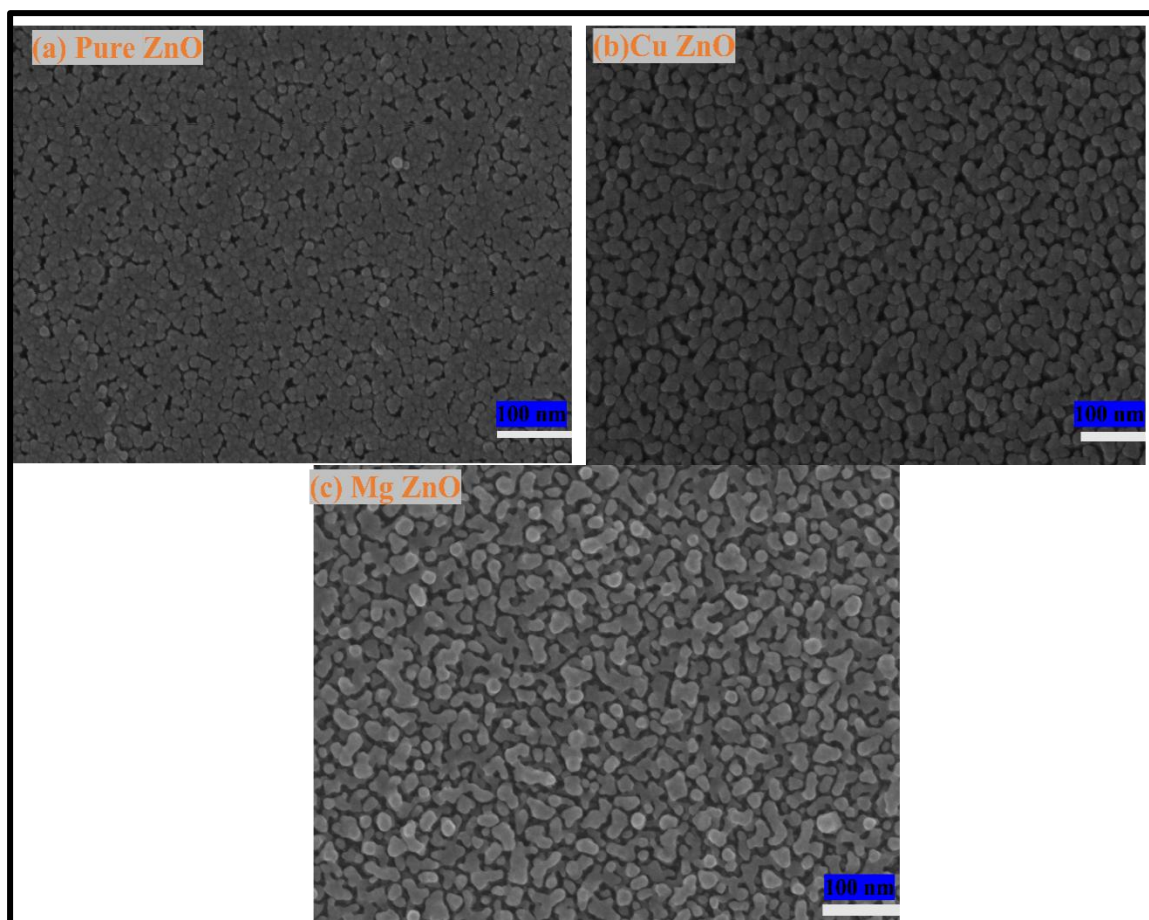
Fig.4.3. (a,b,c) FE-SEM for pure ZnO, Cu: ZnO, and Mg: ZnO thin films.

4.2.3.1 Thickness Analysis

The formation of thin films, which possess thicknesses varying from the nanometer to the micrometer scale, involves the sequential deposition of atoms or molecules onto a solid substrate. Applying a thin layer of one substance onto another can alter the underlying material's attributes, including its optical characteristics, mechanical strength, and ability to conduct electricity. One of the most significant factors in evaluating transparent conducting oxide thin films is their thickness. The thickness of pure ZnO, Cu-doped ZnO, and Mg-doped ZnO thin films (at a 1.0% concentration), analyzed using FE-SEM at a magnification of 45000 within a specific particle size range(100nm) after annealing at 500°C for five hours, is illustrated in Figure 4.4. The measurements revealed a thickness of 189 nm for pure ZnO, 222 nm for Cu-doped ZnO,

and 233 nm for Mg-doped ZnO. The thickness of Cu doped ZnO and Mg-doped ZnO thin films rises with the doping concentration of Cu and Mg on ZnO material.
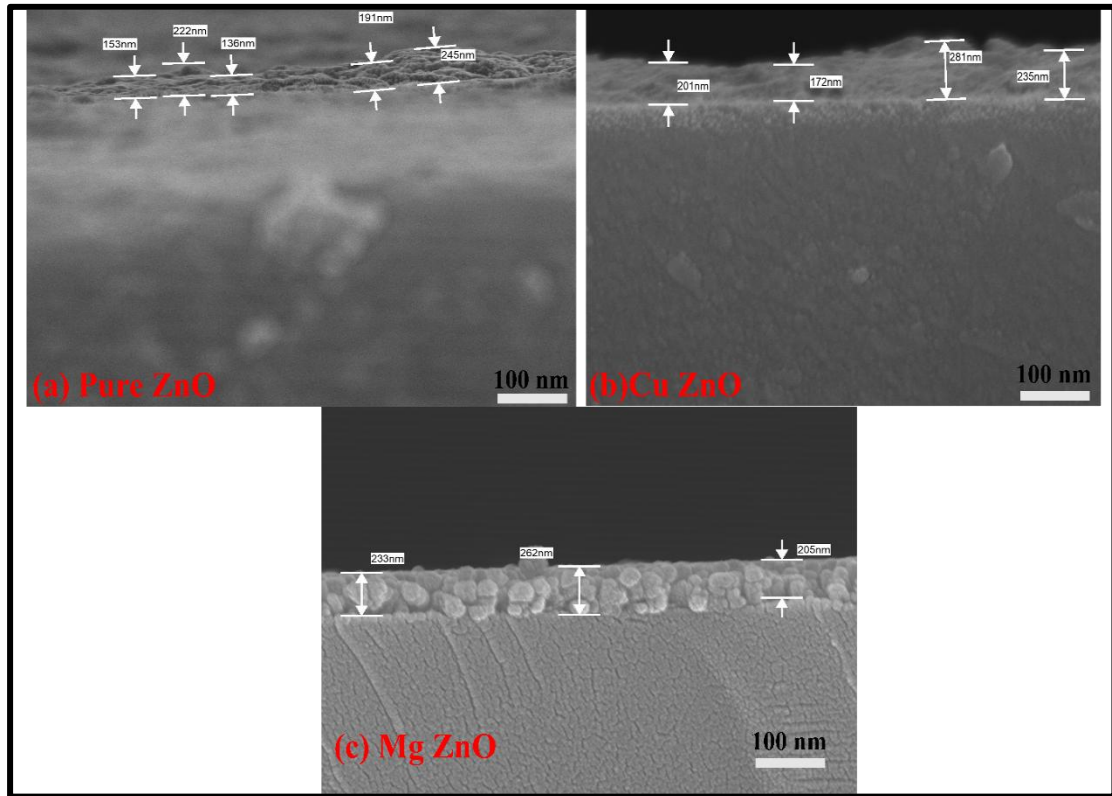
Fig.4.4. Thickness of (a) pure ZnO, (b) Cu: ZnO thin films (c) Mg: ZnO thin film.

4.2.3.2 EDX and Mapping

The Elemental composition of the prepared thin films, as measured by EDX analysis (using FE-SEM instrument). It reveals the existence of the elements in the prepared thin films. Figure 4.5 (a) depicts the elemental composition of pure ZnO, revealing the existence of zinc (Zn) and oxygen(O) along with their atomic and weight percentage. Figure 4.5 (b,c) indicates that the dopants, copper (Cu) and magnesium (Mg), have been successfully introduced into the pure ZnO, along with their respective atomic and weight percentages. It also demonstrated that no other elements were introduced. EDX mapping depicts the homogeneous distribution of the elements. Figures 4.5(d) and 6(e) demonstrate a uniform spread of zinc (Zn) and oxygen (O) across the entire surface of the sample, while Figures 4.5(f) and 4.5 (g) display the successful integration of dopants Cu and Mg into the pure ZnO structure.
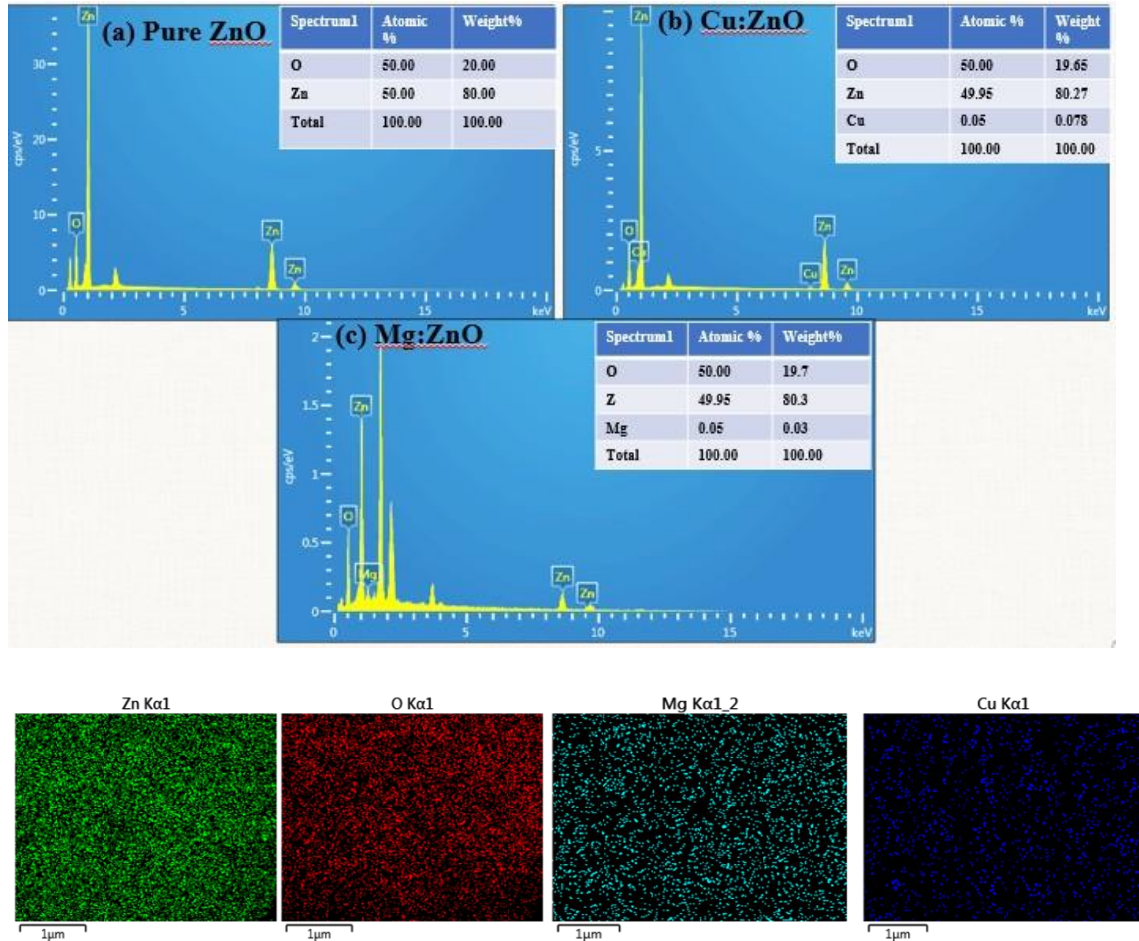
Fig.4.5. EDAX plot of (a) pure ZnO, (b) Cu: ZnO thin films, (c) Mg: ZnO thin film, (d,e,f,g) Mapping of pure ZnO (Zn, O) and Mg and Cu dopants.

4.2.4 Atomic Force Microscopy Study

An atomic force microscopic study was conducted to gain a comprehensive understanding of the surface topography and surface roughness of the prepared thin films formed on the glass substrate. Surface roughness affects light scattering and reflects the quality of the surface, offering valuable information about the growth morphology[156]. It is an essential parameter for transparent and conductive materials. Figure4. 6(a,b) depicts the 2D and 3D micrograph of Pure ZnO, (c, d) presents the 2D and 3D micrograph of Cu-doped ZnO, and (e,f) displays the 2D and 3D micrograph of

Mg-doped ZnO thin film at a range of 2μm × 2μm. All the thin films were prepared using the sol-gel spin coating method and post-annealed for five hours at 500°C. All the thin film micrograph reveals a densely packed, granular surface composed of nanometer-sized spherical grains with a relatively homogeneous distribution. The smooth grain transitions and lack of visible defects suggest a continuous, well-formed film. It exhibited a compact structure without any visible pores or voids. Additionally, it demonstrates the proper effect of doping on the surface morphology of pure ZnO.

81
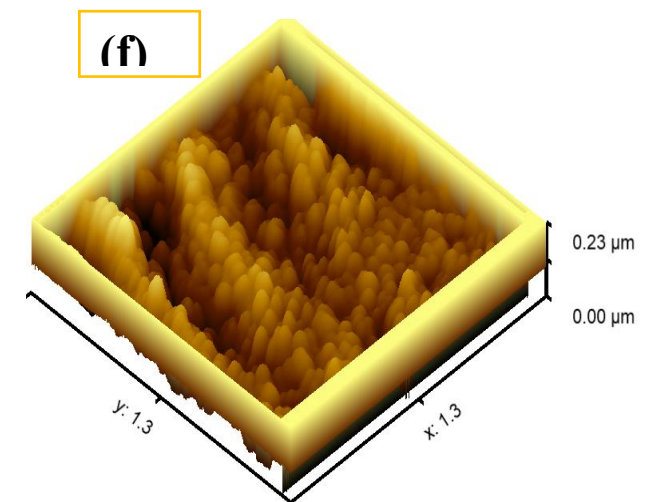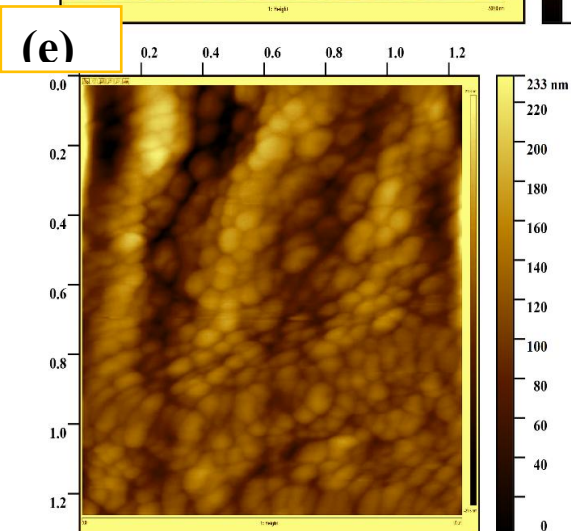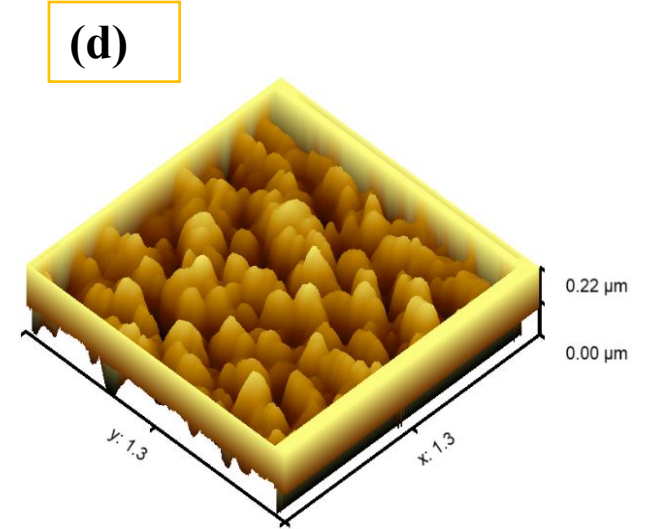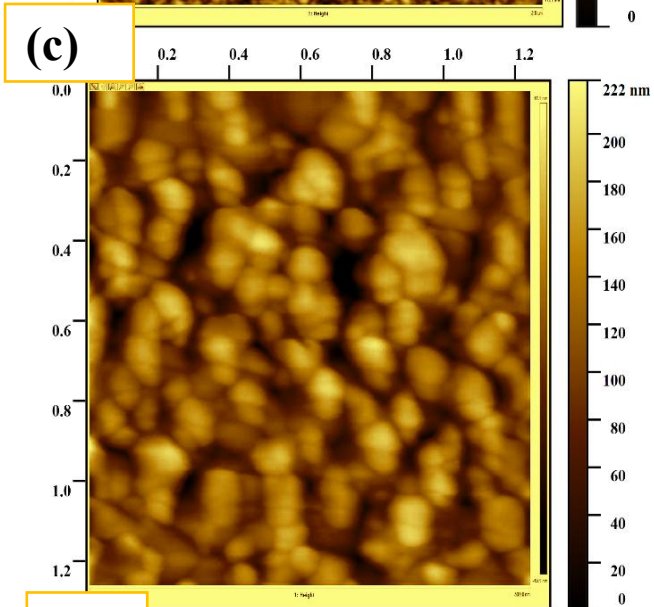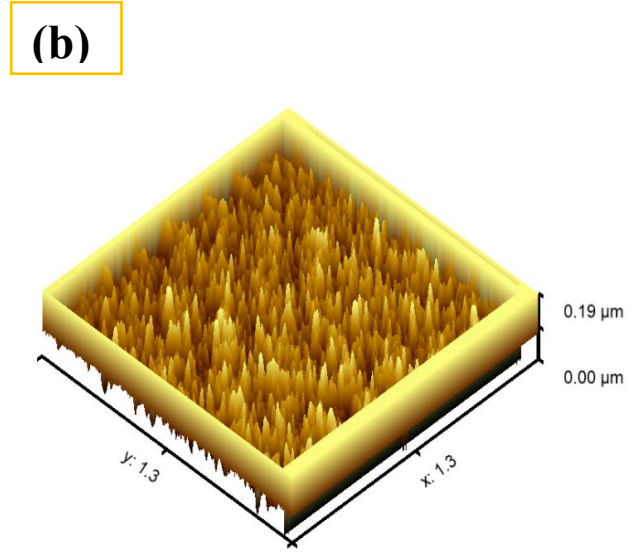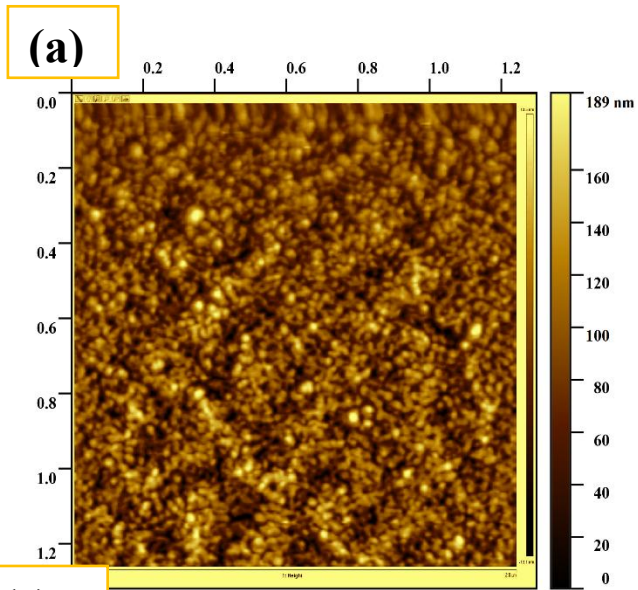
Fig.4.6. Surface topography of (a,b) pure ZnO in 2D and 3D view, (b)0.1% Mg: ZnO thin films in 2D and 3D view, (c) 1.0% Cu: ZnO thin film in 2D and 3D view.

The average roughness (Ra) and root mean square roughness (RMS) values were calculated using equations below (4.1),(4.2)[67].

$$R_{rms} = \sqrt{\frac{1}{N}\sum_{i-1}^{N}(Z_i - Z_m)^2} \tag{4.1}$$

$$R_{av} = \frac{1}{N}\sum_{i=1}^{N}|Z_i - Z_m| \tag{4.2}$$

R_{rms} = root mean square roughness, Rav = average surface roughness, N = the total number of measured points along the surface profile, Z_i = the height of the surface at the ith point, and Zm = the mean surface height. The obtained R_{av} and R_{rms} values for pure ZnO, Cu-doped ZnO, and Mg-doped ZnO thin films are summarized and discussed in the accompanying Table 4.2. Using Gwydion software, the average roughness and root mean square roughness of pure ZnO were found to be 2.44 nm and 5.62 nm, respectively. Following the inclusion of 0.1 % Mg^{2+} into the pure ZnO, these values decreased to an average roughness of 1.96nm and a root mean square roughness of 4.81nm. With the subsequent addition of 1.0% Cu as a second dopant, the average roughness reduced to 1.32 nm, and the root mean square roughness reduced to 3.52 nm. This aligns with earlier research findings[157]. A smooth surface indicates less scattering of light and high transmission, which is proven by UV-Visible spectroscopy. Therefore, the addition of dopants such as Cu and Mg decreases the surface roughness of the materials, smoothes the surface, and enhances transmission and conductivity of the material. This type of surface structure is advantageous for various applications, such as gas sensing, photovoltaics, and optoelectronics devices.

Table 4.2 Surface topography parameters of pure ZnO, Cu doped, and Mg-doped ZnO thin films.

S.No	Prepared Samples	Average roughness (Ra) (nm)	Root mean square roughness (RMS)(nm)
1.	Pure ZnO	2.44	5.62
2.	Mg: ZnO	1.96	4.81
3.	Cu: ZnO	1.32	3.52

4.2.5 Optical study

To measure the optical parameters of pure ZnO and Cu: ZnO, Mg: ZnO thin films (0.1%,0.5%, and 1.0%), ultraviolet-visible (UV-Vis) spectroscopy was considered. These thin films are formed on the glass substrates. The optical characteristics include transmittance, absorbance, optical band gap, extinction coefficient, and refractive index, which are crucial for transparent conducting oxides. The term "transmission" in thin film describes how light or other electromagnetic radiation passes through the material. A thin coating can reflect, absorb, or transmit some light upon interaction. Transmission is affected by numerous variables, including the film's thickness, crystallinity, composition of material, wavelength of light, optical band gap, angle of incidence, surface roughness, interference effect, etc[158].High transmission is a crucial characteristic of a transparent conducting oxide material that may show crystalline quality and morphological uniformity of the films, which is beneficial for optical applications.

Figure 4. 7. (a) displays the optical transmission of pure ZnO and Cu-doped ZnO thin films with doping levels of 0.1%,0.5%, and 1.0% across 400-800nm wavelength spectra. It was monitored that the transmission% rises as the wavelength goes beyond 300nm and attains saturation. The pure ZnO shows 83% average transmission in the visible spectra (400-800nm). As the Cu^{2+} doping level increases from 0.1%,0.5%, and 1.0%, the transmission rises from 88.3%,90.8%, and 96.9%. The comparable ionic radii of Zn^{2+} and Cu^{2+} ions facilitate their substitution, leading to a more uniform and dense film structure, which minimizes light-scattering voids and defects, thus enhancing

transmittance. Consequently, the increased transmittance at higher Cu^{2+} doping levels is attributed to improved film crystallinity, a modified electronic structure reducing absorption, and a more uniform morphology that minimizes light scattering[159]. As confirmed by XRD and AFM analysis, the better crystallinity and surface quality also contributed to this enhancement. Istrate et. al. explained how copper doping influenced ZnO, noting that the transmission reduces from 92% to 71% as Cu doping rises[155]. The transmission outcomes were much improved compared to previous studies [84], [160]. The highest optical transmittance of 96.9% was achieved for the 1.0% Cu^{2+} doped ZnO thin film, exhibiting superior transparency compared to the values reported for ITO thin films in the literature[86]. It is ideal for optoelectronic devices such as transparent conducting oxides (especially for ITOs), solar cells, display devices, etc.

Figure4. 7(b) presents the transmission spectra for pure ZnO and Mg-doped ZnO thin films at doping levels of 0.1%, 0.5%, and 1.0% in the visible range (400-800nm). It was observed that transmission (%) increased as the wavelength extended beyond 300 nm, ultimately reaching a point of saturation. Pure ZnO thin films display transmittance of around 83%. After introducing 0.1% Mg doping enhances the transmittance is enhanced to approximately 90%. It is because of attributes to improved crystallinity and reduced defect density, which minimize light scattering and absorption. However, raising the Mg concentration further to 0.5% and 1.0% results in a gradual reduction in transmittance to about 88% and 85%, respectively. This decline is because of the introduction of lattice strain and defects at higher doping levels, which act as scattering centers, thereby reducing the optical clarity of the films[161]. The outcomes align with existing studies[162]. The transmission values observed with Mg doping are significantly higher than those reported in existing research[163]. Hence,0.1% Mg^{2+} transmission shows the highest transmission (90%).
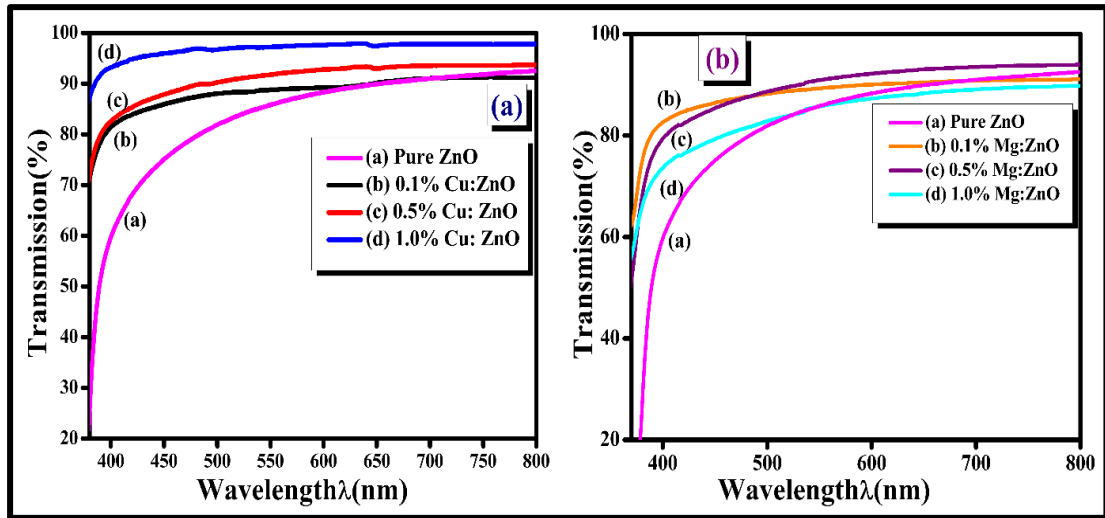
Fig.4.7.(a,b) Transmission plot of ZnO, Cu: ZnO, and Mg: ZnO thin films at various concentrations.

When the UV light travels through the sample, light is absorbed up to some level, depending upon the composition and thickness of the sample. Transmission and absorbance are inversely correlated. ZnO contains four oxygen atoms coordinated to a tetrahedral Zn atom. Absorption occurs when zinc d electrons hybridize with oxygen p electrons to create an energy band gap. The absorption spectra for pure ZnO and Cu-ZnO thin films at 0.1%,0.5%, and 1.0% concentrations are shown in Figure4. 8(a). ZnO shows a high absorption value of 0.30 at 364 nm and low transmission in the UV spectra. With the increase of Cu concentration 0.1%,0.5%, and 1.0%, the absorption value reduces by 0.24,0.20,0.13. In the UV range of 300-400nm, the absorption edge also varies with the rise of Cu concentration. Within this range, all the samples show variation in the absorption edge; after this range, it remains similar. It was observed that the absorption edge shifted with the rise of Cu concentration towards the shorter wavelength from 364nm to 361nm. It's known as "blueshift". This change in the absorption region is responsible for better transmission than pure ZnO thin film, and the broadening of the optical band gap[76]. blueshift in the absorption spectra is commonly attributed to an increase in carrier concentration that blocks the lower state of the conduction band. Hence, the pure ZnO sample with 1.0% Cu doping exhibits the least absorption and the highest transmission.

Figure 4.8 (b) depicts the absorption spectra of pure ZnO and Mg-doped ZnO thin films (1.0%,0.5%, and 1.0%). Pure ZnO exhibits strong light absorption at 364 nm (0.30), indicating reduced transmittance in the ultraviolet region. With the rise of $Mg^{2+,}$ the absorption reduces up to 360nm. Also, the absorption edge gradually shifts towards shorter wavelengths from 364nm to 360nm, indicating a blue shift. It demonstrates an increase in the optical band gap, which is commonly attributed to the substitution of Zn^{2+} ions with smaller Mg^{2+} ions in the ZnO lattice. The blue shift can be explained by the Burstein-Moss effect or changes in the electronic structure due to doping[164]. As a result, ZnO doped with 0.1% Mg shows the minimum absorbance and the maximum transmittance in the visible light region.
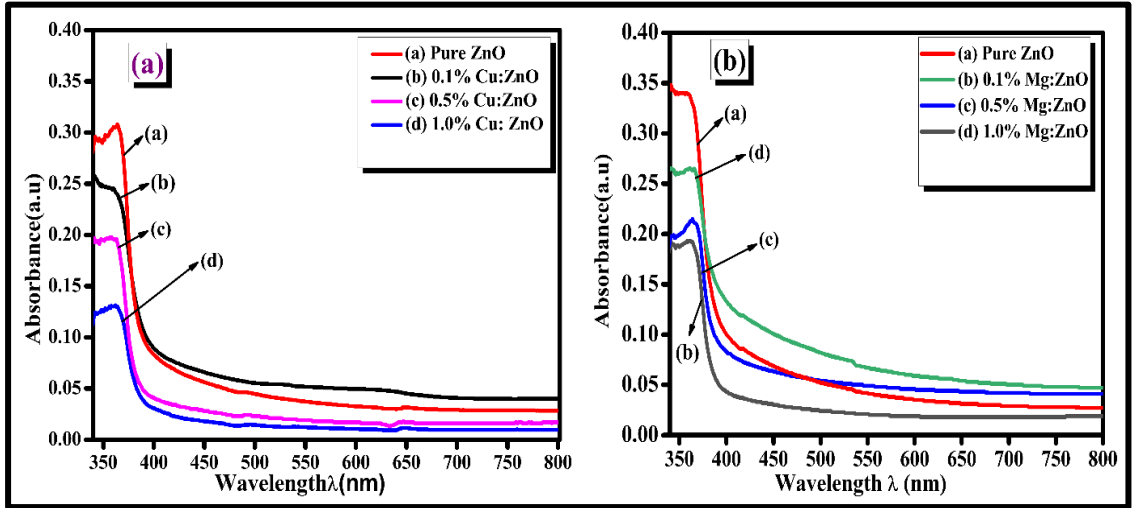
Fig.4.8. (a, b) Absorbance spectra for pure ZnO and Cu: ZnO thin films at various concentrations.

The amount of light lost per unit volume because of scattering and absorption is known as the extinction coefficient. Its value is determined by using an equation(4.3)[165].

$$k = {\alpha\lambda}/{4\pi} \tag{4.3}$$

K shows the extinction coefficient, α indicates the absorption coefficient, λ represents wavelength. Fig.4.9(a) displays the plot of the extinction coefficient of pure ZnO and Cu-doped ZnO thin films (0.1%,0.5%, and 1.0%). The trends in k and α. They are closely related since k is dependent on α and α is influenced by the absorbance (A). It was found that the extinction coefficient is reduced with the photon energy due to the

86

corresponding reduction in absorbance. Figure 4 (a) indicates the extinction coefficient of Pure ZnO and Cu doped ZnO (0.1%,0.5%, and 1.0% doping concentration). Cu doping in pure ZnO thin films caused the peak shift towards a shorter wavelength (called Blueshift). As the Cu concentration rises (0.1%, 0.5%, and 1.0%), both the extinction coefficient and absorbance decrease. This reduction is attributed to the increase in carrier concentration and the decrease in surface roughness, as proven by AFM and Hall measurements. The extinction coefficient of Pure ZnO and Mg^{2+} doped ZnO at 0.1%,0.5%, and 1.0% doping concentration is displayed in Figure 4.9. (b). Pure ZnO shows the highest extinction coefficient. Mg^{2+} doping in pure ZnO reduces the extinction coefficient and shifts towards lower wavelengths, called blueshift, as like absorbance.
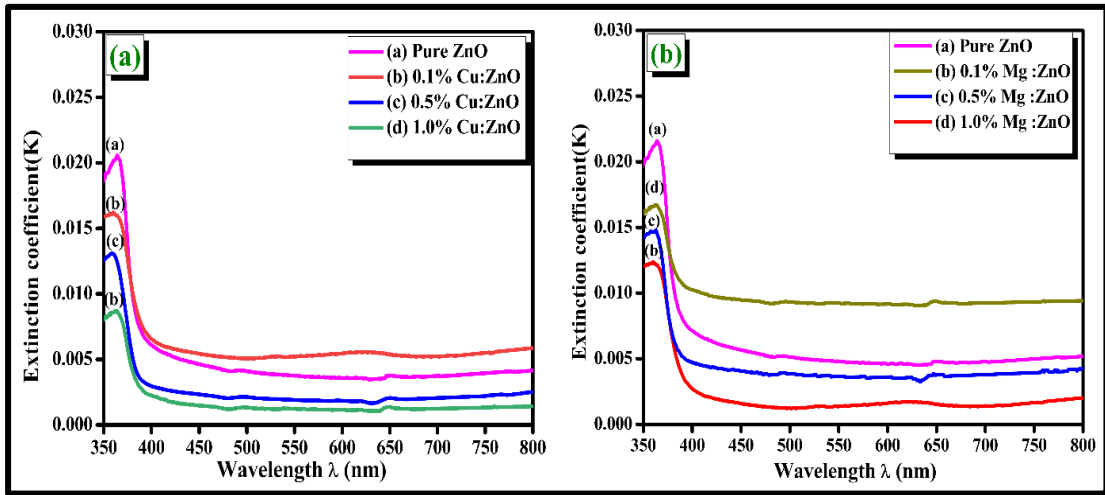
Fig.4.9.(a,b) Extinction coefficient plot for pure ZnO, Cu: ZnO, and Mg: ZnO at various concentrations, annealed at 500°C.

Tauc's approach [166] is utilized to determine the optical band gap value for pure ZnO and Cu-doped ZnO and Mg-doped ZnO thin films at concentrations of 0.1%,0.5%, and 1.0% as described in equation (4.4).

$$(\alpha h v)^m = C\left(h v - E_g\right) \tag{4.4}$$

Where C = constant value, hv = Photon energy, Eg, depicts the optical band gap, α represents the absorption coefficient, m = 2 for the direct band gap. Since ZnO is a direct band gap material, the band gap may be found by extrapolating the linear portion

of the curve to the zero-absorption edge. The band gap variation for pure ZnO and Cu-doped ZnO at doping concentrations of 0.1%, 0.5%, and 1.0% is presented in Figure 4.10 (a). It was found that the band gap of pure ZnO is 3.25 eV, while the incorporation of 0.1% Cu results in a slight reduction to 3.23 eV. Further doping with 0.5% and 1.0% Cu leads to band gap values of 3.22 eV and 3.20 eV, respectively. The optical band gap energy of the ZnO thin films gradually reduced (blue shift) with the incorporation of Cu into the ZnO material. This trend is related to the alignment and interaction between the 3d orbitals of copper and the 2p orbitals of oxygen. The resulting hybridization between Cu and O led to a reduction of the band gap in the Cu-doped ZnO thin film[167]. The band gap narrowing with the Cu doping is related to previous research[168], [169]. Therefore, a reduction in the bandgap, resulting from alterations in the electronic structure, renders Cu-doped ZnO thin films appropriate for ultraviolet device applications, transparent conducting oxide thin films[139].

The band gap in pure ZnO is formed due to the hybridization of localized 3d electrons of zinc with 2p electrons of oxygen [170]. Figure 4.10 illustrates the band gap energies for pure ZnO and for ZnO doped with Mg at concentrations of 0.1%, 0.5%, and 1.0%. It was noted that the band gap for pure ZnO is 3.25 eV. With the introduction of Mg, the band gap gradually decreases: 3.23 eV for 0.1% Mg, 3.17 eV for 0.5% Mg, and 3.14 eV for 1.0% Mg doping. A common trend in n-type semiconductors is that the band gap energy widens with the addition of donor impurities and reduces with the introduction of acceptor impurities. The role of Magnesium (Mg) as either an acceptor or a donor element is determined by the characteristics of the host material. The incorporation of Mg dopants into ZnO leads to a reduction in the band gap energy (blue shift). It might happen because of the presence of defects, which is further confirmed by the strain in XRD analysis. A comparable pattern has been reported in earlier studies[140], [171]. These changes imply that Mg doping effectively tunes the optical band gap of ZnO, making it suitable for applications in UV photodetectors, optoelectronic devices, and transparent conductive films.
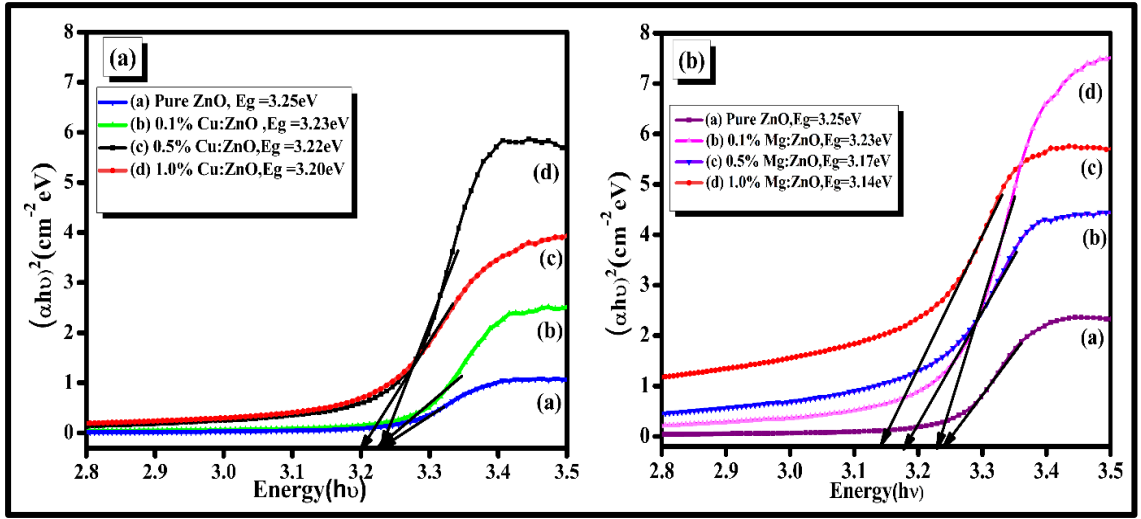
Fig.4.10. (a,b) Band gap plot for pure ZnO, Mg: ZnO, and Cu: ZnO thin films at various concentrations.

Determining the refractive index n is necessary for optical characterization of optical devices, including modulation, filters, optical switches, and other optoelectronic devices, especially Transparent conducting oxides[172]. The refractive index(n) determines how much a ray of light bends when it goes from one medium to another. In other words, it defines the speed at which light moves through a specific medium. The equation(4.5)(4.6) determines it[173].

$$R = 1 - \sqrt{T \exp(A)} \qquad (4.5)$$

$$n = \frac{(1+\sqrt{R})}{(1-\sqrt{R})} \qquad (4.6)$$

R represents reflectance, n denotes the refractive index, A signifies absorbance, and T indicates transmission. The refractive index values were derived from the Reflectance data. Figure 4.11(a) demonstrates the refractive index spectra for both pure ZnO and Cu-doped ZnO at 0.1%,0.5%, and 1.0% doping concentration. All the samples exhibit anomalous behavior, which can be attributed to factors such as size effects, film morphology, surface engineering, and anisotropic properties[174]. It was observed that as Cu doping rises, transmission improves while the refractive index, reflectance, and absorbance decrease. This inverse relationship is attributed to a more uniform film with

less surface roughness, leading to higher transparency and lower polarization. The calculated value of all the samples is summarized in Table 4.3.

Figure 4.11(b) presents a graph illustrating the refractive index of pure ZnO and Mg-doped ZnO thin films at doping concentrations of 0.1%, 0.5%, and 1.0%. As previously discussed, the transmission and refractive index values are inversely dependent on each other. Pure ZnO exhibits a high refractive index. However, as the concentration of Mg dopant rises, the refractive index in the visible region decreases, correlating with an observed increase in transmission. The observed reduction in the refractive index can be attributed to a reduction in polarizability, optical surface dispersion, and optical losses. These factors may arise from a reduction in surface roughness and an increase in carrier concentration[175].
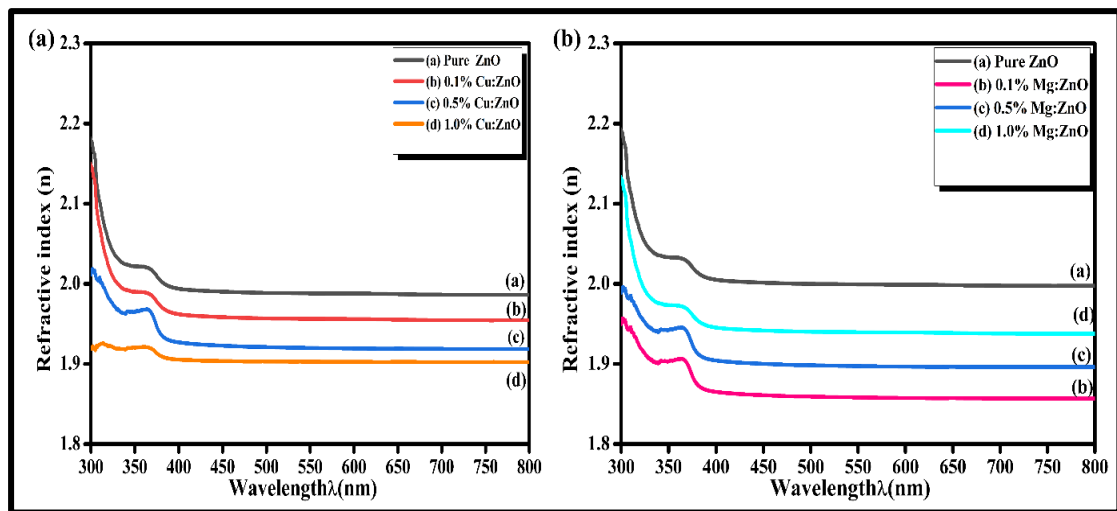
Fig.4.11. (a,b) Refractive index plot for pure ZnO and Cu: ZnO at various concentrations.

Table4.3. Optical characteristics of pure ZnO, Cu: ZnO, and Mg: ZnO thin films at various concentrations.

Samples	Transmission (%)		Band gap (ev)		Refractive index in the visible region	
	Cu: ZnO	Mg:ZnO	Cu: ZnO	Mg: ZnO	Cu:ZnO	Mg:ZnO
Pure ZnO	83.0	83	3.25	3.25	1.99	1.99

90

0.1%	88.3	89	3.23	3.23	1.96	1.86
0.5%	90.8	87	3.22	3.17	1.92	1.91
1.0%	96.8	85	3.20	3.14	1.90	1.94

4.2.6. Electrical Analysis

Figures 4.12(a) and 12(b) indicate the current-voltage (IV) characteristics of Pure ZnO, Cu doped ZnO, and Mg-doped ZnO thin films at 0.1%,0.5% and 1.0% doping concentrations. These measurements were taken at room temperature using a two-probe method, with applied voltages ranging from 0 to 50V. The linear nature confirms that all the examined thin films exhibit ohmic behavior (V=I/R). Doping the ZnO structure with Cu and Mg leads to a decrease in resistance, as clearly illustrated in Figures 4.12(a) and 4.12(b), respectively. The resistance of Cu-doped ZnO decreases with the rise of doping concentration from 0.1% to 1.0%, whereas the resistance of Mg-doped ZnO decreases at 0.1% and then increases at 0.5% and 1.0%. Therefore, doping of Cu and Mg significantly affects the resistance of ZnO thin films.
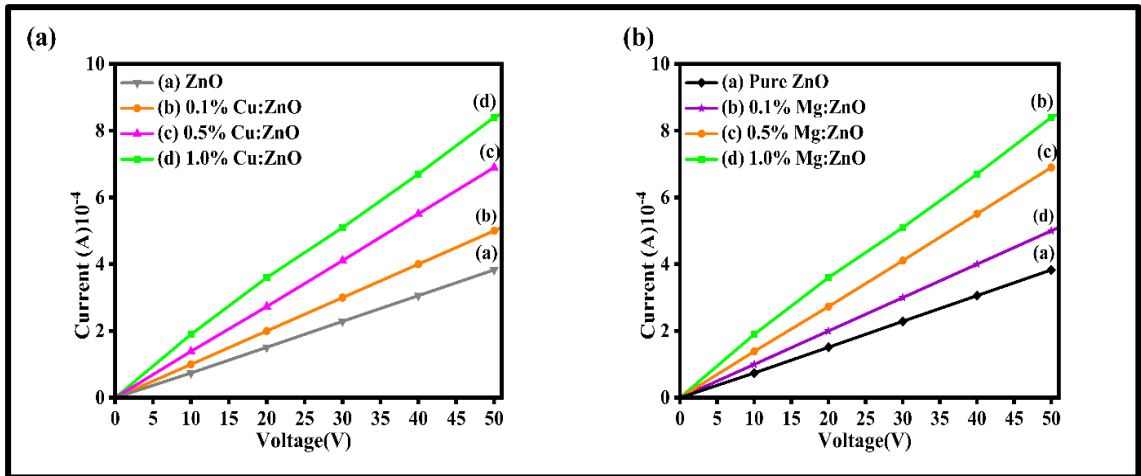
Fig.4.12. (a,b) Current-Voltage plot for pure ZnO, Mg: ZnO, and Cu: ZnO thin films at various concentrations.

4.2.5.1 Hall measurements

The electrical characteristics of pure ZnO, Cu-doped, and Mg-doped ZnO thin films, including carrier concentration(ne), conductivity(σ), mobility(μ), resistivity (ρ), and

Hall coefficient (n or p type), are measured at room temperature using the van der Pauw method.

The electrical conductivity, carrier concentration, carrier mobility, and carrier type of pure ZnO and ZnO thin films doped with Cu^{2+} at concentrations of 0.1%, 0.5%, and 1.0% are shown in Figure 4.13. ZnO crystallizes in a wurtzite structure, comprising a stable arrangement of Zn^{2+} and O^{2-} ions. When Cu^{2+} ions are added, they commonly replace Zn^{2+} sites due to their comparable ionic sizes. This replacement causes local lattice distortion and disrupts the overall charge equilibrium. Pure ZnO exhibits a conductivity of 1.01×10^4 (Scm^{-1}), a carrier concentration of 1.68×10^{21} cm^{-3}, and a mobility of 37.5 cm²/V·s, indicating its nature as an n-type semiconductor. When Cu^{2+} is doped into ZnO at concentrations of 0.1%, 0.5%, and 1.0%, noticeable alterations occur in carrier concentration, mobility, and conductivity. At 0.1% Cu doping, the carrier concentration enhances moderately (3.08×10^{21} cm^{-3}) because of the formation of oxygen vacancies and shallow donor levels introduced by Cu substituting Zn^{2+} in the lattice. This rise in free electrons slightly boosts conductivity (1.04×10^4 Scm^{-1}), although mobility begins to reduce (21.2cm²/V·s) due to minor lattice distortions and impurity scattering. After adding 0.5% Cu doping, the carrier concentration rises (3.97×10^{21} cm^{-3}) further, reaching its peak as more donor-like effects are introduced. This results in a higher value of conductivity,1.01×10^4 (Scm^{-1}), despite a continued reduction in mobility, which now becomes more significant due to increased structural disorder and scattering centers. At 1.0% Cu doping, the mobility drops further (10.4 cm²/V·s) because of heavier distortion in the crystal lattice; however, the carrier concentration remains high (6.92×10^{21} cm^{-3}), which leads to the highest value of conductivity (1.05×10^4 Scm^{-1}), among all samples. Generally, the movement of charge carriers within a material is restricted by two primary mechanisms: scattering from ionized impurities and scattering at grain boundaries. Above a carrier concentration of 10^{20} cm^{-3}, ionized impurities become the dominant factor affecting their movement. Conversely, when the carrier concentration is less than 10^{20} cm^{-3}, then mobility is influenced by grain boundary scattering[176]. So, the reduction in mobility is because of the ionized impurity scattering mechanism. A similar trend occurred in the previous research[169], [177]. Throughout all doping concentrations, the thin films maintain n-

type conductivity, as the increased free electrons dominate electrical behavior. The calculated electrical parameters are summarized in the table4. Therefore, the 1.0% Cu-doped ZnO thin film demonstrates the maximum electrical conductivity among all the samples, exceeding the values reported for ITO thin films in the literature[86], thereby emphasizing its potential as a promising material for transparent conducting oxide applications.
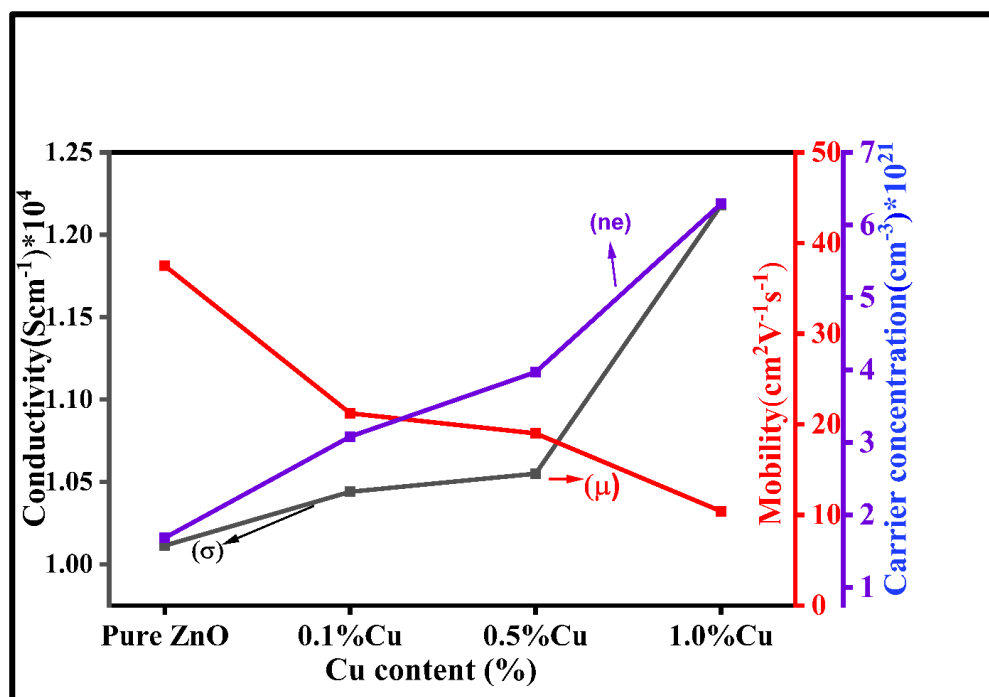
Fig.4.13. Conductivity, mobility, and carrier concentration plot for pure ZnO and Cu: ZnO thin films at various concentrations.

Figure 4.14. describes the variation in conductivity, carrier concentration, mobility, and carrier type with 0.1%, 0.5%, and 1.0% Mg doping in ZnO thin films. Pure ZnO exhibits a conductivity of 1.01×10^4 Scm^{-1}, a carrier concentration of $1.68 \times 10^{21} cm^{-3}$, and a mobility of 37.5 $cm^2/V \cdot s$, indicating its nature as an n-type semiconductor. Introducing Mg^{2+} at 0.1%, 0.5%, and 1.0% into pure ZnO changes its conductivity, carrier concentration, and mobility. The incorporation of 0.1% Mg^{2+} into the host material results in a rise in conductivity, reaching $1.12 \times 10^4 Scm^{-1}$, while the carrier sconcentration becomes $1.68 \times 10^{21} cm^{-3}$ and the mobility reaches 47 $cm^2/V \cdot s$. This enhancement is attributed to the substitution of Zn^{2+} ions by Mg^{2+} ions, which possess similar ionic radii (0.72 Å and 0.74 Å, respectively), thereby improving the material's

crystalline structure and decreasing the concentration of inherent defects, including oxygen vacancies and interstitials, as proved by XRD analysis[178]. After that, 0.5% Mg^{2+} was introduced the excess Mg atoms start introducing lattice strain and defects, such as Mg interstitials or Mg-related defect complexes. These defects act as scattering centres for the charge carriers, reducing mobility to 38 cm²/V·s. and slightly lowering the carrier concentration to 2.22×10^{21} cm^{-3}, thus decreasing the conductivity to 1.02 $\times 10^4$Scm^{-1}. Finally, at 1.0% Mg^{2+}doping concentration, the conductivity, carrier concentration, and mobility also reduced to 0.90×10^4 Scm^{-1},1.19×10^{21} cm$^{-3,}$ and 32cm²/V·s. This is because the excessive addition of Mg^{2+} severely distorts the lattice structure, leading to the formation of defect clusters and a high density of trapping centers. All the thin films represented n-type behaviour. Hence, 0.1% Mg^{2+} depicts the highest conductivity compared to other dopants. A similar trend occurred in another research study [90], [179]. Table 4.4. indicated the measured electrical parameters.
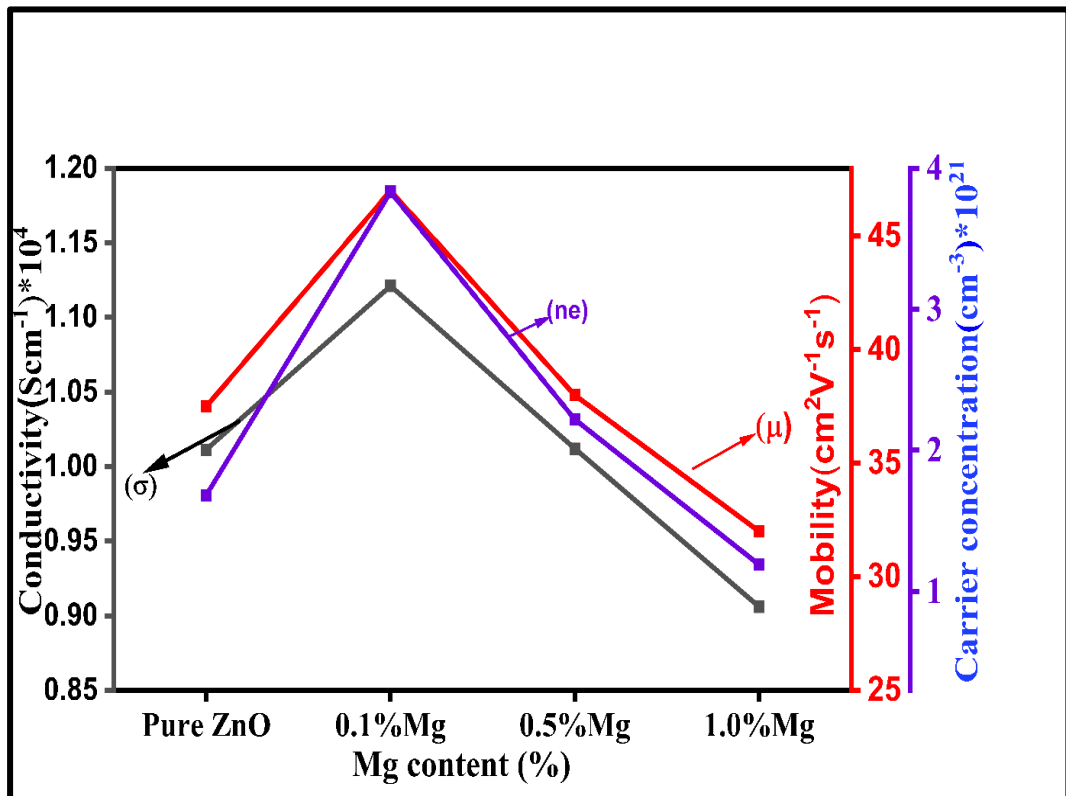
Fig.4.14. Conductivity, mobility, and carrier concentration plot for pure ZnO and Mg: ZnO at various concentrations.

Table 4.4. Electrical characteristics of pure ZnO and Cu doped ZnO thin films at 0.1%,0.5%, and 1.0% concentrations.

Material	Carrier concentration(cm^{-3}) $\times 10^{21}$		Conductivity (Scm^{-1}) $\times 10^4$		Mobility(cm^{2}V^{-1}s^{-1})		Type of carrier	
	Cu:ZnO	Mg:ZnO	Cu:ZnO	Mg:ZnO	Cu:ZnO	Mg:ZnO	Cu:ZnO	Mg:ZnO
Pure ZnO	1.68	1.68	1.01	1.01	37.5	37.5	n	n
0.1%	3.08	3.83	1.04	1.11	21.2	47.0	n	n
0.5%	3.97	2.22	1.05	1.02	19.0	38.0	n	n
1.0%	6.29	1.19	1.21	0.90	10.4	32.0	n	n

4.2.6.2. Activation energy analysis

In terms of electrical properties, activation energy signifies the least amount of energy that charge carriers (such as electrons or holes) need to surpass a potential barrier and participate in electrical conduction within a substance[180]. This idea is particularly relevant in semiconductors, ionic conductors, and materials where electrical conduction is not solely metallic. The electrical conductivity of many materials, particularly semiconductors and ionic solids, rises with temperature. This phenomenon arises because thermal energy assists charge carriers in overcoming the activation energy barrier, enabling them to move more readily and contribute to the flow of electric current. An Arrhenius-type equation frequently describes how electrical conductivity ($\sigma_{D.C.}$) changes with temperature, as described below[181] :

$$\sigma = \sigma_1 \ \exp\left(\frac{-Ea_1}{kT}\right) + \sigma_2 \ \exp\left(\frac{-Ea_2}{kT}\right) \tag{4.7}$$

Conductivity and activation energy of the first and second areas are indicated by σ_1 and Ea_1 and σ_2 and Ea_2. To understand how conductivity changes with temperature, a plot of the logarithm of ($\sigma_{D.C.}$) against (1000/T) in kelvin is required; this graphical representation elucidates the temperature dependence. Graphs of the logarithm of ($\sigma_{D.C.}$) against (1000/T) for pure ZnO, Cu^{2+}, and Mg^{2+} doped ZnO thin films (0.1%, 0.5%, and 1.0%) are shown in Figure 4.15 (a,b). The slope between these two

parameters indicates the value of activation energy. It displays two conduction regions (Ea$_1$ and Ea$_2$) for each of these thin films across the different doping concentrations. In the first area, which is called the high temperature region (Less 1000/T). A slope is steeper, which signifies greater activation energy, lower conductivity. At higher temperatures, conductivity is dominated by intrinsic conduction, arising from thermally generated charge carriers. It reflects the substantial energy needed to create these carriers, significantly exceeding the energy required for their movement. Consequently, the electrical conductivity at elevated temperatures is primarily governed by these thermally induced intrinsic charge carriers. In the second area, which is known as the low temperature region (high 1000/T). It depicts a less steep slope compared to the first area, indicating less activation energy (Ea$_2$). In this area (Ea$_2$), conductivity is primarily governed by hopping mechanisms (such as variable range hopping or polaron hopping) between localized states or defect levels within the band gap. Due to insufficient thermal energy for band conduction, electrons move through these localized states, leading to a weaker dependence of conductivity on temperature.
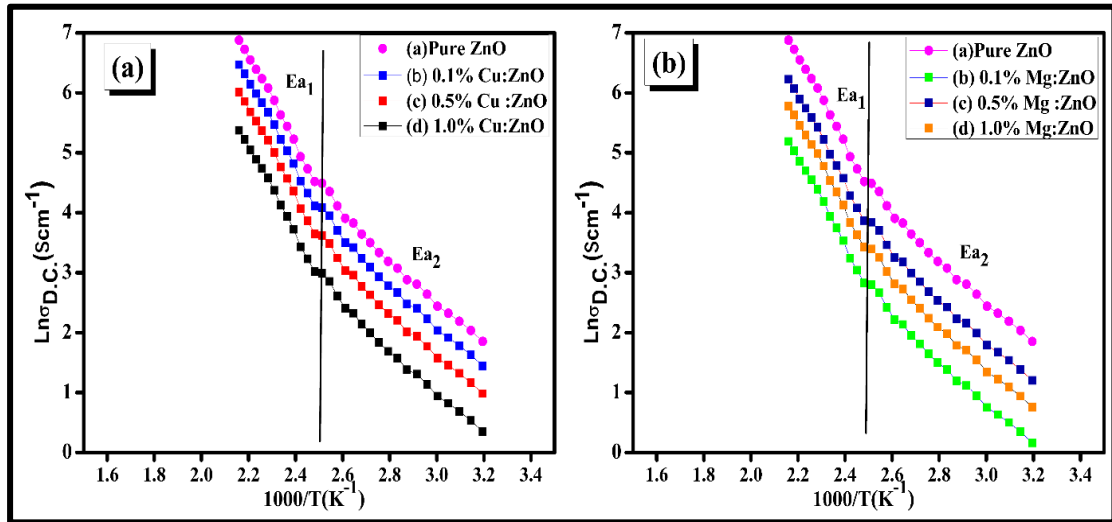
Fig.4.15. (a,b) Activation energies plot for pure ZnO, Cu: ZnO, and Mg: ZnO at various concentrations, annealed at 500℃.

The measured value of activation energies (Ea$_1$ and Ea$_2$) of all the thin films is summarized in Table 4.5. This illustrates the impact of copper and magnesium doping on ZnO thin films. Pure ZnO exhibits activation energies of 0.58 eV (Ea$_1$) and 0.34 eV (Ea$_2$). It depicts high activation energy and lower conductivity. Following the

introduction of copper doping, ranging from 0.1% to 1.0%, a reduction in the activation energy values was observed. Specifically, with a 1.0% copper doping concentration, the activation energies were found to be 0.32 eV (Ea_1) and 0.18 eV (Ea_2). It happens because of the introduction of impurity states, narrowing of the band gap, and improved microstructure, all of which facilitate easier movement of charge carriers and enhance conductivity. Further doping of magnesium (Mg^{2+}) from 0.1% to 1.0% also reduces the activation energy compared to pure ZnO thin films. It occurs because of the introduction of shallow donor levels and defect states, which facilitate easier excitation and hopping of charge carriers. 0.1% Magnesium shows low activation energy valueEa_1 is 0.30eV and Ea_2 is 0.16eV. As a result, conduction becomes more efficient, and the electrical properties of ZnO are significantly improved.

Table 4.5. The measured values of activation energies for pure ZnO, Cu: ZnO, and Mg: ZnO.

Materials (wt%)	Activation Energy (eV) (Cu: ZnO)		Activation Energy (eV) (Mg: ZnO)	
	Ea_1	Ea_2	Ea_1	Ea_2
ZnO	0.58	0.34	0.58	0.34
0.1	0.50	0.30	0.30	0.16
0.5	0.45	0.27	0.42	0.23
1.0	0.32	0.18	0.48	0.27

4.2.6.3. Optoelectronic analysis

Transparent conducting oxides (TCOs) are critically evaluated using a key metric called the Figure of Merit (FOM**)**, which serves as a standardized benchmark for comparing their efficiency and applicability in optoelectronic devices[56]. The FOM quantifies the balance between two competing properties: electrical conductivity (measured by sheet resistance, R_{sh} and optical transparency (expressed as transmittance, T^{10})[104]. A higher FOM represents superior performance, reflecting low sheet resistance (for efficient charge transport) and high transmittance (for light penetration). FOM enables

the evaluation of different TCOs by considering their electrical sheet resistance and optical transmittance. The Figure of Merit (FOM) is determined through the Hacke equation (4.8)[182].

$$\Phi_{TC} = \frac{T^{10}}{R_S} \tag{4.8}$$

Transmission denoted by T^{10}, and the sheet resistance, denoted by Rs. Figure 4.16 illustrates the figure of merit for pure ZnO, Cu-doped ZnO, and Mg-doped ZnO after being post-heated for five hours at 500 °C. Pure ZnO shows a figure of merit of $1.5 \times 10^{-1} \ \Omega^{-1}$. With Cu doping, the figure of merit progressively increases as the doping concentration rises from 0.1% to 1.0%. Among all doping levels, 1.0% Cu-doped ZnO achieves the highest figure of merit value, reaching $2.2 \times 10^{-1} \ \Omega^{-1}$. Hence, at this doping concentration, it displays better transmission and conductivity performance. Further doping with Mg^{2+}, the Figure of merit value initially rises, then declines, yet remains higher than pure ZnO, but more than pure ZnO. The 0.1% Mg-doped ZnO exhibits the highest figure of merit ($1.9 \times 10^{-1} \ \Omega^{-1}$), surpassing the values observed at other Mg doping concentrations. Thus, the 1.0% Cu-doped sample demonstrates the highest figure of merit among all the samples. The results obtained in this study surpass those reported in earlier research[183]. Hence, the 1.0% Cu-doped ZnO thin film exhibits the highest figure of merit value of $2.2 \times 10^{-1} \ \Omega^{-1}$, which is significantly higher than that reported for ITO thin films ($8.68 \times 10^{-4} \ \Omega^{-1}$)[86]. A high figure of merit in TCO materials is essential for applications in optoelectronic devices, including display technologies, solar cells, and flat panel displays.
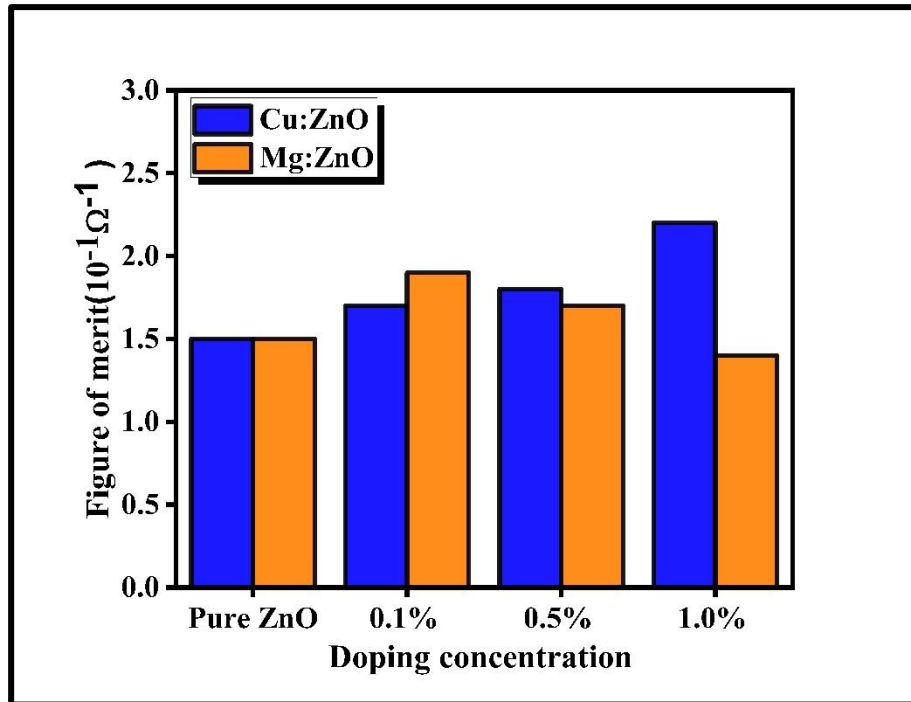
Fig.4.16. Figure of merit plot for pure ZnO, Cu: ZnO, and Mg: ZnO thin films at various concentrations.

4.3 Conclusion

1) This chapter describes the successful synthesis of pure ZnO thin films using the sol-gel spin coating route, followed by a five-hour post-heating treatment at 500°C. Furthermore, it explores the effects of magnesium and copper doping at concentrations of 0.1%, 0.5%, and 1.0%.

2) The hexagonal wurtzite structure was verified for all the thin films through X-ray Diffraction study. Moreover, doping with Mg and Cu increases the crystallite size relative to pure ZnO.

3) The confirmation of Zn-O bonding in all the thin films was confirmed by FTIR. Doping impacts the broadening and shifting without variation in the structure of ZnO.

4) The transmission characteristics of pure ZnO, Cu, and Mg-doped thin films are identified by UV-Visible spectroscopy. Cu and Mg doping influence the ZnO thin film transmission (%). 0.1% Mg doping enhances the transmittance up to 90% after which it reduces, and 1.0% Cu doping shows tremendous

transmission up to 96.8% in the visible range. Therefore, copper-doped ZnO thin films exhibited the maximum optical transmittance (96.8%), which is significantly higher than the reported range for ITO thin films (80-90%). This enhanced transparency makes it highly suitable for applications requiring efficient light transmission, such as solar cells and display technologies.

5) Pure ZnO depicts a conductivity of 1.01×10^4 (Scm^{-1}), carrier concentration is 1.68×10^{21} cm^{-3}, and mobility is 37.5 cm²/V·s, indicating its nature as an n-type semiconductor. Mg and Cu doping influence the conductivity, carrier concentration, and mobility of the host ZnO material. 0.1% Mg^{2+} doping into the host material results show 1.12×10^4 Scm^{-1} conductivity, while the carrier concentration becomes 1.68×10^{21} cm^{-3} and the mobility reach 47 cm²/V·s. 1.0% Cu^{2+} doping depicts the highest conductivity up to 1.21×10^4 Scm^{-1}, among all samples. All the thin films show n-type semiconducting nature. Therefore, Copper doping increases the conductivity among all samples, which shows higher conductivity compared to that of reported ITO thin films ($\sim 10^3$-10^4).

6) Pure ZnO shows a figure of merit of 1.5×10^{-1} Ω^{-1}. The 0.1% Mg-doped ZnO exhibits the highest figure of merit (1.9×10^{-1} Ω^{-1}), surpassing the values observed at other Mg doping concentrations. The 1.0% Cu-doped sample exhibited the highest figure of merit (2.2×10^{-1} Ω^{-1}), a crucial property for transparent conducting oxide (TCO) applications in optoelectronic devices such including flat-panel displays, touch screens, and photovoltaic devices etc.

Chapter 5

The influence of Mg and Cu doping on SnO₂ thin films for the assessment of transparent conducting oxide.

5.1. Introduction

Transparent conducting oxide (TCO) thin films are extensively researched and highly valued by the industry due to their necessity in numerous devices, including gas sensors, solar cells, flat panel displays, display devices, surface acoustic devices, etc[184][185][186][187].Out of this tin Oxide(SnO_2) has generated vast interest because of its n-type semiconductor with a broadband gap ranging from 3.6 to 4.0eV[188]. Also, the electronic configuration of $Sn(1s^2 2s^2 p^6 3s^2 p^6 d^{10} 5s^2 p^2)$ is correlated with $In((1s^2 2s^2 p^6 3s^2 p^6 d^{10} 5s^2 p^1)$[189].Tin oxide ($SnO_2$) thin film is a transparent and conductive material[72].It belongs to the group VIA elements, where oxygen has high mobility[190]. The high transmission is because of the band gap of more than 3eV in the visible spectra and high conductivity because of the occurrence of free electrons in oxygen vacancy[191].Therefore, the SnO_2 material has tremendous qualities applied in numerous applications of optoelectronic devices[192].This chapter represents the formation of undoped SnO_2, Mg, and Cu-doped SnO_2 thin films that have been formed on a glass substrate by the sol-gel spin coating method, post-heated at 500°C for one hour.

The optoelectronic properties of these SnO_2 can be further customized using extrinsic dopants, which generate charge carriers and oxygen vacancies and modify the band structure[193]. The utmost approach to modifying the optical and electrical characteristics of SnO_2 is to dope it with foreign elements, which introduces crystal defects and oxygen vacancies[194]. Magnesium (Mg^{2+}) is a divalent alkaline earth metal belonging to group (II) of the periodic table[195]. Copper ($Cu^{2+)}$ came under the category of transition metal under group (11)[196]. Both dopants display high optical

and electrical parameters. The assimilation of cationic metal ions (Mg^{2+} and Cu^{2+}) into the SnO_2 lattice generates oxygen vacancies at electrically active sites[197]. Here, the value of ionic radii of Mg^{2+} and Cu^{2+} is (0.72Å) and (0.73 Å) is a bit higher than that of Sn^{4+} (0.69Å), so Mg^{2+} and Cu^{2+} can easily replace Sn^{4+} ions in the SnO_2 structure. The presence of these metals alters the band gap, enhancing optical and electrical properties by generating oxygen vacancies[198][100]. Introducing Mg^{2+} and Cu^{2+} dopants can enhance the SnO_2 charge carrier density and electrical conductivity. This is especially beneficial for applications involving sensors, transparent conductive oxides, and optoelectronic devices. For this reason, these dopants are considered.

The goal of this chapter is to explore comprehensively the formation of SnO_2 thin film and the impact of Mg and Cu doping on SnO_2 on the properties of optical and electrical for optoelectronic devices. The approach of this study is to synthesize an easy and low-cost affected sol-gel spin coating method on a glass substrate post-heated at 500℃ for one hour. Also, characterize their structural, morphological, optical, and electrical properties by using X-ray Diffraction (XRD), Field Emission Scanning Electron Microscopy (FE-SEM), Ultraviolet-Visible (UV-Vis) spectroscopy, Atomic Force Microscopy (AFM), Hall effect measurements, and a two-point probe for Transparent conducting oxides. A higher FOM indicates superior performance of the material in terms of transmission and conductivity.

5.2 Results and Discussion

5.2.1. Phase analysis

The XRD study was performed to explore the structure of SnO_2 thin films doped with Mg and Cu. Figures 5.1(a) and 5.2(b) show the XRD spectra for Mg-doped and Cu-doped SnO_2 thin films at concentrations of 0.1%, 0.5%, and 1.0%. These films were formed using the sol-gel method and then post-heated at 500°C for one hour. Prominent diffraction peaks corresponding to the SnO_2 crystalline structure (110), (101), (200), (211), and (220) match JCPDS No. 00-018-1380, indicating that all thin films exhibit a polycrystalline tetragonal rutile structure [67], [199]. When the concentration of Mg dopant is added to the SnO_2 thin film, (110), (220), and (221) peaks in the SnO_2 thin film are enhanced as the Mg dopant concentration increases from 0.1% to 1.0%. Doping

with magnesium reduces structural defects such as dislocations and vacancies in the SnO_2 lattice. This enhancement in crystallinity results in a more ordered structure, leading to an increase in the intensity of diffraction peaks due to enhanced constructive interference of X-rays [200]. The observation was that all the thin films had the same peak and no extra ones, suggesting that Mg dopants were well added to the host lattice without causing structural changes. (110) diffraction peak moved to the lower angle (2θ)with the rise of Mg concentration. This shift is because the Mg^{2+} ion replaces Sn^{4+} at the lattice site [201]. The value of the diameter of Mg^{2+} is 1.44 Å, and Sn^{4+} is 1.38 Å. The diameter value of Mg^{2+} is higher than Sn^{4+}. When Sn^{4+} is replaced with Mg^{2+} in the lattice, the difference in size can cause strain in the lattice. Also, the observed shift of the peak towards a lower angle 2θ value suggests that the material underwent tensile strain during the heating process because of the incorporation of Magnesium dopants [202]. Other possible causes for the peak shift include tensile strain, changes in lattice parameters, and the occupation of interstitial sites in the host lattice by dopants, and vice versa. It was also observed that the (200) plane orientation is higher in Mg-doped SnO_2 compared to Cu-doped SnO_2. It happens because the ionic radii of Mg^{2+}(0.72Å), and Mg^{2+} substitute with minimal distortion. exhibit a closer ionic radius to Sn^{4+} (0.69Å) compared to larger Cu^{2+}(0.73Å). This size compatibility and lower charge difference (+2 for Mg^{2+} Vs +4 for Sn^{4+}) reduce lattice disruption and promote uniform growth along the (200) plane[203][204].

For the Cu-doped SnO_2 thin films, doping concentrations were 0.1%, 0.5%, and 1.0%. After doping with Cu, all the peaks remained consistent with those of the host material, indicating the presence of the rutile phase in all samples (JCPDS No. 00-018-13). No extra peaks in this figure signify that Cu has also been successfully introduced into the host lattice. As the Cu dopant concentration rises, a slight rise was observed in the diffraction peaks of (110), (101), and (211). When Cu was added to the host lattice, the (101) diffraction peak shifted to higher angles (2θ) with increasing Cu concentration, indicating that the dopant was properly introduced into the parent lattice site. This shift can be attributed to Cu^{2+} ions replacing Sn^{4+} ions in the SnO_2 lattice, as Cu^{2+}(0.73Å) has a larger ionic radius compared to Sn^{4+} ions (0.69Å). Therefore, adding the cation with a larger ionic radius can cause an expansion in the lattice parameter and shift the

peak to the left side. This shift is due to the larger ionic radius of Cu^{2+}(0.73 Å) compared to Sn^{4+}(0.69Å), which leads to an expansion of the lattice parameters and a shift of the peak to the left[205].
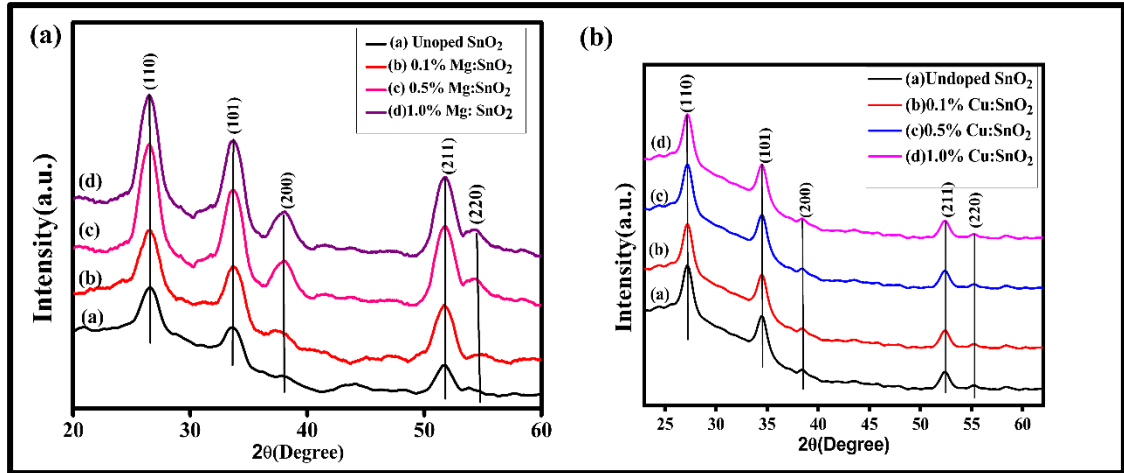
Fig.5.1. XRD study of (a) undoped, Mg: SnO_2 thin films, (b) undoped, Cu: SnO_2 thin films (0.1%, 0.5%, and 1.0%).

With the help of XRD data, other major parameters for undoped SnO_2, Mg-doped, and Cu-doped SnO_2 thin films (at concentrations 0.1%,0.5%, and 1.0%), such as crystallite size, dislocation density, and lattice strain, were measured and illustrated in Table 5.1. By utilizing Scherrer's equation(5.1), the crystallite sizes of the undoped, Mg-doped, and Cu-doped SnO_2 thin films were determined[206][207].

$$D = \frac{K\lambda}{\beta \cos \theta} \qquad (5.1)$$

where D = crystallite size of the thin film, K= Sherrer constant, which is 0.9,β= full-width half maxima (FWHM), 'λ'= wavelength produced by X-ray, 'θ'= angle of diffraction. By the utilization of the value of crystallite size 'D', we can determine the Dislocation density (δ). Equation (5.2) can be utilized to evaluate this type of topological defect [38][208].

$$\delta = \frac{1}{D^2} \qquad (5.2)$$

The lattice strain was another XRD parameter that was measured by utilizing equation (3)[209], [210].

$$\in = \frac{\beta \cot \theta}{4} \tag{5.3}$$

Table 5.1. Structural parameters for undoped, Mg: SnO_2, and Cu: SnO_2 thin films (0.1%, 0.5%, and1.0%).

Mg and Cu Content	(hkl) plane		Crystallite Size(nm)		Strain (ϵ) $\times 10^{-3}$		Dislocation density(δ)(10^{-3}) (nm^{-2})	
	Mg: SnO_2	Cu: SnO_2	Mg: SnO_2	Cu: SnO_2	Mg: SnO_2	Cu: SnO_2	Mg: SnO_2	Cu: SnO_2
Undoped SnO_2	(110)	(110)	10.08	10.08	15.73	15.73	9.85	9.85
0.1%	(110)	(110)	10.46	10.75	15.16	14.36	9.13	8.64
0.5%	(110)	(110)	10.59	11.67	14.67	13.20	8.90	7.33
1.0%	(110)	(110)	11.33	12.57	13.95	12.30	7.78	6.32

First, we discuss the impact of Mg doping on crystallite size, strain, and dislocation density, calculated for the (110) plane illustrated in Table 5.1. It was analyzed that the peak intensity increased with Mg doping in the host at concentrations of 0.1%, 0.5%, and 1.0%, leading to improved crystallite size. The crystallite size for the undoped SnO_2 thin film is 10.08 nm, and it is enhanced to 11.33 nm after doping. This implies that Mg atoms were effectively introduced into the SnO_2 lattice, promoting better crystallinity, larger crystallite formation, and reduced defects. As a result, the crystal lattice increases while strain and dislocation density decrease with increasing Mg doping, indicating that the crystal lattice expands with the addition of Mg. This is correlated with findings from other studies[94].

Further, we examine the influence of another dopant, Cu, at concentrations of 0.1%, 0.5%, and 1.0% on the crystallite size, dislocation density, and strain of SnO_2 thin film as shown in Table 1. With the rise of Cu concentration, the crystallite size also rises. It increases from 10.08 nm to 12.57nm after doping. This increment is because of the ionic radii of Cu^{2+} (0.73), which is higher than the ionic radii of Sn^{4+}(0.69), resulting in the expansion of the crystal lattice[211][212]. Size and distribution are influenced by particle growth, nucleation rate, and agglomeration. This trend of increment coincides

with other research work[213]. Alongside the rise in copper doping, strain and dislocation density are reduced because of improved crystallinity. The strain in the thin film is inversely proportional to the crystallite size, with smaller crystallites typically exhibiting higher strain due to increased dislocation density and defects. In pure SnO_2 thin films, higher strain arises from a greater concentration of oxygen vacancies. Doping alters the behavior of oxygen vacancies, reducing their concentration. Dopants like Mg^{2+} and Cu^{2+} reduce this strain by substituting Sn^{4+}, compensating for defects, and improving crystallinity. This defect reduction minimizes lattice distortion and dislocations, stabilizing the structure[202][78]. A similar trend occurs in this literature [190].

5.2. FTIR analysis

FTIR is an outstanding instrument for finding absorbed functional groups in prepared samples [166]. The number of absorption peaks and the structure of the band depend on the composition of chemicals, morphology, and also on crystalline structure [214].To analyze the chemical group on the surface of annealed samples, an FTIR study was conducted at room temperature in the range of wavenumber from 400-4000cm^{-1}. Fig. 5 .2 (a) displays the FTIR plot of undoped and Mg-doped SnO_2 thin film (b) represents undoped and Cu-doped SnO_2 thin film. The doping concentrations for both dopants were 0.1%, 0.5%, and 1.0%. It depicts a similar absorption band for all the prepared films at distinct intensities. The primary IR features of SnO_2 are found at 420 cm^{-1} and 520 cm^{-1}, corresponding to the O–Sn–O and Sn–O stretching vibrations, which support the bonding of metal oxide and are consistent with the literature[215][216]. The absorption peak at 760 cm^{-1} shows the Sn-O-Sn stretching vibrations. At 890 cm^{-1} wavenumber found a strong absorption band of Sn-OH vibration mode was found because of the molecules of water present in the precursor[217]. The bands at 2879 and 2896 cm^{-1} depict the mode of C-H vibrations[218], while the broad absorption band at 898 cm^{-1} was assigned to Sn-OH vibration modes[219]. The wavenumber greater than 3000 cm^{-1} depicts the O-H stretching vibrations which are caused by water molecules present at the surface of SnO_2[72]. The O-OH$^-$ explains the interaction of absorption bonds at 1404cm^{-1}[220].No additional absorption band corresponding to Mg-O and Cu-O as compared to SnO_2.The stretching mode was shifted to a higher wavenumber due

to the incorporation of dopants. The dopants (Mg^{2+}, Cu^{2+}) have a bit larger ionic radii than the Host (Sn^{4+}), consequently, the dopants influence the lattice of SnO_2. So, the dopant ions occupy the interstitial site due to which broadening and shifting of peaks are observed in the IR spectra without altering the actual structure of the SnO_2 thin film.[16][40].
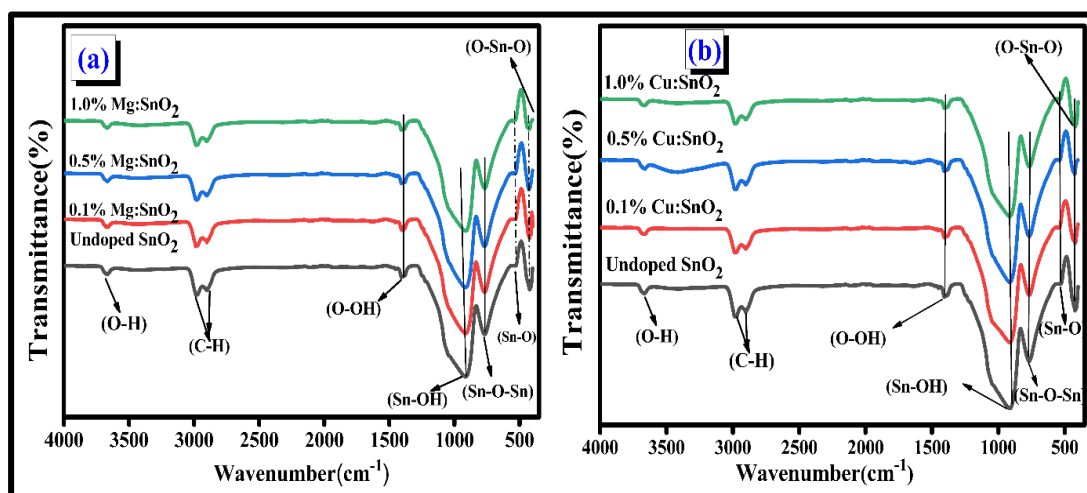
Fig.5.2. FTIR plot of undoped SnO_2 thin film, 0.1%,0.5%,1.0% Mg doped SnO_2 thin film(b) undoped SnO_2, 0.1%0.5%,1.0% Cu doped SnO_2 thin film.

5.2.3 Thickness of thin films study

The thickness of the thin film is a crucial parameter for the assessment of transparent conducting oxide thin films. The value of thickness for undoped SnO_2, 1.0% Mg-doped, and Cu-doped SnO_2 thin films was investigated with the help of a field emission scanning electron microscope (FESEM) at a magnification of 45,000 and a particle size range of 100nm, annealed at 500°C for one hour, as shown in Figure 5.3. The observed thickness for the pure SnO_2, Cu-doped SnO_2, and Mg-doped SnO_2 thin films was determined to be 92.8 nm, 195 nm, and 212 nm, respectively. The thickness value increases with the doping of Mg and Cu.
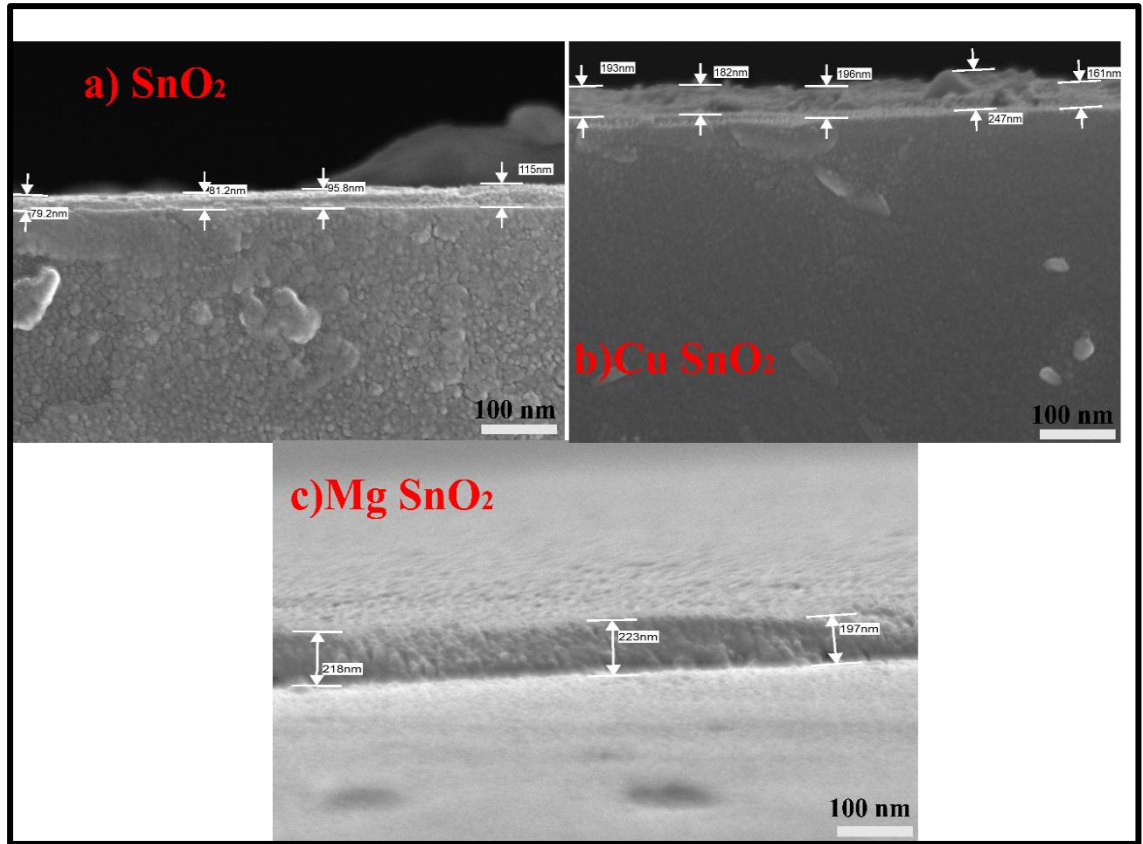
Fig.5.3. Thickness images of (a) undoped SnO$_2$ thin film, (b)Cu-doped SnO$_2$ thin film, (c)Mg-doped SnO$_2$ thin film.

5.2.4 Surface roughness study

In this work, the topography of the surface and surface roughness were analyzed using Atomic Force Microscopy (AFM). The surface roughness is a crucial parameter for an optical surface. Surface roughness impacts light scattering and indicates surface eminence, providing insights into growth morphology. In this study, we investigate the surface roughness of the sample in both 2D and 3D.

Fig5.4(a) depicts the 2D image and (b) 3D image of undoped SnO$_2$ thin film,(c) explains the 2D image and (d) 3D image of Cu doped SnO$_2$ thin film, (e) displays a 2D image and (f) shows a 3D image of Mg-doped SnO$_2$ thin film over the scanning range of 2μm$\times2\mu$m prepared by sol-gel spin coating method and post-heated at 500°C for one hour. Therefore, analyzing surface roughness is important to verify how surface morphology affects the functional properties[221]. All the films grew evenly over the

surface with a clear granular structure without forming clusters or lumps. The surface of all the thin films shows uniform peaks or valley-like structures. The Rrms indicate the film's surface quality, and its measurement is done using the following Eq. (4)[67].

$$R_{rms} = \sqrt{\frac{1}{N}\sum_{i-1}^{N}(Z_i - Z_m)^2} \qquad (5.4)$$

where R_{rms} = root mean square roughness, N = total number of observations, Zi actual value for the ith observation, Zm measured value.

The average roughness of the thin films was determined with the help of equation (5.5)

$$R_{av} = \frac{1}{N}\sum_{i=1}^{N}|Z_i\text{-}Z_m| \qquad (5.5)$$

Where Rav is the average surface roughness, N indicates the total number of measured points along the surface profile, Zi depicts the height of the surface at the ith point, and Zm shows the mean surface height.

Table 5.2. Surface roughness analysis of undoped, Mg-doped SnO_2, and Cu-doped SnO_2 thin films.

S.No	Mg and Cu Content	Average roughness (Ra) (nm)	Root mean square roughness (RMS)(nm)
1.	Undoped SnO_2	1.65	2.99
2.	Cu-doped SnO_2 thin film	1.26	1.70
3.	Mg-doped SnO_2 thin film	1.00	1.39

Table 5.2. exhibits the values of average roughness (Ra) and root mean square roughness (R_{rms}) of undoped SnO_2 thin film, Mg-doped and Cu-doped SnO_2 thin film. It was analysed with the help of Gwyddion software. It was observed that adding 0.5% of Mg and Cu dopants to the undoped SnO_2 thin film reduced its average roughness from 1.65 nm to 1.00 nm, and its root mean square roughness from 2.99 nm to 1.39 nm.

This reduction in surface roughness contributes to higher transmission because a smooth surface shows less scattering of light, confirmed by UV-visible spectroscopy. This finding is consistent with previous studies [212], [222]. When the surface roughness increases, the electrical resistivity also increases because the carrier mobility decreases, while the carrier concentration remains mostly unchanged. This helps in understanding the influence of surface morphology on electrical transport[72]. Hence, it concluded that the reduction in roughness in Mg and Cu-doped SnO_2 is primarily because of the influence of Mg and Cu diffusing into the lattice of tin oxide, filling surface voids, and forming clusters which smooth the surface. Additionally, Mg and Cu doping grain growth in the tin oxide results in a more uniform surface with fewer defects and irregularities[66].
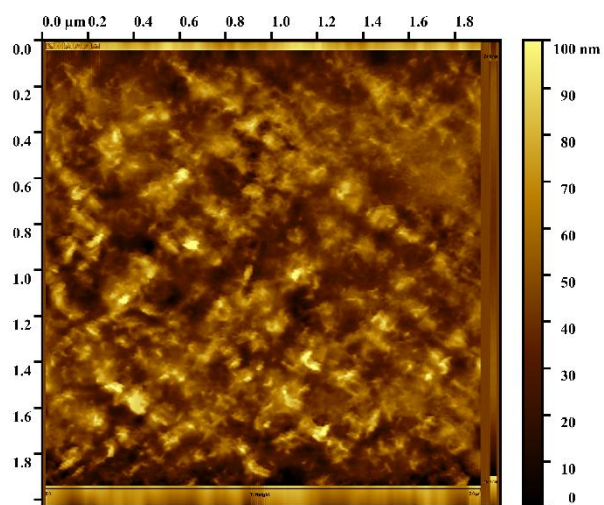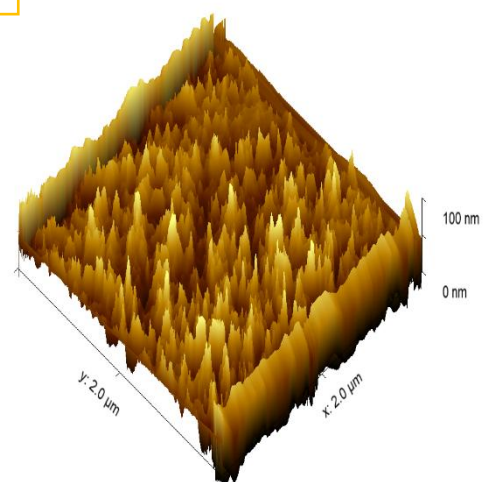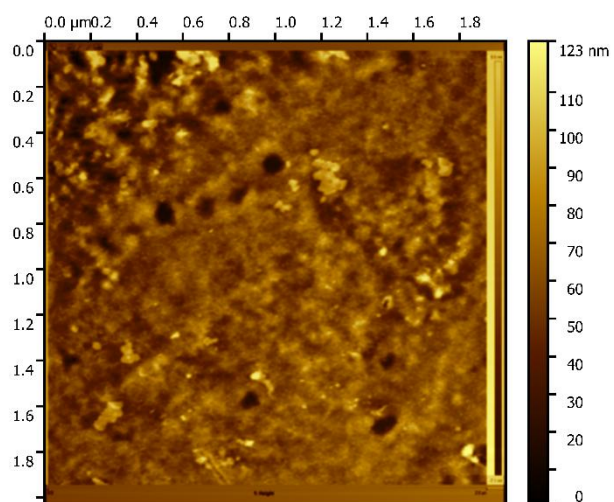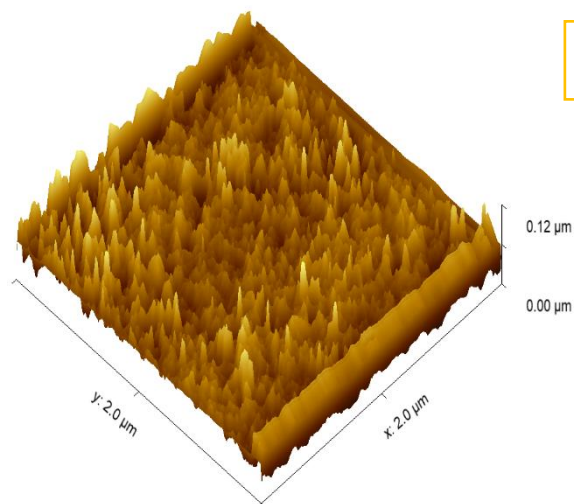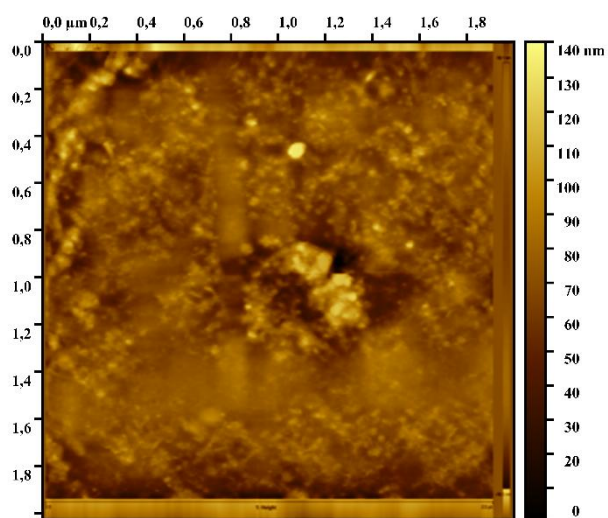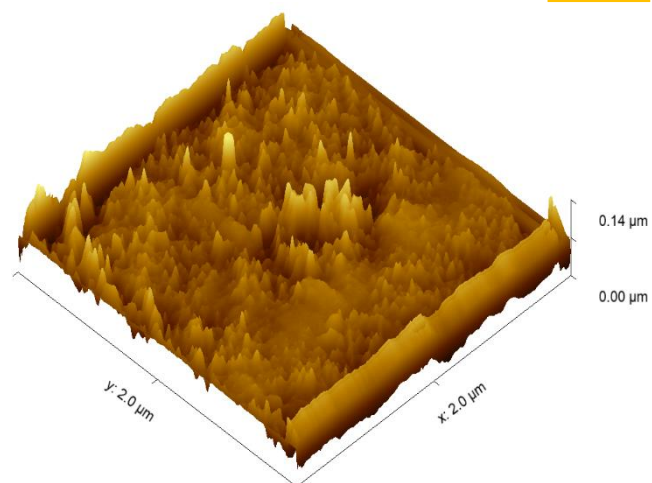
Fig.5.4.AFM images (a)2D, (b) 3D image of undoped SnO$_2$ thin film(c)2D (d)3D image of Cu-doped SnO$_2$ thin film (e) 2D (f) 3D image of Mg-doped SnO$_2$ thin film.

5.2.5 EDX and Mapping

Utilizing a Scanning Electron Microscope (SEM), Energy Dispersive X-ray Analysis (EDX) is a technique that identifies the elements in a prepared material. It also confirms the existence of these elements in the prepared thin films. Fig.5.5(a) illustrates the elemental composition of an undoped SnO$_2$ thin film. It depicts the presence of tin (Sn) and Oxygen (O) and their atomic and weight percentage. The evidence of incorporation of Mg and Cu is shown in Fig.5.5(b, c) along with their atomic and weight percentage, respectively, indicating that no additional elements are present in the prepared material. Fig. 5 .5 (d, e) indicates the homogenous distribution of tin (Sn)and oxygen (O) over the entire sample. Well, the distribution of Cu and Mg into the host is shown in Fig.5.5(f, g).

Spectrum1	Atomic %	Weight %
O	66.67	21.22
Sn	33.33	78.78
Total	100.00	100.00

Spectrum1	Atomic %	Weight %
O	66.67	21.37
Sn	33.00	78.46
Mg	0.33	0.16
Total	100.00	100.00

Spectrum1	Atomic %	Weight %
O	66.67	21.32
Sn	33.00	78.24
Cu	0.33	0.42
Total	100.00	100.00
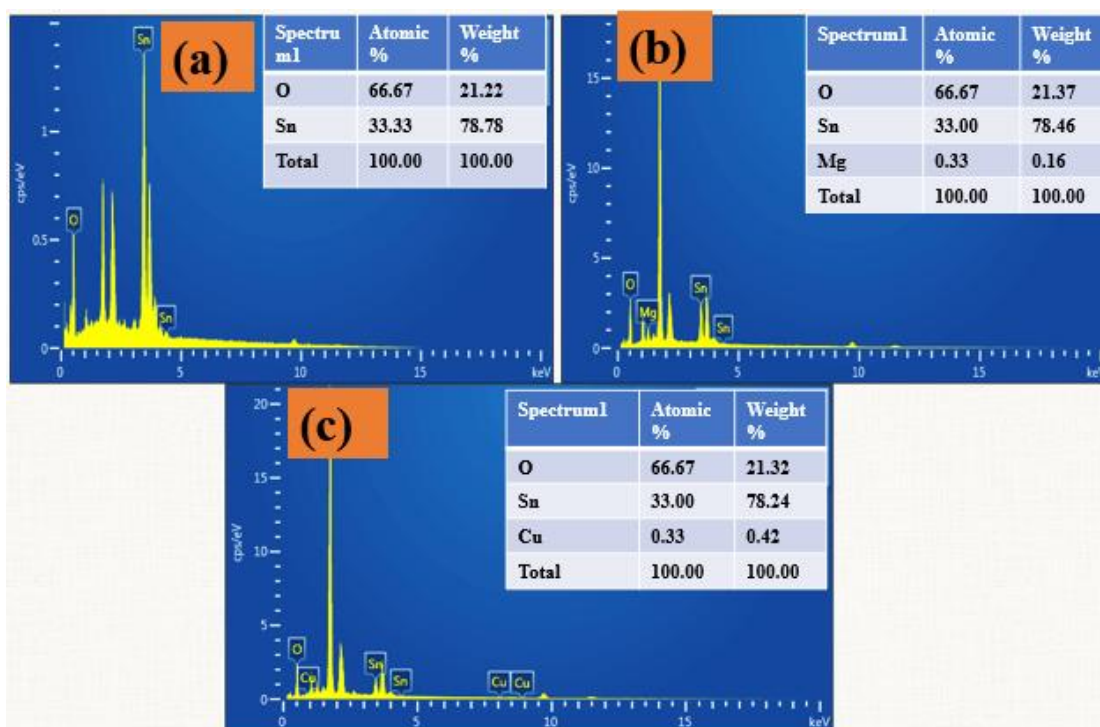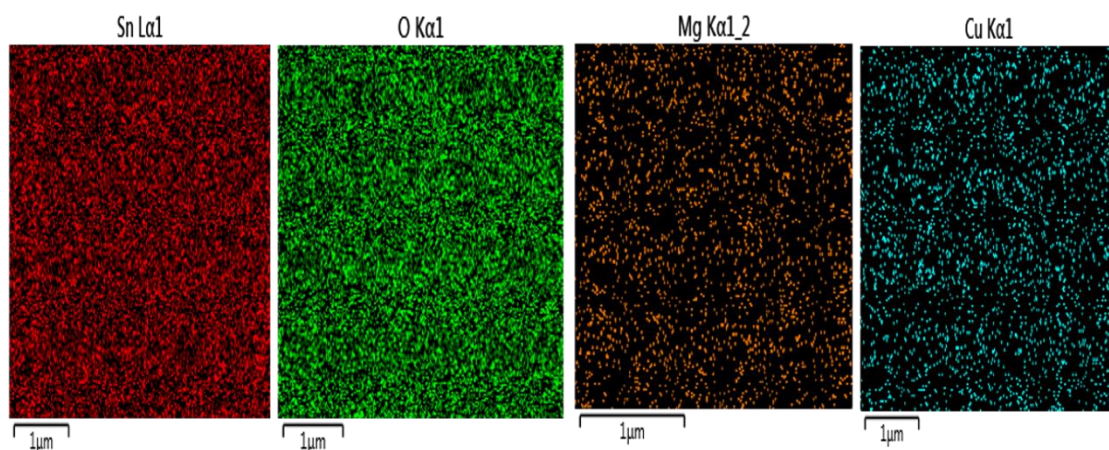
Fig5.5. (a, b, c) EDAX spectra for undoped,0.5%Mg-doped, and Cu-doped thin films.
Fig5.5. (d, e, f, g) mapping of Sn, O, Mg, Cu).

5.2.6 Optical analysis

5.2.6.1 UV -visible analysis

A UV-visible spectrophotometer instrument was utilized to investigate the interaction of light with undoped SnO_2 and Mg and Cu-doped SnO_2 thin films formed on a glass substrate and post-heated at 500˚C for one hour. Optical measurements of transparent semiconducting films are crucial for solar cell applications and optoelectronic devices. The results obtained from these optical analyses involve transmittance, absorbance, reflectance, extinction coefficient, optical band gap, and refractive index. In the general study, the transmission parameter of the thin film is affected by numerous factors, including the thickness of the film, crystallinity, morphology of the surface, optical band gap, surface roughness defects of the crystal, etc [158].

Figure 5.6(a) illustrates the average optical transmission of undoped and Mg-doped SnO_2 thin films across the spectral range of 300 to 800 nm. The concentrations of Mg dopant were 0.1%,0.5%,1.0%. The undoped SnO_2 shows an average transmission of 90.5% in the visible range (400-800 nm). As the Mg doping concentration rises to 0.1%, 0.5%, and 1.0%, the transmission enhances up to 97.6%, 99.5%, and 98.9%, respectively[146]. It has been noted that doping greatly raises the film's transmittance in the visible spectrum. At 0.1% of Mg doping, transmission rises, due to the reduced concentration of doping reduces grain boundaries and defects. As the doping

113

concentration rises to 0.5%, the transmission still rises to a certain level because of better crystallinity, reduction in defect states, and less surface roughness confirmed from AFM and XRD results. At higher concentrations (1.0%), the transmission decreases. It happens because excessive dopant atoms can incorporate more scattering centres and defects. Hence,0.5% Mg-doped SnO_2 exhibits higher transmittance up to 99.5% (in the visible spectra) in comparison to other concentrations, making it suitable for TCO applications. The high transmission means that a low amount of light is absorbed or scattered because of improved crystallinity and surface quality[83]. As we know, Absorbance, transmission, and reflection together add up to 100%, meaning all incoming light is either absorbed, transmitted, or reflected. Figure 5.7(a). also depicts the absorption spectra for undoped SnO_2 and Mg-doped SnO_2 (0.1%, 0.5%, and 1.0%). The undoped material exhibits the highest absorption in the 300-340 nm range and low transmission. As the rise of Mg doping concentration rises from 0.1% to 1.0%, the absorption spectra decrease. The 0.5% Mg-doped film shows the lowest light absorption, as it has the highest transmission among the samples. It is also observed that with the increase of Mg doping, the absorption edge for undoped SnO_2 moves towards a longer wavelength. This shift in the absorption edge after doping is known as a redshift. It happens due to the transfer of charge transition between the valence band or conduction band of SnO_2 and localized d electrons of Mg ion[223].

 According to Figure 5.6(b), the average transmission of undoped SnO_2 in the 400-800 nm range is about 90.5%. This transmission improves with increasing copper doping. Specifically, copper doping levels of 0.1%, 0.5%, and 1.0% enhance the transmission to 98.4%, 99.2%, and 95.8%, respectively. This is consistent with findings from another study as well [224], [225]. At higher doping levels(1.0%), the Cu atom can occupy the interstitial site and cause the metallic nature, which lowers the transmission[168]. Therefore, SnO_2 doped with 0.5% Cu has the highest transmission. Figure 7(b). also illustrates the absorption spectra for undoped and SnO_2 thin films doped with 0.1%, 0.5%, and 1.0% Cu. It was observed that undoped SnO_2 exhibited high absorption, but with increasing Cu doping, the absorption spectra were reduced[226]. It also revealed a red shift in the absorption with increasing Cu doping concentration. The redshift can also be explained by the lattice strain created from the addition of Cu into the lattice of

SnO₂ [227]. Therefore, we concluded that 0.5%Cu: SnO₂thin film enhances the transmission (99.5%) and decreases absorption.
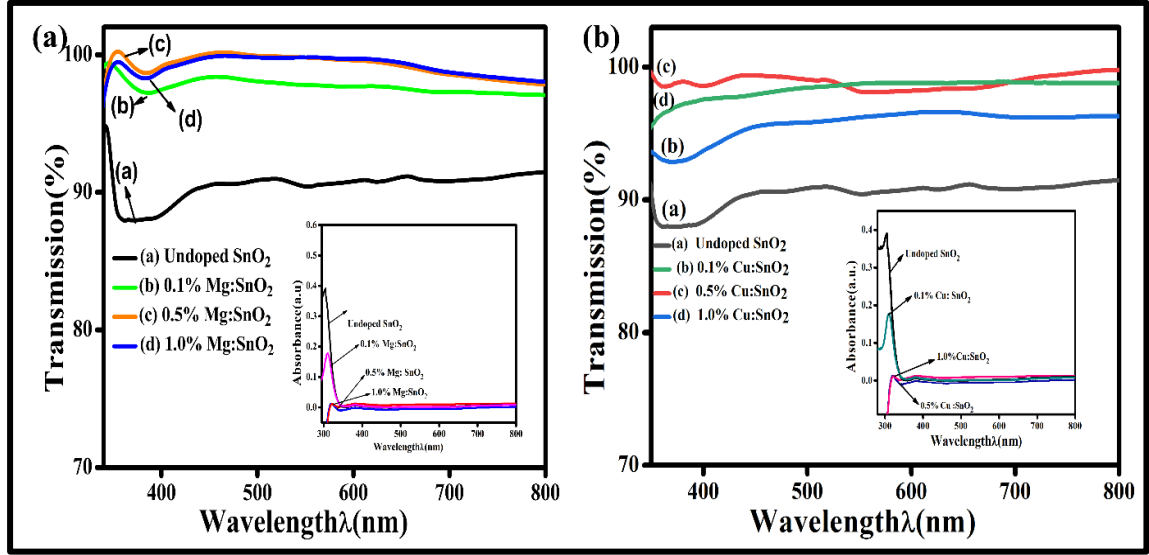
Fig.5.6. Transmission and absorption plot for (a) undoped and 0.1%,0.5%,1.0% Mg-doped SnO₂ thin film (b) undoped and 0.1%,0.5%,1.0%Cu- doped Cu doped SnO₂ thin film post-heated at 500°C for 1 hour.

The optical band gap is the smallest amount of energy needed for an electron to jump from the valence band to the conduction band of a material when it absorbs light. It is a necessary parameter to analyse the optical and electrical characteristics of materials, mostly in semiconductors and insulators. To determine the value of the optical band gap (E g) of the thin films, first have to find the value of the absorption coefficient(α), which is estimated by the following equation(5.6)[166]

$$\alpha = \frac{1}{d}\ln\left(\frac{100}{T}\right) \tag{5.6}$$

where 'T' presents transmission, and 'd' indicates the thickness of the films.

To further analyze the values of the optical band gap, equation (5.7), called the Tauc plot equation, was utilized[228]

$$(\alpha h v)^m = B(h v - E_g) \tag{5.7}$$

'B' depicts the constant, h' is the Planck constant, and 'm' represents the coefficient that varies based on the kind of transition,'m' is equivalent to 2 (for allowed direct

transition), and 'm' is equivalent to 1/2 (for allowed indirect transition). For SnO_2 thin film, m =2 is considered because of its parabolic band structure[229]. By utilizing the plot of $(\alpha hv)^2$ appears in the y-axis vs photon energy (hv) existing in the x-axis i.e, α =0 as shown in Figure 6(a, b), the optical band gap Eg for all the thin films was calculated. The optical band gap for undoped SnO_2 and 0.1%, 0.5%, and 1.0% Mg-doped SnO2 thin films is shown in Fig.5. 7(a). In this study, the optical band gap of undoped SnO_2 is 3.95eV, which is more than the 3.6eV band gap of bulk SnO_2. This might be due to the quantum size effect, and it aligns with previous analyses [67], [94], [224], [230]. The measured optical band gap (Eg) values are 3.94 eV for 0.1% Mg: SnO_2, 3.79 eV for 0.5% Mg: SnO_2, and 3.74 eV for 1.0% Mg: SnO_2 thin films. As the concentration of Mg enhances, the observed Eg value reduces. Typically, in n-type semiconductors, the Eg value increases with donor doping and decreases with acceptor doping[231][232]. Mg can act as either an acceptor or donor depending on the host material. In SnO_2, Mg acts as an acceptor when it replaces Sn ions, which results in a decrease in the band gap. The substitution of Mg on the site of Sn produces two holes due to the lower valence state of Mg^{2+} compared to Sn^{4+}[233]. S. Vadivel et al also observed the band gap reduction with Mg doping by a chemical bath deposition method[201]. The findings align with earlier studies[146], [198], [230].

The band gap values for undoped SnO_2 and Cu-doped SnO_2 at various concentrations (0.1%, 0.5%, and 1.0%) are shown in Fig.5.7(b). The measured values of band gap are 3.95 eV for undoped SnO_2, 3.92 eV for 0.1% Cu-doped SnO_2, 3.86 eV for 0.5% Cu-doped SnO_2, and 3.88 eV for 1.0% Cu-doped SnO_2. It shows a decreasing trend with the increase in copper doping concentration. This is aligned with the quantum confinement effect and is due to the shifts between the s electrons present in Cu ions and the valence or conduction band in SnO_2, known as S_2P interaction. Introducing low concentrations (e.g., 0.1% to 1.0%) of Cu into the host site of Sn^{4+} results in the release of surplus free electrons into the conduction band[234]. A similar pattern was observed in previous research as well[78], [211], [225], [235], [236]. Moreover, the decrease in band gap with increasing Cu concentration is attributed to both defects and the size of crystallites. Thus, these findings align with structural changes (in the XRD). Hence, the variation in band gap is also based on dislocation density, thickness, surface

morphology, lattice distortion, crystallinity, and position of the dopant. The materials with smaller band gaps are more conductive. The table5.3 presents the measured band gap values for undoped, Mg-doped SnO_2, and Cu-doped SnO_2 at concentrations of 0.1%, 0.5%, and 1.0%.
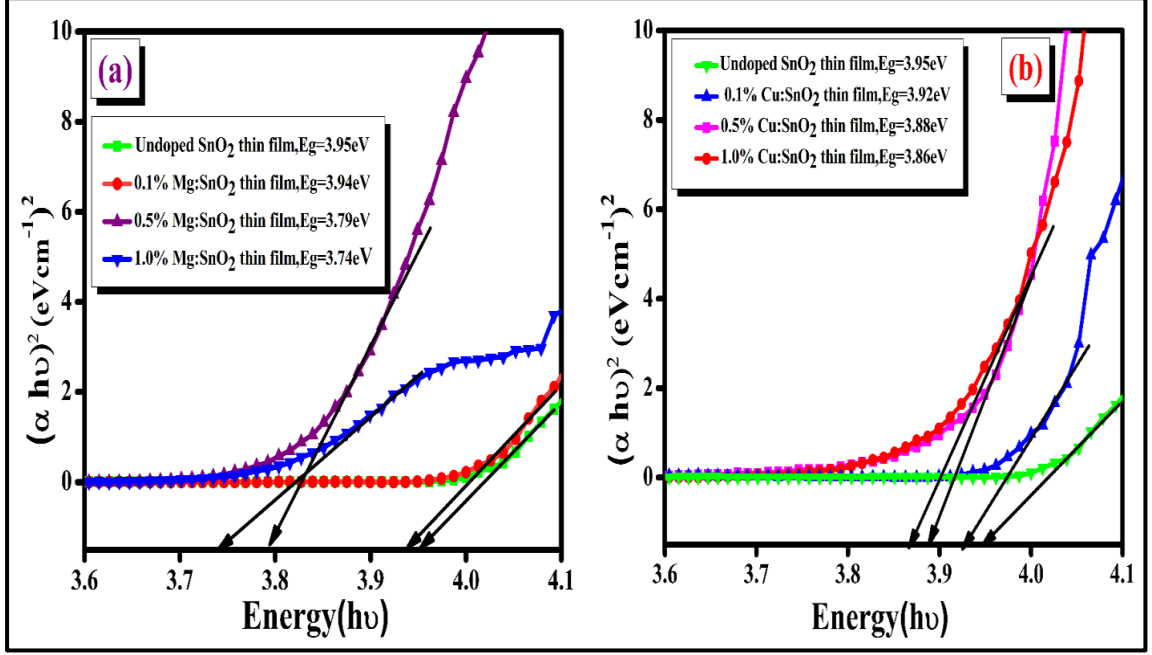
Fig.5.7. Optical band gap for (a) undoped and 0.1%,0.5%,1.0% Mg-doped SnO_2 thin film, (b) undoped and 0.1%,0.5%,1.0%Cu- doped Cu doped SnO_2 thin film post-heated at 500°C for 1 hour.

The refractive index is another essential parameter for studying the electrical and optical properties of transparent conducting oxide material, which are crucial for applications of solar cells, display devices, and heterostructure devices[237]. Reflectance (R) is used to get the refractive index value. Reflectance(R) is connected to transmittance (T) and absorbance (A) through the relationship described in equation (8)[238].

$$R = 1 - \sqrt{T \exp{(A)}} \qquad (5.8)$$

Equation(9) describes the relation between Reflectance (R) and refractive index (n)[239].

$$n = \frac{(1+\sqrt{R})}{(1-\sqrt{R})} \qquad (5.9)$$

Figure (5.8) (a) indicates the value of the refractive index for undoped SnO_2 and 0.1%,0.5%, and 1.0% concentration of Mg: SnO_2 thin films. The refractive index was observed to be high for undoped samples and decreases with increasing Mg doping concentration. This trend aligns with the transmission data shown in Figure 5.9(a). Our investigation reveals that the refractive index is inversely related to transmission, as transmission increases with Mg doping, reflectance (R), and absorbance (A), and the refractive index decreases. This occurs due to the film's homogeneity, reduced surface roughness, improved transparency, and decreased polarization. The table indicates the calculated values of undoped and Mg: SnO_2 thin films (0.1%,0.5% and 1.0%). A similar trend has been described in previous research[83], [240].

The trend of the refractive index concerning wavelength for undoped SnO_2 and Cu-doped SnO_2 thin films (0.1%, 0.5%, and 1.0%) is shown in Figure 5.8(b). It was found that the refractive index value reduced as Cu doping rose from 0.1% to 1.0%. As previously discussed, transmission and refractive index exhibit an inverse relationship. Therefore, copper doping is consistent with the transmission data shown in Figure 6(a). This decrease in refractive index in the visible region with copper doping is due to uniformity, improved surface roughness, less polarization, and high transparency[241].The measured values of undoped SnO_2 and Cu-doped SnO_2 are presented in Table5.3. In conclusion, 0.5% doping of Mg and Cu in SnO_2 thin films results in better transparency and a lower refractive index. This makes it ideal for transparent conducting oxides used in display devices, flat panels, solar cells, etc.

Table 5.3. Optical parameters of undoped, Mg: SnO_2, and Cu: SnO_2 thin films. (0.1%,0.5%and 1.0%).

Mg and Cu Content	Transmission (%)		Band gap (ev)		Refractive index in the visible region	
	Mg: SnO_2	Cu: SnO_2	Mg: SnO_2	Cu: SnO_2	Mg: SnO_2	Cu: SnO_2
Undoped SnO_2	90.5	90.5	3.95	3.95	2.24	2.24
0.1%	97.6	98.4	3.94	3.92	2.12	2.13
0.5%	99.5	99.2	3.79	3.88	2.06	2.02

| 1.0% | 98.9 | 95.8 | 3.74 | 3.86 | 2.08 | 2.07 |
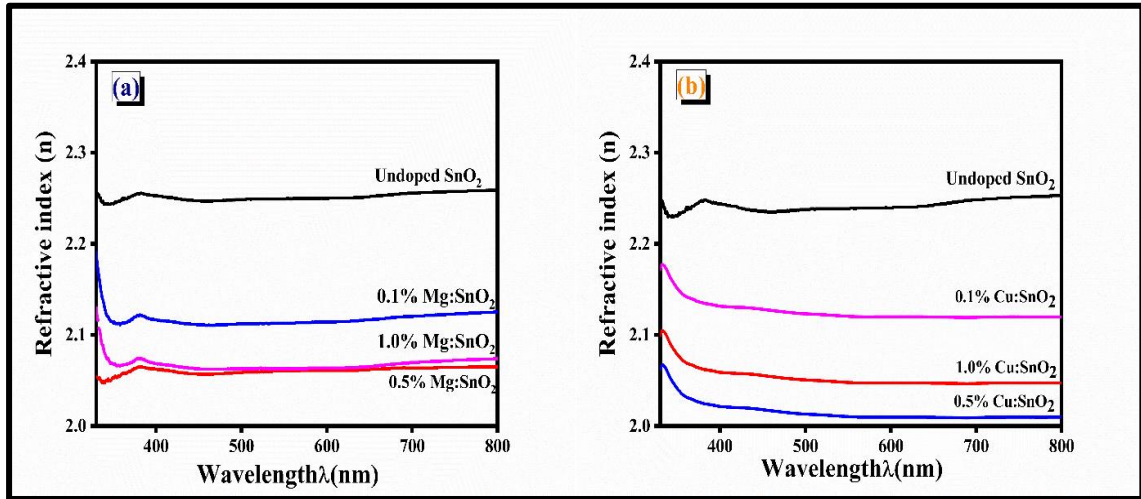
Fig.5.8. Refractive index for (a) undoped and 0.1%,0.5%,1.0% Mg-doped SnO₂ thin film, (b) undoped and 0.1%,0.5%,1.0%Cu- doped Cu doped SnO₂ thin film post-heated at 500°C for 1 hour.

5.2.7. Electrical Analysis

The two-point probe technique was employed to investigate the electrical properties of undoped SnO₂ and Mg and Cu-doped SnO₂ thin films. Fig.5.9(a, b) shows the I-V characteristics of these films. With the variation of voltage from 0 V to 20 V at room temperature, the current was measured. It can be seen from the I-V diagram that there is a linear relationship between the current and voltage. Ohm's law is supported by this behavior, indicating that the contact placed on the films is appropriate. The doping of Cu and Mg decreases the resistance and is observed in Fig. 5.9(a) and 5.9(b).

119
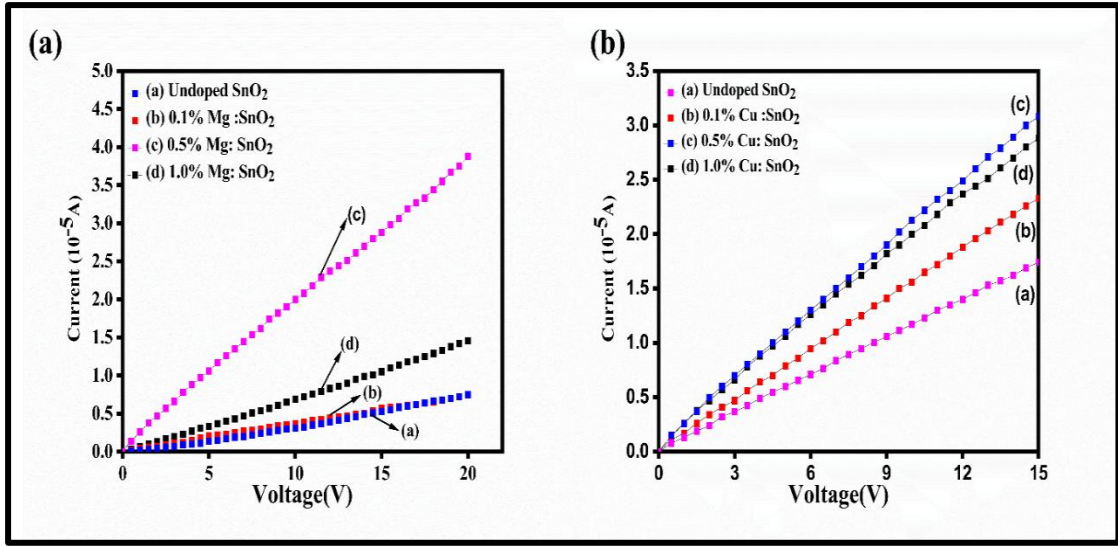
Fig.5.9. (a, b) IV characteristics of undoped, Mg: SnO₂, and Cu: SnO₂ thin films (0.1%,0.5%, and 1.0%).

5.2.7.1. Hall Effect

Undoped SnO₂ thin films are usually n-type semiconductors. It results from excess oxygen vacancies in areas of the crystal structure absent of oxygen ions. Because of these oxygen vacancies, shallow donor levels are present in the conduction band, resulting in SnO₂ being an n-type semiconductor with a lot of free electrons[233]. Hall Effect measurements (Vander paw technique) were used to investigate the electrical properties of undoped SnO₂ and Mg and Cu-doped SnO₂ thin films, including conductivity (σ), resistivity (ρ), carrier type, carrier concentration (ne), and mobility (μ). The Hall coefficient's sign (negative or positive) indicated whether the carrier type was n-type or p-type.

Fig.5.10. shows the conductivity, carrier concentration, and mobility of undoped SnO₂ and Mg-doped SnO₂ thin films (0.1%, 0.5%, and 1.0%). The conductivity of the undoped SnO₂ thin film is 2.21×10^3 (Scm⁻¹). As the concentration of Mg doping rises from 0.1% to 1.0%, the conductivity first decreases (1.04×10^3 Scm⁻¹), then drastically increases to 8.42×10^3 Scm⁻¹ and finally decreases by 1.19×10^3 Scm⁻¹ again. The highest conductivity, 8.42×10^3 Scm⁻¹, is observed with 0.5% Mg doping. The mobility of Mg-doped SnO₂ thin films ranges from 16.5 to 67.8 cm²/V·s, while the carrier concentration varies from 1.04 to 6.96×10^{19} cm⁻³. When dopant 0.1% Mg²⁺ is

introduced in the undoped SnO_2 thin film, it can make positive holes (in excess form) (Vo^{++}), these holes neutralize the free electrons formed by oxygen vacancies in the undoped SnO_2 thin film. The reduction of free electrons decreases conductivity. At certain doping concentrations, such as 0.5%, the interaction between Mg^{2+} and SnO_2 lattice might enhance the crystal structure or add another mechanism that enhances conductivity. Another necessary mechanism for the highest conductivity in TCO thin films is the ionized impurity, lattice vibration, and scattering mechanism. In this study, grain boundary scattering is identified as the primary factor affecting the mobility of thin films[86]. Larger grains decrease grain boundary scattering, leading to an increase in conductivity. In polycrystalline materials, grain boundary scattering significantly influences carrier transport[83]. This concentration exhibits the highest conductivity ($8.42 \times 10^3 Scm^{-1}$), among others, because of the highest carrier concentration ($5.27 \times 10^{19} cm^{-3}$) and mobility (67.8 cm²/V·s) with minimum influence of defects. The rise of carrier concentration could be caused by the Mg^{2+} ion replacing the SnO_2 lattice, which releases a large number of free electrons. Further increase of concentration of 1.0%Mg doping the production of positive holes (Vo^{++}), surpasses that of free electrons, leading to the reduction of the carrier concentration and transforming the conductivity from n-type to p-type semiconductor[242]. It also reduced carrier concentration and mobility, which might lead to the insertion of Mg^{2+} ion rather than replacement in the interstitial location of SnO_2 location which would minimize free electron density. 0.1% and 0.5% Mg show n-type semiconductors, and 1.0% show p-type semiconductors. At a particular acceptor doping concentration, the number of electrons is reduced as compared to holes, leading to a dominant p-type conduction. Benouis et al. found that 2% Al doping transforms the n to p-type conductivity. This phenomenon has a resemblance to bulk crystalline semiconductors, whereas n-type semiconductors can be converted to p-type semiconductors through doping with acceptors[230]. Table 5.4. explains the measured values of conductivity, carrier concentration, and mobility, and the type of carrier of undoped and Mg-doped SnO_2 thin films (0.1%,0.5%, and 1.0%). These outcomes align with another study [48][233][102].
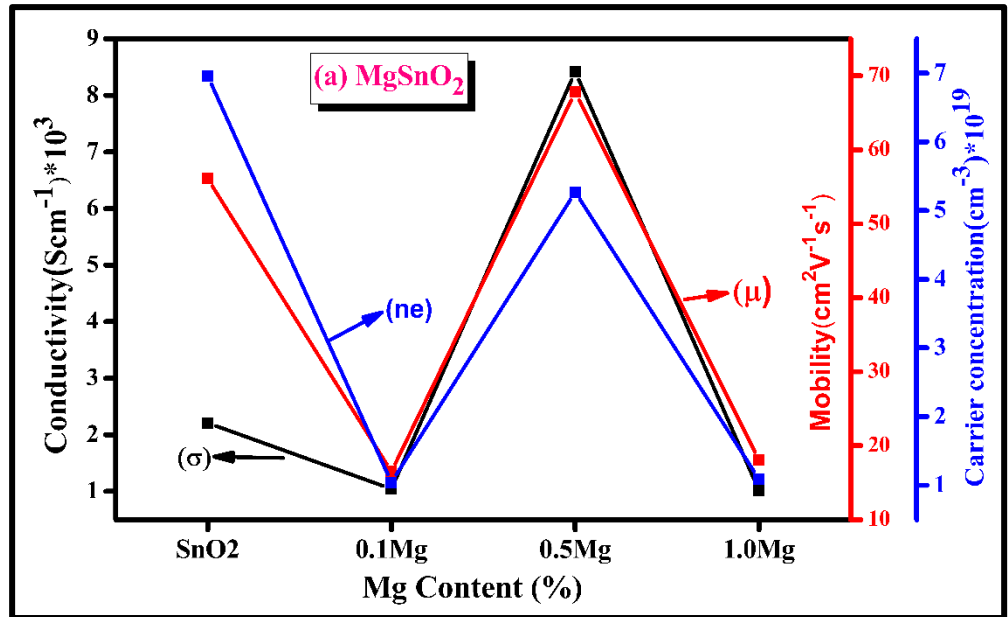
Fig.5.10. Conductivity, carrier concentration, and mobility of undoped SnO_2 and Mg-doped SnO_2 thin films (0.1%,0.5%and 1.0%).

Fig.5.11. depicts the conductivity, carrier concentration, and mobility of undoped SnO_2 and Cu-doped SnO_2 thin films doped with 0.1%, 0.5%, and 1.0%. Copper (Cu) behaves as either an n-type or p-type dopant, it depends on the host material it will introduce and how it interacts with the lattice structure of the material. In this research, the conductivity, carrier concentration, and mobility value for undoped SnO_2 thin film are 2.21×10^3 Scm^{-1}, 6.96×10^{19} cm^{-3}, and 56.28 cm²/V·s. Incorporating 0.1% Cu into an undoped SnO_2 thin film significantly increases conductivity by 6.14×10^3 Scm^{-1}. This enhancement is attributed to the introduction of free electrons to the conduction band, which boosts both conductivity and carrier concentration. The mobility of 0.1% Cu-doped SnO_2 also improves slightly, as the low concentration of Cu does not create significant defects or scattering centers. At 0.5% Cu doping, conductivity reaches its optimal level due to the incorporation of additional free electrons, further increasing carrier concentration compared to the 0.1% doping level. Mobility also reaches its highest point because doping levels are properly maintained carrier concentration without adding an excessive number of defects or scattering centers. However, at higher doping levels, such as 1.0%, conductivity decreases to 5.05×10^3 Scm^{-1}. This reduction is caused by the excessive doping of Cu, which introduces defects and impurity states

that act as scattering centers, reducing mobility. Despite the decrease in mobility, the carrier concentration remains high [211]. These results coincide with another literature work[41][243]. The undoped SnO_2 thin film exhibits n-type conductivity because of free electrons that are provided by tin interstitials and oxygen vacancies that behave as donors[244]. At low doping concentrations of 0.1%, Sn atoms in the lattice are replaced by Cu. Although Cu may exist in many oxidation states, in this specific case, Cu behaves as a donor and increases the free electrons in the conduction region. Hence enhances the n-type conduction. At 0.5% Cu doping, the SnO_2 exhibits optimal conductivity and mobility, maintaining its n-type characteristics with an increased number of free electrons. However, excessive Cu doping at 1.0% introduces defects that reduce both mobility and conductivity, even though the carrier concentration remains high. The material remains n-type, but defect-induced scattering diminishes its performance. The measured value of conductivity, carrier concentration, mobility, and type of carrier for undoped SnO_2 and Cu-doped SnO_2 thin films for various concentrations are represented in Table 4.A consistent pattern was observed in Mg^{2+}, Cu^{2+} and Ru^{2+} doped SnO_2 thin film[225][245][233][246].
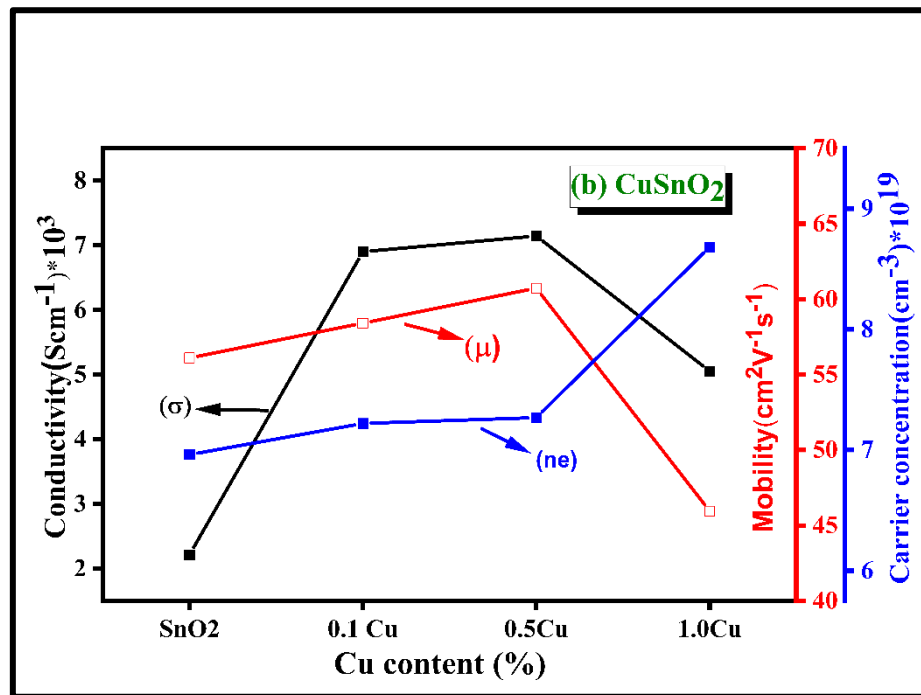
Fig.5.11. Conductivity, carrier concentration, and mobility of undoped SnO_2 and Cu-doped SnO_2 thin films (0.1%,0.5%and 1.0%).

Table 5.4. Electrical Parameters of Undoped SnO_2, Mg, and Cu doped SnO_2 thin films (0.1%,0.5%and 1.0%).

Mg and Cu Content	Carrier concentration(cm^{-3})10^{19}		Conductivity (Scm^{-1})10^3		Mobility($cm^2V^{-1}s^{-1}$)		Type of carrier	
	Mg:SnO_2	Cu:SnO_2	Mg:SnO_2	Cu:SnO_2	Mg:SnO_2	Cu:SnO_2	Mg:SnO_2	Cu:SnO_2
Undoped SnO_2	6.96	6.96	2.21	2.21	56.2	56.2	n	n
0.1%	1.04	7.22	1.04	6.14	16.5	58.4	n	n
0.5%	5.27	7.26	8.42	7.89	67.8	60.8	n	n
1.0%	1.09	8.68	1.19	5.05	18.1	45.9	p	n

5.2.7.2. Activation Energy

Given that electrical conductivity in semiconductors is a thermally stimulated process, the conductivity often rises exponentially with rising temperature. To analyze the temperature dependence mechanism of conductivity, it is necessary to plot log ($\sigma_{D.C.}$) which shows DC conductivity Vs 1000/T(k) explaining temperature. The conductivity, temperature, and activation energy are related to each other and can be explained by Arrhenius laws in equation (5.10)

$$\sigma = \sigma_1 \ \exp\left(\frac{-Ea_1}{kT}\right) + \sigma_2 \ \exp\left(\frac{-Ea_2}{kT}\right) + \sigma_3 \ \exp\left(\frac{-Ea_3}{kT}\right) \qquad (5.10)$$

Where σ_1, σ_2 and σ_3 represent three electrical conductivities at a temperature, Ea_1 Ea_2 and Ea_3 shows three activation energies of the thin film, T is the absolute temperature in kelvin, and K is known as the Boltzmann constant. Fig5.12(a, b) displays the plot of log ($\sigma_{D.C.}$) which shows DC conductivity Vs 1000/T(k) explains temperature for undoped SnO_2, Mg-doped SnO_2 thin films and Cu doped SnO_2 thin films at various concentrations 0.1%,0.5% and 1.0%). It illustrates three conduction regions for undoped SnO_2, Mg-doped SnO_2, and Cu-doped SnO_2 thin films at various concentrations. In terms of the first region, the high-temperature area (lower value of 1000/T), the value of activation energy (Ea_1) is high, and the conductivity is lower. The conductivity in this area is analyzed by intrinsic defects, therefore, it is known as

intrinsic conduction. The value of energy activation (Ea$_1$) is high in this area due to the reason that the energy required to produce defects is significantly more than that of energy needed for their drift. Due to this reason, the electrical conductivity of the samples at high temperatures is determined by intrinsic defects that are produced by thermal fluctuations[247].In the second region(moderate 1000/T), as the temperature reduces, the slope of the curve alters, depicting the distinct activation energy (Ea$_2$). Conduction in this area is because of impurity or defect states. It produces localized states inside the band gap that make carrier transportation easier. It is known as impurity conduction. In the area of the low-temperature region (higher value of 1000/T), the slope shows a low activation energy (Ea$_3$). This suggests that in the low-temperature region, a distinct conduction mechanism occurs, such as hopping conduction or less energy process. At low temperatures, thermal energy is insufficient to excite electrons over large energy gaps. Rather, the capacity of an electron to "hop" between localized states that contain defects or impurities is referred to as hopping conduction. Compared to intrinsic or impurity conduction, this process requires less energy.
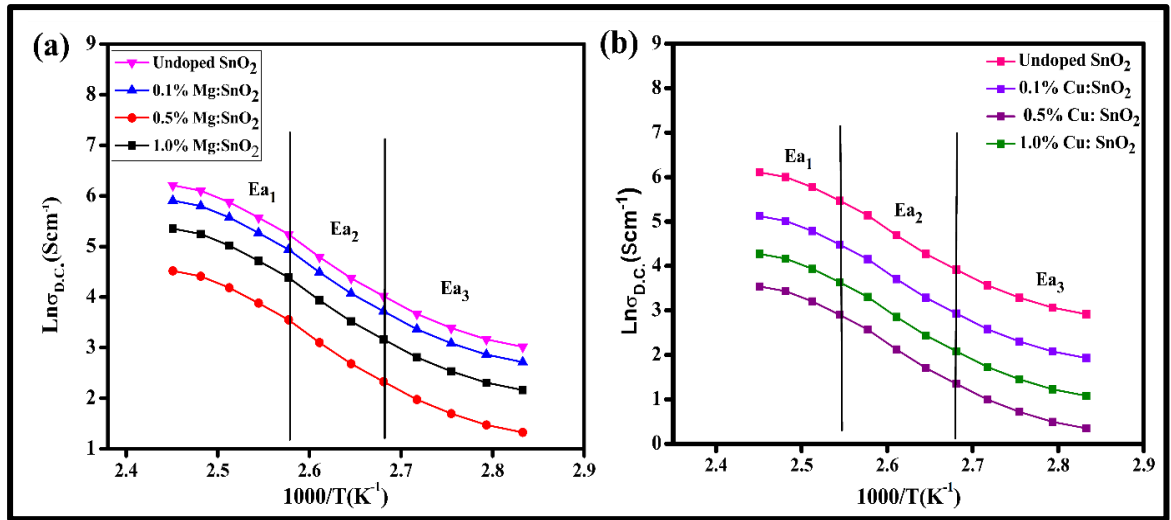
Fig.5.12. (a,b) Plot for logσ_{DC} as a function of inverse temperature 1000 /T for undoped SnO$_2$, Mg-doped, and Cu-doped SnO$_2$ thin films (0.1%,0.5%, and 1.0% concentrations).

Furthermore, Table 5.5. presents the activation energy values (Ea$_1$, Ea$_2$, and Ea$_3$) for undoped SnO$_2$, as well as Mg and Cu-doped SnO$_2$ thin films, measured over the temperature range of 408K to 353K. These values are calculated using equations (11). For the undoped SnO$_2$ thin film, the activation energies are Ea$_1$ = 0.79 eV and Ea$_2$ =

0.65 eV, Ea_3=0.69eV indicating high activation energy and low conductivity. As the Mg concentration increases in the SnO_2 thin film, the activation energy decreases. Specifically, 0.1%, 0.5%, and 1.0% Mg-doped SnO_2 thin films show activation energies of Ea_1 =0.71 eV and Ea_2 = 0.60 eV, Ea_3=0.64, Ea_1 = 0.60 eV and Ea_2 = 0.51 eV, Ea_3=0.59 and Ea_1 = 0.68 eV and Ea_2 = 0.58 eV, Ea_3=0.62 respectively. The 0.5% Mg doping exhibits the lowest activation energy compared to the others, due to its higher conductivity. `This occurs because the mobility of charge carriers is enhanced, reducing the energy required for electron excitation. When another dopant, Cu doped into SnO_2 thin films, it reduces the activation energy by adding additional charge carriers and altering the electronic structure. Specifically, 0.1% and 0.5% copper doping reduce the activation energies to Ea_1 = 0.69 eV, Ea_2 = 0.58 eV, Ea_3=0.62 and Ea_1 = 0.63 eV, and Ea_2 = 0.54 eV, Ea_3=0.59eV respectively. This happens due to copper atoms that can make shallow donor levels, which improve conductivity and reduce the energy needed for electron excitation. However, at 1.0% copper doping, the activation energies increase to Ea_1 = 0.68 eV and Ea_2 = 0.60 eV, Ea_3=0.63eV likely due to the formation of defect states or clustering of dopant atoms, which can hinder charge carrier mobility. The lowest activation energy is observed at 0.5% copper doping, indicating an optimal balance between increased carrier concentration and minimal defect formation.

Table 5.5. Activation energies for undoped, Mg-doped, and Cu-doped SnO_2 thin films.

Mg and Cu Content	Activation Energy (Mg: SnO_2)			Activation Energy (Cu: SnO_2)		
	Ea_1 (eV)	Ea_2(eV)	Ea_3 (eV)	Ea_1(eV)	Ea_2(eV)	Ea_3(eV)
Undoped SnO_2	0.79	0.65	0.69	0.79	0.65	0.69
0.1%	0.71	0.60	0.64	0.69	0.58	0.62
0.5%	0.60	0.51	0.59	0.63	0.54	0.59
1.0%	0.68	0.58	0.62	0.67	0.60	0.63

5.2.7.3. Optoelectronics property

To enhance semiconductor material's conductivity, it is essential to make the band gap minor in between the conduction band and valence band. However, as light travels

through the photon is absorbed by the material due to the photoelectric effect, hence, a bigger band gap reduces the absorption of photons, and optical transmittance is enhanced, leading to lower conductivity, which reduces carrier concentration. Thus, it is challenging to simultaneously enhance both transmittance and conductivity. To evaluate this figure of merit (Φ_{TC}) is introduced[56]. The Figure of Merit (FOM) measures the quality and performance of any transparent conducting oxide (TCO) material. It is a major parameter for the applications of optoelectronic devices. To evaluate the performance of various transparent conductors, the Haacke formula in equation(5.11) defines the most widely used figure of merit.[182].

$$\Phi_{TC} = \frac{T^{10}}{R_S} \tag{5.11.}$$

Where Transmission is denoted by T^{10}, and R_s shows the sheet resistance of undoped, Mg-doped, and Cu-doped SnO_2 thin films at various concentrations. There, a higher figure of merit indicates the superior performance of the TCO thin films. Figure 5.13 illustrates the figure of merit for undoped, Cu-doped SnO_2, and Mg-doped SnO_2 thin films post-heated at 500°C for one hour. It was observed that as the doping level increased from 0.1, 0.5 to 1.0%, the highest figure of merit $(2.9 \times 10^{-2}\,\Omega^{-1})$ was achieved at 0.5% doping, indicating that 0.5% Mg doping enhances both conductivity and transparency. Figure 5.14 displays the figure of merit for undoped SnO_2 and Cu-doped SnO_2, with doping concentrations of 0.1, 0.5, and 1.0%. Here, 0.5% Cu doping exhibits the highest figure of merit $(2.4 \times 10^{-2}\Omega^{-1})$, which then declines with higher concentrations. A high figure of merit TCO is desirable for optoelectronic devices such as flat panels, display devices, and solar cells.
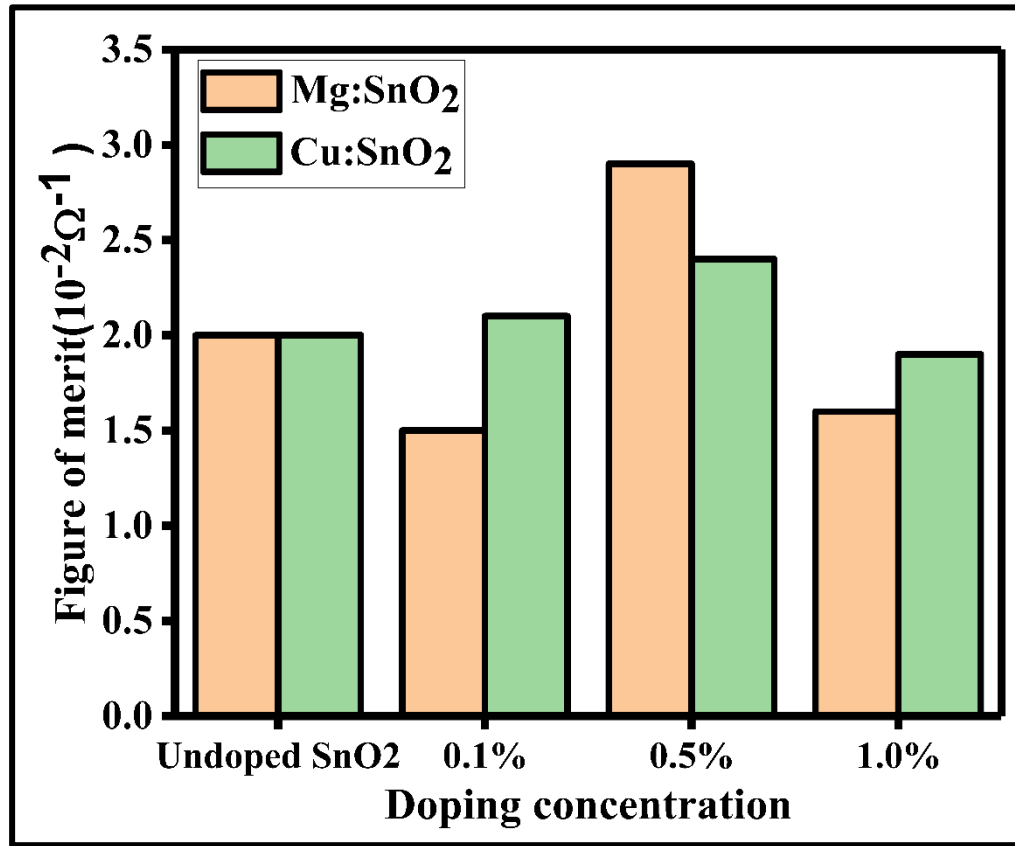
Fig.5.13. Figure of merit for undoped SnO_2, Mg-doped, and Cu-doped SnO_2 thin films (0.1%,0.5%, and 1.0%).

5.3. Conclusion

The recent research synthesized the sol-gel spin coating approach to growing undoped tin oxide (SnO_2) thin film, magnesium-doped SnO_2, and copper-doped SnO_2 thin films annealed at 500℃ for one hour. It also determines the comprehensive influence of Mg and Cu on SnO_2 thin films on the transmission and conductivity of Transparent Conducting Oxides (TCO's). Concentrations of dopants were 0.5, 1.0, and 1.5 % for Mg-SnO_2 and Cu-SnO_2 thin films. Phase study through X-ray diffraction (XRD) analysis displayed that all the prepared thin films had a polycrystalline tetragonal rutile crystal structure. Increasing the doping levels leads to an increase in the crystallite size. EDAX (Energy-Dispersive X-ray) investigation verified that the elements Sn, O, Cu, and Mg were included. Atomic force microscopy (AFM) was utilized to study the surface morphology and roughness of undoped, Mg, and Cu-doped SnO_2 thin films. Using Fourier transform infrared spectroscopy (FTIR), it was demonstrated that all the

prepared thin films had vibration peaks for Sn–O, O–Sn–O, Sn–OH, and O–OH. Doping results in a shift of these peaks without altering the overall structure. Optical studies indicated the transmission of undoped, Mg-doped, and Cu-doped films in the visible spectra. Doping with Mg and Cu enhanced the transmission of undoped SnO_2 thin films, with 0.5% Mg doping achieving the highest transmission rate of 99.5%. Conductivity, carrier concentration, mobility, and carrier type were analysed by utilizing Hall measurements. Mg^{2+} doping at 0.5% resulted in the highest conductivity values, with 8.418×10^3 Scm^{-1}, respectively. It also demonstrates the transformation from n to p-type conduction after Mg doping. The highest figure of merit (2.9×10^{-2} Ω^{-1}) examined in 0.5% Mg-doped SnO_2 thin films supports their use as cost-effective transparent conducting oxide films in optoelectronic devices, including flat panels, display devices, photovoltaic devices, and solar cells.

Chapter 6

Transparent conductive ZnS in its pure form and Cu²⁺and Mg²⁺doped ZnS thin films.

6. 1. Introduction

Zinc sulfide (ZnS) stands out as a highly adaptable material, finding significant utility across diverse technological domains, notably in optoelectronics [248], photovoltaic devices[249], and as a component in transparent conductive layers[250]. Zinc sulfide (ZnS), an II–VI group semiconductor, has garnered significant attention due to its wide band gap (~3.6 eV) and excellent optical transparency in the visible region[251]. Owing to its promising optoelectronic properties, ZnS thin films are extensively used in photodetectors, electroluminescent devices, solar cells, and gas sensors. A primary benefit of ZnS is its exceptional transparency within the visible portion of the electromagnetic spectrum. This characteristic renders it particularly well-suited for incorporation into transparent conductive coatings used in touch screens and display devices.[252]. ZnS exists in two primary crystalline forms: zincblende (ZB) and hexagonal wurtzite. This chapter describes the formation of ZnS thin films with the help of the sol-gel spin coating method, which is a cost-effective technique. The ZnS host material was subjected to a post-heating process at 500°C for five hours, a condition informed by existing literature.

Doping with suitable metal ions was incorporated into the ZnS host material to improve its transmission and electrical conductivity for transparent conducting applications. In this context, Cu^{2+} and Mg^{2+} ions are chosen as dopants due to their compatibility with the Zn^{2+} lattice. Cu^{2+}, with an ionic radius (0.73 Å) comparable to Zn^{2+} (0.74 Å), can substitute Zn sites without significantly distorting the host lattice, potentially enhancing electrical conductivity through the generation of shallow donor levels[85]. Conversely, Mg^{2+} (ionic radius ~0.65 Å) introduces compressive strain due to its smaller size, which can also influence charge carrier mobility and defect density.

This chapter centres on the formation of transparent conductive Zinc Sulfide (ZnS) thin films, both in their undoped form and when doped with copper (Cu^{2+}) and magnesium

(Mg^{2+}). These thin films were produced using the sol-gel spin coating technique, followed by a five-hour annealing process at 500°C. The doping levels investigated were 0.1%, 0.5%, and 1.0%. The resulting thin films were analyzed using X-ray Diffraction (XRD), Field Emission Scanning Electron Microscopy (FE-SEM), Ultraviolet-Visible (UV-Vis) spectroscopy, Atomic Force Microscopy (AFM), Hall effect measurements, and a two-point probe. The suitability of the material for transparent conductive film applications was assessed by evaluating its figure of merit (FOM), where a higher FOM signifies better performance in terms of optical transmittance and electrical conductivity.

6.2. Results and Discussion

6.2.1 Structural study

X-ray diffraction serves as an effective technique for investigating the crystalline phases and structural properties of the prepared ZnS thin films and Cu^{2+} and Mg^{2+} doped thin films at distinct doping concentrations, such as 0.1%,0.5%, and 1.0%. These films were post-heated at 500 °C for five hours. Figure 6.1. (a,b) indicates the XRD structure of ZnS thin film and Cu^{2+} and Mg-doped ZnS thin film at distinct doping levels. It reveals that both ZnS host and dopants Cu^{2+} and Mg^{2+} show three distinct peaks at 2θ values of 28.80°, 48.36°, and 57.28 °. These peaks correspond to the (111), (220), and (311) crystallographic planes of the zinc blende phase of ZnS[85]. All the thin films depict the poly-crystalline and Zinc Blende structure, which aligns with JCPDS Card No 80-0020. Furthermore, the X-ray diffraction patterns of the Copper (Cu) and Magnesium (Mg) doped samples of all concentrations did not reveal any additional impurity peaks. This observation suggests that the dopant ions were successfully integrated into the Zinc Sulfide (ZnS) crystal lattice. Compared to another peak, 111) is the highest and prominent peak. It revealed a rise in the intensity of the diffraction peak corresponding to the (111) crystallographic plane upon the introduction of the dopants. This observation is attributed to a more pronounced growth orientation along the (111) plane because of the doping process[253]. Figure 6.1(a) illustrates that the introduction of Copper (Cu) dopant initially causes a slight rise in peak intensity at low concentrations, followed by a further increase at intermediate concentrations, and

subsequently a decrease at higher concentrations. After the addition of copper dopant, the (110) peaks were minutely shifted towards the higher angle. This phenomenon is attributed to the difference in ionic radii between Cu^{2+} and Zn^{2+} ions within the crystal lattice[254]. This strain is called compressive strain. Figure 6.1 (b) also displays the role of Mg^{2+} on the ZnS lattice. Notably, it also depicts the minor shift of (110) diffraction peaks towards a higher angle because the ionic radius of Mg^{2+} is less than that of Zn^{2+}. When a dopant with a smaller ionic radius occupies sites in a host material with larger ionic radii, it induces compressive strain within the lattice[255].
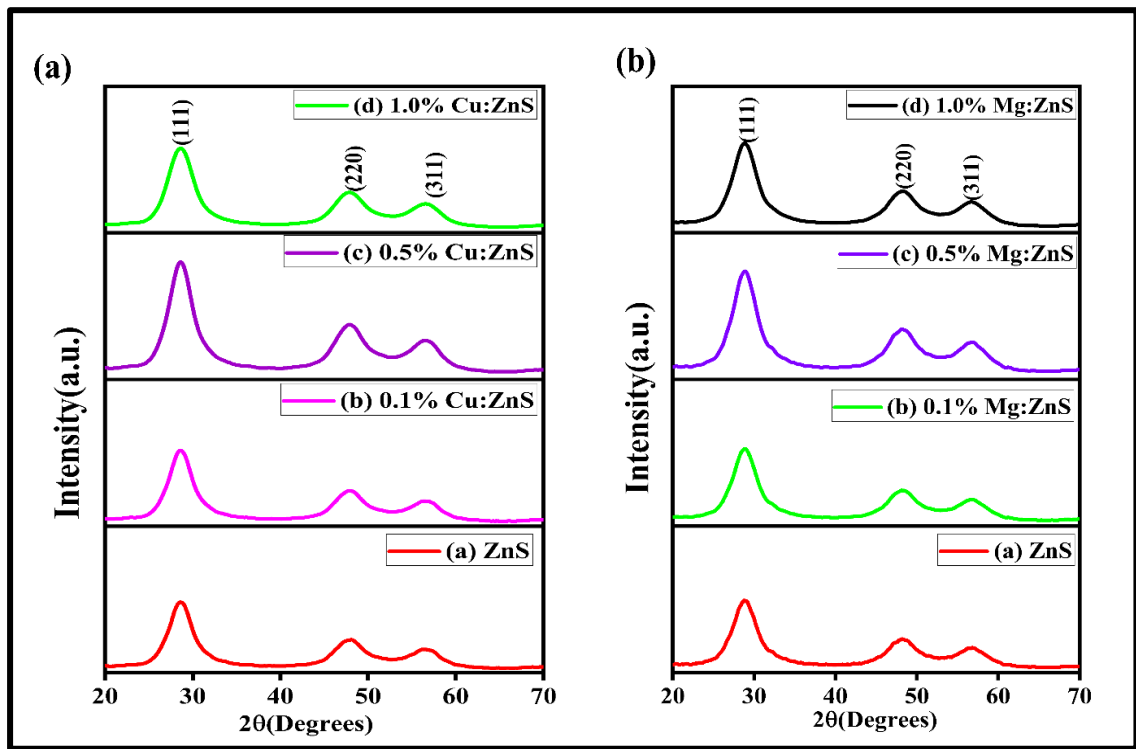
Fig.6.1.(a, b) XRD spectra for ZnS, Cu^{2+} and Mg^{2+} ZnS thin films at various concentrations.

The crystallite size for each of the samples was calculated using the Debye-Scherrer equation[256] explained in (3.1), and also another parameter, lattice strain and dislocation density, were determined with the help of equations (3.2),(3.3)[257], [258]. The calculated values of crystallite size, strain, and dislocation density of ZnS, Cu^{2+}, and Mg^{2+} doped ZnS thin films at various concentrations are shown in Table 6.1. It was observed that copper (Cu^{2+}) doping influenced the crystallite size, strain, and dislocation density of ZnS. ZnS depicts 4.10 nm of crystallite size. After the

132

incorporation, it rises to 5.46nm. 0.5% doping of copper shows intense peaks and a high crystallite size. After that, it reduces to 4.14 nm, which is more than the host material. Strain and dislocation density reduce with doping because it inversely dependent on crystallite size. The results resemble the previous literature[253], [259], [260]. Also, it reveals the influence of another dopant, which is Magnesium (Mg^{2+}). ZnS depicts 4.10 nm of crystallite size. With magnesium (Mg^{2+}) doping, crystallite size first rises at 0.1% and 0.5%, which 4.18nm and 5.00 nm, then reduces to 4.25nm, but more than the host crystallite size. It shows that the dopant is properly incorporated into the lattice of ZnS and increasing the crystal structure and reducing defects as compared to the host material. Therefore, crystallite size rises and dislocation density, and strain rise with the doping. These findings align with another study[69], [261].

Table6.1. The measured values of structural parameters of ZnS, $Cu^{2+,}$ and Mg^{2+} doped ZnS thin films.

Mg and Cu Content	(hkl) plane		Crystallite Size(nm)		Dislocation density(δ) × (10^{-3}) (nm^{-2})		Strain (ε) ×10^{-3}	
	Cu: ZnS	Mg: ZnS	Cu: ZnS	Mg: ZnS	Cu: ZnS	Mg: ZnS	Cu: ZnS	Mg: ZnS
ZnS	(111)	(111)	4.10	4.10	59.44	59.44	33.90	33.90
0.1%	(111)	(111)	4.20	4.18	55.93	57.09	32.88	33.22
0.5%	(111)	(111)	5.46	5.00	33.44	39.97	25.43	27.80
1.0%	(111)	(111)	4.14	4.25	59.15	55.36	33.82	32.72

6.2.2 FTIR Study

FTIR plot of ZnS and ZnS doped with Cu^{2+} and Mg^{2+} at distinct doping levels(0.1%,0.5%, and 1.0%) displayed in Figures 6.2 (a,b). It indicates that all synthesized thin films exhibit the same absorption bands, with variations observed solely in the intensity of these peaks. The strong, broad absorption peak observed around 3430 cm^{-1} is attributed to the stretching vibration of O-H bonds originating from water molecules incorporated within the ZnS lattice. Another major absorption band observed at 465, 602, and 667 cm^{-1}, which indicates the stretching vibrations of

ZnS[261], [262]. At 1403 and 1565 cm^{-1}, absorption peaks show that the asymmetric stretching vibrations of C=O[263]. A minor absorption peak at 938 cm belongs to the C-H bond. Also, another minor absorption peak is 1013 and 1109 cm^{-1}, suggesting the occurrence of resonant coupling among the vibrational modes of the sulfide ions within the crystal lattice[264]. It verified the existence of the Zn-S bond in all the prepared samples. While magnesium and copper doping on the ZnS thin film did not lead to the appearance of significant new peaks, minor shifts and alterations in the intensity of the Zn–S stretching vibrations were observed. It confirms the addition of dopants without disrupting the basic ZnS lattice.
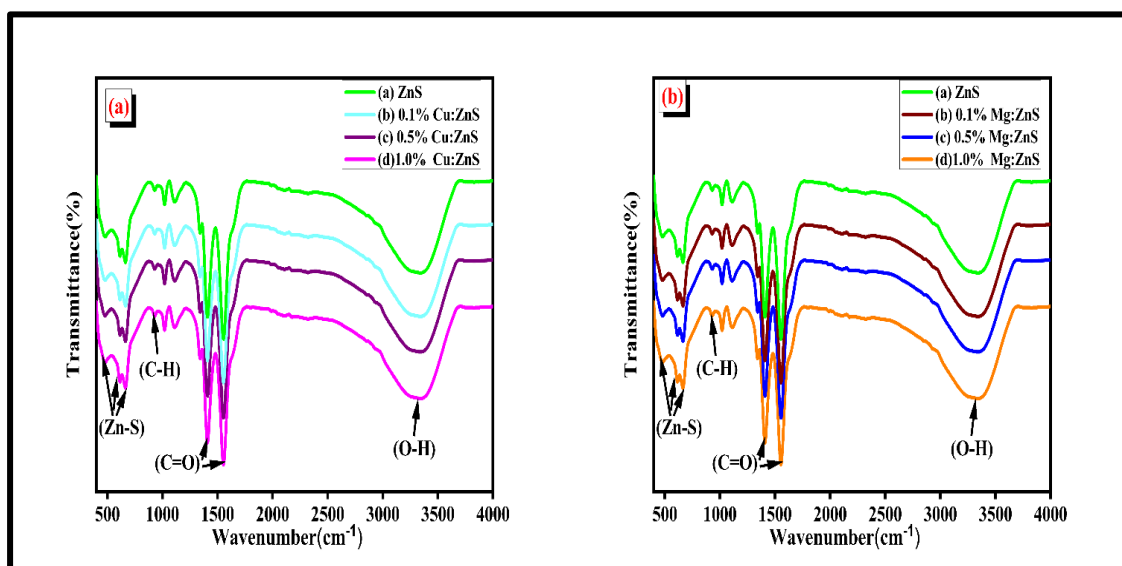
Fig.6.2 (a, b) FTIR spectra for ZnS, ZnS doped with Cu^{2+} and Mg^{2+} thin films at various concentrations.

6.2.3 FESM analysis

Thin film morphology of surface, thickness, and particle size was analyzed with the use of an FE-SEM instrument. Figure6. 3 (a,b,c) depicts the micrographs of ZnS, Cu, and Mg-doped ZnS thin films. These micrographs were captured at a magnification of 45,000 times, revealing particle details within a 100nm size range. All the films were formed by sol sol-gel spin coating approach and post-heated at 500 °C for five hours. Observation revealed that all the thin films were uniformly deposited on the glass substrate, exhibiting a crack-free surface and a homogeneous distribution of material.

In the ZnS, grains are closely arranged with very few voids, suggesting the formation of a dense and compact layer, and very small agglomerations occur[265]. After the introduction of Mg doping, agglomeration reduces, and more rounded and fine grains are formed compared to ZnS, and the particle size also rises. Further incorporation of copper doping, there in no agglomeration, and grains are densely packed, and particle size rises. Therefore, the introduction of Magnesium and Copper dopants alters the surface morphology of ZnS thin films, affecting grain size, shape, and packing density compared to the host. This variation in morphology can have significant implications for the optical and electrical characteristics of the materials.
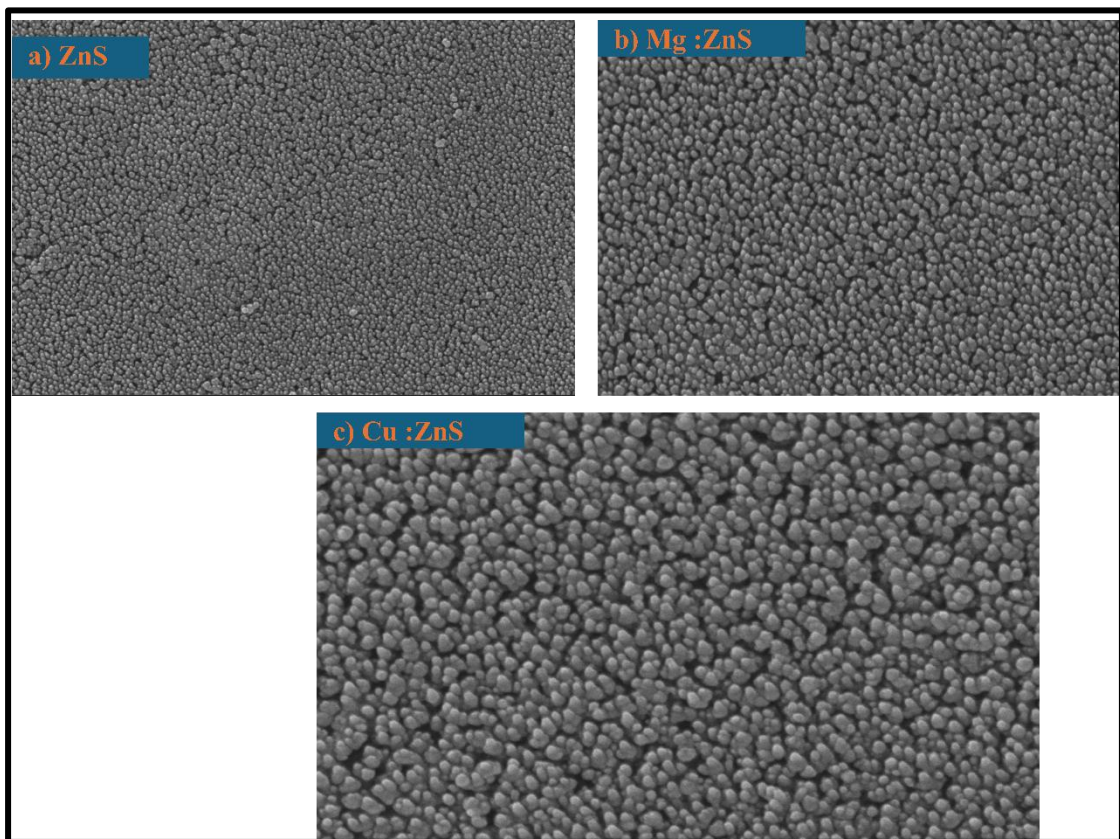
Fig.6.3(a, b, c) FE-SEM for ZnS, ZnS doped with Cu^{2+} and Mg^{2+} thin films.

6.2.3.1 Thickness Analysis

Thin film thickness is another essential factor that contributes to transparent conducting material's electrical and optical properties. It is due to the thin film's dimensions at the nanoscale that directly influence how electrons move through the material (influencing conductivity) and how light interacts with it (determining transparency and other optical

characteristics). Figure 6.4 illustrates the thickness micrographs of ZnS, Cu^{2+} doped ZnS, and Mg^{2+} doped ZnS thin films. These thin films underwent a post-heating process at 500°C for five hours. These micrographs were captured using an FE-SEM instrument at a 45000 magnification, focusing on particles within the 100 nm size range. The thickness of the ZnS film was found to be 165 nm. For the ZnS doped with Cu^{2+}, the measured thickness was 190nm, and the Mg^{2+} doped ZnS film exhibited a thickness of 200nm. Its value enhances with the dopants. It aligns with earlier studies[266].
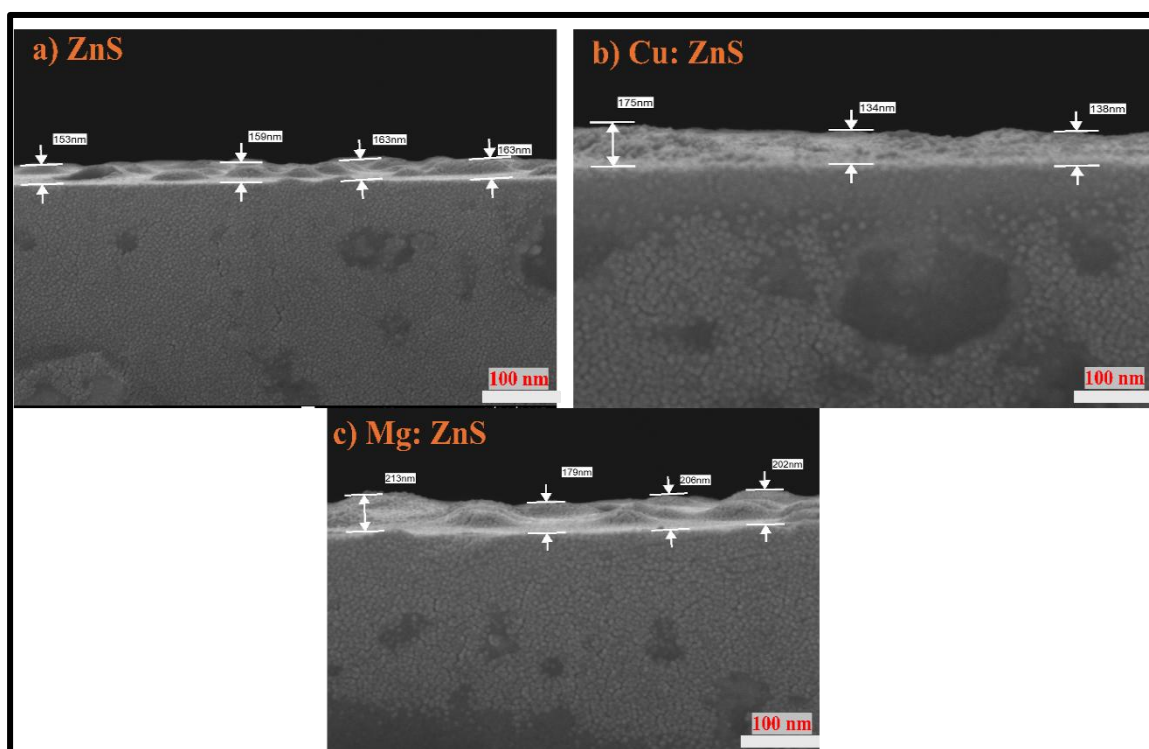
Fig.6.4. Thin film thickness micrographs of (a) ZnS, (b) Cu: ZnS, and (c) Mg: ZnS thin film.

6.2.3.2 EDX and Mapping

An EDX study using the FE-SEM instrument verifies the existence of elements in the synthesized material. The elemental composition of the prepared ZnS and ZnS doped with Cu^{2+} and Mg^{2+} thin films that were formed using the sol-gel spin coating approach and post-heated at 500°C for five hours is displayed in Figure 6. 5 (a, b, c). Analyses verify the existence of Zinc (Zn), sulfur (S), copper (Cu^{2+}), and magnesium (Mg^{2+}) and quantify their atomic and weight percentages. It also presents the atomic and weight

percentage of all the elements. These findings demonstrate that the dopants (Cu^{2+} and Mg^{2+}) were properly incorporated into the ZnS structure. It depicts that no additional elements were detected. EDX mapping shows how evenly the elements are distributed. Specifically, Figures 6.5(d) and 6.5(e) show a consistent dispersion of zinc (Zn) and sulfur (S) throughout the surface of the thin film. Furthermore, Figures 6.5(f) and 6.5(g) provide evidence of the effective homogeneous addition of dopants (Cu^{2+} and Mg^{2+}) within the ZnS structure.
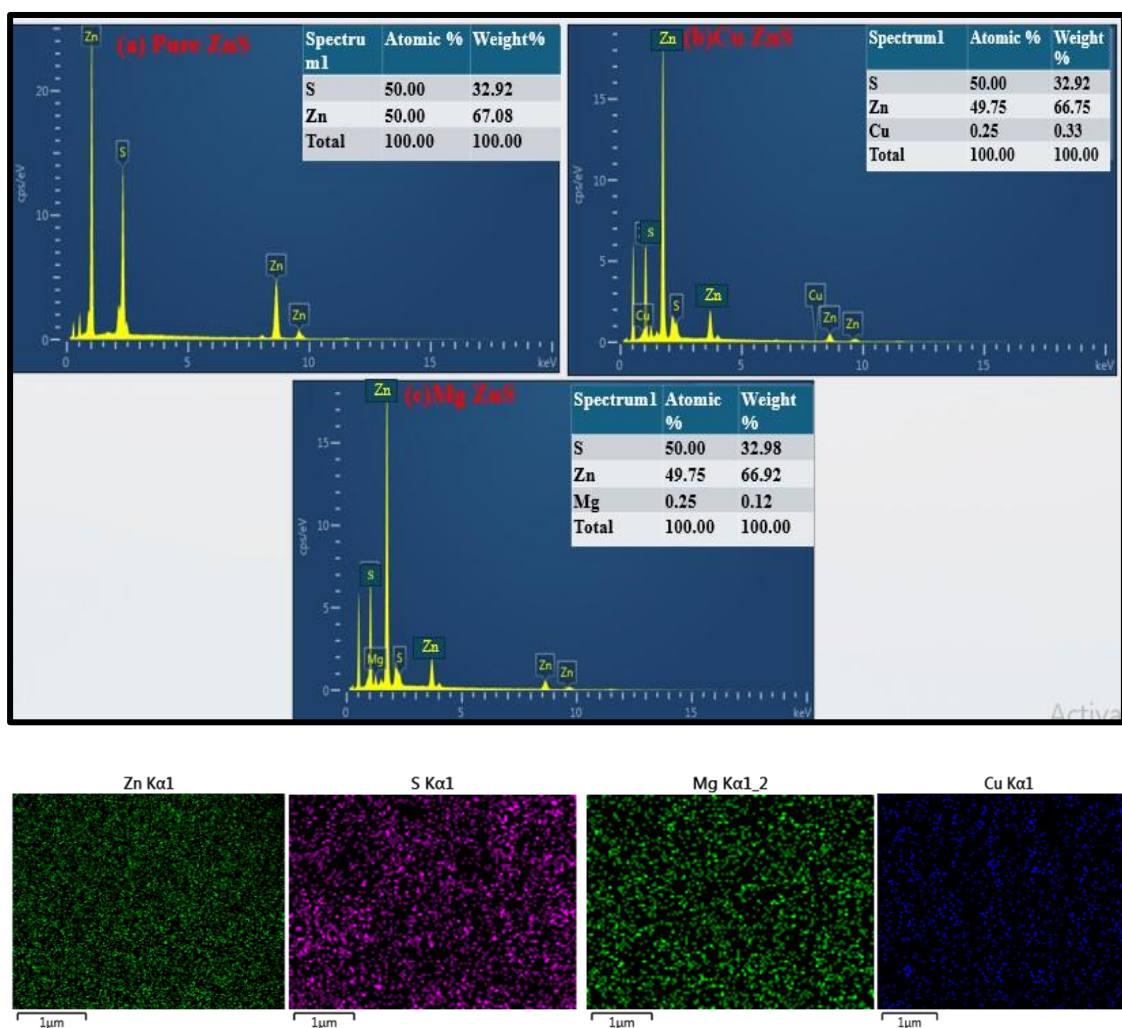
Fig.6.5. EDAX plot of (a) ZnS, (b) 0.5%Cu: ZnS thin films, (c) 0.5% Mg: ZnS thin film, (d,e,f,g) Mapping of pure ZnS (Zn, S) and Mg and Cu dopants.

6.2.4 Atomic Force Microscopy study

The Atomic force microscopy study was performed to thoroughly investigate the surface texture and roughness of the thin films deposited on the glass substrate. The

roughness of the Surface influences light scattering and serves as an indicator of surface quality, providing important insights into the growth morphology. This characteristic is crucial for materials that need to be both transparent and conductive. In this research, the roughness micrograph at 2D and 3D views. The surface topography of prepared thin films of ZnS, ZnS doped with Mg^{2+} and Cu^{2+} thin films at 2D and 3D micrographs is shown in Figure 6.6 (a, b, c, d, e, f). All the thin films exhibit a uniform, densely packed structure devoid of pinholes, implying a narrow grain size distribution and a crystalline nature due to their even dispersion. It appears compact and well-adhered to the substrate, with no visible cracks. Furthermore, the images illustrate the influence of doping on the surface morphology of the ZnS.
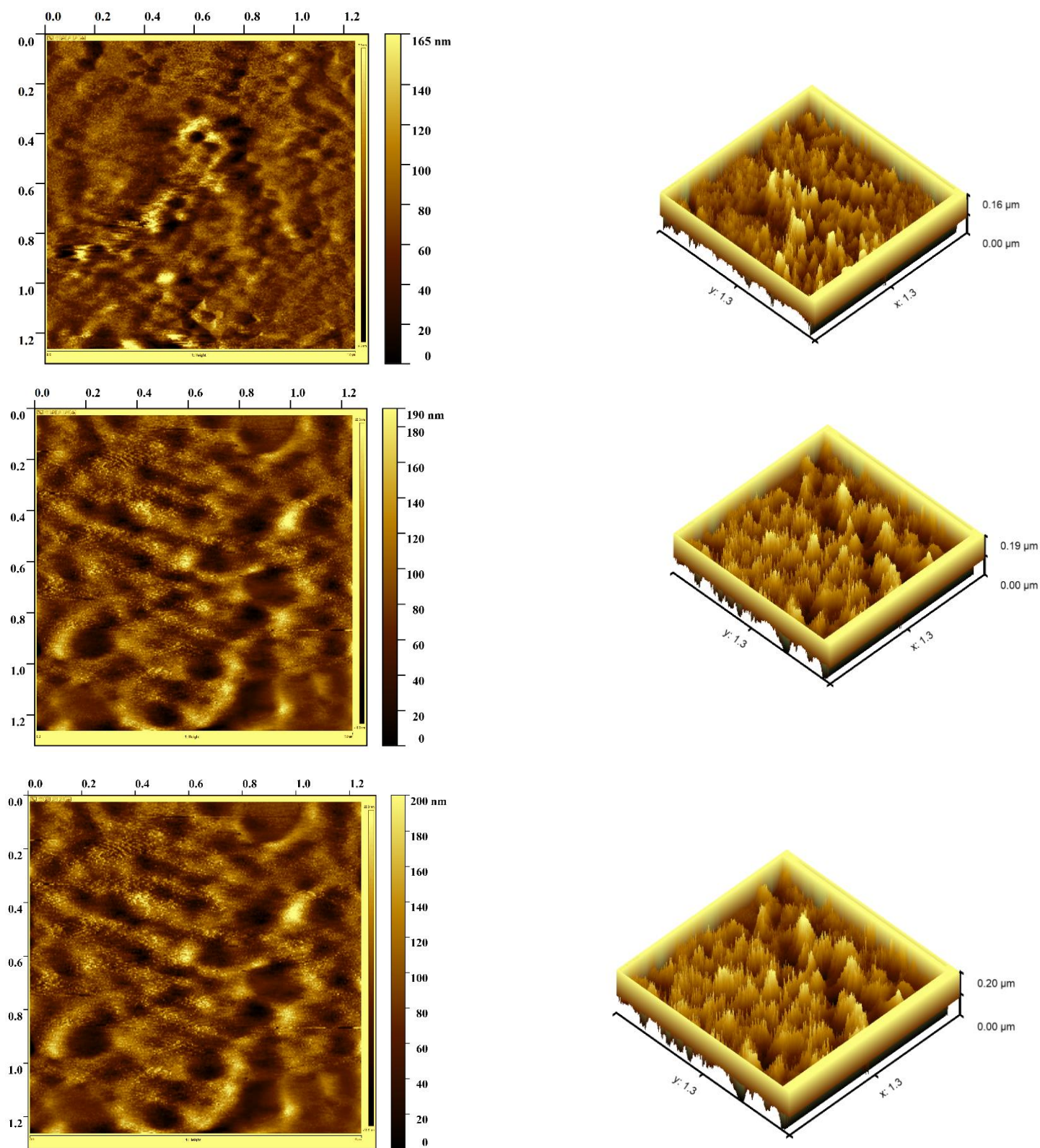
Fig.6.6. Surface topography of (a,b) ZnS in 2D and 3D view, (b)0.5% Mg: ZnS thin films in 2D and 3D view, (c)0.5%Cu: ZnS thin film in 2D and 3D view.

Average roughness (Ra) and root mean square roughness (RMS) values were determined using a mathematical formula. Further, the images are analyzed with Gwydion software. Table 6.2. depicts the average roughness (Ra) and root mean square roughness (RMS) of ZnS, ZnS doped with 0.5% of $Mg^{2+,}$ and Cu^{2+}. The analyses revealed that the incorporation of these dopants (0.5% of Mg^{2+} and Cu^{2+}) resulted in a reduction of the average roughness from 2.80 nm to 1.43 nm and root mean square roughness from 4.73 nm to 3.38nm. It occurs because of the improved crystal structure and grain morphology resulting from the doping process. Copper ions (Cu^{2+}) have an ionic radius very close to that of zinc ions (Zn^{2+}), which allows Cu to substitute Zn in the ZnS lattice with minimal distortion. This substitution leads to more uniform grain growth and enhanced crystallinity, producing smoother film surfaces with lower average and root mean square roughness values. Magnesium doping also influences the grain size, often resulting in smaller and more compact grains that reduce surface irregularities. However, it may introduce some lattice strain due to a difference in ionic size. This results in a smoother surface and improves thin film homogeneity when adding Mg^{2+} and Cu^{2+} dopants. A smooth surface is essential for the optimal performance of optoelectronic devices, such as solar cells, transparent conducting materials, and LEDs, making this improvement highly beneficial.

Table6.2. It represents surface topography parameters of ZnS, ZnS doped with Cu, and Mg thin films.

S. No	Prepared Samples	Average roughness (Ra) (nm)	Root mean square roughness (RMS)(nm)
1.	ZnS	2.80	4.73
2.	Mg: ZnS	2.54	4.10
3.	Cu: ZnS	1.43	3.38

6.2.5 Optical study

An optical study is essential for transparent conducting materials. A UV-Visible spectroscopy instrument was employed to determine the optical characteristics of ZnS thin films, both undoped and with varying doping concentrations (0.1%, 0.5%, and 1.0%) of Cu^{2+} and Mg^{2+}. A glass substrate was used for the formation of thin films. Transparency, or the ability to transmit light, is a fundamental requirement for transparent conducting materials. This property depends upon the various factors such as thickness, material composition, morphology, and roughness of the surface, annealing temperature, band gap, etc. A key attribute of transparent conducting materials, essential for their utility in optical and electronic applications, is high transmission, often indicative of the film's crystalline quality and uniformity, and smoothness in morphology. Figure 6.7 (a) illustrates the visible spectra transmission spectrum for ZnS, which is doped with Cu^{2+} thin films (0.1%,0.5%, and 1.0% doping concentrations). It was observed that ZnS thin film shows an average transmission of 95% in the visible range. With the addition of Cu^{2+} ions into the ZnS lattice, a noticeable enhancement in optical transmittance is observed. In particular, the thin film doped with 0.1% Cu^{2+} shows a transmittance of 97.09%, and at 0.5% doping, it rises to 98.80%. At 1.0% Cu^{2+}, the transmittance was reduced to 97.2%, although more than that of the host thin film. This enhancement in optical transmittance can be attributed to the role of Cu^{2+} ions in reducing intrinsic defects within the ZnS lattice, such as sulfur vacancies or zinc interstitials, which typically act as scattering centers and impede light transmission. Additionally, Cu^{2+} doping may improve the crystallinity of the thin films, resulting in fewer grain boundaries and less light scattering. The modification of the electronic structure by Cu^{2+} ions can also reduce sub-bandgap absorption, further increasing transparency.XRD and AFM analyses confirmed that the improved crystallinity and surface quality were also factors in this enhancement. According to Biswajit Barman et al.[107],doping ZnS with copper leads to a decrease in transmission from 85% to 50%. Compared to the previous study, the transmission results showed an improvement[267], [268]. As compared to other concentrations, 0.5% doping depicts the best transmission, indicating its superior suitability for transparent conducting material applications.

Overall, controlled Cu^{2+} doping enhances the optical quality of ZnS thin films, making them more suitable for optoelectronic and photovoltaic applications.

The visible light transmission spectra of ZnS thin films doped with Mg^{2+} ions at varying concentrations of 0.1%, 0.5%, and 1.0% are shown in Figure 6.7 (b). The pure ZnS film demonstrates a high average optical transmission of approximately 95% across the visible spectrum. When Mg^{2+} ions are introduced as dopants into the ZnS matrix, the optical transmission properties improve notably. This quick rise in transmission is indicative of well-formed crystalline grains. Specifically, ZnS films doped with 0.1% Mg^{2+} exhibit an increased average transmission of 96.43%, while those with 0.5% Mg^{2+} doping show a slightly higher transmission of 96.63%. However, at a higher doping concentration of 1.0% Mg^{2+}, the transmission slightly decreases to 95.64%, though it remains comparable to pure ZnS. It indicates that low to moderate Mg^{2+} doping enhances the transparency of ZnS thin films in the visible region, likely due to modifications in the thin film's microstructure or electronic band structure that reduce light scattering or absorption. The slight reduction at the highest doping level may be attributed to increased defect states or scattering centers introduced by excessive dopant incorporation. The improvement in transmission was also attributed to the improved crystallinity and surface quality, as verified by XRD and AFM studies. Existing research demonstrates a consistent pattern[71]. Overall, Mg^{2+} doping in ZnS thin films effectively tunes the optical transmission, with optimal improvement observed around 0.5% doping concentration.
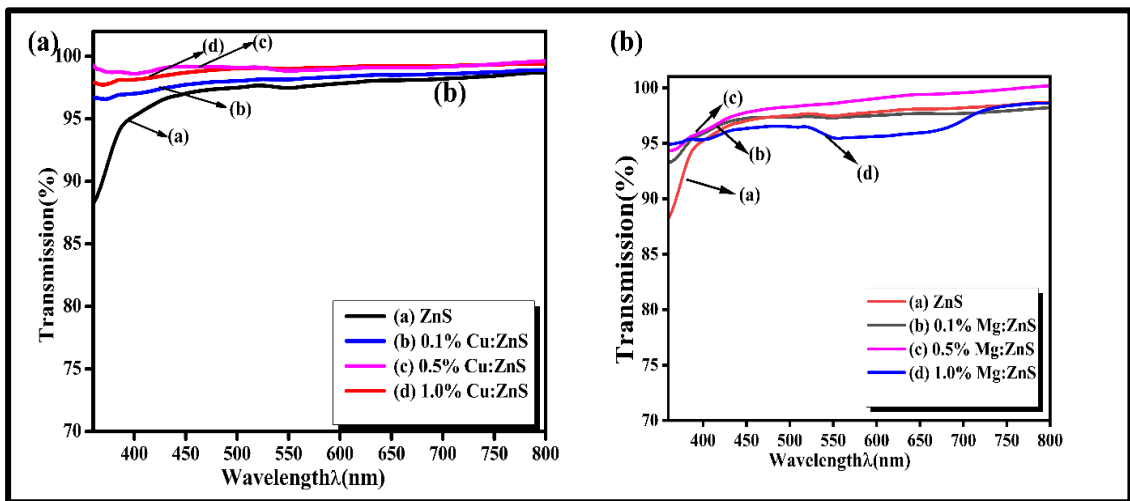
Fig.6.7(a, b) Transmission plot for ZnS and doped with Cu^{2+} and Mg^{2+} thin films at distinct doping levels.

When ultraviolet (UV) light interacts with the thin film, it may undergo absorption, reflection, or transmission. Figure 6.8(a) indicates the absorbance spectra of ZnS and ZnS doped with Cu^{2+} at 0.1%,0.5%, and 1.0% doping concentrations. ZnS shows maximum absorbance at 357nm in the UV region (300-400nm). With the introduction of 0.1% to 1.0% Cu^{2+} dopant on the ZnS host, the absorbance of the material reduces. A similar trend occurs in the previous study [269]. Furthermore, a slight shift in the absorbance spectrum towards shorter wavelengths is observed, a phenomenon known as a blue shift. This phenomenon could be attributed to quantum confinement effects arising from the size of the nanocrystals[270]. Consequently, the ZnS thin film doped with Cu^{2+} demonstrates the least absorption and the greatest transmission of light in the visible range. Figure 6.8 (b) shows the spectra of absorbance for ZnS host and ZnS doped with Mg^{2+} at distinct concentrations (0.1%,0.5%, and 1.0%). It demonstrates that ZnS exhibits the highest absorbance at 357nm in the UV range and the lowest transmission. A slight reduction in the material's absorbance is observed after the introduction of 0.1%,0.5%, and 1.0% of Mg^{2+}. It also indicated the minute shift in the absorbance spectrum towards lower wavelengths.
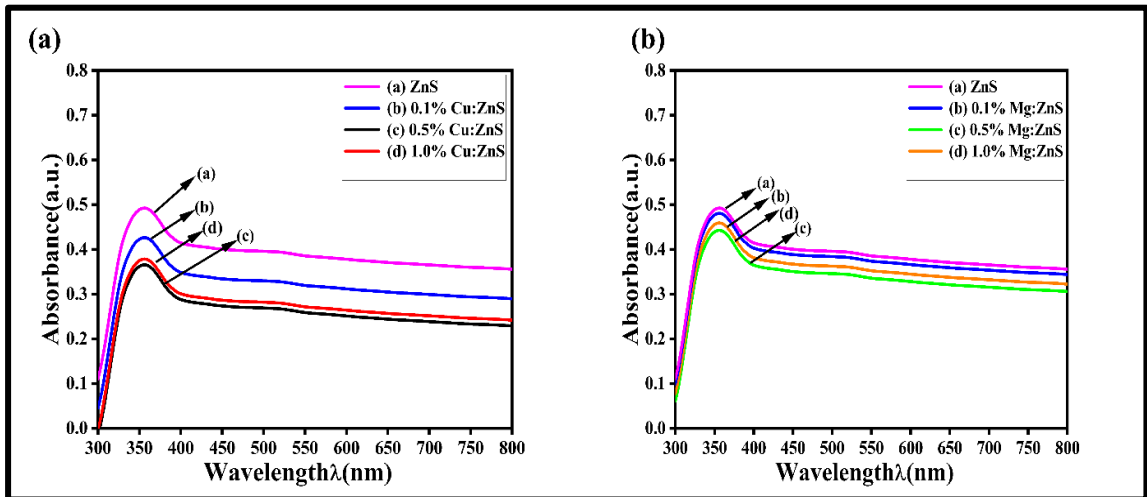
Fig.6.8(a, b) Absorption spectra for ZnS and doped with Cu^{2+} and Mg^{2+} thin films at distinct doping levels.

The extinction coefficient (k) quantifies light loss per unit volume due to scattering and absorption, and it can be calculated using equation (5). It's related to the absorption coefficient (α) and wavelength (λ). Figures 6.9(a) and 6.9 (b) show the extinction coefficient spectra for ZnS and ZnS doped with varying concentrations of Cu^{2+} and Mg^{2+}, respectively. In Cu^{2+}-doped ZnS (Fig. 9a), increasing Cu^{2+} concentration leads to a blue shift (peak shift to shorter wavelengths) and a reduction in both k and absorbance. This reduction is attributed to increased carrier concentration and reduced surface roughness. Similarly, in Mg^{2+}-doped ZnS (Fig.6.9b), Mg doping reduces the extinction coefficient and causes a blue shift, like the effect on absorbance, with pure ZnS exhibiting the highest K. It is a function of the light's wavelength and the film's material properties[208].
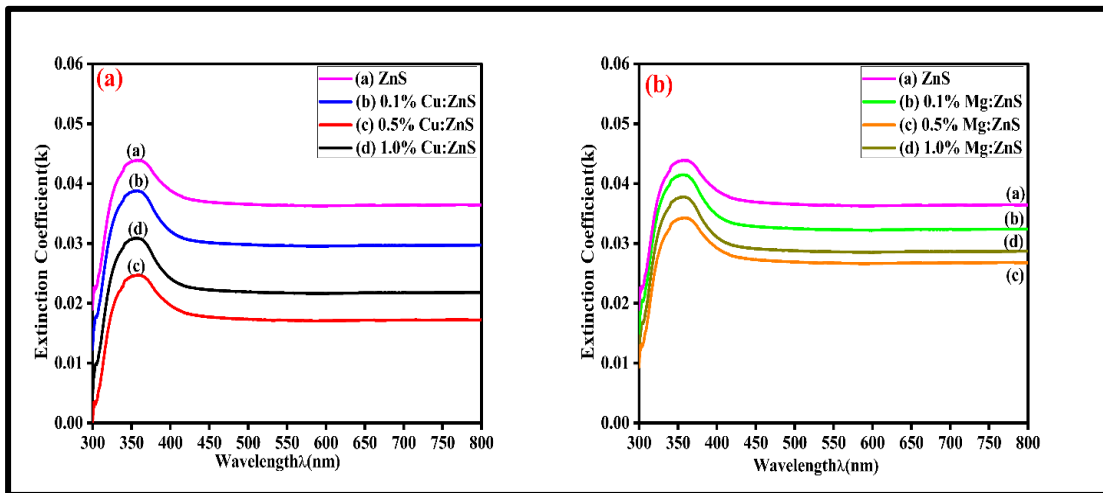
Fig.6.9. (a, b) Extinction coefficient plot for ZnS, doped with Cu^{2+} and Mg^{2+} at various concentrations.

Utilizing the Tauc method[271] on the absorption data for the determination of the direct band gap of the ZnS films and ZnS doped with Mg^{2+} and Cu^{2+} (0.1%,0.5%, and 1.0%(doping levels). Equation (5.8) indicates the mathematical tool for the determination of the optical band gap. The optical band gap values for Zinc Sulfide (ZnS) thin films and those doped with Cu^{2+} at different concentrations are illustrated in Figure 6.10 (a). The Zinc Sulfide (ZnS) thin film exhibits a band gap of 3.64 eV, classifying it as a wide band gap semiconductor. Its determined value is consistent with findings in the literature study[268]. Introducing Copper at a 0.1% concentration leads

144

to a minor decrease in the band gap to 3.62 eV. Increasing the Copper concentration further to 0.5% results in a more substantial reduction of the band gap to 3.57 eV. However, when the Copper concentration is raised to 1.0%, the band gap increases to 3.61 eV, which is slightly higher than the 0.5% doped sample but still lower than the 3.64 eV of pure ZnS. Overall, copper doping reduces the band gap. This reduction occurs because the interaction between Copper's 3d orbitals and Sulfur's 3p orbitals (in the ZnS valence band) elevates the valence band maximum and creates localized energy states within the band gap. The observed decrease in the band gap due to Copper doping aligns with findings from earlier studies[65], [107]. Figure 6.10 (b) also depicts the band gap value of ZnS and Mg^{2+} doped ZnS thin film at distinct doping levels. The Zinc Sulfide (ZnS) thin film exhibited a band gap of 3.64 eV. The introduction of Magnesium doping altered this value. At a low doping concentration of 0.1%, the band gap decreased to 3.60 eV. Increasing the Magnesium concentration to 0.5% resulted in a further reduction of the band gap to 3.59 eV. However, at a high doping concentration of 1.0%, the band gap increased to 3.61 eV, a value still lower than that of ZnS. Overall, it was observed that the Mg^{2+} introduced into the ZnS films reduced the band gap value. This might improve their electronic performance. This happens because the incorporation of magnesium dopants influences the electronic and optical characteristics. Furthermore, the decrease in the energy gap towards lower values could be linked to a lower concentration of defects and localized energy states, alongside an increase in the size of the crystallites[64].The observed reduction in the band gap correlated with the previous research[69], [85]. This combined evidence underscores the potential for engineering specific optical properties in ZnS films by controlled doping techniques, which could benefit applications in electronic and optoelectronic devices.
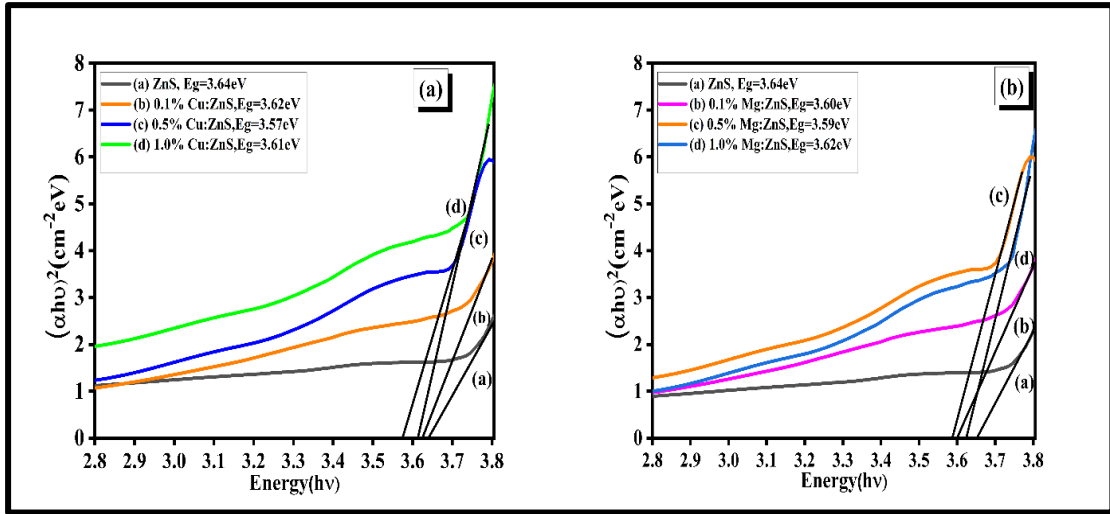
Fig.6.10. (a,b) Band gap plot for pure ZnS, Mg: ZnS, and Cu: ZnS thin films at various concentrations.

The refractive index is a significant parameter in device design, particularly for integrated optics and optoelectronic devices. Furthermore, the lowest energy band gap is a crucial factor in semiconductor physics, influencing the refractive index alongside other variables[272]. It is also a necessary factor in the transparent conducting field. It is determined with the use of reflectance data[273]. Equations (5.8) and (5.9) describe the mathematical formula for the refractive index value[82]. Figure (6.11a) depicts the refractive index of ZnS and ZnS doped with Cu^{2+}(0.1%,0.5%, and 1.0% doping levels) as a function of wavelength. It is observed that the refractive index reduces rapidly in the ultraviolet region (200–400 nm) and further becomes flat in the visible spectrum. This indicates that all samples show the normal dispersion behaviour of the material [274]. An observation was made that enhancing Cu^{2+} doping leads to enhanced transmission, whereas the refractive index, reflectance, and absorbance diminish. This inverse correlation is likely due to forming a more homogeneous film with reduced surface irregularities, resulting in greater transparency and lower polarization. The determined values for all analysed samples are compiled in Table 6.3.

Figure 6.11(b) shows the refractive index of ZnS and ZnS doped with Mg^{2+} thin films at doping levels of 0.1%, 0.5%, and 1.0%. As mentioned earlier, transmission and refractive index have an inverse relationship. ZnS has a high refractive index. However, when the concentration of Mg^{2+} dopant increases, the refractive index goes down,

146

which aligns with the earlier finding of increased transmission. This decrease in refractive index is likely due to less polarizability, reduced optical surface dispersion, and lower optical losses. These changes could be a result of a smoother film surface and a higher number of charge carriers within the material. All the determined values are summarized in the Table6.3.
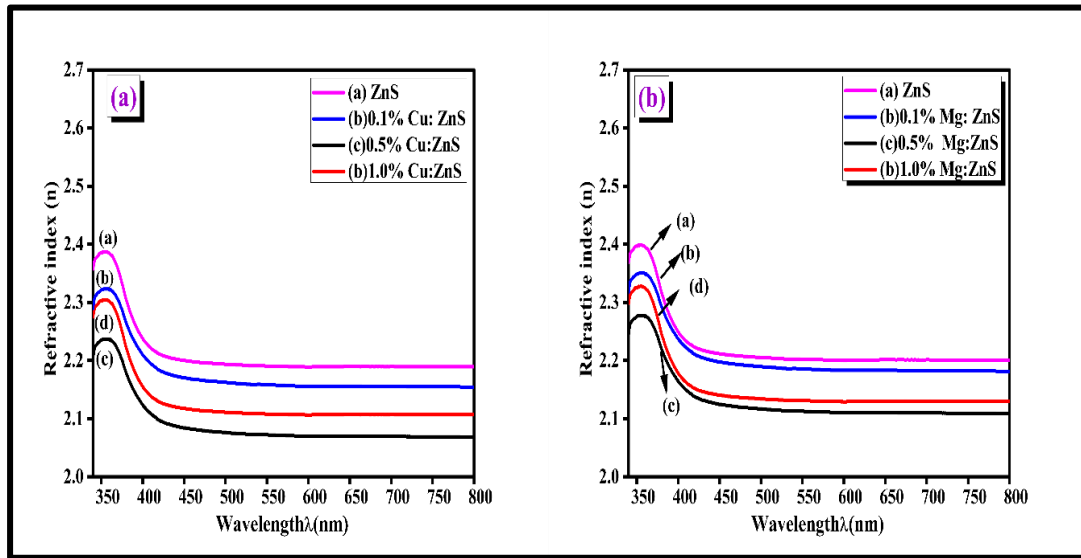
Fig.6.11. (a, b) Refractive index plot for ZnS, ZnS doped with Cu^{2+} and Mg^{2+} at various concentrations.

Table6.3. Optical characteristics of ZnS and ZnS doped with Cu^{2+} and Mg^{2+} thin films.

Samples	Transmission (%)		Band gap (eV)		Refractive index in the visible region	
	Cu: ZnS	Mg:ZnS	Cu: ZnS	Mg: ZnS	Cu:ZnS	Mg:ZnS
ZnS	95	83	3.64	3.64	2.23	2.23
0.1%	97	96.4	3.62	3.60	2.20	2.22
0.5%	98.7	96.6	3.57	3.59	2.12	2.15
1.0%	97.3	95.6	3.61	3.62	2.15	2.16

6.2.6. Electrical Analysis

Figures 6.12(a) and 6.12(b) illustrate the current-voltage (I-V) characteristics of ZnS and ZnS thin films doped with Cu^{2+} and Mg^{2+}.0.1%, 0.5%, and 1.0% are the doping levels. These measurements were conducted at room temperature using a two-probe

setup with applied voltages spanning 0 to 50V. The current voltage (I-V) curves are straight lines, which means the current increases steadily with voltage. This straight-line relationship shows that all the films follow Ohm's law (V = I/R), indicating good electrical contact. The electrical conductivity of the films can be found from the slope of the line in these plots.
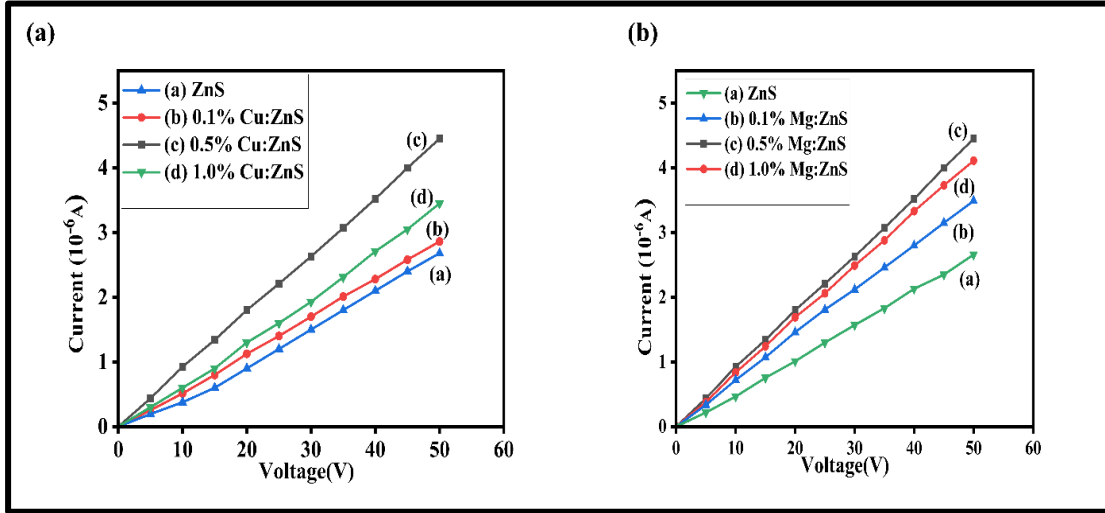
Fig.6.12. (a,b) Current-Voltage plot for ZnS and doped with Cu^{2+} and Mg^{2+} thin films at various concentrations.

6.2.6.1 Hall measurements

Examining the Hall measurement utilizing the van der Pau method at room temperature in ZnS and ZnS doped with Mg^{2+} and Cu^{2+} thin films is essential for determining the mobility, carrier nature, carrier concentration, and conductivity. ZnS is an II–VI semiconductor where electrical conductivity is primarily governed by the concentration of intrinsic defects (like sulfur vacancies, V_S) and how easily charge carriers can move (mobility). The measured value of conductivity, mobility, and carrier concentration of ZnS and ZnS doped with Cu^{2+} at doping levels of 0.1%,0.5%, and 1.0% are depicted in Figure 6.13. ZnS thin film depicts a conductivity of 5.29 $\times 10^2$ (Scm^{-1}), carrier concentration is 0.36$\times$ 10^{18} cm$^{-3,}$ and mobility is 79 cm²/V·s, revealing its n-type semiconducting behaviour. It was observed that doping of Cu^{2+}(0.1%,0.5%, and 1.0%) influenced the conductivity, carrier concentration, and mobility of the host material. When 0.1% of Cu^{2+} is added to the ZnS host, Cu^{2+} ions substitute for Zn^{2+} in the ZnS lattice, introducing additional charge carriers and leading to a notable rise in the value

of carrier concentration 1.59×10^{18} cm^{-3}. Furthermore, this replacement caused minor structural distortions and created new scattering points, resulting in a slight reduction in carrier mobility to 67 cm²/V·s. The conductivity values rise to 5.29×10^2 Scm^{-1} with the rise of carrier concentration. With a Copper (Cu) doping level of 0.5%, the carrier concentration peaked at 1.59×10^{18} cm^{-3}, resulting in the highest conductivity observed at 7.85×10^2 Scm^{-1}, even though the mobility further decreased to 49 cm²/V·s. This occurs because the significant rise in the number of charge carriers has a more dominant effect on conductivity than the decrease in their mobility because of increased defects and scattering at grain boundaries. Grain boundaries are crucial in semiconducting materials and are utilized to enhance their electrical properties[109]. Finally, at 1.0% Cu^{2+}, the carrier concentration value again reduces to 2.99×10^{18} cm^{-3} and the mobility value rises to 70 cm²/V·s. Carrier concentration drops as some carriers are trapped or compensated. However, mobility rises, possibly due to partial reordering of the lattice or reduction in certain types of scattering. The conductivity value also reduces to 5.29×10^2 Scm^{-1} due to the decline of the carrier concentration. There was a similar pattern in another investigation[107], [275]. All the prepared films exhibited n-type semiconducting behavior. Consequently, the Zinc Sulfide (ZnS) film doped with 0.5% Cu^{2+} displayed the highest conductivity among all synthesized samples. This characteristic makes it a promising material for optoelectronic applications, including transparent conducting materials.
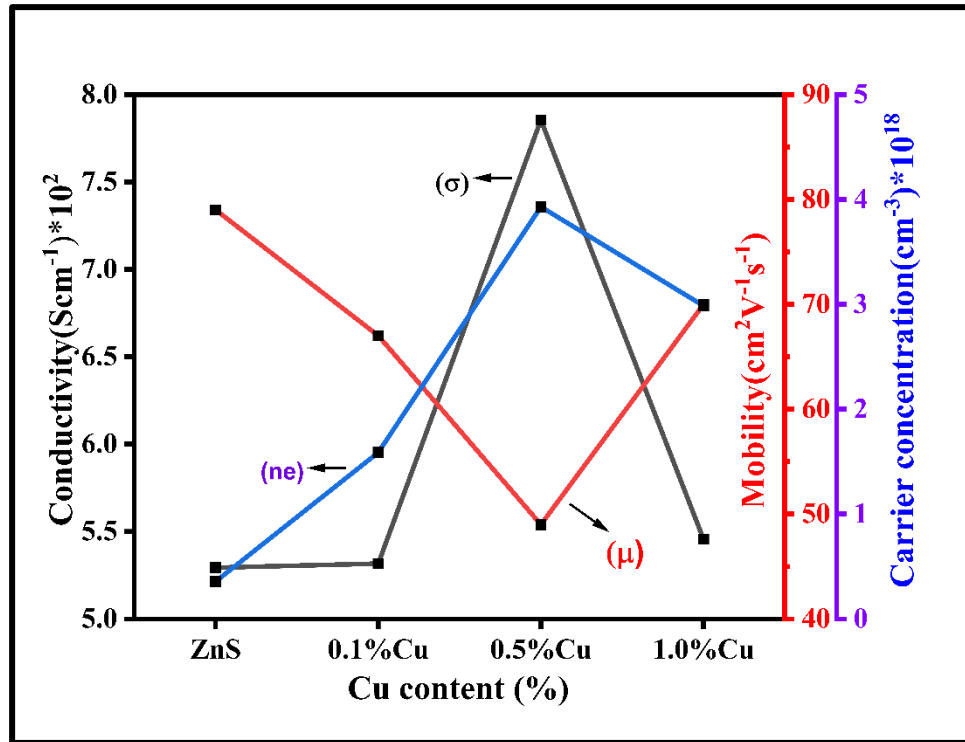
Fig.6.13. Conductivity, mobility, and carrier concentration plot for ZnS and ZnS doped with Cu^{2+} thin films at various concentrations.

The conductivity, carrier type, mobility, and carrier concentration were quantified for both ZnS and ZnS samples incorporating Magnesium ions at doping concentrations of 0.1%, 0.5%, and 1.0% are shown in Figure 6.14. ZnS thin film depicts a conductivity of 5.29×10^2 Scm^{-1}, carrier concentration is 0.36×10^{18} cm^{-3}, and mobility is 79 cm²/V·s, revealing its n-type semiconducting behaviour. Introducing Magnesium ions (Mg^{2+}), which possess a size comparable to Zinc ions (Zn^{2+}), into the ZnS lattice generally results in Magnesium replacing Zinc atoms, thereby modifying the material's defect characteristics and its electronic arrangement. At 0.1% Mg doping, Mg^{2+} ions substitute Zn^{2+} in the lattice without adding extra charge but promote the formation of sulfur vacancies, which act as shallow donors and increase carrier concentration to 1.40×10^{18} cm³. Consequently, the increased number of impurity atoms introduces scattering points, causing a slight reduction in carrier mobility to 62 cm²/V. The resulting conductivity of 5.64×10^2 Scm^{-1} is a consequence of the interplay between the reduced mobility and the enhanced carrier concentration. When the Magnesium (Mg^{2+}) doping level reaches 0.5%, the number of donor-type imperfections in the material peaks,

leading to the maximum carrier concentration of 3.22×10^{18} cm^{-3}. While the mobility of these carriers experiences a further decline to 62 cm²/V due to increased disorder in the crystal lattice and scattering from impurity atoms, the substantial carrier concentration at this specific doping level results in the highest measured conductivity of 6.23×10^2 Scm^{-1}. At 1.0% of Mg^{2+} doping, defect compensation (possibly via neutral Mg complexes or donor saturation) reduces carrier concentration up to 3.22×10^{18} cm^{-3}. Although mobility partially recovers, 58 cm²/V might be because of better crystallinity or less grain boundary scattering, the carrier concentration drop dominates, causing a decline in the conductivity value of 5.52×10^2 Scm^{-1}. All the synthesized films exhibited n-type semiconducting characteristics. Consequently, the Zinc Sulfide (ZnS) thin film doped by 0.5% Mg^{2+} demonstrated the highest electrical conductivity among all the prepared samples. These findings suggest the potential suitability of this material for applications requiring transparent conducting properties. A similar trend occurred in another research study [64], [276]. The measured values of ZnS, ZnS doped with Cu$^{2+,}$ and Mg^{2+} across all doping concentrations are summarized in tables6.4, revealing their conductive properties.
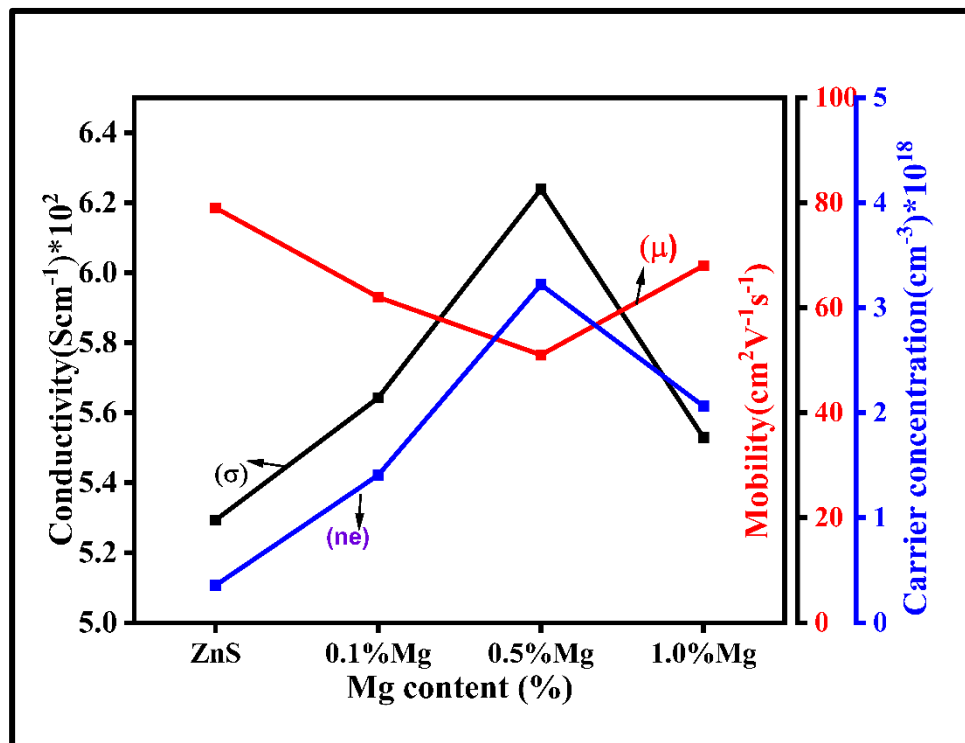
Fig.6.14. Conductivity, mobility, and carrier concentration plot for ZnS and ZnS doped with Mg^{2+} thin films at various concentrations.

Table 6.4. Electrical characteristics of ZnS and ZnS doped with Cu^{2+} and Mg^{2+} at distinct concentrations.

Material	Carrier concentration(cm^{-3}) $\times 10^{18}$		Conductivity (Scm^{-1}) $\times 10^2$		Mobility(cm^{2}V^{-1}s^{-1})		Type of carrier	
	Cu:ZnS	Mg:ZnS	Cu:ZnS	Mg:ZnS	Cu:ZnS	Mg:ZnS	Cu:ZnS	Mg:ZnS
ZnS	0.36	0.36	5.29	5.29	79	79	n	n
0.1%	1.59	1.40	5.31	5.64	67	62	n	n
0.5%	3.93	3.22	7.85	6.23	49	51	n	n
1.0%	2.99	2.06	5.45	5.52	70	68	n	n

6.2.6.2. Activation energy analysis

Regarding the electrical characteristics of the material, activation energy represents the minimum energy required for charge carriers (such as electrons or holes) to overcome an energy barrier and contribute to electrical current within a material. It is related to the thermal temperature and conductivity. The relation between electrical conductivity ($\sigma_{D.C.}$) changes with temperature, explained with the use of an Arrhenius-type equation[277](6.1).

$$\sigma = \sigma_1 \ \exp\left(\frac{-Ea_1}{kT}\right) \qquad (6.1)$$

σ_1 and Ea_1 represent the Conductivity and activation energy. To analyze the temperature dependence of conductivity, a graph plotting the logarithm of conductivity ($\sigma_{D.C.}$) against the reciprocal of temperature (1000/T, in Kelvin) is necessary. Figure 6.15 indicates the graphs of the logarithm of ($\sigma_{D.C.}$) against (1000/T) for ZnS and $Cu^{2+,}$ and Mg^{2+} doped ZnS thin films (0.1%, 0.5%, and 1.0%). All the synthesized thin films exhibited a straight line in the provided plot. The slope of this line corresponds to the activation energy value. Doping Magnesium and copper influenced the host materials. ZnS shows a steeper slope with high activation energy and less conductivity. As the concentration of copper dopant increased from 0.1% to 1.0%, the slope became shallower, indicating a lower activation energy and higher electrical conductivity.0.5%

Cu doped ZnS shows a shallower slope and minimum activation because of high conductivity and carrier concentration. Another dopant, Magnesium, also influenced the ZnS lattices. Mg doping from (0.1% to 1.0%) reduces the slope, indicating a lower activation energy and easier charge carrier excitation. The introduction of Mg^{2+} dopants modifies the energy barriers and the atomic arrangement within the material, thereby promoting more efficient charge transport. 0.5% Mg-doped ZnS shows minimum activation because of high conductivity and carrier concentration. The determined activation energy values (Ea_1) for the undoped ZnS thin film and samples doped with 0.1%, 0.5%, and 1.0% of Cu^{2+} and Mg^{2+} are presented in the following table 6.5.
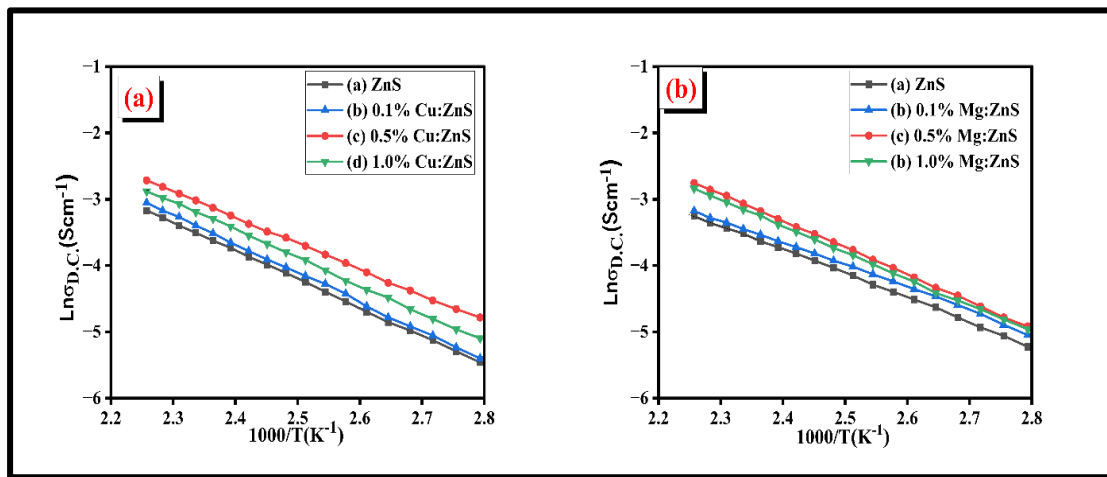
Fig.6.15(a,b) Activation energies plot for pure ZnS, Cu: ZnS, and Mg: ZnS at various concentrations, annealed at 500℃.

Table6.5. It displays the calculated activation energy value for ZnS, Cu doped ZnS, and Mg-doped ZnS.

Material	Activation energy (Ea_1)	
	Cu	Mg
ZnS	1.19	1.19
0.1%	1.02	1.15
0.5%	0.81	0.90
1.0%	0.98	0.91

6.2.6.3. Optoelectronic analysis

Transparent conducting materials are assessed utilizing a crucial parameter known as the Figure of Merit (FOM), which acts as a standard measure for evaluating their effectiveness and suitability in optoelectronic devices such as solar cells, display devices, transparent conducting oxides, photovoltaic devices, etc. FOM was evaluated with the use of sheet resistance (Rs) and transmission(T^{10}) properties. A superior Figure of Merit value indicates that the material exhibits excellent performance.The Hacke equation[182] is utilized to determine the value of the Figure of Merit (Φ_{TC}). Equation (6.2) depicts the mathematical relation.

$$\Phi_{TC} = \frac{T^{10}}{R_S} \tag{6.2}$$

Figure 6.16 illustrates the Figure of merit (Φ_{TC})for ZnS thin film and ZnS thin film doped with Mg^{2+} and Cu^{2+} at distinct doping concentrations (0.1%,0.5%, and 1.0%). The data indicate that both dopants (Cu^{2+} and Mg^{2+}) affected the conductivity and transmission properties of the ZnS films. Among all the prepared samples, 0.5% of Cu^{2+} on ZnS depicts the highest figure of merit of $1.54 \times 10^{-3}\ \Omega^1$. This indicates that the 0.5% doping level resulted in the best balance of high optical transmission and high electrical conductivity among the prepared materials. It is well applicable for optoelectronic devices such as solar cells, display devices, flat panels, transparent conducting materials, etc.
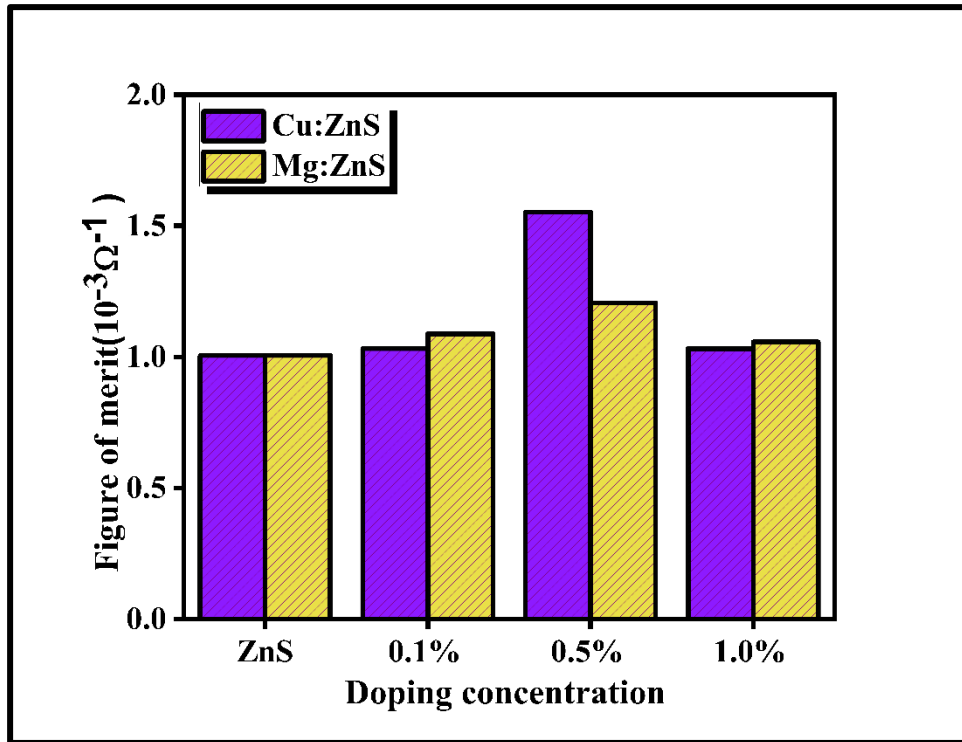
Fig.6.16. Figure of merit plot for ZnS, Cu: ZnS, and Mg: ZnS thin films at distinct concentrations.

6.3. Conclusion

1) This chapter indicates the comprehensive analysis of ZnS and Cu^{2+}/Mg^{2+}doped ZnS thin films synthesized by the sol-gel spin coating method and post-annealed at 500 °C for five hours, revealing significant improvements in structural, morphological, optical, and electrical properties due to 0.1%,0.5% and 1.0% doping concentrations.

2) X-ray diffraction (XRD) confirmed that all films retained the zinc blende structure with prominent (111), (220), and (311) planes, and no impurity phases were detected. The successful substitution of Zn^{2+} by Cu^{2+} and Mg^{2+} ions were evidenced by peak shifts and enhanced (111) diffraction intensity, indicating improved crystallinity and growth orientation.

3) FTIR analysis verified the presence of Zn–S bonds and indicated that doping did not alter the fundamental lattice structure, though slight shifts in Zn–S vibrational bands were observed. Surface morphology studied by FE-SEM showed crack-free, densely packed films, with grain size and compactness

155

improving with Cu^{2+} and Mg^{2+} incorporation. Thickness increased with doping, enhancing film uniformity.

4) Elemental analysis using EDX confirmed the homogeneous and successful incorporation of Cu^{2+} and Mg^{2+} dopants without introducing extraneous elements. AFM results demonstrated reduced surface roughness upon doping, especially at 0.5% concentration, consistent with improved grain structure and enhanced film smoothness, beneficial for optoelectronic applications such as Transparent conducting materials.

5) UV-Visible spectroscopy revealed high transparency of ZnS and Cu^{2+}/Mg^{2+} doped ZnS thin film (~95–98%) in the visible range for all films. As compared to other concentrations, 0.5% Cu^{2+} doping depicts the best transmission, indicating its superior suitability for transparent conducting material applications.

6) Doping of Mg^{2+} and Cu^{2+} significantly influenced the conductivity, carrier concentration, and mobility of the ZnS thin film. At 0.5% Cu^{2+}, the highest conductivity 7.85×10^2 Scm^{-1} is observed, driven by an optimal carrier concentration of 1.59×10^{18} cm^{-3}. Despite reduced mobility (49 cm²/V·s) due to increased grain boundary scattering, the enhanced carrier density dominates the conductivity.

7) Overall, ZnS thin films doped with 0.5% Cu^{2+} or Mg^{2+} exhibit superior electrical and optical characteristics, making them strong candidates for use in transparent conducting applications such as solar cells, display panels, flat-panel displays, and other optoelectronic devices.

Chapter 7

To synthesize Zn (O, S) and Zn (Sn, S) and study optical and electrical properties.

7.1. Introduction

Transparent conducting oxides (TCOs) thin films behave as critical components in optoelectronic devices, demanding a balance between high optical transparency and electrical conductivity. Among the most widely investigated TCO host materials are Zinc oxide (ZnO), Zinc sulfide (ZnS), and tin oxide (SnO_2), each offering distinct functional advantages and intrinsic limitations. ZnO is renowned for its high electrical conductivity of 1.01×10^4 Scm^{-1} but offers only moderate transparency 83%, resulting in a relatively high figure of merit of $1.5 \times 10^{-1} \Omega^{-1}$. In contrast, ZnS thin films depict exceptional optical transparency of 95% but suffer from normal conductivity (5.29×10^2 Scm^{-1}), giving a much lower figure of merit of $1.0 \times 10^{-3} \Omega^{-1}$. SnO_2 thin films present a balanced profile, combining high transparency of 90% with moderate conductivity of 2.21×10^3 Scm^{-1}, resulting in a figure of merit of 2.0×10^{-2} Ω^{-1}.

To overcome individual trade-offs, composite strategies are proposed. In this study, two composites were explored: Zn (O, S) ZnO: SnO_2 and Zn (S, Sn) SnO_2: ZnS Composite thin films. The ZnO- SnO_2 composite aims to achieve an optimized balance between electrical conductivity and optical transparency. Zinc Oxide (ZnO) is known for its high electrical conductivity, while Tin Oxide (SnO_2) offers superior optical transparency. By combining these two materials, the objective is to leverage ZnO's strong electrical performance while enhancing the overall transparency, thereby mitigating the trade-off often observed in single-component transparent conductive oxides. Similarly, the SnO_2-ZnS composite focuses on improving the electrical conductivity of a highly transparent material. Zinc Sulfide (ZnS) possesses excellent optical transparency, but its conductivity is typically lower than desired for certain applications. By incorporating SnO_2, which has better electrical conductivity, into the ZnS matrix, the composite is designed to enhance the electrical performance without significantly compromising the high transparency of ZnS. These hybrid thin films hold significant promise as next-

generation TCOs, suitable for integration in solar cells, flat-panel displays, smart windows, and transparent electronics.

This chapter outlines the synthesis of both ZnO:SnO₂ and ZnS:SnO₂ thin film composites, detailing their preparation with various compositional weight ratios. The ZnO:SnO₂ composite samples were prepared and designated as follows: Z50Sn50 (50% ZnO, 50% SnO₂), Z40Sn10 (40% ZnO, 10% SnO₂), Z30Sn20 (30% ZnO, 20% SnO₂), Z20Sn10 (20% ZnO, 10% SnO₂), and Z10Sn40 (10% ZnO, 40% SnO₂). Similarly, the ZnS:SnO₂ composites were prepared and labeled as: 50ZS40Sn (50% ZnS:50% SnO₂), 40ZS10Sn (40% ZnS:10% SnO₂), 30ZS20Sn (30% ZnS:20% SnO₂), 20ZS10Sn (20%ZnS:10% SnO₂), and 10ZS40Sn (10% ZnS: 40% SnO₂). All the composites were prepared by the sol-gel spin coating method.

Table 7.1. Transmission, Conductivity, and Figure of Merit of the host material.

S. No.	Host Material	Transmission (%)	Conductivity $(Scm^{-1}) \times 10^{-4}$	Figure of Merit $(\Phi_{TC}) \times 10^{-1}$
1.	ZnO	83	1.01	1.5
2.	SnO₂	90	0.22	0.02
3.	ZnS	95	0.05	0.1

7.2. Results and Discussion of Zn(O, S) ZnO: SnO₂ composite with different weight ratios.

7.2.1 Phase study

The X-ray diffraction (XRD) patterns, presented in Figure 7.1, provide insight into the structural characteristics of the pure ZnO, SnO₂, and Zn(O,S) composite thin films. These composite thin films were prepared with various ZnO/SnO₂ ratios, specifically Z10Sn40, Z20Sn30, Z30Sn20, Z40Sn10, and Z50Sn50. The observed X-ray diffraction peaks for ZnO, located at 2θ values of 31.77°, 34.42°, 36.25°, 47.54°, 56.60°, correspond to the (100), (002), (101), (102), (110) crystallographic planes, respectively. This pattern confirms the hexagonal wurtzite structure of pure ZnO, consistent with JCPDS Card No. 36-1451[278]. X-ray diffraction analysis of SnO₂ thin films revealed

peaks at 2θ angles of 26.61°, 33.89°, and 51.78°. These peaks are consistent with the (110), (101), and (211) lattice planes of tetragonal rutile SnO_2, as referenced in JCPDS card no. 41-1445[279]. The diffraction peaks marked with * identify ZnO peaks, while those marked with # indicate the presence of SnO_2 peaks. In the composite samples (Z10Sn40, Z20Sn30, Z30Sn20, Zn40Sn10, and Z50Sn50), both ZnO and SnO_2 peaks are present, indicating the successful formation of a two-phase composite system without the formation of any secondary or impurity phases. The 50:50 composition of ZnO and SnO_2 composite thin film depicts the proper formation of both phases (mixed phases). The present observations are consistent with existing literature [80]. As the Zn content increases in the composites, the intensity of ZnO peaks becomes more dominant, while the SnO_2 peak intensities diminish, reflecting the compositional change. The presence of sharp and well-defined peaks across all samples suggests good crystallinity. Overall, the XRD results confirm that the ZnO–SnO_2 composites retain the individual crystalline structures of both parent materials, and their relative phase contributions vary systematically with the Zn(O, S) ratio.

Calculations of crystallite size (D) using the Scherrer formula, along with dislocation density and lattice strain, were performed for all the samples. It was determined with the use of equations explained in previous chapters. Table7.2. provides a comprehensive overview of the materials phases, along with their respective crystallite sizes, strain, and dislocation values.

Table 7.2. Structural properties, including the phase, crystallite size, strain, and dislocation values of pure ZnO, SnO_2, and Zn(O, S) thin film composites with different ratios.

S. no	Prepared Materials	Phase	D(nm)	Strain (ϵ)×10^{-3}	Dislocation density (δ)(10^{-3}) (nm^{-2})
1.	ZnO	Hexagonal wurtzite	32.14	0.34	0.95
2.	Z50Sn50	Mixed Phase	40.30	0.28	0.61
3.	Z40Sn10	Mixed Phase	36.29	0.31	0.75
4.	Z30Sn20	Mixed Phase	39.92	0.30	0.62
5.	Z20Sn30	Mixed Phase	25.84	0.42	1.49

6.	Z10Sn40	Mixed Phase	21.63	0.53	2.66
7.	SnO$_2$	Tetragonal rutile	24.65	0.43	1.75
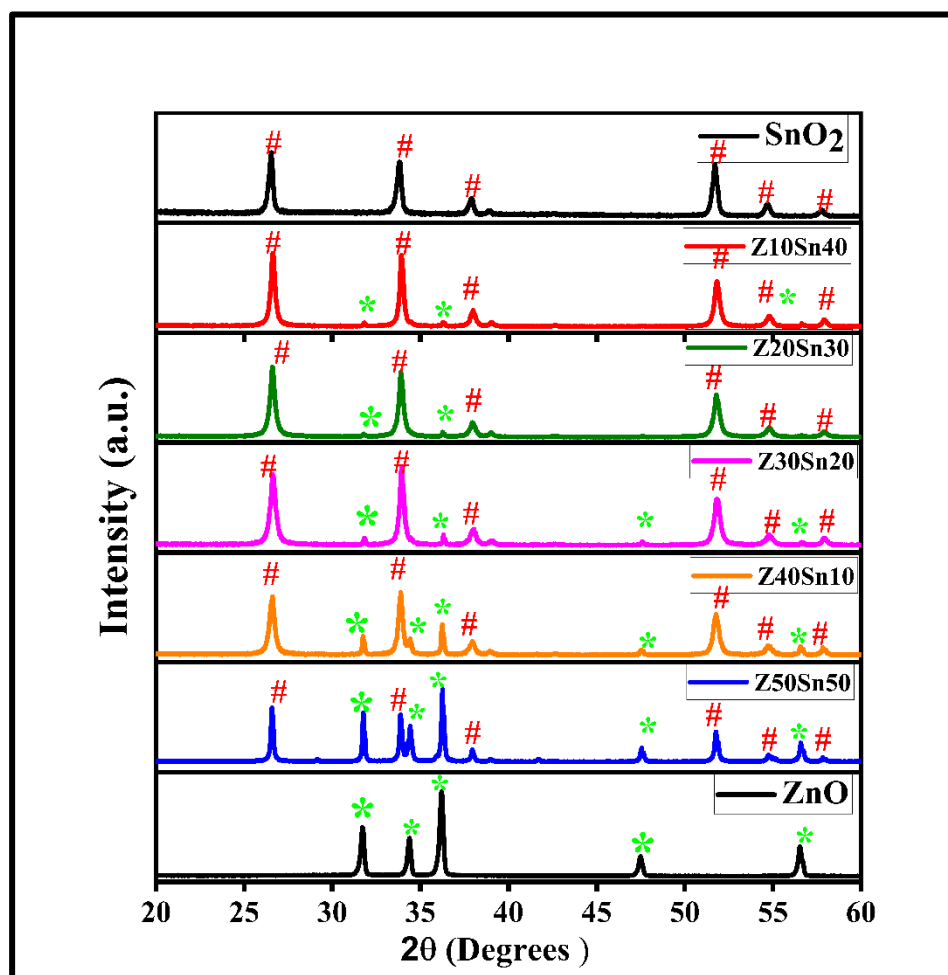
Fig.7.1. The XRD plot for pure ZnO, SnO$_2$, and Zn(O,S) thin film composites with different weight ratios.

7.2.2 FTIR Study

The chemical bonding in ZnO: SnO$_2$ composite material with different compositions Z10Sn40, Z20Sn30, Z30Sn20, Z40Sn10, and Z50Sn50 was examined using FTIR analysis, and the corresponding results are presented in Figure 7.2. It reveals significant changes in vibrational modes associated with the Zn–O and Sn–O bonds. It was observed that five synthesized composites displayed three characteristic peaks at 605

cm^{-1},684 cm^{-1}, and 463cm^{-1}[280]. These peaks unequivocally confirm the successful integration of Sn–O bonds, O-Sn-O bonds, and Zn–O into the composite formation[281]. The spectrum shows characteristic absorption bands near 690cm^{-1} and 460 cm^{-1}, which correspond to the stretching vibrations of Sn–O and Zn–O bonds, respectively. As the ZnO and SnO$_2$ concentration varies, they influence the broadness of the peak and also the intensity. Z50:Z50 depicts the broader and higher intensity.Z40:Z10 indicates the peaks are very much broader and shift the ZnO peak into 413 cm^{-1}. Therefore, all the composites depict the bonding of Zn(O,S), ZnO, and SnO$_2$.
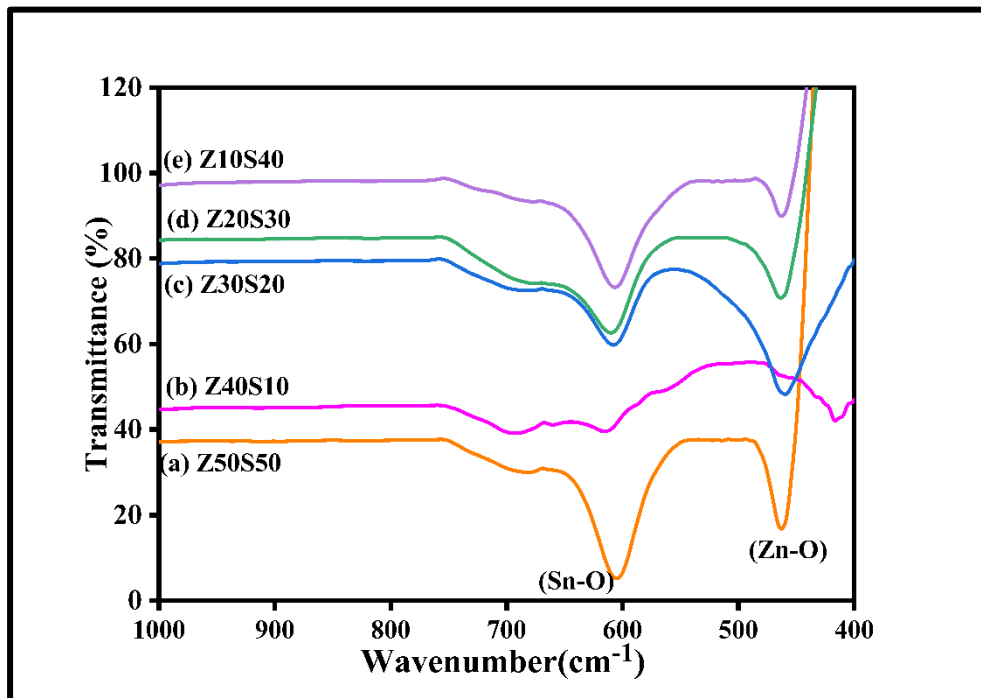
Fig.7.2 The FTIR spectra for pure Zn(O, S) thin film composites with different ratios.

7.2.3 FESM analysis

FE-SEM illustrates the surface morphology micrographs of pure ZnO, SnO$_2$, and the composite of Zn(O, S), which is 50Z:50Sn thin films. Figure 7.3 (a,b,c) illustrates the morphology of individual materials and their composite materials. The ZnO thin film presents a compact and uniform morphology with fine, rounded grains having a particle size of 34nm, suggesting well-organized crystal growth. In comparison, SnO$_2$ thin

films display a coarser morphology, having a particle size of 28nm with homogeneous grain distribution. 50% ZnO: 50% SnO$_2$ composite shows a distinctly different texture, characterized by irregularly shaped particles and noticeable agglomeration, having an average particle size of 38nm. It happens because of the interaction of the two materials. The average particle size of composite materials is somewhat higher than the individual materials.
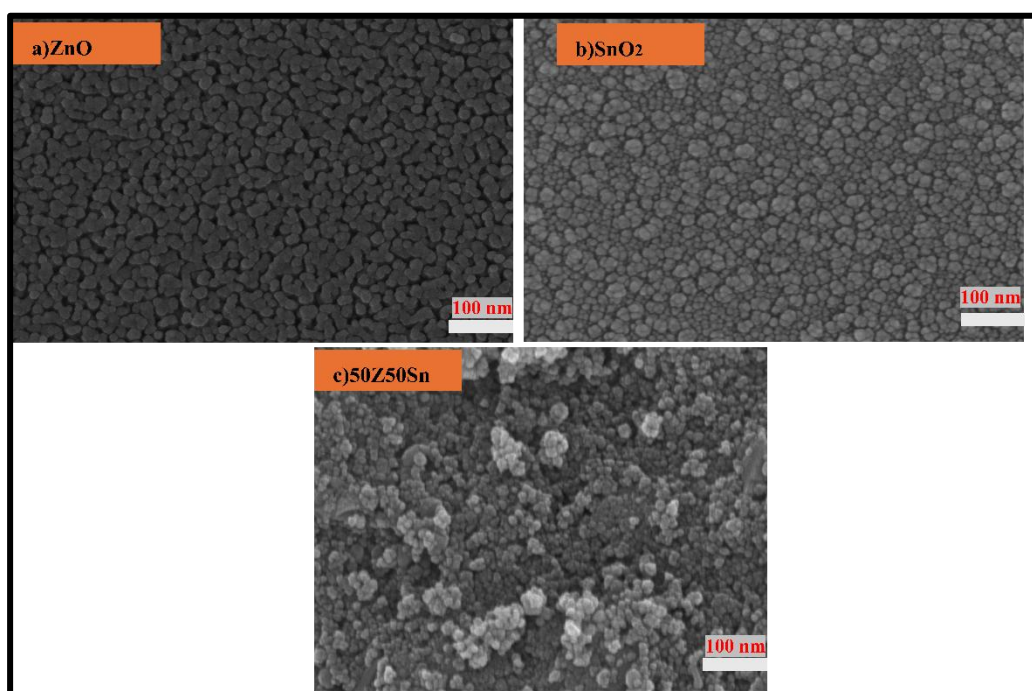
Fig.7.3.Morphology micrograph of (a)ZnO, (b) SnO$_2$,(c) 50%ZnO:50 %SnO$_2$ (50Z50Sn) composite thin films.

7.2.4 EDX

Energy-dispersive X-ray spectroscopy was utilized to examine the elemental composition and verify the successful formation of the materials and their combinations, with results illustrated in Figure 7.4. It depicts that the ZnO sample exhibited characteristic peaks corresponding exclusively to zinc (Zn) and oxygen(O) elements. Also, the SnO$_2$ material displayed distinct peaks for tin (Sn) and oxygen(O) components, as shown in Figures 7.4a and 7.4b, respectively. The composite material demonstrated the presence of both ZnO and SnO$_2$ phases within its spectrum, as presented in Figure 7.4c. It also shows the weight and atomic percentages of all the

samples. It depicts the successful formation of both phases formed by the sol-gel and spin coating preparation route.
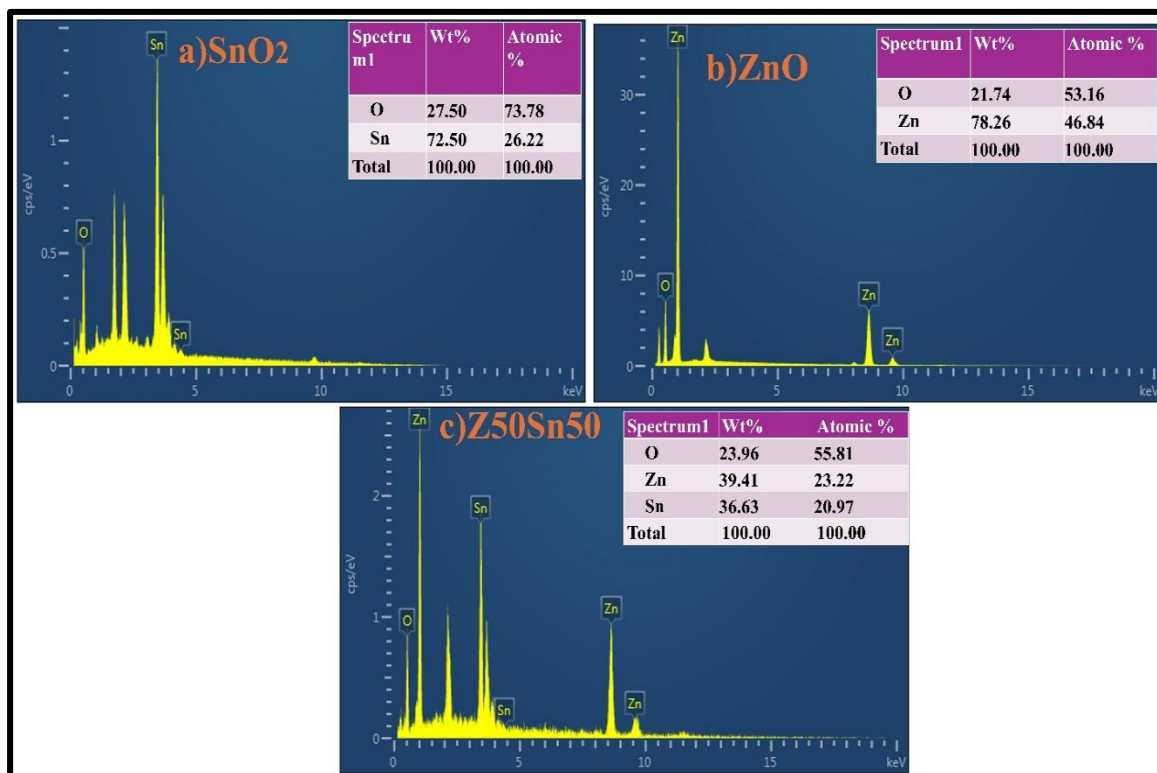
Fig.7.4.EDX spectra of (a) ZnO, (b) SnO$_2$, (c) 50% ZnO:50 % SnO$_2$ (Z50Sn50) composite thin films.

7.2.5. Optical study

UV-Visible spectroscopy provides essential insights into the optical behavior of pure ZnO, SnO$_2$, and ZnO: SnO$_2$ composite thin films prepared with different molar ratios such as Z10Sn40, Z20Sn30, Z30Sn20, Z40Sn10, and Z50Sn50. Sol-gel spin coating was employed to form all samples, which were then deposited onto glass substrates. High transmission, low absorption, and tunable band gap are key traits for high-performance transparent conducting oxides, and these properties are strongly influenced by the film's composition, structure, and morphology. Figure7.5. depicts the transmission spectra for all the samples. The optical transmission properties of thin films reveal notable differences based on their composition. Pure ZnO thin films exhibit a transmission of 83% in the visible region, while pure SnO$_2$ films demonstrate a higher visible light transmission of 90%. When ZnO and SnO$_2$ are combined in various molar

ratios such as Z50Sn50, Z40Sn10, Z30Sn20, Z20Sn30, Z10Sn40 to form composite thin films, the transmission values change significantly, reflecting the influence of composition on optical behavior [92]. The Z50Sn50 composite demonstrated the highest transmittance at 95%, followed closely by Z40Sn10 at 93.15%, indicating excellent optical transparency. As the SnO_2 content increased and the ZnO content decreased, transmittance gradually declined. The Z30Sn20 film showed 76% transmittance, Z20Sn30 exhibited 65%, and Z10Sn40 had the lowest transmittance at 57%. This trend suggests that higher ZnO content contributes to improved optical clarity in the visible region, making Zn-rich compositions more favorable for optoelectronic and transparent conducting applications.
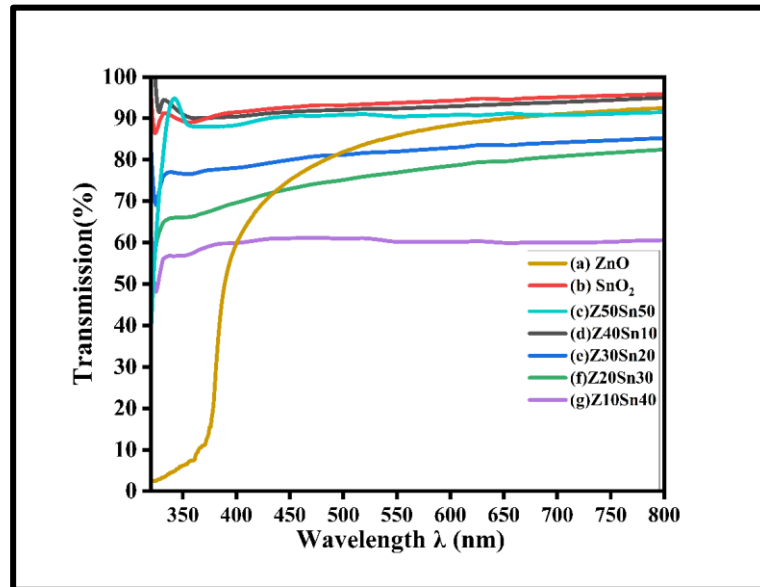
Fig.7.5. Transmission plot for pure ZnO, SnO_2, and Zn(O, S) thin film composites with different weight ratios.

Figure 7.6 depicts the absorbance graph of pure ZnO, SnO_2, and ZnO: SnO_2 composite thin films prepared with different ratios such as Z10Sn40, Z20Sn30, Z30Sn20, Z40Sn10, and Z50Sn50. It is understood that greater light transmission corresponds to reduced absorption. Pure ZnO shows a sharp absorption edge around 364 nm[282]. On the other hand, pure SnO_2 exhibits a broader and less intense absorbance profile, with a slightly blue-shifted absorption edge, aligning with its larger bandgap of around 3.6 eV[283]. When ZnO and SnO_2 are combined to form composite thin films with different ratios, such as Z50Sn50, Z40Sn10, Z30Sn20, Z20Sn30, and Z10Sn40, the

164

absorbance gradually decreases and increases with the variation in the ZnO and SnO₂ content. The Z10Sn40 sample shows the highest absorbance across the visible regions because it shows the lowest transmission. This enhanced absorbance and the redshift in the absorption edge indicate a narrowing of the optical bandgap. This phenomenon is attributed to the formation of heterojunctions between ZnO and SnO₂ phases, which modify the band structure and facilitate better light absorption. Z50Sn50 with equal parts Zn and Sn shows the lowest absorbance among the composites and is even lower than pure ZnO and SnO₂ because it shows the highest transmission.
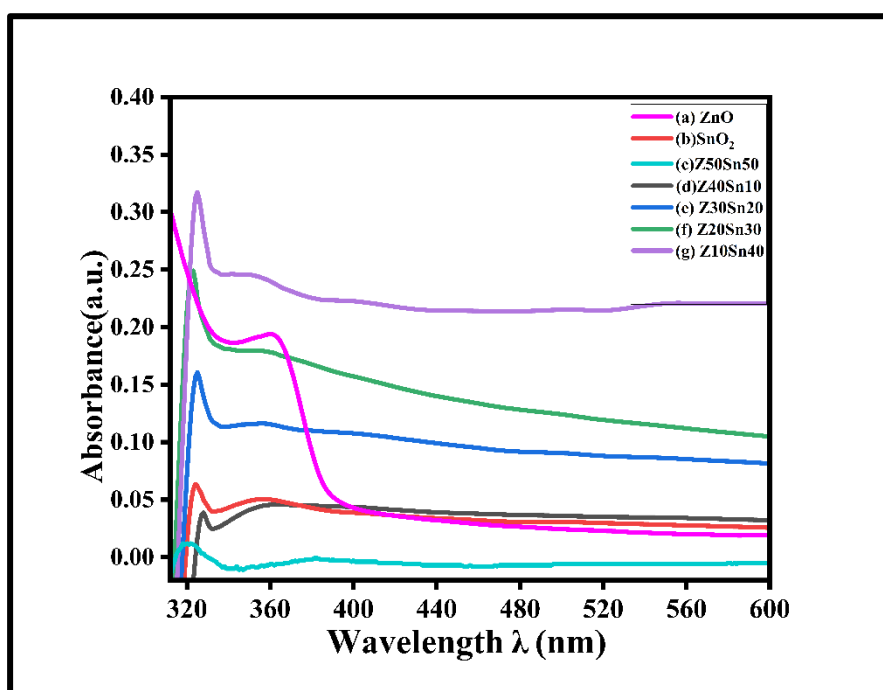
Fig.7.6. Absorbance graph for pure ZnO, SnO₂, and Zn (O, S) thin film composites with different weight ratios.

The band gap energy values for ZnO: SnO₂ composites with various ratios, specifically Z50Sn50, Z40Sn10, Z30Sn20, Z20Sn30, and Z10Sn40, are presented in Figure 7.7. These values were derived by applying the Tauc approach equation[279], defined as $(\alpha h v)^2 = A(h v - E_g)$, where α denotes the absorption coefficient, $h v$ represents the photon energy, A is a constant, and E_g signifies the band gap energy. Pure ZnO exhibits a band gap of 3.25 eV, while SnO₂ possesses a comparatively wider band gap of 3.95 eV. The measured band gap values for ZnO: SnO₂ composite with different ratios Z50Sn50, Z40Sn10, Z30Sn20, Z20Sn30, and Z10Sn40 are 3.57eV, 3.58eV, 3.61eV, 3.68eV and

3.73eV. Their values lie between the host materials. Compared to pure ZnO (3.25 eV) and SnO₂ (3.95 eV), the band gaps of the composites lie in between, indicating successful formation of mixed-phase or alloyed structures.50% ZnO and 50% SnO₂ show band gap values more than the ZnO band gap value and less than the SnO₂ band gap value. As the ZnO content reduces, the SnO₂ content increases the band gap gradually increases from 3.57 to 3.75 eV. This trend is consistent with **a** band gap tailoring mechanism, where SnO₂ incorporation affects the electronic structure of ZnO[284]. The observed reduction in band gap with higher ZnO content is likely due to the dominant influence of ZnO's narrower band gap (3.25 eV). Conversely, higher SnO₂ content leads to a wider band gap due to SnO₂'s inherently larger gap (3.95 eV). Additionally, effects like the Burstein–Moss shift, interface-induced strain, or defect level variations may contribute to these optical properties[80]. This indicates the successful formation of composite or alloyed phases that influence the structural, optical, and electronic structure of the material. Table 7.3. describes all the values of the transmission and band gap.
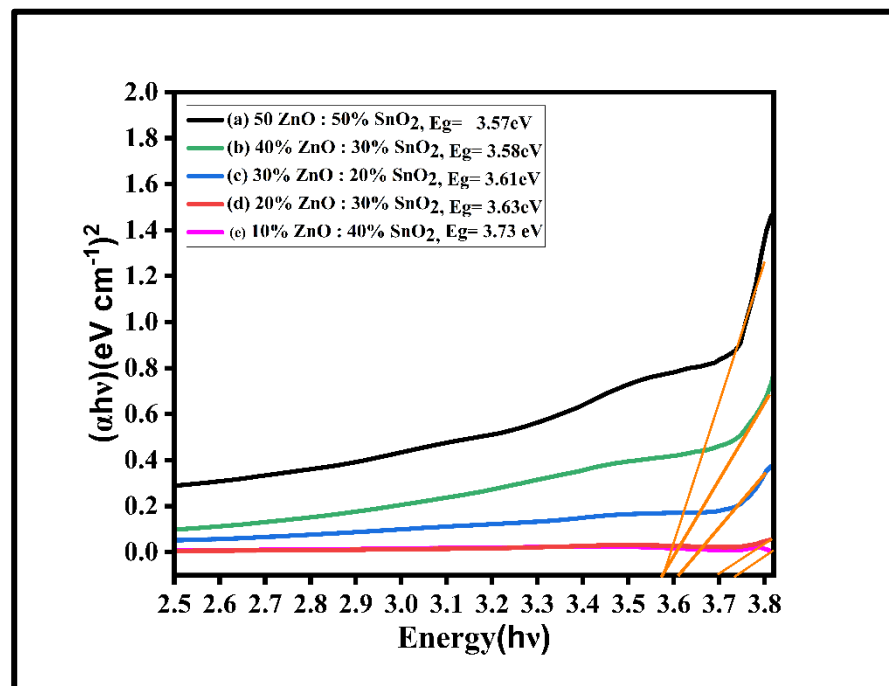
Fig.7.7. Band gap graph for pure ZnO, SnO₂, and Zn(O,S) thin film composites with different weight ratios.

Table7.3. The transmission and band gap of pure ZnO, SnO$_2$, and ZnO: SnO$_2$ thin film composites with different ratios.

S. no	Prepared Materials	Transmission (%)	Band gap (eV)
1.	ZnO	83	3.25
2.	SnO$_2$	90	3.95
3.	Z50Sn50	95	3.57
4.	Z40Sn10	94	3.58
5.	Z30Sn20	76	3.61
6.	Z20Sn30	65	3.63
7.	Z10Sn40	57	3.73

7.2.6. Electrical Analysis

7.2.6.1 Hall measurements

Hall measurement shows the electrical characteristics of the prepared materials. Figure7.8. presents the conductivity, mobility, carrier concentration, and carrier type of ZnO, SnO$_2$, Zn(O,S) composite thin films with different ratios such as 50Z50Sn,40Z10Sn,30Z20Sn, 20Z30Sn, and 10Z40Sn. Pure ZnO exhibited n-type semiconducting behavior with a conductivity of 1.01×10^4 Scm^{-1}, a carrier concentration of 1.68×10^{21} cm^{-3}, and a mobility of 37.5 cm^2/V·s. Similarly, the SnO$_2$ thin film was also n-type, showing a conductivity of 2.21×10^3 Scm^{-1}, carrier concentration (6.96×10^{19} cm^{-3}), and mobility (56.2 cm^2/V·s). The electrical behavior of ZnO: SnO$_2$ composite thin films is highly dependent on their compositional ratio, especially in terms of conductivity, carrier concentration, and mobility. As the proportion of ZnO decreases and SnO$_2$ increases, there is a noticeable reduction in both conductivity and carrier concentration, while mobility shows a gradual increase. This can be attributed to the inherent material properties of ZnO and SnO$_2$. ZnO is known for its high carrier concentration due to intrinsic donor-like defects such as oxygen vacancies and zinc interstitials, which contribute free electrons to the conduction band[285]. These defects enhance electrical conductivity but also increase scattering, which limits electron mobility. In contrast, SnO$_2$ has a lower density of such defects and consequently a lower carrier concentration. However, its more ordered crystalline

structure facilitates higher electron mobility by reducing ionized impurity scattering[283]. As SnO_2 content increases in the composite, the dominance of ZnO's defect-related donors is diluted, leading to a decrease in carrier concentration. Despite the decline in free carriers, mobility improves due to reduced defect scattering, resulting in a trade-off between these properties. The optimal electrical performance is typically achieved at intermediate compositions, such as 40% ZnO and 10% SnO_2, where a reasonable balance between conductivity and mobility is maintained. This makes such composites promising candidates for applications in transparent conductive oxides and gas sensors, where both high mobility and sufficient conductivity are essential. Hence, the composite shows the conductivity, carrier concentration, and mobility between the ZnO and SnO_2. Also, all the thin films show n-type behavior. The measured values of the host.
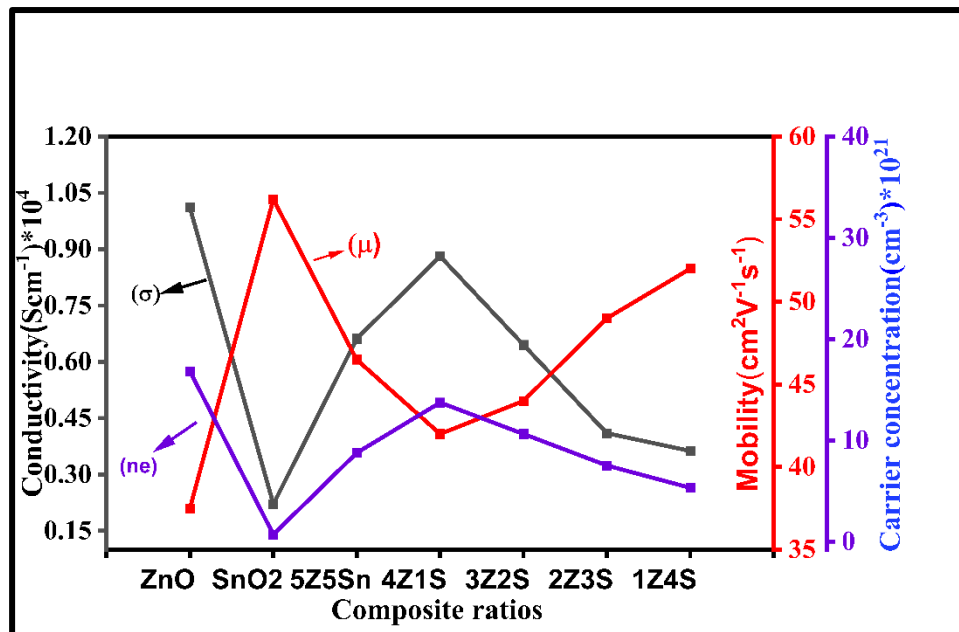
Fig.7.8. Conductivity, carrier concentration, and mobility graph for ZnO, SnO_2, and Zn(O,S) thin film composites with different ratios.

Table7.4. The electrical characteristics of ZnO, SnO_2, and Zn(O,S) thin film composites with different ratios.

S. No.	Prepared Materials	Conductivity $(Scm^{-1}) \times 10^4$	Carrier concentration(cm^{-3}) $\times 10^{21}$	Mobility($cm^2V^{-1}s^{-1}$)	Carrier type
1.	ZnO	1.01	1.68	37.5	n
2.	SnO_2	0.22	0.09	56.2	n
3.	50Z50Sn	0.66	0.88	46.9	n
4.	40Z10Sn	0.88	1.37	41.0	n
5.	30Z20Sn	0.65	1.06	44.9	n
6.	20Z30Sn	0.41	0.75	49.8	n
7.	10Z40Sn	0.36	0.53	52.5	n

7.2.6.2 Figure of merit analysis

The bar graph in the figure7.9. depicts the Figure of Merit (FOM) for pure ZnO, SnO_2, and their composite Zn(O,S) thin films (Z50Sn50, Z40Sn10, Z30Sn20, Z20Sn30, and Z10Sn10), which assesses transparent conducting material performance based on conductivity and transparency, with higher FOM indicating better efficiency. Pure ZnO exhibits the highest FOM ($1.5 \times 10^{-1} \Omega^{-1}$), while pure SnO_2 shows the lowest ($0.2 \times 10^{-1} \Omega^{-1}$). Among composites, 40Z10Sn is the most effective, achieving an FOM of $\approx 1.1 \times 10^{-1} \Omega^{-1}$. ZnO materials exhibit superior performance compared to SnO_2. Composite ratios impact the material's characteristics, with all composites showing an improved figure of merit over pure SnO_2 but remaining below that of pure ZnO. Overall, they represent an enhancement in performance. As a result, the 40Z10Sn composite demonstrates the highest figure of merit compared to the other prepared composites.
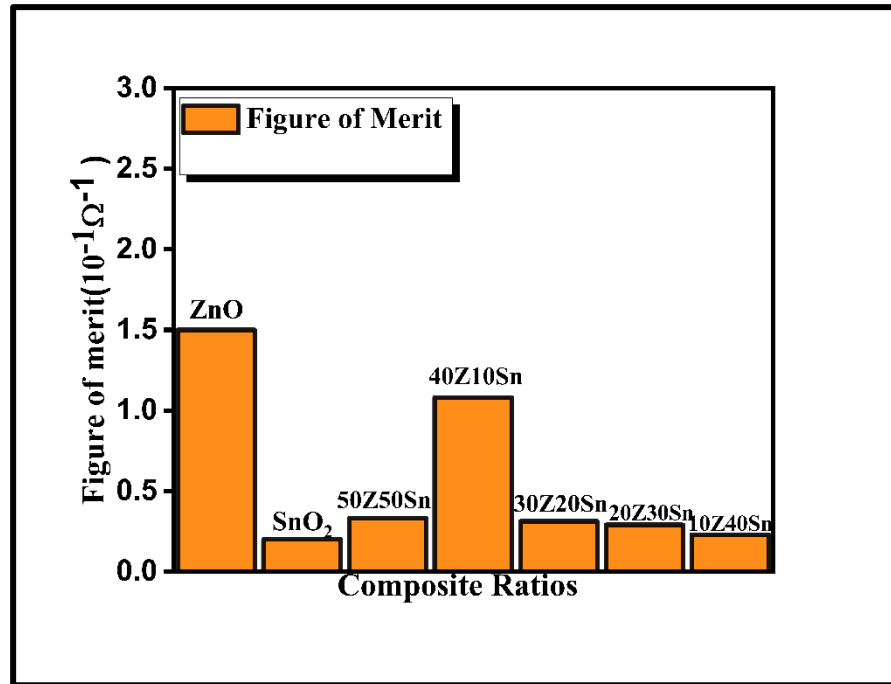
Fig.7.9. Figure of merit plot for pure ZnO, SnO$_2$, and Zn (O,S)thin film composites with different ratios.

7.2.7. Conclusion

Successfully synthesized ZnO–SnO$_2$ composite thin films by the sol–gel spin coating method exhibit clear compositional dependence on structural, optical, and electrical properties.

1. XRD analysis confirmed the formation of a mixed-phase structure, maintaining the distinct crystal lattices of ZnO and SnO$_2$ without secondary phases. Variations in crystallite size, strain, and dislocation density suggest an optimized microstructure at intermediate compositions.

2. FTIR confirmed the presence of Zn–O and Sn–O bonds, indicating successful chemical integration, while EDX mapping showed uniform elemental distribution with no impurities.

3. Optical measurements revealed tunable transmission and band gaps between those of pure ZnO and SnO$_2$. The Z50Sn50 film showed the highest transparency (~95%) and an intermediate band gap (~3.57 eV), ideal for optoelectronic use.

170

4. All samples exhibited n-type conductivity. Zn-rich films had higher conductivity and carrier concentration due to intrinsic defects, whereas Sn-rich films displayed enhanced mobility from reduced scattering. Z40Sn10 and Z50Sn50 compositions offered an optimal balance, making them suitable for transparent conducting oxides (TCOs) and gas sensors.

In conclusion, compositional tuning in sol–gel Zn(O,S) ZnO–SnO$_2$ thin films effectively tailors their properties for use in transparent electronics, sensors, and optoelectronics, with Z50Sn50 emerging as a highly promising multifunctional TCO material.

7.3. Results and Discussion of Zn(S,Sn) ZnS:SnO$_2$ composite with different weight ratios.

7.3.1. XRD Study

The XRD patterns illustrate the structural composition of pure ZnS, pure SnO$_2$, and their composite mixtures Zn(S,Sn) in Figure 7.10. These composite thin films were prepared with various Zn(S,Sn) ratios, specifically ZS50Sn50, ZS40Sn10, ZS30Sn20, ZS20Sn30, ZS10Sn40. In the XRD patterns of ZS40Sn10 and ZS10Sn40, both ZnS and SnO$_2$ phases are present. X-ray diffraction analysis of SnO$_2$ thin films showed distinct peaks at 2θ values of 26.61°, 33.89°, and 51.78°, which correspond to the (110), (101), and (211) planes of the tetragonal rutile structure of SnO$_2$, in agreement with JCPDS card no. 41-1445[158]. In another XRD analysis, three diffraction peaks appear at 2θ values of 28.91°, 48.06°, and 57.28°, which are likely associated with the (111), (220), and (311) planes of the zinc blende phase of ZnS[286]. These results are consistent with the standard cubic ZnS pattern referenced by JCPDS Card No. 00-005-0566. Both host materials show good crystallinity. In the composite samples labeled 40ZS10Sn, both ZnS and SnO$_2$ peaks are visible, with ZnS peaks being more prominent, suggesting a higher proportion or better crystallinity of ZnS. Conversely, in the 10ZS40Sn sample, the pattern is dominated by SnO$_2$ peaks with no visible ZnS signals, indicating SnO$_2$ is the major phase in this composition. Hence, the XRD analysis confirms the mixed formation of ZnS:SnO$_2$ composite thin films and shows how the phase dominance shifts

and crystallinity improve with varying ratios[287]. No additional impurity phases were detected.

Crystallite size (D) was calculated for all samples using the Scherrer formula, along with evaluations of dislocation density and lattice strain based on the corresponding equations. A detailed summary of the material phases, including their crystallite sizes, strain, and dislocation densities, is presented in Table 7. 5.

Table7.5. Structural properties, including the phase, crystallite size, strain, and dislocation values of pure ZnS, SnO$_2$, and Zn (S, Sn) thin film composites with different ratios.

S. no	Prepared Materials	Phase	D(nm)	Strain (ϵ)×10^{-3}	Dislocation density (δ)(10^{-3}) (nm^{-2})
1.	ZnS	Zinc Blende	4.10	8.45	59.44
2.	SnO$_2$	Tetragonal rutile	24.65	1.43	1.75
3.	40ZSSn10	Mixed Phase	13.06	4.94	27.04
4.	10ZSSn40	Tetragonal rutile	8.80	4.08	14.44
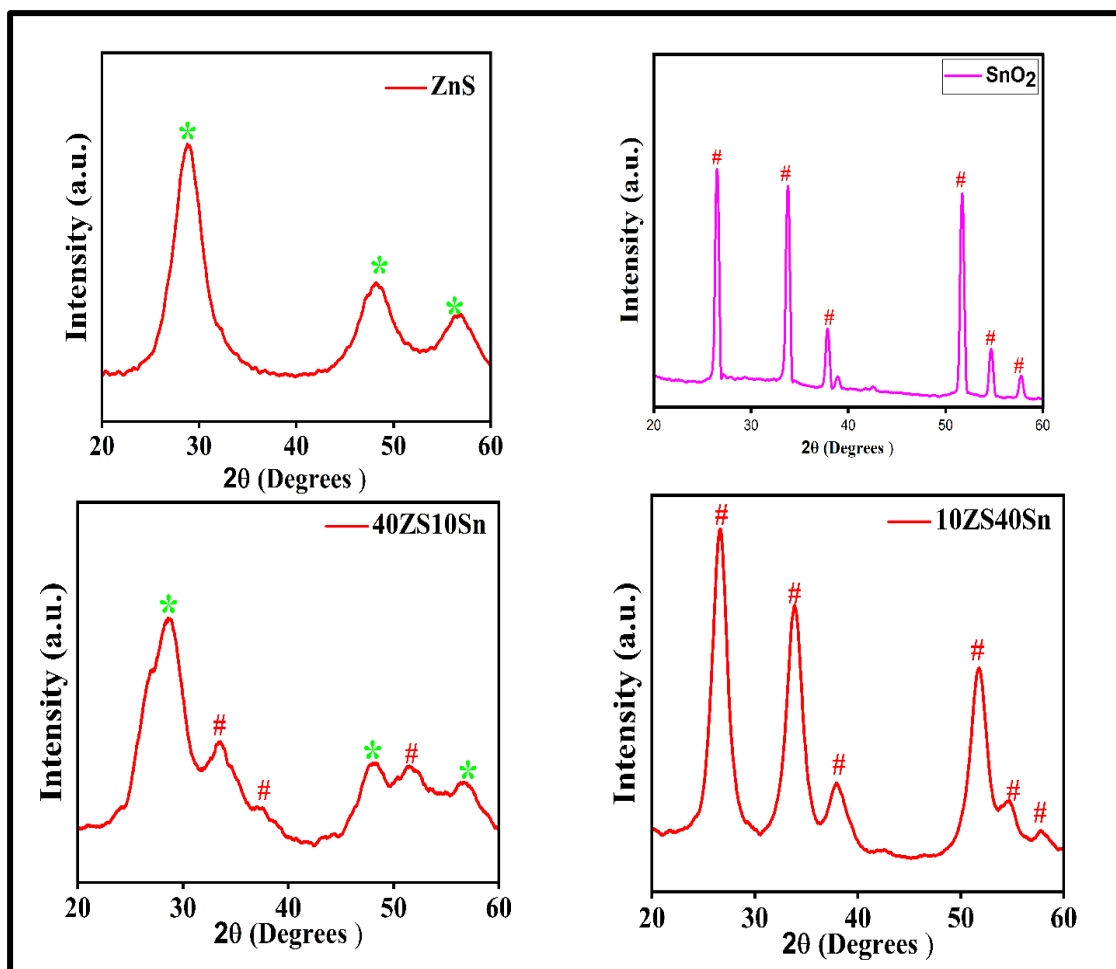
Fig.7.10. The XRD plot for ZnS, SnO$_2$, and Zn(S,Sn) thin film composites with different ratios.

7.3.2. FTIR Study

The FTIR study of ZnS: SnO$_2$ composite thin films with different compositional ratios, including 50ZS50Sn,40ZS10Sn,30ZS20Sn,20ZS30Sn, and 10ZS40Sn, highlights the presence of characteristic chemical bonds and functional groups (Figure7.11). Vibrational bands observed around 470 cm^1 to 620 cm^1 are attributed to Zn–S and Sn–O stretching modes, respectively, indicating the successful formation of both ZnS and SnO$_2$ in the material[288], [289]. As the proportion of ZnS and SnO$_2$ varies, the peak intensity and broadening of peaks vary. Also, with the variation, the Sn–O peak becomes more dominant, while the Zn–S signal diminishes, reflecting a shift in composition. A noticeable absorption near 1000 cm^{-1} is related to C=O stretching, possibly originating from atmospheric CO$_2$ or residual organics. The band around 1600

cm^{-1} is associated with H–O–H bending, implying the presence of adsorbed water molecules, and a broad absorption near 3400 cm^{-1} corresponds to O–H stretching, indicating hydroxyl groups on the surface[290]. Additionally, the gradual rise in transmittance suggests enhanced transparency and fewer surface defects. Hence, all the composites depict ZnS and SnO$_2$ bonding.
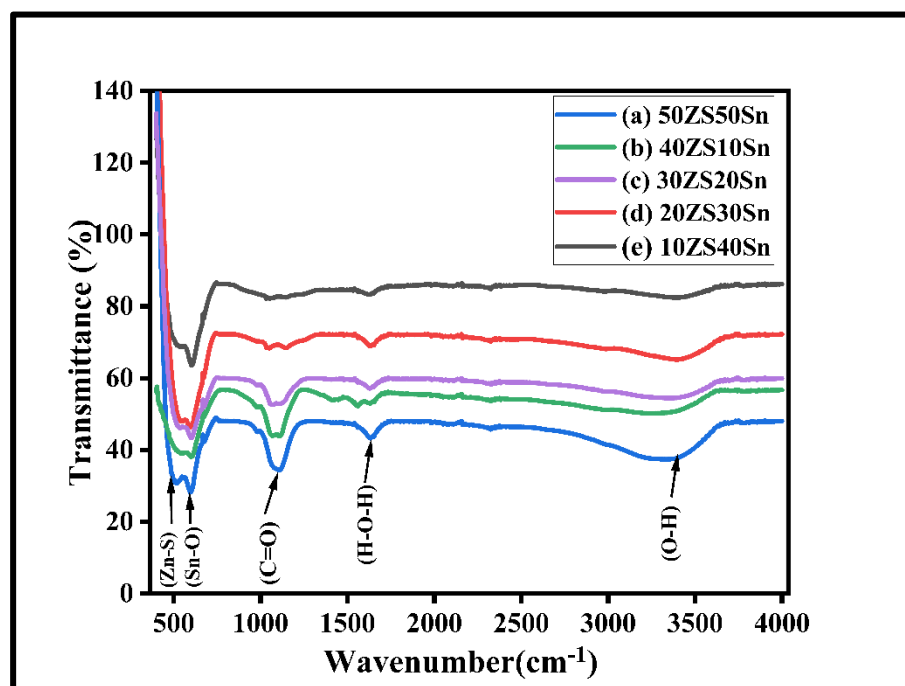
Fig.7.11. The FTIR spectra for pure ZnS: SnO$_2$ thin film composites with different ratios.

7.3.3. FESM analysis

FE-SEM images reveal distinct morphological differences among ZnS, SnO$_2$, and their 50:50 Zn(S, Sn) composite thin films. The average particle size was quantified using ImageJ software. The ZnS film figure (7.12 a) shows a uniform, densely packed structure with fine, spherical grains having an average particle size of 15nm, indicating smooth and consistent growth. Figure 7.12 (b) depicts that SnO$_2$ displays a coarser morphology, having a particle size of 28nm with homogeneous grain distribution. Figure 7.12 (c) illustrates the 50% ZnS and 50% SnO$_2$ composite, revealing a porous surface with notable particle agglomeration and an average particle size of 32 nm,

which is larger than that of the individual host materials. The combined morphologies of the two distinct materials result in a snow-like structure[287].
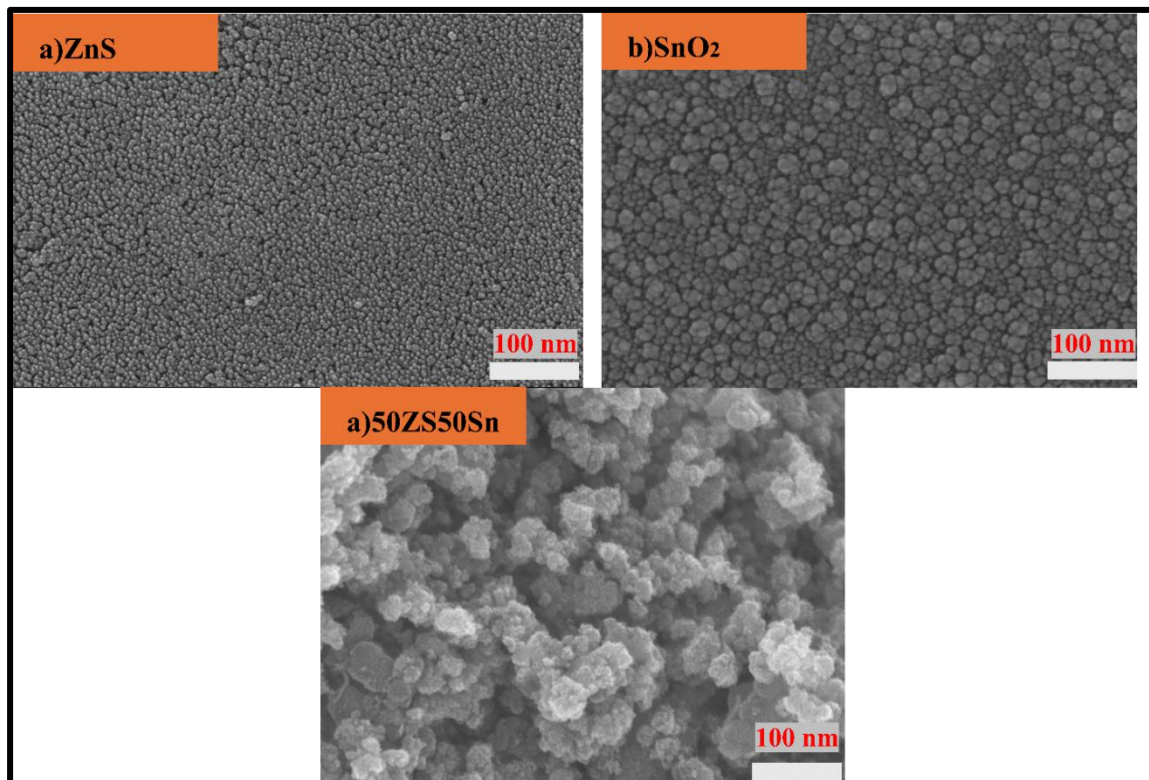
Fig.7.12.Morphology micrograph of (a)ZnS, (b) SnO$_2$, (c) Zn(S,Sn) 50%ZnS:50%SnO$_2$ composite thin films.

7.3.4. EDX and Mapping

The elemental composition and formation of the materials and their composites were elucidated through EDX analysis, as presented in Figure 7.13(a, b, c). For instance, the ZnS spectrum exclusively displayed peaks for Zn and S (Figure 7.13a). In contrast, the SnO$_2$ spectrum (Figure 7.13b) clearly showed the presence of Sn and oxygen. When examining the composite spectrum (Figure 7.13c), a discernible combination of signals from both ZnS and SnO$_2$ was evident, with all expected peaks well-resolved. Such distinct elemental signatures underscore the high purity of the samples produced through the sol-gel method. This EDX confirmation of product phase purity is in excellent agreement with the observations from FESEM and XRD studies. It indicates the successful formation of both materials (50% ZnS:50 % SnO$_2$) through the sol-gel and spin coating methodology.
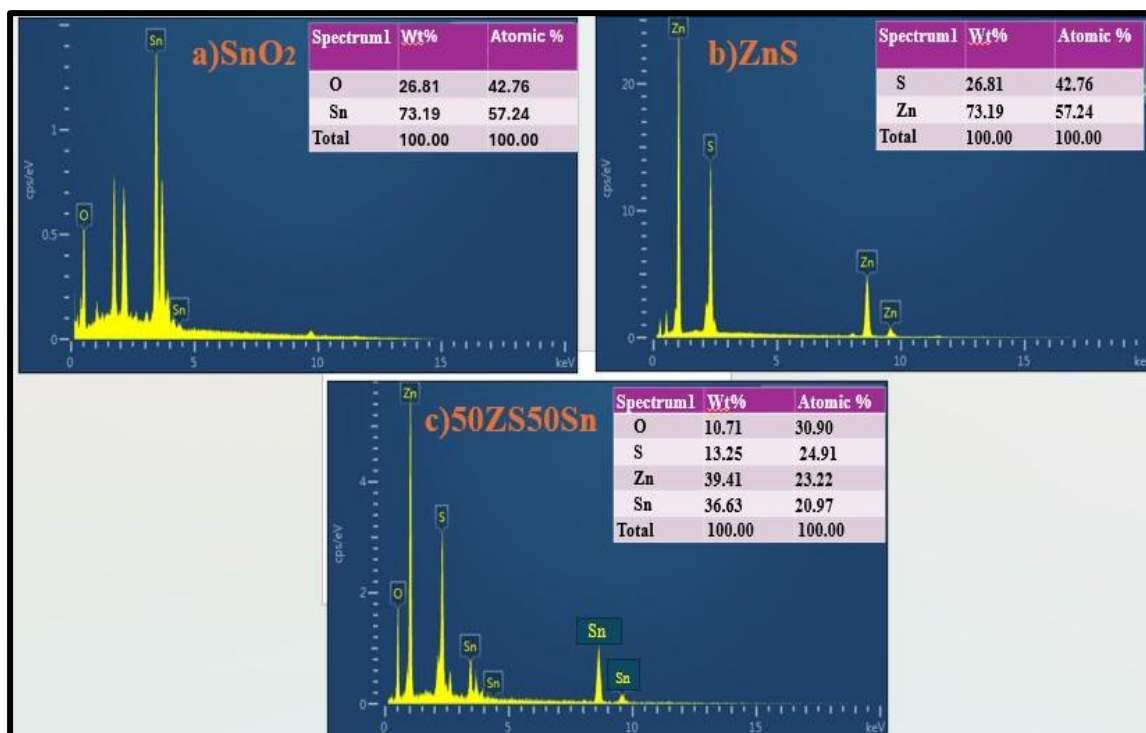
Fig.7.13.EDX spectra of (a)SnO$_2$ (b) ZnS (c) 50%ZnS:50%SnO$_2$ Zn(S,Sn) composite thin films.

7.3.5. Optical study

The optical characteristics of ZnS, SnO$_2$, and their composite films Zn(S,Sn) were investigated through UV-Visible spectroscopic analysis. These thin films were synthesized using sol-gel methodology, followed by spin-coating deposition on glass surfaces. Various compositional ratios were examined, including 50ZS50Sn, 40ZS30Sn, 30ZS20Sn, 20ZS30Sn, 10ZSSn40, and formulations, alongside ZnS and SnO$_2$ materials. This spectroscopic technique enabled a comprehensive evaluation of the light absorption and transmission properties across the different film compositions. The figure 7.14. provides a representation of the optical transmittance of ZnS, SnO$_2$, and their composite materials. It was observed that the optical transmission of ZnS: SnO$_2$ composite films varies noticeably with composition. Pure ZnS and SnO$_2$ show high transparency at 95% and 90%, respectively. Surprisingly, the 50% ZnS:50 % SnO$_2$ blend achieves the highest transmission of 96%, which may result from a well-balanced structure with fewer defects and better phase compatibility. However, as SnO$_2$ content increases beyond this point, the transmission steadily declines, falling to 93% at ZnS

40%: SnO_2 10%, 88% at ZnS 30%: SnO_2 20%, 80% at ZnS 20%: SnO_2 30%, and reaching just 55% at ZnS 10%: $SnO_2$40%. This decline is likely due to increased defect states, oxygen vacancies, and interfacial scattering introduced by the SnO_2 phase. These factors lead to higher optical absorption and lower light transmission[82]. Thus, while a balanced mix of ZnS and SnO_2 improves transparency, excessive SnO_2 content causes structural disorder that degrades optical performance. As a result, composite materials offer enhanced light transmission, positioning them as viable candidates for transparent conductive applications, including display technologies, solar energy conversion, and flat panel etc.
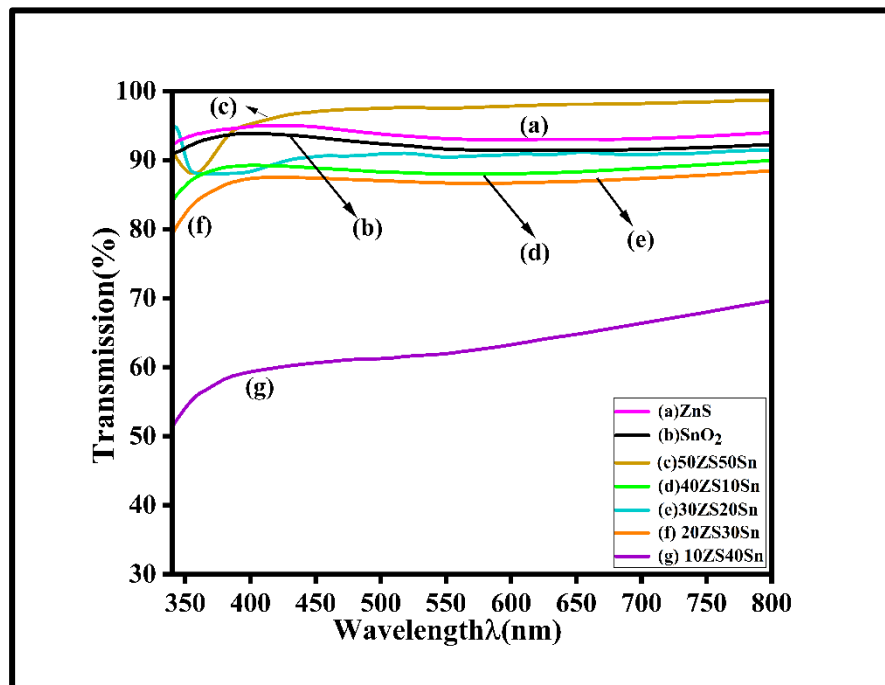
Fig.7.14. Transmission plot for pure ZnS, SnO_2, and ZnS: SnO_2 thin film composites with different ratios.

The absorbance graph for ZnS, SnO_2, and ZnS:SnO_2 composite thin films prepared with different ratios, including 50ZS50Sn,40ZS10Sn, 30ZS20, 20ZS30Sn, and 10ZS40Sn represented in Figure 7.15. High absorbance is related to low transmission. The 50% ZnS:50% SnO_2 composite shows the lowest absorbance (~0.05) across the UV-visible range, indicating the highest optical transparency among all samples. This can be attributed to its balanced microstructure, which likely results in reduced defect states, minimal light scattering, and fewer oxygen vacancies or surface traps. As the SnO_2

177

content increases beyond 50%, the absorbance progressively rises, reaching a maximum of ~0.65 for the 10%ZnS:40%SnO$_2$ composition. This increase in absorbance is due to enhanced oxygen vacancies, grain boundary defects, and interfacial scattering, which cause higher light absorption, especially in the UV region[291], [292]. Therefore, Zn(S,Sn) 50%ZnS:50%SnO$_2$ forms a more optically transparent, low-absorbance, and structurally uniform film.
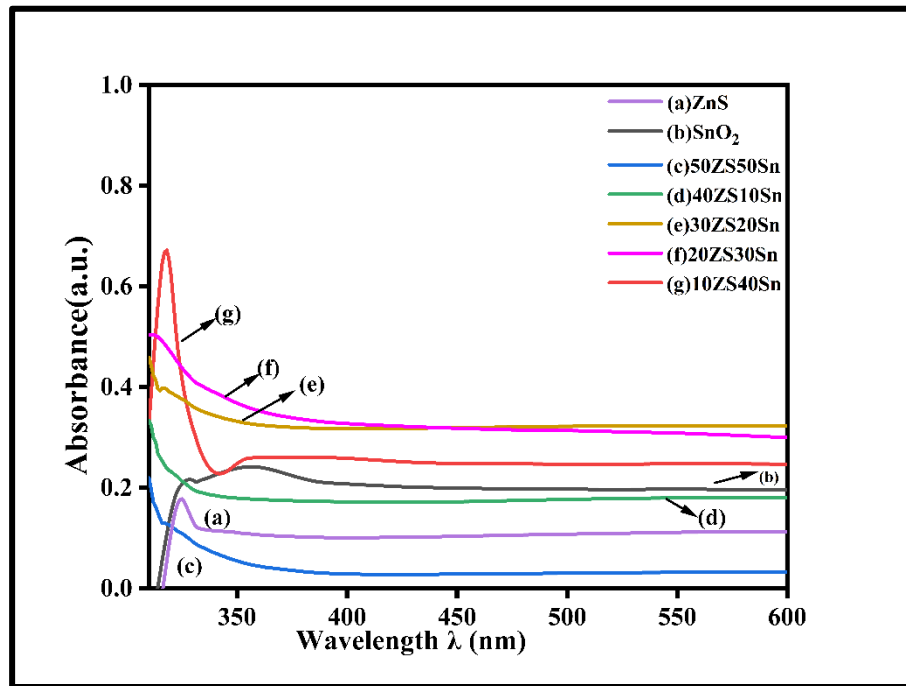
Fig.7.15. Absorbance graph for pure ZnO, SnO$_2$, and ZnO: SnO$_2$ thin film composites with different weight ratios.

Figure7.16. depicts the optical band gap plot of Zn(S,Sn) ZnS-SnO$_2$ semiconductor composites with varying compositions, including 50ZS50Sn, 40ZS10Sn, 30ZS20Sn, 20ZS30Sn, and 10ZS40Sn. These values were analyzed with the help of the Tauc plot[293]. It shows the proper variations of ZnS: SnO$_2$ composite thin films with different ZnS and SnO$_2$ ratios. The data reveal a systematic trend where the optical band gap rises progressively from 3.72 eV to 3.86 eV as the ZnS content decreases while the SnO$_2$ content increases correspondingly[294]. The enhancement in the band gap values indicates a systematic blue shift in the absorption edge as the SnO$_2$ content rises[295]. This progressive band gap widening occurs because SnO$_2$ possesses a larger band gap (3.95 eV) compared to ZnS (3.65 eV), and the composite materials display intermediate

values that correlate with their relative compositions. This shift shows more SnO_2 into the ZnS matrix, effectively broadening the composite's band gap. This behavior demonstrates the tunability of the optical properties through compositional adjustments in the $ZnS–SnO_2$ composite thin films. These findings thus confirm the successful formation of two materials in varying proportions and highlight their impact on optical properties. Such enhanced characteristics render this composite material suitable for optoelectronic applications like transparent conductive elements, flat panels, and display devices.
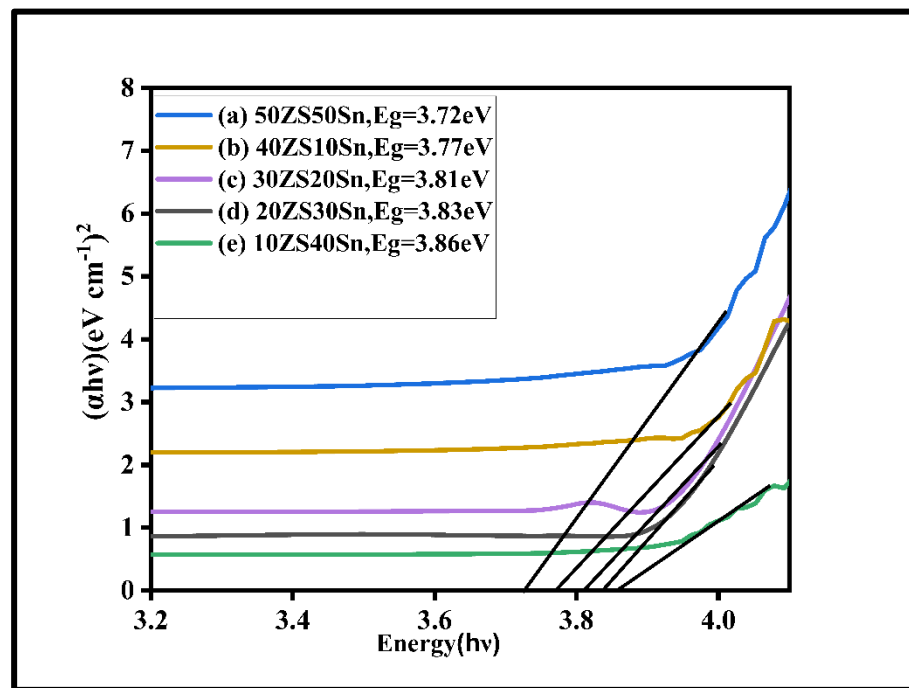
Fig.7.16. Band gap graph for Zn (S, Sn) thin film composites with different ratios.

Table7.6. The transmission and band gap of pure ZnS, SnO_2, and Zn (S, Sn) thin film composites with different weight ratios.

S. no	Prepared Materials	Transmission (%)	Band gap(eV)
1.	ZnS	95	3.65
2.	SnO_2	90	3.95
3.	50ZS50Sn	96	3.72
4.	40ZS10Sn	93	3.77
5.	30ZS10Sn	88	3.81

6.	20ZS30Sn	85	3.83
7.	10ZS40Sn	55	3.86

7.3.6. Electrical Analysis

7.3.6.1 Hall measurements

Hall measurement shows the electrical characteristics of the prepared materials. Figure 7.17. presents the conductivity, mobility, carrier concentration, and carrier type of ZnS, SnO_2, and $Zn(S,Sn)$ composite thin films with different ratios, including 50ZS50Sn,40ZS10Sn,30ZS20Sn, 20ZS:30Sn, and 10ZS40Sn.The electrical characteristics of ZnS–SnO_2 composite thin films exhibit considerable variation with changes in their composition, a consequence of the distinct properties of the two constituent materials. Zinc Sulfide (ZnS) shows low conductivity (5.29×10^2 Scm^{-1}), relatively low carrier concentration (0.36×10^{19} cm^{-3}), but possesses high electron mobility (79 cm^2/V·s). Conversely, Tin Oxide (SnO_2) contributes a higher conductivity (5.29×10^2 Scm^{-1}), higher carrier concentration (6.96×10^{19} cm^{-3}), and a moderate mobility (56.2 cm^2/V·s). However, as more SnO_2 is introduced and ZnS concentration reduces, mobility tends to reduce slightly. This is due to increased scattering from structural imperfections, grain boundaries, and interfacial defects brought about by the SnO_2 phase[296].Despite this minor decline in mobility, the overall conductivity improves because the gain in carrier concentration more than offsets the loss in mobility. For instance, at a 50%ZnS:50%SnO_2 composite thin film, carrier concentration rises 3.66×10^{19} cm^{-3}, while mobility remains at a reasonably high value of around 67.6 cm^2/V·s, resulting in a conductivity of nearly 3.96×10^3 Scm^{-1}. All the composite thin films exhibit n-type semiconducting characteristics. This consistent trend across various compositions confirms that incorporating SnO_2 significantly improves the electrical performance of ZnS-SnO_2-based composite thin film, making them promising candidates for applications in transparent electronics and gas sensing technologies[297]. Table 7.7. illustrates the calculated electrical parameters of the host and composite thin films.
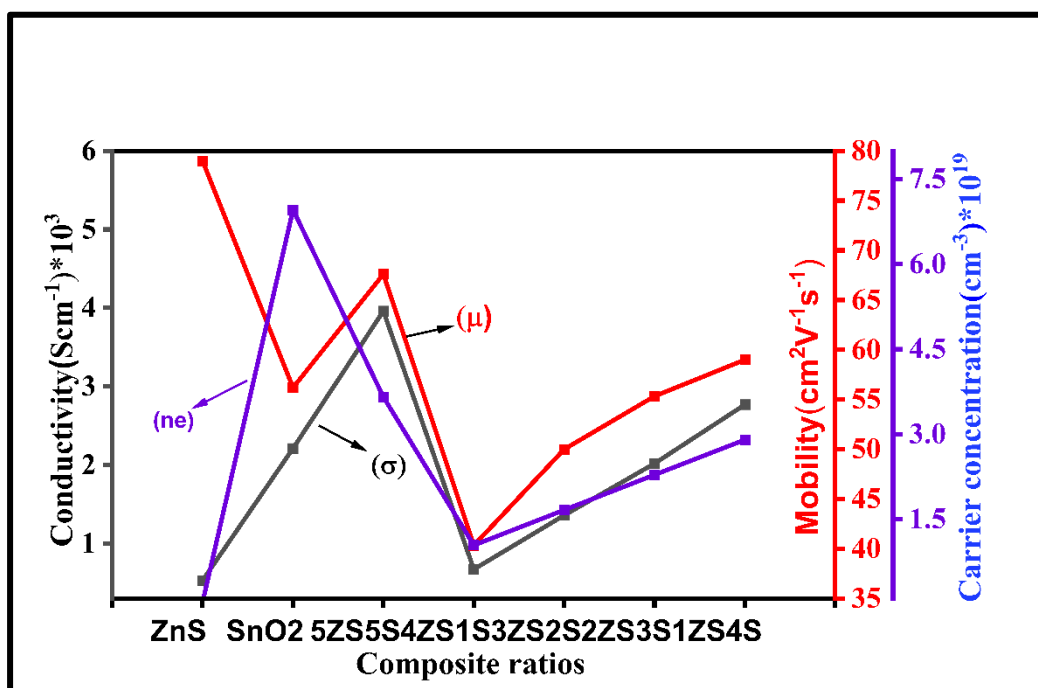
Fig.7.17. Conductivity, carrier concentration, and mobility graphs for ZnS, SnO$_2$, and Zn (S, Sn) thin film composites with different weight ratios.

Table7.7. The electrical characteristics of ZnS, SnO$_2$, and Zn(S,Sn) thin film composites with different weight ratios.

S. No.	Prepared Materials	Conductivity (Scm^{-1}) $\times 10^3$	Carrier concentration(cm^{-3}) $\times 10^{19}$	Mobility(cm^{2}V^{-1}s^{-1})	Carrier type
1.	ZnS	0.53	0.36	79.0	n
2.	SnO$_2$	2.12	6.96	56.2	n
3.	50ZS50Sn	3.96	3.66	67.6	n
4.	40ZS10Sn	0.67	1.04	40.3	n
5.	30ZS20Sn	1.37	1.66	50.9	n
6.	20ZS30Sn	2.02	2.28	55.3	n
7.	10ZS40Sn	2.77	2.90	59.7	n

7.3.6.2 Figure of merit analysis

Figure7.18. illustrates the bar graph of the Figure of merit of pure ZnS, SnO₂, and their composite thin films (ZS50Sn50, ZS40Sn10, ZS30Sn20, ZS20Sn30, and ZS10Sn10), which assesses transparent conducting material performance based on conductivity and transparency. A Higher Figure of merit depicts superior performance. Pure ZnS exhibits the lowest FoM of $1.0 \times 10^{-3} \Omega^{-1}$ while pure SnO₂ shows a considerably higher value of $2.0 \times 10^{-2} \Omega^{-1}$. Among all the composite samples, the 50% ZnS:50% SnO₂ composite (50ZS50Sn) demonstrates the highest Figure of Merit (FoM) of $2.5 \times 10^{-2} \Omega^{-1}$, signifying optimal electrical and optical performance. Increasing SnO₂ content in the composites generally enhances the FoM, with 10ZS40Sn, 20ZS30Sn, and 30ZS20Sn all displaying relatively high values. However, the 40ZS10Sn composite shows a distinct drop in the Figure of merit, nearing that of pure ZnS. Overall, the different compositions properly affect the material. It enhances the figure of merit value compared to ZnS and SnO₂ materials. As a result, the 50ZS50Sn composite demonstrates the highest figure of merit compared to the other prepared composites. This trend suggests that SnO₂ is crucial for Figure of merit enhancement, and higher SnO₂ incorporation substantially improves the material's suitability for electronic and optoelectronic applications.
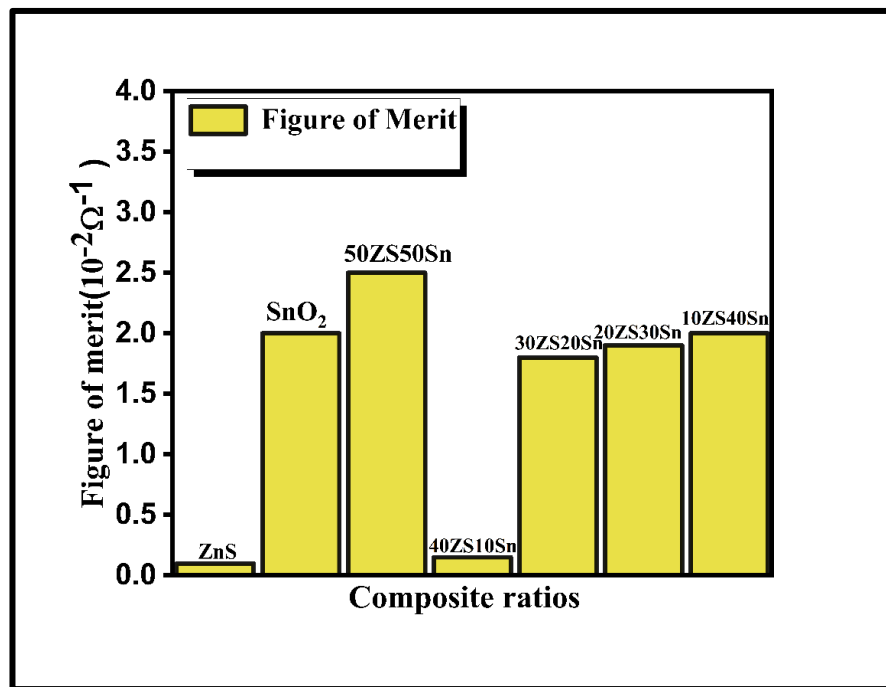
Fig.7.18. Figure of merit plot for pure ZnS, SnO₂, and Zn (S, Sn) thin film composites with different ratios.

7.3.7. Conclusion

This chapter indicated that Zn(S,Sn) ZnS-SnO$_2$ composite thin films were successfully formed by the sol–gel spin coating approach at different ratios, including ZS50Sn50, ZS40Sn10, ZS30Sn20, ZS20Sn30, ZS10Sn40.

1. XRD investigations demonstrated the successful formation of a mixed ZnS and SnO$_2$ phase structure. The study also revealed systematic changes in crystallite size, strain, and dislocation density, while confirming the absence of any secondary phases.

2. FTIR results confirmed the formation of Zn–S and Sn–O bonds, demonstrating chemical integration. Additionally, EDX mapping indicated a consistent elemental distribution across the samples, with no impurities.

3. FE-SEM images demonstrated morphological changes from uniform grain structures in pure films to increased agglomeration and particle size in composites, suggesting interfacial interaction between ZnS and SnO$_2$ composite thin films.

4. The transmission and band gap were investigated by UV-Visible spectroscopy. The different ratios of ZnS: SnO$_2$ composite thin films proper variation in the transmission and band gap. 50%ZnS:50%SnO$_2$ shows the highest transmission of 96% among all the compositions.

5. All composite thin films exhibited n-type semiconducting behavior. Notably, the 50% ZnS:50% SnO$_2$ composite achieved the highest conductivity (3.96×10^3) among all composite ratios and individual materials. This composition also displayed the superior figure of merit across all samples. Consequently, it is concluded that the 50% ZnS:50% SnO$_2$ composition significantly enhances the transmission and conductivity of the materials, rendering them suitable for applications as transparent conducting oxides (TCOs) and in gas sensors.

Chapter8

Summary, Conclusion, and Future Scope

8.1. Summary

The study presents a comparative analysis of various host materials. ZnO, SnO_2, and ZnS thin films, along with their doped variations incorporating Mg and Cu, and their composite Zn (O, S) and Zn (S, Sn). The materials were evaluated for their optical and electrical properties, including transmission (%), conductivity, carrier concentration, and figure of merit. The following are the main findings of the study.

❖ Among the three host materials analysed, such as ZnO, SnO_2, and ZnS thin films, the ZnS thin film exhibits the highest optical transmission at 95%, making it the most transparent. However, its electrical conductivity is significantly lower (5.29×10^2 Scm^{-1}) compared to ZnO (1.01×10^4 Scm^{-1}) and SnO_2 (2.21×10^3 Scm^{-1}). The figure of merit follows a similar trend, with ZnO demonstrating the highest value of $1.5 \times 10^{-1} \Omega^{-1}$, indicating a superior balance between optical transparency and electrical performance. Additionally, ZnO exhibits the highest carrier concentration ($1.68 \times 10^{21} cm^{-3}$), which contributes to its enhanced conductivity. In contrast, ZnS has a considerably lower carrier concentration ($0.36 \times 10^{18} cm^{-3}$), reflecting its reduced electrical performance despite its superior transparency. Overall, ZnO emerges as the most effective material for applications requiring a balance of high conductivity and reasonable transparency in optoelectronic devices such as flat panels, displays, photovoltaic devices, and solar cells. while ZnS could be favored for applications where optical clarity is the primary consideration.

❖ The doping of ZnO with Cu and Mg significantly alters its electrical and optical properties. Pure ZnO exhibits a carrier concentration of 1.68×10^{21} cm^{-3} with a conductivity of 1.01×10^4 Scm^{-1} and 83% optical transmission. Cu doping enhances carrier concentration, reaching 6.29×10^{21} cm^{-3} at 1.0% doping, while conductivity increases to 1.21×10^4 Scm^{-1} and transmission improves to 96.8%. Similarly, Mg doping also modifies properties, with a maximum carrier

concentration of 3.83×10^{21} cm^{-3} at 0.1% doping, but conductivity decreases at higher concentrations. Overall, Cu: ZnO demonstrates superior electrical properties with enhanced carrier concentration and conductivity, while Mg: ZnO offers improved transparency but exhibits reduced electrical performance at higher doping levels.

❖ Doping SnO$_2$ with Mg and Cu leads to significant modifications in its electrical and optical properties. Undoped SnO$_2$ exhibits a carrier concentration of 6.96×10^{19} cm^{-3} with a conductivity of 2.21×10^3 Scm^{-1} and a transmission of 90.5%. With increasing Mg content, the highest transmission (99.5%) is achieved at 0.5% doping, along with improved conductivity (8.42×10^3 Scm^{-1}). However, the figure of merit value is also higher, which is 2.9×10^{-2} for 0.5% Mg: SnO$_2$ doping. Cu doping enhances electrical properties, with a carrier concentration reaching 8.68×10^{19} cm^{-3} and a conductivity value 7.899×10^3 Scm^{-1} for 0.5% doping, though optical transmission and conductivity reduce at 1.0% doping to 95.8% and 5.053×10^3 Scm^{-1}. Overall, 0.5% Mg-doped SnO$_2$ demonstrates superior electrical performance compared to Cu doped SnO$_2$. Thus, 0.5% Mg-doped SnO$_2$ film also exhibited the highest figure of merit ($2.9 \times 10^{-2} \Omega^{-1}$), affirming its potential as a cost-effective TCO in optoelectronic devices such as flat panels, displays, photovoltaic devices, and solar cells.

❖ Doping ZnS with Cu and Mg affects its electrical and optical properties, leading to noticeable variations in carrier concentration, conductivity, and transmission. Undoped ZnS has a carrier concentration of 0.36×10^{18} cm^{-3}, a conductivity of 5.29×10^2 Scm^{-1}, and a high transmission of 95%. Cu doping at 0.5% significantly enhances carrier concentration to 3.93×10^{18} cm^{-3} and increases conductivity to 7.85×10^2 Scm^{-1}, while transmission reaches 98.7%, indicating improved optoelectronic properties. Mg doping, while improving transmission to a maximum of 96.7% at 0.5%, results in comparatively lower electrical conductivity (6.23×10^2 Scm^{-1}). The highest figure of merit value 1.55×10^{-3} $^2\Omega^{-1}$ was achieved at 0.5% Cu doping, while Mg doping maintains lower values. Overall, Cu doping provides superior electrical conductivity and enhanced transparency.

❖ Transparent conductive materials, including ZnS, SnO_2, and ZnO-based composites, in terms of carrier concentration, electrical conductivity, optical transmission, and figure of merit.

   o Carrier Concentration: The highest carrier concentration is observed in ZnO-based materials (10^{21} cm^{-3} range), indicating superior charge carrier density compared to ZnS and SnO_2-based composites.

   o Electrical Conductivity: ZnO exhibits the highest conductivity ($\sim 10^4$ Scm^{-1}), making it a highly efficient transparent conductive oxide. SnO_2 and ZnS-based materials show lower conductivity.

   o Optical Transmission ZnS and its doped composites generally demonstrate high transparency (>95%), while ZnO-based materials exhibit slightly lower transparency (~ 83–94%), depending on composition.

   o Figure of Merit: ZnO-based materials, particularly the composition of ZnO: SnO_2 (40:10%) show the highest FOM ($\sim 1.1 \times 10^{-1} \Omega^{-1}$), suggesting an optimal balance between conductivity and transparency. ZnS-based materials exhibit much lower ($\sim 10^{-3}$ range), implying their lower suitability for applications requiring high electrical conductivity.

ZnO-based composites, especially ZnO: SnO_2 (40:10%), present the best combination of high conductivity and moderate transparency, making them promising candidates for optoelectronic applications. ZnS-based materials are highly transparent but have much lower conductivity, suggesting their primary use in applications where optical clarity is critical rather than charge transport efficiency. This evaluation suggests ZnO-based materials, particularly ZnO: SnO_2 composites, are more suitable for applications requiring high-performance transparent conductive oxides (TCOs).

8.2. Conclusion

To conclude, the study provides a comprehensive evaluation of ZnO, SnO_2, and ZnS-based transparent conductive materials, including their doped variations with Cu and Mg. The key findings highlight the superior balance of electrical conductivity and

optical transparency in ZnO-based materials, particularly the ZnO: SnO_2 (40%:10%) composite, making them the most suitable candidates for optoelectronic applications requiring efficient charge transport and light transmission.

8.2.1 Key Finding

- ZnO-based materials exhibit the highest carrier concentration ($\sim 10^{21}$ cm^{-3}) and electrical conductivity ($\sim 10^4$ Scm^{-1}), making them the best-performing transparent conductive oxides (TCOs).
- ZnS-based materials offer exceptional optical transmission (>95%) but suffer from low conductivity, limiting their suitability for applications requiring efficient charge transport.
- Cu doping generally enhances carrier concentration and electrical conductivity, improving material performance, while Mg doping optimizes transparency but may reduce conductivity at higher concentrations.
- ZnO-SnO_2 composites achieve an optimal balance, with ZnO: SnO_2(40:10%) demonstrating one of the highest figures of merit ($\sim 1.1 \times 10^{-1}$), confirming its potential for transparent electrodes and optoelectronic applications.

In summary, ZnO materials and ZnO-based composites, especially ZnO, provide the best combination of electrical and optical properties, making them the most promising candidates for next-generation transparent conductive materials. ZnS-based variants, while highly transparent, are better suited for applications where optical clarity is prioritized over conductivity.

8.3. Future Scope

Transparent conducting oxides (TCOs) such as ZnO, SnO_2, In_2O_3, ITO, and FTO are widely used as sensing materials due to their excellent electrical conductivity, optical transparency, and chemical stability. They operate as chemiresistive or optical sensors, where interaction with gases, humidity, or biomolecules alters their electrical or optical properties. TCO-based sensors find applications in environmental and biomedical monitoring. In air-quality monitoring, ZnO and SnO_2 thin film sensors detect toxic and

flammable gases such as CO, NO_2, and H_2S at trace levels. In biomedical domains, TCOs are utilized in breath analyzers to detect volatile organic compounds (VOCs) indicative of diseases such as diabetes or lung infections. Additionally, glucose biosensors based on ITO electrodes immobilized with enzymes (e.g., glucose oxidase) enable non-invasive and highly sensitive glucose detection through electrochemical or optical readouts. Doping and nanostructuring enhance their sensitivity and selectivity. Due to their transparency and flexibility, TCOs are also integrated into wearable health devices and smart display-based environmental sensors.

References

[1]   J. Jang, Y. Kang, D. Cha, J. Bae, and S. Lee, "Thin-Film Optical Devices Based on Transparent Conducting Oxides: Physical Mechanisms and Applications," *Crystals*, vol. 9, no. 4, p. 192, Apr. 2019, doi: 10.3390/cryst9040192.

[2]   Preeti and S. Kumar, "Extraction and analysis of TCO coated glass from waste amorphous silicon thin film solar module," *Sol. Energy Mater. Sol. Cells*, vol. 253, p. 112227, May 2023, doi: 10.1016/j.solmat.2023.112227.

[3]   P. Kwaśnicki, A. Gronba-Chyła, A. Generowicz, J. Ciuła, A. Makara, and Z. Kowalski, "Characterization of the TCO Layer on a Glass Surface for PV IInd and IIIrd Generation Applications," *Energies*, vol. 17, no. 13, p. 3122, Jun. 2024, doi: 10.3390/en17133122.

[4]   G. T. Chavan *et al.*, "A Brief Review of Transparent Conducting Oxides (TCO): The Influence of Different Deposition Techniques on the Efficiency of Solar Cells," *Nanomaterials*, vol. 13, no. 7, p. 1226, Mar. 2023, doi: 10.3390/nano13071226.

[5]   J. Jeong *et al.*, "Transparent conducting oxides SrNbO3 thin film with record high figure of merit," *J. Eur. Ceram. Soc.*, vol. 44, no. 11, pp. 6764–6770, Sep. 2024, doi: 10.1016/j.jeurceramsoc.2024.04.050.

[6]   P. P. Edwards, A. Porch, M. O. Jones, D. V. Morgan, and R. M. Perks, "Basic materials physics of transparent conducting oxides," *Dalt. Trans.*, no. 19, p. 2995, 2004, doi: 10.1039/b408864f.

[7]   J. Gosciniak and J. B. Khurgin, "Transparent conductive oxides as a material platform for a realization of all-optical photonic neural networks," *Sci. Rep.*, vol. 15, no. 1, pp. 1–10, 2025, doi: 10.1038/s41598-025-96226-w.

[8]   S. C. Dixon, D. O. Scanlon, C. J. Carmalt, and I. P. Parkin, "N-Type doped transparent conducting binary oxides: An overview," *J. Mater. Chem. C*, vol. 4, no. 29, pp. 6946–6961, 2016, doi: 10.1039/c6tc01881e.

[9]   S. Yun *et al.*, "New-generation integrated devices based on dye-sensitized and perovskite solar cells," *Energy Environ. Sci.*, vol. 11, no. 3, pp. 476–526, 2018, doi: 10.1039/C7EE03165C.

[10]   J. Werner *et al.*, "Parasitic Absorption Reduction in Metal Oxide-Based Transparent Electrodes: Application in Perovskite Solar Cells," *ACS Appl. Mater. Interfaces*, vol. 8, no. 27, pp. 17260–17267, Jul. 2016, doi: 10.1021/acsami.6b04425.

[11]   G. R. A. Kumara *et al.*, "Large area dye-sensitized solar cells: material aspects of fabrication," *Prog. Photovoltaics Res. Appl.*, vol. 14, no. 7, pp. 643–651, Nov. 2006, doi: 10.1002/pip.695.

[12]   Y. Zhang, L. Li, H. Su, W. Huang, and X. Dong, "Binary metal oxide: advanced energy storage materials in supercapacitors," *J. Mater. Chem. A*, vol. 3, no. 1, pp. 43–59, 2015, doi: 10.1039/C4TA04996A.

[13]   M. Morales-Masis *et al.*, "An Indium-Free Anode for Large-Area Flexible OLEDs: Defect-Free Transparent Conductive Zinc Tin Oxide," *Adv. Funct. Mater.*, vol. 26, no. 3, pp. 384–392, Jan. 2016, doi: 10.1002/adfm.201503753.

[14]   J. T. Wang *et al.*, "Morphology control of fluorine-doped tin oxide thin films for enhanced light trapping," *Sol. Energy Mater. Sol. Cells*, vol. 132, pp. 578–588, Jan. 2015, doi: 10.1016/j.solmat.2014.09.043.

[15]   Y. Sun *et al.*, "Antimony-Doped Tin Oxide Nanorods as a Transparent Conducting Electrode for Enhancing Photoelectrochemical Oxidation of Water by Hematite," *ACS Appl. Mater. Interfaces*, vol. 6, no. 8, pp. 5494–5499, Apr. 2014, doi: 10.1021/am405628r.

[16]   M. Boomashri, P. Perumal, H. T. Das, V. Ganesh, and I. S. Yahia, "Effect of Ag on ammonia sensing of nanostructured SnO2 films at ambient room conditions," *J. Mater. Sci.*, vol. 57, no. 16, pp. 7941–7953, 2022, doi: 10.1007/s10853-022-07166-z.

[17]   H. Kim *et al.*, "High-Durable AgNi Nanomesh Film for a Transparent Conducting Electrode," *Small*, vol. 10, no. 18, pp. 3767–3774, Sep. 2014, doi:

10.1002/smll.201400911.

[18]   K. Bädeker, "Über die elektrische Leitfähigkeit und die thermoelektrische Kraft einiger Schwermetallverbindungen," *Ann. Phys.*, vol. 327, no. 4, pp. 749–766, Jan. 1907, doi: 10.1002/andp.19073270409.

[19]   K. L. Chopra, S. Major, and D. K. Pandya, "Transparent conductors—A status review," *Thin Solid Films*, vol. 102, no. 1, pp. 1–46, Apr. 1983, doi: 10.1016/0040-6090(83)90256-0.

[20]   "Constitution and mechanism of the selenium rectifier photocell," *Proc. R. Soc. London. Ser. A. Math. Phys. Sci.*, vol. 202, no. 1071, pp. 449–466, Aug. 1950, doi: 10.1098/rspa.1950.0112.

[21]   E. A. Danilov, V. M. Samoilov, V. S. Dmitrieva, A. V. Nikolaeva, D. V. Ponomareva, and E. I. Timoshchuk, "Manufacturing Transparent Conducting Films Based on Directly Exfoliated Graphene Particles via Langmuir–Blodgett Technique," *Inorg. Mater. Appl. Res.*, vol. 9, no. 5, pp. 794–802, 2018, doi: 10.1134/S2075113318050064.

[22]   D. B. Fraser and H. D. Cook, "Highly Conductive, Transparent Films of Sputtered In[sub 2−x]Sn[sub x]O[sub 3−y]," *J. Electrochem. Soc.*, vol. 119, no. 10, p. 1368, 1972, doi: 10.1149/1.2403999.

[23]   L. Holland and G. Siddall, "the properties of some reactively sputtered metal oxide films," *Vacuum*, vol. 3, no. 4, pp. 375–391, Oct. 1953, doi: 10.1016/0042-207X(53)90411-4.

[24]   G. Haacke, "Transparent Conducting Coatings," *Annu. Rev. Mater. Sci.*, vol. 7, no. 1, pp. 73–93, Aug. 1977, doi: 10.1146/annurev.ms.07.080177.000445.

[25]   Z. M. Jarzebski, "Preparation and physical properties of transparent conducting oxide films," *Phys. status solidi*, vol. 71, no. 1, pp. 13–41, May 1982, doi: 10.1002/pssa.2210710102.

[26]   Y. Xu *et al.*, "Indium tin oxide as a dual-band compatible stealth material with low infrared emissivity and strong microwave absorption," *J. Mater. Chem. C*,

vol. 11, no. 5, pp. 1754–1763, 2023, doi: 10.1039/D2TC04722E.

[27]   M. Lokanc, R. Eggert, and M. Redlinger, "The Availability of Indium: The Present, Medium Term, and Long Term," *Natl. Renew. Energy Lab.*, no. October, pp. 1–90, 2015, [Online]. Available: www.nrel.gov/publications.%0Ahttp://www.osti.gov/servlets/purl/1327212/%0 Ahttps://www.nrel.gov/docs/fy16osti/62409.pdf

[28]   "Mineral commodity summaries 2015," 2015. doi: 10.3133/70140094.

[29]   M. Lokanc, R. Eggert, and M. Redlinger, "The Availability of Indium: The Present, Medium Term, and Long Term," Golden, CO (United States), Oct. 2015. doi: 10.2172/1327212.

[30]   European Commission, *Critical Raw Materials Factsheets (2020)*. 2020. doi: 10.2873/92480.

[31]   A. K. Sahoo, W.-C. Au, and C.-L. Pan, "Characterization of Indium Tin Oxide (ITO) Thin Films towards Terahertz (THz) Functional Device Applications," *Coatings*, vol. 14, no. 7, p. 895, Jul. 2024, doi: 10.3390/coatings14070895.

[32]   R. Ramanathan, A. Kumar, H. Rao, and R. K. Samudrala, "Enhancement of Optoelectronic Properties of Ag-Doped SnO 2 Thin Film-Based Electrodes for DSSC Application," *ACS Omega*, Nov. 2025, doi: 10.1021/acsomega.5c05553.

[33]   Y. Kumar, M. S. Shishodia, and B. P. Singh, "Transparent conducting oxides (TCOs) based gratings for light absorption in near infrared spectrum," *Results Opt.*, vol. 13, p. 100542, Dec. 2023, doi: 10.1016/j.rio.2023.100542.

[34]   C. K. T. Chew, C. Salcianu, P. Bishop, C. J. Carmalt, and I. P. Parkin, "Functional thin film coatings incorporating gold nanoparticles in a transparent conducting fluorine doped tin oxide matrix," *J. Mater. Chem. C*, vol. 3, no. 5, pp. 1118–1125, 2015, doi: 10.1039/C4TC02275K.

[35]   D. S. Bhachu, G. Sankar, and I. P. Parkin, "Aerosol Assisted Chemical Vapor Deposition of Transparent Conductive Zinc Oxide Films," *Chem. Mater.*, vol. 24, no. 24, pp. 4704–4710, Dec. 2012, doi: 10.1021/cm302913b.

[36] S. Kahraman, H. M. Çakmak, S. Çetinkaya, F. Bayansal, H. A. Çetinkara, and H. S. Güder, "Characteristics of ZnO thin films doped by various elements," *J. Cryst. Growth*, vol. 363, pp. 86–92, Jan. 2013, doi: 10.1016/j.jcrysgro.2012.10.018.

[37] S. Jin *et al.*, "Tuning the Properties of Transparent Oxide Conductors. Dopant Ion Size and Electronic Structure Effects on CdO-Based Transparent Conducting Oxides. Ga- and In-Doped CdO Thin Films Grown by MOCVD," *Chem. Mater.*, vol. 20, no. 1, pp. 220–230, Jan. 2008, doi: 10.1021/cm702588m.

[38] M. Fujita, "Nanocavity brightens silicon," *Nat. Photonics*, vol. 7, no. 4, pp. 264–265, Apr. 2013, doi: 10.1038/nphoton.2013.65.

[39] L. Pauling, "THE NATURE OF THE CHEMICAL BOND. IV. THE ENERGY OF SINGLE BONDS AND THE RELATIVE ELECTRONEGATIVITY OF ATOMS," *J. Am. Chem. Soc.*, vol. 54, no. 9, pp. 3570–3582, Sep. 1932, doi: 10.1021/ja01348a011.

[40] K. Dagenais, M. Chamberlin, and C. Constantin, "Modeling Energy Band Gap as a Function of Optical Electronegativity for Binary Oxides," *J. Young Investig.*, vol. 25, no. 3, pp. 73–78, 2013.

[41] S. Mishra and B. Ganguli, "Effect of p–d hybridization, structural distortion and cation electronegativity on electronic properties of ZnSnX2 (X=P, As, Sb) chalcopyrite semiconductors," *J. Solid State Chem.*, vol. 200, pp. 279–286, Apr. 2013, doi: 10.1016/j.jssc.2013.01.007.

[42] S. Chen, X. G. Gong, and S. H. Wei, "Band-structure anomalies of the chalcopyrite semiconductors CuGa X2 versus AgGa X2 (X=S and Se) and their alloys," *Phys. Rev. B - Condens. Matter Mater. Phys.*, vol. 75, no. 20, pp. 1–9, 2007, doi: 10.1103/PhysRevB.75.205209.

[43] A. Klein *et al.*, "Transparent Conducting Oxides for Photovoltaics: Manipulation of Fermi Level, Work Function and Energy Band Alignment," *Materials (Basel).*, vol. 3, no. 11, pp. 4892–4914, Nov. 2010, doi:

10.3390/ma3114892.

[44] M. Sygletou, S. Benedetti, A. di Bona, M. Canepa, and F. Bisio, "Doping-Dependent Optical Response of a Hybrid Transparent Conductive Oxide/Plasmonic Medium," *J. Phys. Chem. C*, vol. 126, no. 4, pp. 1881–1889, Feb. 2022, doi: 10.1021/acs.jpcc.1c07567.

[45] A. Sultanov, I. Zhirkov, K. Nussupov, A. Kusainova, N. Abdyldayeva, and N. Beisenkhanov, "Investigation on optical and electrical properties of multilayer ITO/AZO/ITO transparent conductive oxides," *Opt. Mater. (Amst).*, vol. 155, p. 115850, Sep. 2024, doi: 10.1016/j.optmat.2024.115850.

[46] Materion, "TransparentConductiveOxideThinFilms.pdf," *Materion*, 2016, [Online]. Available: https://fdocuments.in/document/transparent-conductive-oxide-thin-films-materion.html

[47] L. Castañeda, "Present Status of the Development and Application of Transparent Conductors Oxide Thin Solid Films," *Mater. Sci. Appl.*, vol. 02, no. 09, pp. 1233–1242, 2011, doi: 10.4236/msa.2011.29167.

[48] A. Regoutz, K. H. L. Zhang, R. G. Egdell, D. Wermeille, and R. A. Cowley, "A study of (111) oriented epitaxial thin films of In 2 O 3 on cubic Y-doped ZrO 2 by synchrotron-based x-ray diffraction," *J. Mater. Res.*, vol. 27, no. 17, pp. 2257–2264, Sep. 2012, doi: 10.1557/jmr.2012.162.

[49] B. Huang, H.-L. Chu, M.-C. Wang, W.-S. Hwang, C. Liu, and X. Zhao, "Crystallite growth and optical properties of cadmium oxide thin films annealed at various temperatures for various durations," *J. Taiwan Inst. Chem. Eng.*, vol. 80, pp. 842–851, Nov. 2017, doi: 10.1016/j.jtice.2017.07.007.

[50] V. N. Jafarova and G. S. Orudzhev, "Structural and electronic properties of ZnO: A first-principles density-functional theory study within LDA(GGA) and LDA(GGA)+U methods," *Solid State Commun.*, vol. 325, p. 114166, Feb. 2021, doi: 10.1016/j.ssc.2020.114166.

[51] A. Svane and E. Antoncik, "Electronic structure of rutile SnO2, GeO2 and TeO2," *J. Phys. Chem. Solids*, vol. 48, no. 2, pp. 171–180, Jan. 1987, doi:

10.1016/0022-3697(87)90081-3.

[52] N. Dengo, A. Vittadini, M. M. Natile, and S. Gross, "In-Depth Study of ZnS
Nanoparticle Surface Properties with a Combined Experimental and
Theoretical Approach," *J. Phys. Chem. C*, vol. 124, no. 14, pp. 7777–7789,
Apr. 2020, doi: 10.1021/acs.jpcc.9b11323.

[53] L. K. Ping, D. D. Berhanuddin, A. K. Mondal, P. S. Menon, and M. A.
Mohamed, "Properties and perspectives of ultrawide bandgap Ga2O3 in
optoelectronic applications," *Chinese J. Phys.*, vol. 73, pp. 195–212, Oct. 2021,
doi: 10.1016/j.cjph.2021.06.015.

[54] H. Sato, T. Minami, S. Takata, and T. Yamada, "Transparent conducting p-type
NiO thin films prepared by magnetron sputtering," *Thin Solid Films*, vol. 236,
no. 1–2, pp. 27–31, Dec. 1993, doi: 10.1016/0040-6090(93)90636-4.

[55] J. Singh and P. Bhardwaj, *Progress in Developing Highly Efficient p-Type
TCOs for Transparent Electronics: A Comprehensive Review*, vol. 53, no. 12.
Springer US, 2024. doi: 10.1007/s11664-024-11445-7.

[56] Q. Shen, P. Yang, N. Li, M. Li, F. Chen, and L. Zhang, "Comprehensive
optimization of electrical and optical properties for ATO films prepared by
pulsed laser deposition," *J. Wuhan Univ. Technol. Sci. Ed.*, vol. 31, no. 1, pp.
20–26, Feb. 2016, doi: 10.1007/s11595-016-1323-x.

[57] T. W. Colburn, G. Crane, A. C. Flick, A. Carbone, R. D. Miller, and R. H.
Dauskardt, "Large-Area Ultrasonic Spray Manufacturing with Open-Air
Plasma Curing of Transparent Conducting Oxides for Thin Film Solar Cells
with High Figures of Merit via Solution Combustion Synthesis," *ECS Meet.
Abstr.*, vol. MA2024-02, no. 19, pp. 1749–1749, Nov. 2024, doi:
10.1149/MA2024-02191749mtgabs.

[58] S. Bakshi and S. Rani, "Investigating the Impact of Annealing and Thickness
on the Optical and Electrical Characteristics of ZnO (TCO) for Optoelectronics
Devices," *Int. J. Thin Film Sci. Technol.*, vol. 14, no. 2, pp. 139–149, May
2025, doi: 10.18576/ijtfst/140210.

[59] V. A. Coleman and C. Jagadish, "Basic Properties and Applications of ZnO," in *Zinc Oxide Bulk, Thin Films and Nanostructures*, Elsevier, 2006, pp. 1–20. doi: 10.1016/B978-008044722-3/50001-4.

[60] Z. M. Jarzebski and J. P. Marton, "Physical Properties of SnO2 Materials: II . Electrical Properties," *J. Electrochem. Soc.*, vol. 123, no. 9, pp. 299C-310C, Sep. 1976, doi: 10.1149/1.2133090.

[61] S. Mandal, S. K. Singh, P. Kumar, and U. P. Singh, "Tailoring the properties of ZnO thin films by low energy ion beam interaction," *J. Mater. Sci. Mater. Electron.*, vol. 36, no. 6, pp. 1–9, 2025, doi: 10.1007/s10854-025-14446-2.

[62] A. A. Al-Bayati and H. F. Ali, "Synthesis, Structural, and Optical Characterization of ZnO/SnO2 Nanocomposites Thin Films Prepared by Spin Coating and Pulse Laser Deposition," *Iraqi J. Phys.*, vol. 23, no. 1, pp. 68–77, Mar. 2025, doi: 10.30723/ijp.v23i1.1334.

[63] F. Ceh-Cih, E. Camacho-Espinosa, I. Rimmaudo, R. Mis-Fernández, S. Uc-Canché, and J. L. Peña, "Mg-doped SnO2 properties modulation applied to all-sputtered CdTe solar cells," *Sol. Energy*, vol. 273, no. April, p. 112549, May 2024, doi: 10.1016/j.solener.2024.112549.

[64] O. El Khouja *et al.*, "Investigation of structural and optical properties of Mg doped ZnS thin films prepared by Mist-CVD technique: Experimental and theoretical aspects," *Mater. Chem. Phys.*, vol. 313, no. August 2023, p. 128707, Feb. 2024, doi: 10.1016/j.matchemphys.2023.128707.

[65] R. S. R. Mummadi and K. Shaik, "Structural, Optical, and Electrical Properties of Cu-Doped ZnS Nanoparticles Prepared by Solid-State Reaction," *Brazilian J. Phys.*, vol. 54, no. 3, pp. 1–13, 2024, doi: 10.1007/s13538-024-01457-3.

[66] G. Mathew, P. Chamoli, A. Philip, and A. R. Kumar, "Effects of Copper Doping on the Electrochemical Performance of Tin Oxide Synthesised by Facile Co-precipitation Root," *Int. J. Environ. Res.*, vol. 18, no. 3, p. 48, Jun. 2024, doi: 10.1007/s41742-024-00587-5.

[67] H. S. Akkera, V. Mann, B. N. Varalakshmi, M. Ploloju, N. Kambhala, and G.

Venkatesh, "Effect of Sr-doped on physical and photoluminescence properties of SnO2 transparent conducting oxide thin films," *J. Mater. Sci. Mater. Electron.*, vol. 34, no. 12, p. 1044, Apr. 2023, doi: 10.1007/s10854-023-10473-z.

[68]   G. M. Mirza, M. M. H. Tusher, N. Sakib, and M. N. Islam, "Effect of Al-doping on morphology, structure, and optical band gap of ZnO thin films synthesized by sol–gel spin-coating technique," *J. Mater. Sci. Mater. Electron.*, vol. 34, no. 20, pp. 1–10, 2023, doi: 10.1007/s10854-023-10958-x.

[69]   R. S. Ali, H. S. Rasheed, N. D. Abdulameer, N. F. Habubi, and S. S. Chiad, "Physical properties of Mg doped ZnS thin films via spray pyrolysis," *Chalcogenide Lett.*, vol. 20, no. 3, pp. 187–196, Mar. 2023, doi: 10.15251/CL.2023.203.187.

[70]   P. Kumar, N. Prosenjit, S. Sachin, S. B. C. K. Mishra, and R. S. Katiyar, "The influence of post - growth heat treatment on the optical properties of pulsed laser deposited ZnO thin films," *Appl. Phys. A*, vol. 128, no. 5, pp. 1–9, 2022, doi: 10.1007/s00339-022-05511-2.

[71]   A. Tounsi, R. Khalfi, D. Talantikite-Touati, H. Merzouk, and A. Souici, "Characterization of cerium-doped zinc sulfide thin films synthesized by sol–gel method," *Appl. Phys. A Mater. Sci. Process.*, vol. 128, no. 4, pp. 1–11, 2022, doi: 10.1007/s00339-022-05409-z.

[72]   G. Kiruthiga, K. S. Rajni, N. Geethanjali, T. Raguram, E. Nandhakumar, and N. Senthilkumar, "SnO2: Investigation of optical, structural, and electrical properties of transparent conductive oxide thin films prepared by nebulized spray pyrolysis for photovoltaic applications," *Inorg. Chem. Commun.*, vol. 145, no. April, p. 109968, 2022, doi: 10.1016/j.inoche.2022.109968.

[73]   "Dopant-Concentration Dependent Optical and Structural Properties of Cu-Doped Zns Thin Films," vol. 12, no. 2, pp. 330–342, 2022, doi: 10.22052/JNS.2022.02.010.

[74]   A. Goudarzi, S. M. Langroodi, M. Arefkhani, and N. Samadani Langeroodi,

"Study of optical properties of ZnS and MnZnS (ZnS/MnS) nanostructure thin films; Prepared by microwave-assisted chemical bath deposition method," *Mater. Chem. Phys.*, vol. 275, no. August 2021, p. 125103, 2022, doi: 10.1016/j.matchemphys.2021.125103.

[75]] A F A M Yusof *et al.*, "Preparation And Characterization Of Composited Zinc Oxide (Zno)/ Tin Oxide (Sno 2) Nanostructure Film-Based Humidity Sensor By Electrospraying Method," *J. Pharm. Negat. Results ¦*, vol. 13, no. 7, p. 2022, 2022, doi: 10.47750/pnr.2022.13.S07.877.

[76] F. J. Serrao, N. N. Bappalige, K. M. Sandeep, and S. Raghavendra, "Dominance of c-axis orientation on the carrier transport properties of Sn doped ZnO thin films," *Thin Solid Films*, vol. 722, no. February, p. 138579, 2021, doi: 10.1016/j.tsf.2021.138579.

[77] J. Onyeka Emegha, B. Olofinjana, K. Eghonghon Ukhurebor, J. Taye Adegbite, and M. Adebola Eleruja, "Electrical Properties of Semiconducting Copper Zinc Sulphide Thin Films," *Curr. Appl. Sci. Technol.*, vol. 22, no. 1, pp. 1–9, May 2021, doi: 10.55003/cast.2022.01.22.003.

[78] S. I. Abbas, S. F. Hathot, A. S. Abbas, and A. A. Salim, "Influence of Cu doping on structure, morphology and optical characteristics of SnO2 thin films prepared by chemical bath deposition technique," *Opt. Mater. (Amst).*, vol. 117, p. 111212, Jul. 2021, doi: 10.1016/j.optmat.2021.111212.

[79] W. Fu *et al.*, "Achieving p-type conductivity in wide-bandgap SnO2 by a two-step process," *Appl. Phys. Lett.*, vol. 118, no. 11, Mar. 2021, doi: 10.1063/5.0045663.

[80] E. M. Bayan, V. V. Petrov, M. G. Volkova, V. Y. Storozhenko, and A. V. Chernyshev, "SnO2-ZnO nanocomposite thin films: The influence of structure, composition and crystallinity on optical and electrophysical properties," *J. Adv. Dielectr.*, vol. 11, no. 5, pp. 1–8, 2021, doi: 10.1142/S2010135X21600080.

[81] V. V. Petrov *et al.*, "Synthesis, Characterization and Gas Sensing Study of ZnO-SnO2 Nanocomposite Thin Films," *Chemosensors*, vol. 9, no. 6, p. 124,

May 2021, doi: 10.3390/chemosensors9060124.

[82] O. Osanyinlusi, "Preparation and Characterization of ZnS Thin Films Grown by Spin Coating Technique," *Tanzania J. Sci.*, vol. 46, no. 2, pp. 534–547, 2020, [Online]. Available: www.ajol.info/index.php/tjs/

[83] A. Islam, J. Robaiat, M. Faruk, H. A. M. M. Tanveer, and K. Kamruzzaman, "Alkaline and rare-earth metals doped transparent conductive tin oxide thin fi lms," *J. Sol-Gel Sci. Technol.*, pp. 304–313, 2020, doi: 10.1007/s10971-020-05362-4.

[84] K. R. Devi *et al.*, "Effect of Cu2+ doping on the structural, optical, and vapor-sensing properties of ZnO thin films prepared by SILAR method," *J. Mater. Sci. Mater. Electron.*, vol. 31, no. 19, pp. 16548–16560, 2020, doi: 10.1007/s10854-020-04210-z.

[85] Z. K. Heiba, M. B. Mohamed, A. M. El-naggar, and A. A. Albassam, "Effect of Mg and Cu doping on structural, optical, electronic, and thermal properties of ZnS quantum dots," *J. Mater. Sci. Mater. Electron.*, vol. 31, no. 23, pp. 21342–21354, Dec. 2020, doi: 10.1007/s10854-020-04647-2.

[86] L. Dong *et al.*, "Preparation of indium tin oxide (ITO) thin film with (400) preferred orientation by sol–gel spin coating method," *J. Mater. Sci. Mater. Electron.*, vol. 30, no. 8, pp. 8047–8054, Apr. 2019, doi: 10.1007/s10854-019-01126-1.

[87] M. A. Sayeed, M. R. Hasan, H. K. Rouf, and K. M. A. Hussain, "Structural and Optical Characterization of Tin (Sn) Doped Zinc Sulfide (ZnS) Thin Film," in *2019 4th International Conference on Electrical Information and Communication Technology (EICT)*, IEEE, Dec. 2019, pp. 1–5. doi: 10.1109/EICT48899.2019.9068756.

[88] T. Hurma, "The structural and optical properties of ZnS films optained by spraying solutions at different molarities," *Mater. Today Proc.*, vol. 18, no. May, pp. 1875–1881, 2019, doi: 10.1016/j.matpr.2019.06.676.

[89] W. Wu *et al.*, "Impact of thiourea concentration on the properties of sol–gel

derived Zn(O,S) thin films and Cu(In,Ga)Se2 solar cells," *J. Sol-Gel Sci. Technol.*, vol. 86, no. 2, pp. 266–273, May 2018, doi: 10.1007/s10971-018-4632-z.

[90] G. El Hallani *et al.*, "Comparative study for highly Al and Mg doped ZnO thin films elaborated by sol gel method for photovoltaic application," *J. Appl. Phys.*, vol. 121, no. 13, 2017, doi: 10.1063/1.4979724.

[91] K. M. Salman, M. Zikriya, and C. G. Renuka, "Impact of modified spin coating variations on electrical resistivity and UV detector responsivity in Mg-doped ZnO thin films," *Opt. Mater. (Amst).*, vol. 158, no. November 2024, p. 116460, 2025, doi: 10.1016/j.optmat.2024.116460.

[92] A. A. Hameed, J. F. Mohammad, and I. M. Ibrahim, "High sensitivity of UV photodetector based on - SnO 2 - ZnO / P - Si heterojunctions prepared by hydrothermal method," *Opt. Quantum Electron.*, vol. 57, no. 1, pp. 1–17, 2025, doi: 10.1007/s11082-024-08031-w.

[93] R. N. Jeyad and L. K. Abbas, "Optical And Structural Characteristics Of Sn-doped ZnS Thin Films For Sensing H2 Gas," *J. Opt.*, 2025, doi: 10.1007/s12596-025-02558-1.

[94] D. Namoune *et al.*, "Mg doping effect on the properties of SnO2 thin films synthesized by dip-coating method," *Phys. B Condens. Matter*, vol. 682, no. January, p. 415880, 2024, doi: 10.1016/j.physb.2024.415880.

[95] A. A. Ahmad, A. B. Migdadi, and Q. M. Al-Bataineh, "Structural, optical, and electrical properties of strontium-doped tin dioxide films for high photoconductivity," *Thin Solid Films*, vol. 796, no. July 2023, p. 140312, 2024, doi: 10.1016/j.tsf.2024.140312.

[96] B. El Filali, T. V Torchynska, I. C. B. Rodríguez, G. Polupan, and J. Douda, "Impact of Al and In co - doping on transmittance , bandgap energy , and electrical characteristics of ZnO films for TCO applications," *J. Mater. Sci. Mater. Electron.*, vol. 35, no. 16, pp. 1–6, 2024, doi: 10.1007/s10854-024-12773-4.

[97] O. Gençyılmaz, İ. Akyüz, and F. Atay, "Binary ZnS–ZnO films as an alternative buffer layer for solar cell applications," *Appl. Phys. A*, vol. 130, no. 4, p. 227, Apr. 2024, doi: 10.1007/s00339-024-07382-1.

[98] Q. Wang, J. Hu, and A. Song, "Influence of Oxygen Flow on Structural, Optical, and Electrical Properties of Al:SnO2 Films Deposited at Room Temperature," *J. Electron. Mater.*, vol. 53, no. 4, pp. 2094–2103, Apr. 2024, doi: 10.1007/s11664-023-10907-8.

[99] M. K. Abdel-Latif *et al.*, "Effect of doping on the structural, optical and electrical properties of La-doped ZnO thin films," *J. Mater. Sci. Mater. Electron.*, vol. 34, no. 4, pp. 1–14, 2023, doi: 10.1007/s10854-022-09477-y.

[100] I. Saoula, C. Siad, K. Djedidi, N. Allag, and A. Chala, "EFFECT OF (Al, Zn, Cu, AND Sr) DOPING ON STRUCTURAL, OPTICAL AND ELECTRICAL PROPERTIES OF SPRAYED SnO2 THIN FILMS," *Acta Metall. Slovaca*, vol. 29, no. 2, pp. 59–62, 2023, doi: 10.36547/ams.29.2.1730.

[101] B. Chander Joshi and A. K. Chaudhri, "Sol–Gel-Derived Cu-Doped ZnO Thin Films for Optoelectronic Applications," *ACS Omega*, vol. 7, no. 25, pp. 21877–21881, Jun. 2022, doi: 10.1021/acsomega.2c02040.

[102] P. Senthilkumar, S. Raja, R. Ramesh Babu, and G. Vasuki, "Enhanced electrical and optoelectronic properties of W doped SnO2 thin films," *Opt. Mater. (Amst).*, vol. 126, no. March, p. 112234, 2022, doi: 10.1016/j.optmat.2022.112234.

[103] K. Salim, "Study of the Effects of Annealing Temperature on the Properties of ZnO Thin Films Grown by Spray Pyrolysis Technique for Photovoltaic Applications," *Int. J. Thin Film Sci. Technol.*, vol. 11, no. 1, pp. 19–28, Jan. 2022, doi: 10.18576/ijtfst/110103.

[104] K. Derrar *et al.*, "Preparation of Sb:SnO2 thin films and its effect on opto-electrical properties," *J. Mater. Sci. Mater. Electron.*, vol. 33, no. 13, pp. 10142–10153, May 2022, doi: 10.1007/s10854-022-08004-3.

[105] L. Nulhakim, M. Rozana, B. Yuliarto, and H. Makino, "Electrical and optical

properties of Ga-doped ZnO thin films deposited by DC magnetron sputtering," *J. Sci. Appl. Technol.*, vol. 4, no. 1, p. 15, 2020, doi: 10.35472/jsat.v4i1.264.

[106] V. S. Ganesha Krishna and M. G. Mahesha, "Characterization of transparent p-type Cu:ZnS thin films grown by spray pyrolysis technique," *J. Alloys Compd.*, vol. 848, p. 156568, Dec. 2020, doi: 10.1016/j.jallcom.2020.156568.

[107] B. Barman, K. V. Bangera, and G. K. Shivakumar, "Preparation of thermally deposited Cux(ZnS)1-x thin films for opto-electronic devices," *J. Alloys Compd.*, vol. 772, pp. 532–536, 2019, doi: 10.1016/j.jallcom.2018.09.192.

[108] P. S., R. M. J., D. A. K. K., S. K. P.S., P. S., and A. L., "Physical properties of rare earth metal (Gd3+) doped SnO2 thin films prepared by simplified spray pyrolysis technique using nebulizer," *Optik (Stuttg).*, vol. 194, p. 162887, Oct. 2019, doi: 10.1016/j.ijleo.2019.05.093.

[109] C. Sabitha, I. H. Joe, K. D. A. Kumar, and S. Valanarasu, "Investigation of structural, optical and electrical properties of ZnS thin films prepared by nebulized spray pyrolysis for solar cell applications," *Opt. Quantum Electron.*, vol. 50, no. 3, p. 153, Mar. 2018, doi: 10.1007/s11082-018-1418-z.

[110] S. V. Borisov and N. V. Podberezskaya, "X-ray diffraction analysis: A brief history and achievements of the first century," *J. Struct. Chem.*, vol. 53, no. S1, pp. 1–3, Dec. 2012, doi: 10.1134/S0022476612070013.

[111] A. A. Bunaciu, E. gabriela Udriştioiu, and H. Y. Aboul-Enein, "X-Ray Diffraction: Instrumentation and Applications," *Crit. Rev. Anal. Chem.*, vol. 45, no. 4, pp. 289–299, Oct. 2015, doi: 10.1080/10408347.2014.949616.

[112] S. Zhang *et al.*, "Preparation method investigation and structure identification by XRD and Raman techniques for A 2 B 2 O 7 composite oxides," *J. Am. Ceram. Soc.*, vol. 107, no. 5, pp. 3475–3496, May 2024, doi: 10.1111/jace.19645.

[113] F. Gao, Z. Jia, Z. Cui, Y. Li, and H. Jiang, "Evolution of macromolecular structure during coal oxidation via FTIR, XRD and Raman," *Fuel Process. Technol.*, vol. 262, p. 108114, Oct. 2024, doi: 10.1016/j.fuproc.2024.108114.

[114] A. Chauhan, "Powder XRD Technique and its Applications in Science and Technology," *J. Anal. Bioanal. Tech.*, vol. 5, no. 6, 2014, doi: 10.4172/2155-9872.1000212.

[115] F. Berna, "Fourier Transform Infrared Spectroscopy (FTIR)," 2017, pp. 285–286. doi: 10.1007/978-1-4020-4409-0_15.

[116] A. Dutta, "Fourier Transform Infrared Spectroscopy," in *Spectroscopic Methods for Nanomaterials Characterization*, Elsevier, 2017, pp. 73–93. doi: 10.1016/B978-0-323-46140-5.00004-2.

[117] Z. Bacsik, J. Mink, and G. Keresztury, "FTIR Spectroscopy of the Atmosphere. I. Principles and Methods," *Appl. Spectrosc. Rev.*, vol. 39, no. 3, pp. 295–363, Dec. 2004, doi: 10.1081/ASR-200030192.

[118] H.-H. Chang, C.-L. Cheng, P.-J. Huang, and S.-Y. Lin, "Application of scanning electron microscopy and X-ray microanalysis: FE-SEM, ESEM-EDS, and EDS mapping for studying the characteristics of topographical microstructure and elemental mapping of human cardiac calcified deposition," *Anal. Bioanal. Chem.*, vol. 406, no. 1, pp. 359–366, Jan. 2014, doi: 10.1007/s00216-013-7414-z.

[119] J. Liu, "High-Resolution and Low-Voltage FE-SEM Imaging and Microanalysis in Materials Characterization," *Mater. Charact.*, vol. 44, no. 4–5, pp. 353–363, Apr. 2000, doi: 10.1016/S1044-5803(99)00076-5.

[120] Y. Yuan, Y. Shimada, S. Ichinose, and J. Tagami, "Qualitative analysis of adhesive interface nanoleakage using FE-SEM/EDS," *Dent. Mater.*, vol. 23, no. 5, pp. 561–569, May 2007, doi: 10.1016/j.dental.2006.03.015.

[121] M. Abd Mutalib, M. A. Rahman, M. H. D. Othman, A. F. Ismail, and J. Jaafar, "Scanning Electron Microscopy (SEM) and Energy-Dispersive X-Ray (EDX) Spectroscopy," in *Membrane Characterization*, Elsevier, 2017, pp. 161–179. doi: 10.1016/B978-0-444-63776-5.00009-7.

[122] H. Takagi, H. Shima, T. Ui, and E. Asada, "A fundamental parameter method for measurement of the thickness of pure element films by an EDX technique

with a proportional detector," *X-Ray Spectrom.*, vol. 13, no. 4, pp. 182–186, Apr. 1984, doi: 10.1002/xrs.1300130412.

[123] G. Binnig, C. F. Quate, and C. Gerber, "Atomic Force Microscope," *Phys. Rev. Lett.*, vol. 56, no. 9, pp. 930–933, Mar. 1986, doi: 10.1103/PhysRevLett.56.930.

[124] N. Ishida, "Atomic force microscopy," in *Non-Destructive Material Characterization Methods*, Elsevier, 2024, pp. 89–125. doi: 10.1016/B978-0-323-91150-4.00011-2.

[125] M. S. H. Akash and K. Rehman, "Ultraviolet-Visible (UV-VIS) Spectroscopy," in *Essentials of Pharmaceutical Analysis*, Singapore: Springer Nature Singapore, 2020, pp. 29–56. doi: 10.1007/978-981-15-1547-7_3.

[126] D. F. Swinehart, "The Beer-Lambert Law," *J. Chem. Educ.*, vol. 39, no. 7, p. 333, Jul. 1962, doi: 10.1021/ed039p333.

[127] J. Tauc, R. Grigorovici, and A. Vancu, "Optical Properties and Electronic Structure of Amorphous Germanium," *Phys. status solidi*, vol. 15, no. 2, pp. 627–637, Jan. 1966, doi: 10.1002/pssb.19660150224.

[128] Y. SINGH, "ELECTRICAL RESISTIVITY MEASUREMENTS: A REVIEW," *Int. J. Mod. Phys. Conf. Ser.*, vol. 22, pp. 745–756, Jan. 2013, doi: 10.1142/S2010194513010970.

[129] L. Shen, J. Li, B. M. Liaw, F. Delale, and J. H. Chung, "Modeling and analysis of the electrical resistance measurement of carbon fiber polymer–matrix composites," *Compos. Sci. Technol.*, vol. 67, no. 11–12, pp. 2513–2520, Sep. 2007, doi: 10.1016/j.compscitech.2006.12.020.

[130] D. H. Petersen, O. Hansen, R. Lin, and P. F. Nielsen, "Micro-four-point probe Hall effect measurement method," *J. Appl. Phys.*, vol. 104, no. 1, Jul. 2008, doi: 10.1063/1.2949401.

[131] E. H. Hall, "On a New Action of the Magnet on Electric Currents," *Am. J. Math.*, vol. 2, no. 3, p. 287, Sep. 1879, doi: 10.2307/2369245.

[132] A. A. Ramadan, R. D. Gould, and A. Ashour, "On the Van der Pauw method of resistivity measurements," *Thin Solid Films*, vol. 239, no. 2, pp. 272–275, Mar. 1994, doi: 10.1016/0040-6090(94)90863-X.

[133] Y. Wu, F. Cao, and X. Ji, "Optical and electrical properties of Al-doped ZnO thin films by atomic layer deposition," *J. Mater. Sci. Mater. Electron.*, vol. 31, no. 20, pp. 17365–17374, 2020, doi: 10.1007/s10854-020-04292-9.

[134] K. Park *et al.*, "Stretchable, Transparent Zinc Oxide Thin Film Transistors," *Adv. Funct. Mater.*, vol. 20, no. 20, pp. 3577–3582, Oct. 2010, doi: 10.1002/adfm.201001107.

[135] S. Jaballah *et al.*, "Effect of al and mg doping on reducing gases detection of zno nanoparticles," *Chemosensors*, vol. 9, no. 11, pp. 1–17, 2021, doi: 10.3390/chemosensors9110300.

[136] C. Zhou *et al.*, "ZnO for solar cell and thermoelectric applications," *Oxide-based Mater. Devices VIII*, vol. 10105, p. 101051K, 2017, doi: 10.1117/12.2262772.

[137] S. S. Bhat, S. J. Shetty, M. P. Shilpa, S. Shet, K. M. Eshwarappa, and S. C. Gurumurthy, "Neutron irradiation induced transmuted Ga-doping of ZnO thin films: Structural and opto-electronic investigations," *Ceram. Int.*, vol. 51, no. 2, pp. 2695–2700, 2024, doi: 10.1016/j.ceramint.2024.11.252.

[138] A. Zaidi, K. Tiwari, R. R. Awasthi, and K. C. Dubey, "Effect of sintering temperature on the structural, morphological and humidity sensing properties of ZnO nanostructure," *J. Ovonic Res.*, vol. 19, no. 4, pp. 411–419, Aug. 2023, doi: 10.15251/JOR.2023.194.411.

[139] A. Aravind, M. K. Jayaraj, M. Kumar, and R. Chandra, "Optical and magnetic properties of copper doped ZnO nanorods prepared by hydrothermal method," *J. Mater. Sci. Mater. Electron.*, vol. 24, no. 1, pp. 106–112, Jan. 2013, doi: 10.1007/s10854-012-0911-6.

[140] A. Jogi, A. Ayana, and B. V. Rajendra, "Modulation of optical and photoluminescence properties of ZnO thin films by Mg dopant," *J. Mater. Sci.*

Mater. Electron., vol. 34, no. 7, pp. 1–11, 2023, doi: 10.1007/s10854-023-09999-z.

[141] C. Abed, A. B. G. Trabelsi, F. H. Alkallas, S. Fernandez, and H. Elhouichet, "Transport Mechanisms and Dielectric Features of Mg-Doped ZnO Nanocrystals for Device Applications," *Materials (Basel).*, vol. 15, no. 6, 2022, doi: 10.3390/ma15062265.

[142] M. M. Rahman, K. S. Rahman, M. Rokonuzzaman, B. Z. Bhari, N. A. Ludin, and M. A. Ibrahim, "Impact of aluminium doping in magnesium-doped zinc oxide thin films by sputtering for photovoltaic applications," *J. Mater. Sci.*, vol. 59, no. 21, pp. 9472–9490, 2024, doi: 10.1007/s10853-024-09801-3.

[143] F. Hussain *et al.*, "An insight of Mg doped ZnO thin films: A comparative experimental and first-principle investigations," *Phys. E Low-Dimensional Syst. Nanostructures*, vol. 115, p. 113658, 2020, doi: 10.1016/j.physe.2019.113658.

[144] B. Chander Joshi and A. K. Chaudhri, "Sol–Gel-Derived Cu-Doped ZnO Thin Films for Optoelectronic Applications," *ACS Omega*, vol. 7, no. 25, pp. 21877–21881, Jun. 2022, doi: 10.1021/acsomega.2c02040.

[145] K. Joshi, M. Rawat, S. K. Gautam, R. G. Singh, R. C. Ramola, and F. Singh, "Band gap widening and narrowing in Cu-doped ZnO thin films," *J. Alloys Compd.*, vol. 680, pp. 252–258, Sep. 2016, doi: 10.1016/j.jallcom.2016.04.093.

[146] N. Siregar, Motlan, and J. Panggabean, "The effect magnesium (Mg) on structural and optical properties of ZnO:Mg thin film by sol-gel spin coating method," *J. Phys. Conf. Ser.*, vol. 1428, no. 1, p. 012026, Jan. 2020, doi: 10.1088/1742-6596/1428/1/012026.

[147] A. R. Abhijith, A. K. Srivastava, and A. Srivastava, "Synthesis and Characterization of Magnesium Doped ZnO Using Chemical Route," *J. Phys. Conf. Ser.*, vol. 1531, no. 1, p. 012005, May 2020, doi: 10.1088/1742-6596/1531/1/012005.

[148] K. Vijayalakshmi and K. Karthick, "Influence of annealing on the

photoluminescence of nanocrystalline ZnO synthesized by microwave processing," *Philos. Mag. Lett.*, vol. 92, no. 12, pp. 710–717, Dec. 2012, doi: 10.1080/09500839.2012.725947.

[149] N. H. Hashim, S. Subramani, M. Devarajan, and A. R. Ibrahim, "Properties of undoped ZnO and Mg doped ZnO thin films by sol-gel method for optoelectronic applications," *J. Aust. Ceram. Soc.*, vol. 53, no. 2, pp. 421–431, Oct. 2017, doi: 10.1007/s41779-017-0051-9.

[150] U. S. U. Thampy *et al.*, "Spectral Investigations on Cu2+-Doped ZnO Nanopowders," *Appl. Magn. Reson.*, vol. 41, no. 1, pp. 69–78, 2011, doi: 10.1007/s00723-011-0234-4.

[151] K. J. Arun, A. K. Batra, A. Krishna, K. Bhat, M. D. Aggarwal, and P. J. Joseph Francis, "Surfactant Free Hydrothermal Synthesis of Copper Oxide Nanoparticles," *Am. J. Mater. Sci.*, vol. 5, no. 3A, pp. 36–38, 2015, doi: 10.5923/s.materials.201502.06.

[152] A. Goktas, A. Tumbul, Z. Aba, and M. Durgun, "Mg doping levels and annealing temperature induced structural, optical and electrical properties of highly c-axis oriented ZnO:Mg thin films and Al/ZnO:Mg/p-Si/Al heterojunction diode," *Thin Solid Films*, vol. 680, no. August 2018, pp. 20–30, 2019, doi: 10.1016/j.tsf.2019.04.024.

[153] S. Bhardwaj *et al.*, "Comparative structural and optical studies of Al-/Sn-doped ZnO-textured films for optoelectronic application," *J. Mater. Sci. Mater. Electron.*, vol. 33, no. 17, pp. 13757–13770, 2022, doi: 10.1007/s10854-022-08308-4.

[154] L. Arab *et al.*, "Nanostructure zinc oxide with cobalt Dopant by PLD for gas sensor applications," *J. Mater. Sci. Mater. Electron.*, vol. 4, no. 2, p. 109968, 2020, doi: 10.1016/j.ceramint.2021.01.209.

[155] A. I. Istrate, I. Mihalache, C. Romanitan, O. Tutunaru, R. Gavrila, and V. Dediu, "Copper doping effect on the properties in ZnO films deposited by sol–gel," *J. Mater. Sci. Mater. Electron.*, vol. 32, no. 4, pp. 4021–4033, 2021, doi:

10.1007/s10854-020-05144-2.

[156] V. Doni Pon *et al.*, "Enhancement of optoelectronic properties of ZnO thin films by Al doping for photodetector applications," *Superlattices Microstruct.*, vol. 151, no. June 2020, 2021, doi: 10.1016/j.spmi.2020.106790.

[157] S. K. Singh and P. Hazra, "Performance analysis of undoped and Mg-doped ZnO/p-Si heterojunction diodes grown by sol–gel technique," *J. Mater. Sci. Mater. Electron.*, vol. 29, no. 6, pp. 5213–5223, 2018, doi: 10.1007/s10854-017-8486-x.

[158] E. C. Nwanna, P. E. Imoisili, and T.-C. Jen, "Synthesis and characterization of SnO2 thin films using metalorganic precursors," *J. King Saud Univ. - Sci.*, vol. 34, no. 5, p. 102123, Jul. 2022, doi: 10.1016/j.jksus.2022.102123.

[159] G. K. Mani and J. B. B. Rayappan, "Influence of copper doping on structural, optical and sensing properties of spray deposited zinc oxide thin films," *J. Alloys Compd.*, vol. 582, pp. 414–419, Jan. 2014, doi: 10.1016/j.jallcom.2013.07.146.

[160] A. Kumar and M. I. Ahmad, "Role of defects in the electronic properties of Al doped ZnO films deposited by spray pyrolysis," *J. Mater. Sci.*, vol. 57, no. 16, pp. 7877–7895, 2022, doi: 10.1007/s10853-022-07136-5.

[161] İ. Polat, S. Yılmaz, E. Bacaksız, Y. Atasoy, and M. Tomakin, "Synthesis and fabrication of Mg-doped ZnO-based dye-synthesized solar cells," *J. Mater. Sci. Mater. Electron.*, vol. 25, no. 7, pp. 3173–3178, Jul. 2014, doi: 10.1007/s10854-014-2000-5.

[162] N. Siregar, Motlan, and J. Panggabean, "The effect magnesium (Mg) on structural and optical properties of ZnO:Mg thin film by sol-gel spin coating method," *J. Phys. Conf. Ser.*, vol. 1428, no. 1, 2020, doi: 10.1088/1742-6596/1428/1/012026.

[163] I. Benaicha *et al.*, "SILAR-engineered ZnO thin films: exploring the impact of Ni, Co, and Fe dopants on structural, optical, and electronic properties," *J. Mater. Sci. Mater. Electron.*, vol. 35, no. 13, pp. 1–9, 2024, doi:

10.1007/s10854-024-12678-2.

[164] Y. Bouachiba *et al.*, "Optoelectronic and birefringence properties of weakly Mg-doped ZnO thin films prepared by spray pyrolysis," *J. Mater. Sci. Mater. Electron.*, vol. 33, no. 9, pp. 6689–6699, 2022, doi: 10.1007/s10854-022-07844-3.

[165] Y. S. Thakur, A. D. Acharya, S. Sharma, and Bhawna, "Reinforcement of V2O5 nanoparticle in polyaniline to improve the optical and UV- shielding properties," *Results Opt.*, vol. 11, no. March, p. 100400, 2023, doi: 10.1016/j.rio.2023.100400.

[166] N. Sharma and R. Kumar, "Zinc doped TiO 2 thin films for ethanol detection," *Inorg. Chem. Commun.*, vol. 162, no. October 2023, p. 112224, 2024, doi: 10.1016/j.inoche.2024.112224.

[167] M. Ferhat, A. Zaoui, and R. Ahuja, "Magnetism and band gap narrowing in Cu-doped ZnO," *Appl. Phys. Lett.*, vol. 94, no. 14, Apr. 2009, doi: 10.1063/1.3112603.

[168] M. Khan, M. S. Alam, and S. F. Ahmed, "Synthesis and Characterization of Copper Doped Zinc Oxide Thin Films Deposited by RF/DC Sputtering Technique," *J. Shanghai Jiaotong Univ.*, vol. 28, no. 2, pp. 172–179, Apr. 2023, doi: 10.1007/s12204-022-2462-1.

[169] B. Chander Joshi and A. K. Chaudhri, "Sol-Gel-Derived Cu-Doped ZnO Thin Films for Optoelectronic Applications," *ACS Omega*, vol. 7, no. 25, pp. 21877–21881, 2022, doi: 10.1021/acsomega.2c02040.

[170] Y. Hu, H. Zeng, J. Du, Z. Hu, and S. Zhang, "The structural, electrical and optical properties of Mg-doped ZnO with different interstitial Mg concentration," *Mater. Chem. Phys.*, vol. 182, pp. 15–21, Oct. 2016, doi: 10.1016/j.matchemphys.2016.05.065.

[171] K. Pradeev raj *et al.*, "Influence of Mg Doping on ZnO Nanoparticles for Enhanced Photocatalytic Evaluation and Antibacterial Analysis," *Nanoscale Res. Lett.*, vol. 13, no. 1, p. 229, Dec. 2018, doi: 10.1186/s11671-018-2643-x.

[172] C. R. Dhas, R. Venkatesh, R. Sivakumar, A. M. E. Raj, and C. Sanjeeviraja, "Effect of solution molarity on optical dispersion energy parameters and electrochromic performance of Co3O4 films," *Opt. Mater. (Amst).*, vol. 72, pp. 717–729, Oct. 2017, doi: 10.1016/j.optmat.2017.07.026.

[173] M. R. Rahman *et al.*, "Conductive and optically transparent sol–gel spin coated Al3+ and Sn4+ doped ZnO nano-crystalline thin-films," *J. Mater. Sci. Mater. Electron.*, vol. 35, no. 24, pp. 1–22, 2024, doi: 10.1007/s10854-024-13328-3.

[174] E. F. I. Roberts and D. Ross, "Anomalous optical constants of thin films," *Surf. Sci.*, vol. 56, pp. 425–439, Jun. 1976, doi: 10.1016/0039-6028(76)90463-5.

[175] B. Mehmood, M. I. Khan, M. Iqbal, A. Mahmood, and W. Al-Masry, "Structural and optical properties of Ti and Cu co-doped <scp>ZnO</scp> thin films for photovoltaic applications of dye sensitized solar cells," *Int. J. Energy Res.*, vol. 45, no. 2, pp. 2445–2459, Feb. 2021, doi: 10.1002/er.5939.

[176] G. Rey, C. Ternon, M. Modreanu, X. Mescot, V. Consonni, and D. Bellet, "Electron scattering mechanisms in fluorine-doped SnO2 thin films," *J. Appl. Phys.*, vol. 114, no. 18, Nov. 2013, doi: 10.1063/1.4829672.

[177] M. Ahmed, A. H. Abdel-Aty, K. Alshehri, A. Alshahrie, N. Al-Harbi, and E. R. Shaaban, "Structure, optical properties, and electrical properties of low copper-doped cadmium oxide thin films for optoelectronic applications," *Indian J. Phys.*, vol. 98, no. November, pp. 4161–4170, 2024, doi: 10.1007/s12648-024-03167-7.

[178] B. Santoshkumar *et al.*, "Influence of defect luminescence and structural modification on the electrical properties of Magnesium Doped Zinc Oxide Nanorods," *Superlattices Microstruct.*, vol. 106, pp. 58–66, Jun. 2017, doi: 10.1016/j.spmi.2017.03.039.

[179] S. Salam, M. Islam, and A. Akram, "Sol-gel synthesis of intrinsic and aluminum-doped zinc oxide thin films as transparent conducting oxides for thin film solar cells," *Thin Solid Films*, vol. 529, pp. 242–247, 2013, doi: 10.1016/j.tsf.2012.10.079.

[180] S. K. Misra and N. K. Pandey, "Study of activation energy and humidity sensing application of nanostructured Cu-doped ZnO thin films," *J. Mater. Res.*, vol. 31, no. 20, pp. 3214–3222, 2016, doi: 10.1557/jmr.2016.322.

[181] T. Prasada Rao and M. C. Santhoshkumar, "Effect of thickness on structural, optical and electrical properties of nanostructured ZnO thin films by spray pyrolysis," *Appl. Surf. Sci.*, vol. 255, no. 8, pp. 4579–4584, Feb. 2009, doi: 10.1016/j.apsusc.2008.11.079.

[182] G. Haacke, "New figure of merit for transparent conductors," *J. Appl. Phys.*, vol. 47, no. 9, pp. 4086–4089, Sep. 1976, doi: 10.1063/1.323240.

[183] Y. Wu, F. Cao, and X. Ji, "Optical and electrical properties of Al-doped ZnO thin films by atomic layer deposition," *J. Mater. Sci. Mater. Electron.*, vol. 31, no. 20, pp. 17365–17374, Oct. 2020, doi: 10.1007/s10854-020-04292-9.

[184] N. H. Touidjen, M. LamriZeggar, M. S. Aida, S. Rouabah, and N. Aouabdia, "Volatile Organic Compound Gas Sensing Applications of n-Type SnO2 and p-Type CuO Based on Thin Films," *J. Electron. Mater.*, vol. 53, no. 1, pp. 515–524, 2024, doi: 10.1007/s11664-023-10559-8.

[185] S. Calnan and A. N. Tiwari, "High mobility transparent conducting oxides for thin film solar cells," *Thin Solid Films*, vol. 518, no. 7, pp. 1839–1849, Jan. 2010, doi: 10.1016/j.tsf.2009.09.044.

[186] S. Krishnamoorthy and A. A. Iliadis, "Properties of high sensitivity ZnO surface acoustic wave sensors on SiO2/(100) Si substrates," *Solid. State. Electron.*, vol. 52, no. 11, pp. 1710–1716, Nov. 2008, doi: 10.1016/j.sse.2008.06.039.

[187] R. A. Afre, N. Sharma, M. Sharon, and M. Sharon, "Transparent Conducting Oxide Films for Various Applications: A Review," *Rev. Adv. Mater. Sci.*, vol. 53, no. 1, pp. 79–89, Jan. 2018, doi: 10.1515/rams-2018-0006.

[188] S. Haya, O. Brahmia, O. Halimi, M. Sebais, and B. Boudine, "Sol–gel synthesis of Sr-doped SnO 2 thin films and their photocatalytic properties," *Mater. Res. Express*, vol. 4, no. 10, p. 106406, Oct. 2017, doi: 10.1088/2053-

1591/aa8deb.

[189] J. Ren, K. Li, J. Shen, C. Sheng, Y. Huang, and Q. Zhang, "Effects of rare-earth erbium doping on the electrical performance of tin-oxide thin film transistors," *J. Alloys Compd.*, vol. 791, pp. 11–18, Jun. 2019, doi: 10.1016/j.jallcom.2019.03.277.

[190] S. Maheswari, M. K. L. Bruno, and C. K. Kasirajan, "Room temperature ammonia gas sensor using Nd - doped - SnO 2 thin films and its characterization," *J. Mater. Sci. Mater. Electron.*, vol. 31, no. 15, pp. 12586–12594, 2020, doi: 10.1007/s10854-020-03809-6.

[191] C. Terrier, J. P. Chatelon, and J. A. Roger, "Electrical and optical properties of Sb:SnO2 thin films obtained by the sol-gel method," *Thin Solid Films*, vol. 295, no. 1–2, pp. 95–100, 1997, doi: 10.1016/S0040-6090(96)09324-8.

[192] Jiya, S. D. Lawaniya, G. Pandey, N. Saini, and K. Awasthi, "PANI/CD/SnO2 Ternary Nanocomposite for Efficient Room-Temperature Ammonia Detection," *J. Electron. Mater.*, vol. 53, no. 9, pp. 5103–5117, 2024, doi: 10.1007/s11664-024-11168-9.

[193] S. D. Ponja, B. A. D. Williamson, S. Sathasivam, D. O. Scanlon, I. P. Parkin, and C. J. Carmalt, "Enhanced electrical properties of antimony doped tin oxide thin films deposited via aerosol assisted chemical vapour deposition," *J. Mater. Chem. C*, vol. 6, no. 27, pp. 7257–7266, 2018, doi: 10.1039/C8TC01929K.

[194] D. Fang, C. Li, N. Wang, P. Li, and P. Yao, "Structural and optical properties of Mg-doped ZnO thin films prepared by a modified Pechini method," *Cryst. Res. Technol.*, vol. 48, no. 5, pp. 265–272, May 2013, doi: 10.1002/crat.201200437.

[195] K. K. Singha and S. K. Srivastava, "Dielectric, resistivity, and current–voltage characteristics of magnesium-doped tin oxide for optoelectronics application," *J. Mater. Sci. Mater. Electron.*, vol. 35, no. 21, pp. 1–15, 2024, doi: 10.1007/s10854-024-13231-x.

[196] R. Hong *et al.*, "Compositional Engineering of Cu-Doped SnO Film for

Complementary Metal Oxide Semiconductor Technology," 2024, doi: 10.1021/acs.nanolett.3c03953.

[197] F. H. Aragón *et al.*, "Structural and Surface Study of Praseodymium-Doped SnO 2 Nanoparticles Prepared by the Polymeric Precursor Method," *J. Phys. Chem. C*, vol. 119, no. 16, pp. 8711–8717, Apr. 2015, doi: 10.1021/acs.jpcc.5b00761.

[198] S. A. P. Sakthivel, M. K. Y. Hayakawa, and A. L. G. Ravi, "Improved photocatalytic performance of nanostructured - SnO 2 under visible light irradiation," *Appl. Phys. A*, pp. 1–12, 2020, doi: 10.1007/s00339-020-3441-8.

[199] G. Kiruthiga, K. S. Rajni, N. Geethanjali, T. Raguram, E. Nandhakumar, and N. Senthilkumar, "Sno2 : Investigation of Optical , Structural , and Electrical Properties of Transparent Conductive Oxide Thin Films Prepared by Nebulized Spray Pyrolysis for Photovoltaic Applications SnO 2 : Investigation of optical , structural , and electrical properti," *Inorg. Chem. Commun.*, no. October, p. 109968, 2022, doi: 10.1016/j.inoche.2022.109968.

[200] W. Daranfed, K. Mirouh, N. Guermat, and M. Khalfallah, "Effect of film thickness on the structural and optical properties of SnO <inf>2</inf> thin films prepared by ultrasonic spray pyrolysis," in *2018 International Conference on Communications and Electrical Engineering (ICCEE)*, IEEE, Dec. 2018, pp. 1–4. doi: 10.1109/CCEE.2018.8634557.

[201] S. Vadivel and G. Rajarajan, "Effect of Mg doping on structural, optical and photocatalytic activity of SnO2 nanostructure thin films," *J. Mater. Sci. Mater. Electron.*, vol. 26, no. 5, pp. 3155–3162, 2015, doi: 10.1007/s10854-015-2811-z.

[202] A. Bala, S. Rani, A. Sharma, P. E. Lokhande, and D. Kumar, "Effect of Cobalt doping on luminescence properties of gadolinium aluminum garnet," *J. Mater. Sci. Mater. Electron.*, vol. 34, no. 36, pp. 1–15, 2023, doi: 10.1007/s10854-023-11621-1.

[203] D. Iskenderoğlu and H. Güney, "Effect of Mg dopant on SnO 2 thin films

grown by spray pyrolysis technique," *Mod. Phys. Lett. B*, vol. 33, no. 4, 2019, doi: 10.1142/S0217984919500301.

[204] Z. Gültekin, M. Alper, M. C. Hacıismailoğlu, and C. Akay, "Effect of Mn doping on structural, optical and magnetic properties of ZnO films fabricated by sol–gel spin coating method," *J. Mater. Sci. Mater. Electron.*, vol. 34, no. 5, pp. 1–14, 2023, doi: 10.1007/s10854-023-09886-7.

[205] J. S. Revathy, N. S. C. Priya, K. Sandhya, and D. N. Rajendran, "Structural and optical studies of cerium doped gadolinium oxide phosphor," *Bull. Mater. Sci.*, vol. 44, no. 1, p. 13, Apr. 2021, doi: 10.1007/s12034-020-02299-w.

[206] A. L. Patterson, "The Scherrer Formula for X-Ray Particle Size Determination," *Phys. Rev.*, vol. 56, no. 10, pp. 978–982, Nov. 1939, doi: 10.1103/PhysRev.56.978.

[207] R. Jayaprakash, S. Bakshi, K. Rani, and S. Rani, "Defect Induced high-color-rendering white light emissions from Ag-doped ZnO," *IOP Conf. Ser. Earth Environ. Sci.*, vol. 1285, no. 1, 2024, doi: 10.1088/1755-1315/1285/1/012034.

[208] S. Kumar, S. Bakshi, S. Chaudhary, J. Kaur, A. P. Agrawal, and S. Rani, "Heat Post-Treatment Effect on Optical and Electrical Properties of ZnS Thin Films," *Biointerface Res. Appl. Chem.*, vol. 14, no. 4, p. 100, Aug. 2024, doi: 10.33263/BRIAC144.100.

[209] R. Murugan *et al.*, "Pure and alkaline metal ion (Mg, Ca, Sr, Ba) doped cerium oxide nanostructures for photo degradation of methylene blue," *Mater. Res. Bull.*, vol. 97, pp. 319–325, Jan. 2018, doi: 10.1016/j.materresbull.2017.09.026.

[210] K. Kasirajan, L. Bruno Chandrasekar, S. Maheswari, M. Karunakaran, and P. Shunmuga Sundaram, "A comparative study of different rare-earth (Gd, Nd, and Sm) metals doped ZnO thin films and its room temperature ammonia gas sensor activity: Synthesis, characterization, and investigation on the impact of dopant," *Opt. Mater. (Amst).*, vol. 121, no. August, p. 111554, 2021, doi: 10.1016/j.optmat.2021.111554.

[211] V. S. Jahnavi, S. K. Tripathy, and A. V. N. R. Rao, "Study of the Structural,

Optical, Dielectric and Magnetic Properties of Copper-Doped SnO2 Nanoparticles," *J. Electron. Mater.*, vol. 49, no. 6, pp. 3540–3554, 2020, doi: 10.1007/s11664-020-08028-7.

[212] G. Mathew, P. Chamoli, A. Philip, and A. R. Kumar, "Effects of Copper Doping on the Electrochemical Performance of Tin Oxide Synthesised by Facile Co-precipitation Root," *Int. J. Environ. Res.*, vol. 18, no. 3, pp. 1–14, 2024, doi: 10.1007/s41742-024-00587-5.

[213] S. Nilavazhagan, S. Muthukumaran, and M. Ashokkumar, "Microstructural and band gap exploration on Ni-doped SnO2 nanoparticles co-doped with Cu," *J. Mater. Sci. Mater. Electron.*, vol. 26, no. 6, pp. 3989–3996, Jun. 2015, doi: 10.1007/s10854-015-2935-1.

[214] M. Ashokkumar and S. Muthukumaran, "Zn0.96−xCu0.04FexO (0⩽x⩽0.04) alloys – Optical and structural studies," *Superlattices Microstruct.*, vol. 69, pp. 53–64, May 2014, doi: 10.1016/j.spmi.2014.02.002.

[215] "Studying the Infrared Spectroscopy of the SnO2: Sb (x= 0.00,0.01) Powders," *Chem. Mater. Res.*, May 2020, doi: 10.7176/CMR/10-5-02.

[216] M. A. Y. Barakat, M. Shaban, and A. M. El Sayed, "Structural , ultrasonic and spectroscopic studies of tin oxide thin films ; effect of Ir and (Ni , Ir) double doping Structural , ultrasonic and spectroscopic studies of tin oxide thin fi lms ; effect of Ir and (Ni , Ir) double doping".

[217] A. S. Altowyan, M. Shaban, K. Abdelkarem, and A. M. El Sayed, "The Impact of Co Doping and Annealing Temperature on the Electrochemical Performance and Structural Characteristics of SnO2 Nanoparticulate Photoanodes," *Materials (Basel).*, vol. 15, no. 19, p. 6534, Sep. 2022, doi: 10.3390/ma15196534.

[218] N. C. Horti, M. D. Kamatagi, N. R. Patil, M. N. Wari, and S. R. Inamdar, "Photoluminescence properties of SnO2 nanoparticles: Effect of solvents," *Optik (Stuttg).*, vol. 169, pp. 314–320, Sep. 2018, doi: 10.1016/j.ijleo.2018.05.085.

[219] B. Skariah, J. Naduvath, and B. Thomas, "Effect of long term ageing under humid environment on the LPG sensing properties and the surface composition of Mg-doped SnO 2 thin films," *Ceram. Int.*, vol. 42, no. 6, pp. 7490–7498, May 2016, doi: 10.1016/j.ceramint.2016.01.155.

[220] S. Roguai and A. Djelloul, "Elaboration, characterization and applications of SnO2, 2 %Gd-SnO2 and 2 %Gd-9 %F-SnO2 thin films for the photocatalytic degradation of MB by USP method," *Inorg. Chem. Commun.*, vol. 138, p. 109308, Apr. 2022, doi: 10.1016/j.inoche.2022.109308.

[221] J. Shanthi, A. S., and S. R., "Fabrication of Roughness Enhanced Hydrophobic Coatings," *J. Nano- Electron. Phys.*, vol. 12, no. 2, pp. 02042-1-02042–4, 2020, doi: 10.21272/jnep.12(2).02042.

[222] S. M. Ali, J. Muhammad, S. T. Hussain, S. D. Ali, N. U. Rehman, and M. H. Aziz, "Annealing effect on structural, optical and electrical properties of pure and Mg doped tin oxide thin films," *J. Mater. Sci. Mater. Electron.*, vol. 24, no. 12, pp. 4925–4931, 2013, doi: 10.1007/s10854-013-1499-1.

[223] A. Kubacka, G. Colón, and M. Fernández-García, "Cationic (V, Mo, Nb, W) doping of TiO2–anatase: A real alternative for visible light-driven photocatalysts," *Catal. Today*, vol. 143, no. 3–4, pp. 286–292, May 2009, doi: 10.1016/j.cattod.2008.09.028.

[224] S. M. Meteab and J. F. Mohammad, "Effect of Cu-Doping Levels on the Structural and Optical Properties of SnO2 Thin Films Prepared by Chemical Spray Pyrolysis," *Rev. des Compos. des Mater. Av.*, vol. 33, no. 5, pp. 311–316, 2023, doi: 10.18280/rcma.330505.

[225] E. Eqbal and E. I. Anila, "P type copper doped tin oxide thin films and p-n homojunction diodes based on them," *Opt. Mater. (Amst).*, vol. 118, no. June, p. 111281, 2021, doi: 10.1016/j.optmat.2021.111281.

[226] S. Nilavazhagan and S. Muthukumaran, "Investigation of optical and structural properties of Fe, Cu co-doped SnO2 nanoparticles," *Superlattices Microstruct.*, vol. 83, pp. 507–520, Jul. 2015, doi: 10.1016/j.spmi.2015.03.036.

[227] A. B. Ali Baig, V. Rathinam, and J. Palaninathan, "Facile synthesis of Ce-doped SnO2 nanoparticles with enhanced performance for photocatalytic degradation of organic dye," *J. Iran. Chem. Soc.*, vol. 18, no. 1, pp. 13–27, Jan. 2021, doi: 10.1007/s13738-020-02000-2.

[228] S. V. Mohammadi, F. E. Ghodsi, and J. Mazloom, "Sol-gel combustion synthesis of porous Mg 2 SnO 4 @ SnO 2 nanocomposites : A study on the structural parameters , optical properties , and electrochemical activity," *Ceram. Int.*, vol. 50, no. 4, pp. 6425–6440, 2024, doi: 10.1016/j.ceramint.2023.11.382.

[229] A. M. Ganose and D. O. Scanlon, "Band gap and work function tailoring of SnO 2 for improved transparent conducting ability in photovoltaics," *J. Mater. Chem. C*, vol. 4, no. 7, pp. 1467–1475, 2016, doi: 10.1039/C5TC04089B.

[230] T. N. Soitah, C. Yang, and L. Sun, "Structural, optical and electrical properties of Fe-doped SnO2 fabricated by solgel dip coating technique," *Mater. Sci. Semicond. Process.*, vol. 13, no. 3, pp. 125–131, 2010, doi: 10.1016/j.mssp.2010.03.002.

[231] P. S. Shajira, M. J. Bushiri, B. B. Nair, and V. G. Prabhu, "Energy band structure investigation of blue and green light emitting Mg doped SnO2 nanostructures synthesized by combustion method," *J. Lumin.*, vol. 145, pp. 425–429, Jan. 2014, doi: 10.1016/j.jlumin.2013.07.073.

[232] P. Wu, B. Zhou, and W. Zhou, "Room-temperature ferromagnetism in epitaxial Mg-doped SnO2 thin films," *Appl. Phys. Lett.*, vol. 100, no. 18, Apr. 2012, doi: 10.1063/1.4711220.

[233] X. Li *et al.*, "Effect of Mg doping on optical and electrical properties of SnO2 thin films: An experiment and first-principles study," *Ceram. Int.*, vol. 42, no. 4, pp. 5299–5303, Mar. 2016, doi: 10.1016/j.ceramint.2015.12.059.

[234] S. S. Roy and J. Podder, "Synthesis and optical characterization of pure and Cu doped SnO2 thin films deposited by spray pyrolysis," *J. Optoelectron. Adv. Mater.*, vol. 12, no. 7, pp. 1479–1484, 2010.

[235] M. R. Hasan, M. A. Sayeed, and K. M. A. Hussain, "Effect of Aluminium (Al) and Copper (Cu) Doping on Characteristics of Tin Oxide (SnO2) Thin Film," *2020 IEEE Reg. 10 Symp. TENSYMP 2020*, no. June, pp. 1172–1175, 2020, doi: 10.1109/TENSYMP50017.2020.9230800.

[236] Susilawati, A. Doyan, L. Muliyadi, S. Hakim, and M. Taufik, "The thickness effect to optical properties of SnO 2 thin film with doping fluorine," *J. Phys. Conf. Ser.*, vol. 1572, no. 1, p. 012085, Jun. 2020, doi: 10.1088/1742-6596/1572/1/012085.

[237] T. M. Al-Saadi, B. H. Hussein, A. B. Hasan, and A. A. Shehab, "Study the Structural and Optical Properties of Cr doped SnO2 Nanoparticles Synthesized by Sol-Gel Method," *Energy Procedia*, vol. 157, pp. 457–465, Jan. 2019, doi: 10.1016/j.egypro.2018.11.210.

[238] K. Kesavan, A. Kathalingam, H.-S. Kim, and A. R. U. Sundari, "Effects of fluorine doping on structural, optical and electrical properties of spray deposited CdO thin films," *Superlattices Microstruct.*, vol. 100, pp. 76–88, Dec. 2016, doi: 10.1016/j.spmi.2016.09.004.

[239] L. N. Ezenwaka, N. S. Umeokwonna, and N. L. Okoli, "Optical, structural, morphological, and compositional properties of cobalt doped tin oxide (CTO) thin films deposited by modified chemical bath method in alkaline medium," *Ceram. Int.*, vol. 46, no. 5, pp. 6318–6325, Apr. 2020, doi: 10.1016/j.ceramint.2019.11.106.

[240] S. M. Ali, J. Muhammad, S. T. Hussain, S. A. Bakar, M. Ashraf, and Naeem-Ur-Rehman, "Study of microstructural, optical and electrical properties of Mg dopped SnO thin films," *J. Mater. Sci. Mater. Electron.*, vol. 24, no. 7, pp. 2432–2437, 2013, doi: 10.1007/s10854-013-1114-5.

[241] W. Daranfed, "Analysis of the effect of copper concentration on the structural , morphological , optical and electrical properties of Cu : SnO 2 thin films," no. November 2021, 2022.

[242] X. Li *et al.*, "Effect of Mg doping on optical and electrical properties of SnO2

thin films: An experiment and first-principles study," *Ceram. Int.*, vol. 42, no. 4, pp. 5299–5303, 2016, doi: 10.1016/j.ceramint.2015.12.059.

[243] G. Charrada, M. Ajili, N. Jebbari, and N. T. Kamoun, "Investigation on physical properties of CuO and - SnO 2 : F mixed oxide sprayed thin films for photocatalytic application : coupling effect between oxides," *J. Mater. Sci. Mater. Electron.*, vol. 35, no. 10, pp. 1–17, 2024, doi: 10.1007/s10854-024-12453-3.

[244] H. Bendjedidi *et al.*, "Properties of n-type SnO 2 semiconductor prepared by spray ultrasonic technique for photovoltaic applications," *J. Semicond.*, vol. 36, no. 12, p. 123002, Dec. 2015, doi: 10.1088/1674-4926/36/12/123002.

[245] P. Senthilkumar, S. Raja, R. Ramesh Babu, and G. Vasuki, "Influence of Ru doping on the structural, morphological, optical, electrical and optoelectronic properties of SnO2 thin films," *J. Phys. Chem. Solids*, vol. 174, p. 111177, Mar. 2023, doi: 10.1016/j.jpcs.2022.111177.

[246] V. Kumar, P. Rajaram, and Y. C. Goswami, "Sol gel synthesis of SnO2/CdSe nanocomposites and their optical structural and morphological characterizations," *Optik (Stuttg).*, vol. 127, no. 5, pp. 2490–2494, Mar. 2016, doi: 10.1016/j.ijleo.2015.11.167.

[247] S. KULKARNI and D. PATIL, "Effect of Firing Temperature on Electrical and Structural Characteristics of Screen Printed In2O3 Thick Films," *DEStech Trans. Environ. Energy Earth Sci.*, vol. 3, no. seeie, pp. 879–883, Dec. 2016, doi: 10.12783/dteees/seeie2016/4653.

[248] A. Raza, H. Noor, S. Riaz, and S. Naseem, "Modifying the Optical Properties of ZnS for Optoelectronic Applications," in *INTERACT 2023*, Basel Switzerland: MDPI, Apr. 2023, p. 18. doi: 10.3390/engproc2023032018.

[249] M. T. Sebastian and P. Krishna, "Anomalous photovoltaic effect and disorder in ZnS crystals," *Bull. Mater. Sci.*, vol. 5, no. 3–4, pp. 257–266, Aug. 1983, doi: 10.1007/BF02744040.

[250] C. Wang, B. Hu, L. Chen, and Y. Ye, "The investigation of ZnS/Au/ZnS

transparent conductive films with different Au layer thickness," *Jpn. J. Appl. Phys.*, vol. 59, no. 5, p. 055505, May 2020, doi: 10.35848/1347-4065/ab8c61.

[251] A. M. Abdalla *et al.*, "Evaluation of structural, optical, and scintillation characteristics of Ag activated ZnS nanoparticles," *Radiat. Phys. Chem.*, vol. 210, p. 110999, Sep. 2023, doi: 10.1016/j.radphyschem.2023.110999.

[252] C. Tsu, J. Lee, C. Liu, Y. Su, T. Wu, and M. Yokoyama, "ZnS: Mn thin film electroluminescent display devices using hafnium dioxide as insulating layer," *Vacuum*, vol. 42, no. 16, p. 1047, 1991, doi: 10.1016/0042-207X(91)91286-W.

[253] M. Bhardwaj, D. Gupta, J. Shrivastava, and R. K. Pandey, "Structural, optical and morphological properties of Mn:Cu co-doped ZnS films," *J. Mater. Sci. Mater. Electron.*, vol. 36, no. 6, pp. 1–19, 2025, doi: 10.1007/s10854-025-14420-y.

[254] M. Sathishkumar, M. Saroja, and M. Venkatachalam, "Influence of (Cu, Al) doping concentration on the structural, optical and antimicrobial activity of ZnS thin films prepared by Sol-Gel dip coating techniques," *Optik (Stuttg).*, vol. 182, pp. 774–785, 2019, doi: 10.1016/j.ijleo.2019.02.014.

[255] S. Mandal, S. I. Ali, and A. C. Mandal, "Investigation of structural, optical and photoluminescence properties of the sol–gel synthesized powder ZnS nanoparticles," *Appl. Phys. A Mater. Sci. Process.*, vol. 129, no. 3, pp. 1–10, 2023, doi: 10.1007/s00339-023-06499-z.

[256] Z. Hamed, K. E. Ahmed, and H. Elsheikh, "Synthesis and Characterization of ZnS Nanoparticles by Chemical Precipitation Method," *Aswan Univ. J. Environ. Stud.*, vol. 0, no. 0, pp. 0–0, 2021, doi: 10.21608/aujes.2021.66918.1014.

[257] H. Labiadh, Y. Moualhi, K. Moualhi, A. Othmani, and M. Zouaoui, "Synthesis of ZnS nanoparticles and the investigation of their structural, optical and electrical properties," *Euro-Mediterranean J. Environ. Integr.*, no. March, 2024, doi: 10.1007/s41207-024-00691-0.

[258] L. Pushpadevi and P. Arts, "ELECTRO-OPTICAL PROPERTIES OF CU-

DOPED ZNS THIN FILM USED AS WINDOW LAYER IN SOLAR CELL
Arun S Garde Department of Physics , S P H Arts , Science and Commerce
College Nampur 423204 , India .,” vol. 4, no. 2, pp. 434–445, 2021.

[259] H. Labiadh, Y. Moualhi, K. Moualhi, A. Othmani, and M. Zouaoui, “Synthesis
of ZnS nanoparticles and the investigation of their structural, optical and
electrical properties,” *Euro-Mediterranean J. Environ. Integr.*, no. November,
2024, doi: 10.1007/s41207-024-00691-0.

[260] R. K. Srivastava, N. Pandey, and S. K. Mishra, “Effect of Cu concentration on
the photoconductivity properties of ZnS nanoparticles synthesized by co-
precipitation method,” *Mater. Sci. Semicond. Process.*, vol. 16, no. 6, pp.
1659–1664, 2013, doi: 10.1016/j.mssp.2013.06.009.

[261] M. S. Rana, S. K. Das, M. O. Rahman, F. Ahmed, and M. A. Hossain,
“Vanadium Doped ZnS Nanoparticles: Effect of Vanadium Concentration on
Structural, Optical and Electrical Properties,” *Trans. Electr. Electron. Mater.*,
vol. 22, no. 5, pp. 612–621, Oct. 2021, doi: 10.1007/s42341-020-00265-1.

[262] K. Bera, S. Saha, and P. Chandra Jana, “Temperature dependent Synthesis of
Zinc Sulfide Nanocrystals,” *Orient. J. Chem.*, vol. 34, no. 3, pp. 1665–1669,
Jun. 2018, doi: 10.13005/ojc/340363.

[263] P. Iranmanesh, S. Saeednia, and M. Nourzpoor, “Characterization of ZnS
nanoparticles synthesized by co-precipitation method,” *Chinese Phys. B*, vol.
24, no. 4, p. 046104, Apr. 2015, doi: 10.1088/1674-1056/24/4/046104.

[264] A. H. Ali, H. A. Hashem, and A. Elfalaky, “Preparation, Properties, and
Characterization of ZnS Nanoparticles,” in *ASEC 2022*, Basel Switzerland:
MDPI, Dec. 2022, p. 74. doi: 10.3390/ASEC2022-13829.

[265] S. Dilpazir, M. Siddiq, and A. Iqbal, “Synthesis of Zinc Sulphide
Nanostructures by Co-precipitation: Effects of Doping on Electro-optical
Properties,” *Kenkyu J. Nanotechnol. Nanosci.*, vol. 1, p. 34, 2015.

[266] Ş. Uzun Çam, T. Serin, and A. N. Yazıcı, “Effect of Sn doping concentration
on structural, optical and electrical properties of ZnS/p-Si (111) diodes

fabricated by sol-gel dip-coating method," *Mater. Sci. Semicond. Process.*, vol. 127, no. January, 2021, doi: 10.1016/j.mssp.2021.105693.

[267] X. Xu *et al.*, "Chemical Bath Deposition of p-Type Transparent, Highly Conducting (CuS)x:(ZnS)1-x Nanocomposite Thin Films and Fabrication of Si Heterojunction Solar Cells," *Nano Lett.*, vol. 16, no. 3, pp. 1925–1932, 2016, doi: 10.1021/acs.nanolett.5b05124.

[268] M. Aslam Manthrammel, E. Muhammed Jubeer, P. A. Subha, M. Shkir, and S. AlFaify, "Er-doped ZnS QDs like NPs for optoelectronic applications: a facile microwave-assisted synthesis," *J. Mater. Sci. Mater. Electron.*, vol. 35, no. 19, pp. 1–15, 2024, doi: 10.1007/s10854-024-13045-x.

[269] J. O. Emegha, C. M. Okafor, and K. E. Ukhurebor, "Optical properties of copper-zinc sulphide network from mixed single solid source precursors of copper and zinc dithiocarbamates," *Walailak J. Sci. Technol.*, vol. 18, no. 9, 2021, doi: 10.48048/wjst.2021.9535.

[270] D. J. Vidhya Raj, C. Justin Raj, and S. Jerome Das, "Synthesis and optical properties of cerium doped zinc sulfide nano particles," *Superlattices Microstruct.*, vol. 85, pp. 274–281, Sep. 2015, doi: 10.1016/j.spmi.2015.04.029.

[271] I. Boukhoubza *et al.*, "Graphene oxide coated flower-shaped ZnO nanorods: Optoelectronic properties," *J. Alloys Compd.*, vol. 831, p. 154874, Aug. 2020, doi: 10.1016/j.jallcom.2020.154874.

[272] J. Zhao and J. M. Cole, "Reconstructing Chromatic-Dispersion Relations and Predicting Refractive Indices Using Text Mining and Machine Learning," *J. Chem. Inf. Model.*, vol. 62, no. 11, pp. 2670–2684, Jun. 2022, doi: 10.1021/acs.jcim.2c00253.

[273] M. Caglar, Y. Caglar, and S. Ilican, "Investigation of the effect of Mg doping for improvements of optical and electrical properties," *Phys. B Condens. Matter*, vol. 485, pp. 6–13, Mar. 2016, doi: 10.1016/j.physb.2015.12.049.

[274] A. Jrad, T. Ben Nasr, and N. Turki-Kamoun, "Study of structural, optical and

photoluminescence properties of indium-doped zinc sulfide thin films for optoelectronic applications," *Opt. Mater. (Amst).*, vol. 50, pp. 128–133, Dec. 2015, doi: 10.1016/j.optmat.2015.10.011.

[275] K. S. Duncan *et al.*, "Characterisation of p-type ZnS:Cu transparent conducting films fabricated by high-temperature pulsed laser deposition," pp. 1–7, 2017, [Online]. Available: http://arxiv.org/abs/1711.07579

[276] J. Zimou *et al.*, "Structural, morphological, optical, and electrochemical properties of Co-doped CeO2 thin films," *Mater. Sci. Semicond. Process.*, vol. 135, p. 106049, Nov. 2021, doi: 10.1016/j.mssp.2021.106049.

[277] V. Anand *et al.*, "Rare earth Sm3+ co-doped AZO thin films for opto-electronic application prepared by spray pyrolysis," *Ceram. Int.*, vol. 44, no. 6, pp. 6730–6738, Apr. 2018, doi: 10.1016/j.ceramint.2018.01.088.

[278] A. I. Khudiar, M. K. Khalaf, and A. M. Ofui, "Improvement of the sensing characterizations of ZnO nanostructure by using thermal annealing prepared through R. F. magnetron sputtering technique," *Opt. Mater. (Amst).*, vol. 114, p. 110885, Apr. 2021, doi: 10.1016/j.optmat.2021.110885.

[279] H. Mahmood, M. A. Khan, B. Mohuddin, and T. Iqbal, "Solution-phase growth of tin oxide (SnO2) nanostructures: Structural, optical and photocatalytic properties," *Mater. Sci. Eng. B*, vol. 258, p. 114568, Aug. 2020, doi: 10.1016/j.mseb.2020.114568.

[280] A. Anžlovar, Z. Crnjak Orel, K. Kogej, and M. Žigon, "Polyol-Mediated Synthesis of Zinc Oxide Nanorods and Nanocomposites with Poly(methyl methacrylate)," *J. Nanomater.*, vol. 2012, no. 1, Jan. 2012, doi: 10.1155/2012/760872.

[281] A. A. Kumar and R. K. Jain, "Synthesis and Characterization of the Zinc-Oxide: Tin-Oxide Nanoparticle Composite and Assessment of Its Antibacterial Activity: An In Vitro Study," *Cureus*, Jan. 2024, doi: 10.7759/cureus.53016.

[282] Ü. Özgür *et al.*, "A comprehensive review of ZnO materials and devices," *J. Appl. Phys.*, vol. 98, no. 4, Aug. 2005, doi: 10.1063/1.1992666.

[283] M. Batzill and U. Diebold, "The surface and materials science of tin oxide," *Prog. Surf. Sci.*, vol. 79, no. 2–4, pp. 47–154, 2005, doi: 10.1016/j.progsurf.2005.09.002.

[284] F. Li, P. Li, and H. Zhang, "Preparation and Research of a High-Performance ZnO/SnO2 Humidity Sensor," *Sensors*, vol. 22, no. 1, p. 293, Dec. 2021, doi: 10.3390/s22010293.

[285] L. P. Dai, H. Deng, F. Y. Mao, and J. D. Zang, "The recent advances of research on p-type ZnO thin film," *J. Mater. Sci. Mater. Electron.*, vol. 19, no. 8–9, pp. 727–734, 2008, doi: 10.1007/s10854-007-9398-y.

[286] M. A. Shakil, S. Das, M. A. Rahman, U. S. Akther, M. K. Hassan, and M. K. Rahman, "A Review on Zinc Sulphide Thin Film Fabrication for Various Applications Based on Doping Elements," *Mater. Sci. Appl.*, vol. 09, no. 09, pp. 751–778, 2018, doi: 10.4236/msa.2018.99055.

[287] K. Rafique *et al.*, "Electrochemical performance evaluation of a newly developed ZnS–SnO2 composite in an aqueous electrolyte," *J. Mater. Sci. Mater. Electron.*, vol. 34, no. 24, p. 1717, Aug. 2023, doi: 10.1007/s10854-023-11124-z.

[288] V. Ratchagar and K. Jagannathan, "Synthesis and characterization of SnO2 nano particles for carbon absorbing applications," *Orient. J. Chem.*, vol. 32, no. 1, pp. 207–212, Mar. 2016, doi: 10.13005/ojc/320121.

[289] M. Bodke, H. Khawal, U. Gawai, and B. Dole, "Synthesis and Characterization of Chromium Doped Zinc Sulfide Nanoparticles," *OALib*, vol. 02, no. 05, pp. 1–8, 2015, doi: 10.4236/oalib.1101549.

[290] N. Kumar, S. Verma, J. Park, V. Chandra Srivastava, and M. Naushad, "Evaluation of photocatalytic performances of PEG and PVP capped zinc sulfide nanoparticles towards organic environmental pollutant in presence of sunlight," *Chemosphere*, vol. 298, p. 134281, Jul. 2022, doi: 10.1016/j.chemosphere.2022.134281.

[291] R. Dangi *et al.*, "Effect of Oxygen Vacancy on the Crystallinity and Optical

Band Gap in Tin Oxide Thin Film," *Energies*, vol. 16, no. 6, p. 2653, Mar. 2023, doi: 10.3390/en16062653.

[292] Y. Ding, T. Yang, N. Yin, F. Shu, Y. Zhao, and X. Zhang, "Synthesis of novel branched β-NaLuF4: Yb/Er upconversion luminescence material and investigation of its optical properties," *Opt. Mater. (Amst).*, vol. 79, pp. 408–412, May 2018, doi: 10.1016/j.optmat.2018.04.012.

[293] H. Zhong *et al.*, "Idealizing Tauc Plot for Accurate Bandgap Determination of Semiconductor with Ultraviolet–Visible Spectroscopy: A Case Study for Cubic Boron Arsenide," *J. Phys. Chem. Lett.*, vol. 14, no. 29, pp. 6702–6708, Jul. 2023, doi: 10.1021/acs.jpclett.3c01416.

[294] K. Han, X.-L. Peng, F. Li, and M.-M. Yao, "SnO2 Composite Films for Enhanced Photocatalytic Activities," *Catalysts*, vol. 8, no. 10, p. 453, Oct. 2018, doi: 10.3390/catal8100453.

[295] Q. You *et al.*, "Blue shift in absorption edge and widening of band gap of ZnO by Al doping and Al–N co-doping," *J. Alloys Compd.*, vol. 644, pp. 528–533, Sep. 2015, doi: 10.1016/j.jallcom.2015.05.060.

[296] A. Kaisha *et al.*, "Examining the Desirable Properties of ZnSnO y by Annealing Treatment with a Real-Time Observation of Resistivity," *ACS Omega*, vol. 9, no. 24, pp. 26205–26212, Jun. 2024, doi: 10.1021/acsomega.4c01857.

[297] X. Xu, S. Li, J. Chen, S. Cai, Z. Long, and X. Fang, "Design Principles and Material Engineering of ZnS for Optoelectronic Devices and Catalysis," *Adv. Funct. Mater.*, vol. 28, no. 36, Sep. 2018, doi: 10.1002/adfm.201802029.

List of Papers Published

1. Publication

Research Article

The influence of Mg and Cu doping on SnO_2 thin films for assessment of transparent conducting oxide

Shruti Bakshi, Suman Rani*

Department of Physics, School of Chemical Engineering & Physical Sciences, Lovely Professional University, Punjab 144411, India

ARTICLE INFO

ABSTRACT

This article represents the formation of undoped, Mg, and Cu-doped SnO_2 thin films that have been formed on a glass substrate by sol–gel spin coating method post-heated at 500 °C for one hour. In this research, the study compares thin films of SnO_2 that have been doped with magnesium (Mg^{2+}) and copper (Cu^{2+}) to see how well they conduct while remaining transparent. According to XRD analysis, undoped, Mg-doped, and Cu-doped SnO_2 thin films (at 0.1 %, 0.5 %, and 1.0 % doping levels) display a tetragonal rutile structure. In FTIR spectra, the Sn–O, Sn–O–Sn, and other oxide vibrational bands were identified. According to AFM investigations, the films grew uniformly, and the Mg^{2+} and Cu^{2+} doping reduced the average roughness of the thin films. The element composition for undoped, Mg, and Cu-doped SnO_2 thin films was analyzed by EDAX. The optical properties were investigated by UV–visible spectroscopy. With the doping of Mg and Cu on SnO_2 thin film, the transmission reaches 90 % to 99.5 % and 99.2 % in the visible spectra. The best transmission was achieved at 0.5 % Mg^{2+} doping. Electrical parameters were examined with the Hall effect measurements and the two-point technique. It was observed that with the Mg and Cu doping, the value of conductivity reaches 2.212×10^3 (Scm^{-1}) to 8.418×10^3 (Scm^{-1}) and 7.899×10^3 (Scm^{-1}) with high mobility and carrier concentration. Further, Mg doping shows the transformation of n to p-type conductivity at a high concentration (1.0 %). According to the figure of merit of $2.9 \times 10^{-2} \Omega^{-1}$, 0.5 % Mg-doped SnO_2 thin film performs superior indicating that it could potentially be used as transparent conducting oxides in optoelectronics devices such as photovoltaic devices, solar cells and display devices.

1. Introduction

The rising demand for transparent conducting oxides (TCO) thin films in the field of optoelectronic devices motivates researchers to the creation of affordable, flexible, and stable transparent conducting oxides (TCO) films with excellent transparency and highly conductive [1, 2]

[10] prepared indium tin oxide using a sol–gel spin coating method, achieving transparency of up to 85 %, and observed the lowest resistivity value of $4.14 \times 10^{-3} \Omega$ cm, indicating excellent conductivity — $10^3 \Omega cm^{-1}$. Additionally, their research produced a figure of merit of up to $8.68 \times 10^{-4} \Omega^{-1}$. The best films have been formed by using Indium tin oxide (ITO). But its availability in the market is limited and quite

2.Publication

Investigating the Impact of Annealing and Thickness on the Optical and Electrical Characteristics of ZnO (TCO) for Optoelectronics Devices

Shruti Bakshi and Suman Ravi

Department of Physics, School of Chemical Engineering & Physical Sciences, Lovely Professional University, Punjab-144411, India

Abstract: In this paper, we investigate Transparent Conducting Oxides (TCO) thin films, which have created immense interest in researchers due to their widespread utilization in optoelectronics devices. Annealing and thickness are two main characteristics of thin films that influence the optical and electrical properties of the ZnO thin films in terms of band gap energy. The goal of the study is to analyze the influence of annealing and thickness of thin films on the optical and electrical properties of zinc oxide thin films. The ZnO thin films were prepared with different layers, and annealing temperatures were at 300°C, 400°C and 500°C. In XRD analysis, ZnO thin films exhibit a hexagonal crystal structure and reveal that crystallite size increases with the increase of annealing temperature. The transmission is strongly influenced by annealing temperature and thickness. At 500°C and thickness 189nm, 83% transmission is achieved in the visible region. The conductivity and activation energy of the ZnO thin film increases with the increase of annealing temperature and decreases with the increase of thickness. At 500°C and 189nm thickness, the value of conductivity and activation energy is 1.02×10^{4}(Scm^{-1}) and E_{a_1}=0.570eV, E_{a_2}=0.865eV. The Figure of merit suggests that ZnO thin film will behave better at 500°C with 189nm among six deposition layers supporting its use as an affordable transparent conducting oxide thin film in optoelectronics devices.

Keywords: ZnO thin films, Transmission, Conductivity, Transparent Conducting Oxides, Optoelectronics devices, Solar cells.

1. Introduction

Over the past few decades, Transparent Conducting Oxides (TCO) thin films have created immense interest in researchers due to their widespread utilization in optoelectronics devices such as touch screens, liquid crystal displays, Light Emitting Diodes (LED), and solar cells [1-3]. Transparent Conducting Oxides (TCO) show the properties of high transmission and high electrical conductivity in the spectrum of visible region (380-700nm). Due to its excellent electrical conductivity and high transmission to visible light, Indium tin Oxide (ITO) is the most widely utilized transparent conducting oxide material [4]. However, there is crucial research in finding a suitable alternative material for ITO due to its huge price, toxicity, and scarcity of indium as it is the main component element [5]. In this concern, ZnO material has emerged as a promising candidate in place of ITO due to its lower price, non-toxicity, and thermal and chemical stability [6]. Cost-effectiveness and non-toxicity are crucial components in the part of the practical field [7]. ZnO thin film has tremendous applications in the fields of optoelectronics, electronics, corrosion protection, pharmaceutical industries,

and chemical industry [8]. The optical transparency and electrical properties are greatly affected by the thickness of thin films and their annealing temperature. ZnO thin film has versatile structural as well as optical and electrical properties [9-10]. Due to excellent transmission and conductive features, it is a useful candidate for touch screens, optoelectronics devices, and display devices. ZnO thin films exhibit a major appearance in the II-VI semiconductor material [11]. ZnO is an n-type semiconductor material with a direct wide band gap energy (3.37 eV) and large exciton binding energy (60 meV) at room temperature [12]. ZnO has three different structures: Wurtzite, Zinc Blende, and Rock salt. Pure Zinc oxide has a hexagonal wurtzite crystal structure with lattice parameters such as a=3.248A° and c=5.205A° [13]. Thin films of ZnO were already synthesized by several methodologies such as spray pyrolysis [14], Pulsed Laser Deposition (PLD) [15], hydrothermal process [16], magnetron sputtering[17], dip coating[18], electron beam evaporation[19], spin coating and Sol-gel method [20-24]. In this study, ZnO thin film is formed by the Sol-gel spin coating method over the place of other methods due to their simplicity, cost-benefit, and easy availability. The properties of the prepared thin films are influenced by various properties such as annealing

*Corresponding author E-mail: Suman.ravi@lpu.co.in

3.Publication

CHAPTER 8

Transparent Conducting Oxides Thin Film

SHRUTI BAKSHI and SUMAN RANI

Department of Physics, School of Chemical Engineering and Physical Sciences, Lovely Professional University, Punjab, India

ABSTRACT

Transparent conducting oxides (TCO's) have less absorption of light in the range of visible spectrum and high electrical properties and transmission. In 1907, the first transparent conducting oxide, i.e., cadmium oxide was explained by Badekar. Transparent conducting oxides (TCO's) are a semiconductor with a broadband gap and a high concentration of free electrons in the conduction band. Their energy value is higher than that of visible light. Display devices are transparent and conducting material. For this study increased electron carrier concentration produces electromagnetic radiation absorption in both the visible and infrared sections of the spectrum with the former being more essential. Transparent conducting oxides have vast applications such as solar cells, low e windows, liquid crystals, touch screens, automobile windows, defogging, dye-sensitive solar cells, organic-related solar cells, photovoltaic cells, carbon nanotubes, random metallic networks, perovskites, and LED. Generally, it is present in n-type and enhances the ability of the material. Mostly utilized TCOs are ITO, zinc oxide, aluminum zinc oxide, and P-type films. In this chapter, we focus on the transparent conducting oxide thin film. They are mostly fabricated with thin-film technologies and are also utilized in the areas of optoelectronic devices such as display devices, solar cells.

4.Publication

Heat Post-Treatment Effect on Optical and Electrical Properties of ZnS Thin Films

Sumit Kumar [1], Shruti Bakshi [1], Shilpa Chaudhary [1], Jasmeen Kaur [1], Anant Prakash Agrawal [2], Suman Rani [1,*]

1   Department of Physics, School of Chemical Engineering and Physical Sciences, Lovely Professional University, Punjab, India
2   Noida Institute of Engineering and Technology, Gr. Noida
*   Correspondence: suman.rani@lpu.co.in;

Scopus Author ID 57614868000

Abstract: Heat post-treatment involves subjecting the ZnS thin film to a high-temperature annealing process after deposition on a substrate. The primary goal of heat post-treatment is to improve the crystalline structure of the ZnS film, which can significantly impact its electrical and optical properties. Zinc sulfide (ZnS) films are broadly utilized in photovoltaic instruments because of their versatile properties. In this study, we deposited ZnS films on glass substrates using spin coating at a temperature of 500°C and investigated the impact of film thickness on their optical and electrical characteristics. We employed various characterization techniques such as UV-visible (UV-V) spectroscopy, X-ray diffraction (XRD), and two-point techniques to analyze the electrical and optical properties of ZnS thin films. During the heat treatment, the ZnS film is annealed, which promotes the formation of well-defined crystalline grains and reduces the number of defects in the film. A thin Zinc Sulfide film shows the film's thickness from 445 nm to 1778 nm. The electrical resistivity of the films was also measured and found to be in the range of 8.34×10^3 to 56.71×10^3 Ohm-m. Our results demonstrate the significant impact of film thickness on the electrical and optical properties of ZnS films, which can be useful in developing photovoltaic devices.

Keywords: ZnS; post heat treatment; transparent conducting material; thin films.

1. Introduction

Zinc sulfide (ZnS) is a versatile material with many applications, including optoelectronics, solar cells, and transparent conductive coatings. As a transparent conducting material, ZnS has several advantages over other normally utilized materials, such as fluorine-doped tin oxide (FTO) and indium tin oxide (ITO) [1]. One of the main advantages of ZnS is its high transparency in the visible region of the spectrum, making it suitable for use in transparent conductive coatings for displays and touchscreens [2,3]. Additionally, ZnS has a high refractive index, which can be used to enhance the performance of light-emitting devices and solar cells [4]. ZnS also has good electrical conductivity, making it a viable alternative to ITO and FTO for transparent conducting applications. ZnS has been shown to exhibit better conductivity than ITO in certain situations, particularly at high temperatures. Another advantage of ZnS is its abundance and low cost [5]. Unlike indium, a rare and expensive element, zinc is readily available and relatively inexpensive. This makes ZnS a more sustainable and cost-effective option for transparent conductive applications. Overall, the

5.Publication

Defect Induced high-color-rendering white light emissions from Ag-doped ZnO

R Jayaprakash, S Bakshi¹ ,K Rani¹and S Rani¹*

¹Department of Physics, School of Chemical Engineering & PhysicalSciences,
        Lovely Professional University, Punjab-144411, India
*Corresponding Author: Suman.rani@lpu.co.in

Abstract: It is crucial to find high-quality white-light phosphors that are simple to synthesize in order to create efficient lighting. In this pursuit, the focus has been on achieving the emission of white light in ZnO and Ag-doped ZnO emerging as a promising phosphor candidate. The optimized ZnO nano phosphors demonstrated visible-light emission with ideal Commission international de l E "Eclairage frequently abbreviated as coordinates (x = 0.33, y = 0.33) and a correlated color temperature of 6200 K, and a color rendering index of 100 for equivalent to day white light. Furthermore, under certain ideal processing conditions, neutral white-light emission (x = 0.33, y = 0.33 at λex = 280 and 370 nm) with a Color correlated temperature (CCT) of 5500 K(approx.) was achieved. The Color Rendering Index (CRI) of the ZnO and Ag:ZnO nanoparticles exceeded 90, with high values approaching 96%, which is necessary for accurately portraying object colors in comparison to natural sunshine. The research findings revealed a decrease in the PS emission intensity with all the UV excitation when Ag doped in ZnO, which aligns well with the principles of Stern-Volmer quenching. A reduction in intensity was observed which may be due to the Ag dopant interacting with the luminescent nanoparticles and causing a reduction in their emitted light. The study successfully develops and optimizes ZnO-based nano phosphors with tailored white-light emission characteristics, presenting a promising solution for achieving energy-efficient and high-quality white-light sources for various lighting applications.

Keywords: ZnO, White light emission, Energy-efficient, CIE,CRI, CCT

1. Introduction

ZnO is a semiconductor material that exhibits remarkable properties, making it suitable for white light emitting diode(WLED) It is a semiconductor of having a wide band gap with a high level of exciton binding energy, which allows it to emit ultraviolet (UV) light efficiently when it is excited by an

List of Conferences

1. 4th International Conference on Recent Advances in Fundamentals and Applied Sciences (RAFAS 2023) (March 24- 25, 2023), organized by the School of Chemical Engineering and Physical Sciences, Lovely Professional University, Punjab.

2. International Conference on Energy Materials and Rechargeable Batteries (IEMRB)-2023 (December 19-22, 2023), organized by the Department of Sciences (Physics), Manav Rachna University (MRU), Faridabad, Haryana, India.

3. 5th International Conference on Recent Advances in Fundamentals and Applied Sciences (RAFAS 2023) (March 19- 20, 2024) organized by the School of Chemical Engineering and Physical Sciences, Lovely Professional University, Punjab.

Certificate No. 329020

Certificate of Merit

This is to certify that **Dr./Mr./Ms. Shruti Bakshi** of **Lovely Professional University, Phagwara** stood **Third** in the Oral Presentation on **Optical and Electrical Properties of SnO$_2$ Thin Films with Varied Precursor Molarities** in the **5th International Conference on Recent Advances in Fundamental and Applied Sciences (RAFAS-2024)** held from 19th to 20th April 2024, organized by School of Chemical Engineering and Physical Sciences, Lovely Faculty of Technology and Sciences, at Lovely Professional University, Punjab.

Date of Issue : 20-05-2024
Place : Phagwara (Punjab), India

Prepared by
(Administrative Officer-Records)

Organizing Secretary
(RAFAS-2024)

Head of Faculty
Lovely Professional University

4. 3rd International Conference on Advanced Functional Materials and Devices (AFMD-2025) organised by Department of Physics under the aegis of IQAC ARSD College, University of Delhi (March 03-05,2025)

ATMA RAM SANATAN DHARMA COLLEGE
UNIVERSITY OF DELHI
Accredited Grade 'A++' By NAAC || All India 5th Rank in NIRF (Ministry of Education)

3rd International Conference on
Advanced Functional Materials and Devices (AFMD-2025)
for Sustainable Development
Under the aegis of IQAC and supported by Department of Biotechnology (GoI)

Certificate of Participation

This is to certify that Prof./Dr./Mr./Ms.

SHRUTI BAKSHI

LOVELY PROFESSIONAL UNIVERSITY

has participated in the 3rd International Conference on "Advanced Functional Materials & Devices for Sustainable Development" (AFMD-2025) organised by Department of Physics under the aegis of IQAC ARSD College, University of Delhi, India during March 03-05, 2025 in hybrid mode.

He/She has presented **oral talk** entitled:

OT-144:-Influence of Sintering Temperature on the ZnS Thin Films: Optical and Electrical Properties

Dr. Shankar Subramanian	Dr. Anjali Sharma	Prof. Vinita Tuli	Prof. Gyantosh Kumar Jha
Convener, AFMD-2025	Convener, AFMD-2025	Coordinator, IQAC	Principal/Patron AFMD-2025

Certificate No: ARSD/AFMD25/OT/151

234

List of Workshops

1. Workshop

2. Workshop

3. Workshop

4. Workhop